PHYSIK-DEPARTMENT

First Amplitude Analysis of Resonant Structures in the 5-Pion Continuum at COMPASS

Dissertation von Sebastian Neubert

TECHNISCHE UNIVERSITÄT
MÜNCHEN

TECHNISCHE UNIVERSITÄT MÜNCHEN
Physik-Department E18

First Amplitude Analysis of Resonant Structures in the 5-Pion Continuum at COMPASS

Sebastian Neubert

Vollständiger Abdruck der von der Fakultät für Physik der Technischen Universität München zur Erlangung des akademischen Grades eines

Doktors der Naturwissenschaften

genehmigten Dissertation.

Vorsitzender: Univ. -Prof. Dr. Wolfram Weise

Prüfer der Dissertation:

1. Univ.-Prof. Dr. Stephan Paul
2. Univ.-Prof. Walter Henning, Ph. D.

Die Dissertation wurde am 05.06.2012 bei der Technischen Universität München eingereicht und durch die Fakultät für Physik am 06.07.2012 angenommen.

Für Opa.

Abstract

The study of hadronic scattering amplitudes and in particular the spectroscopy of light mesons provide a unique tool to investigate the strong interaction. At very low energies the meson spectrum is governed by the spontaneous breakdown of the chiral symmetry of the QCD vacuum. At higher masses a series of resonances appears. Their origin and their relation to chiral symmetry breaking is only partly understood. In particular for masses above $\sim 1.6\,\mathrm{GeV}/c^2$ while a large number of states have been reported they are still poorly known experimentally. One complication are multi-body final states into which heavy mesons can decay. In this thesis a method for the amplitude analysis of the $\pi^-\pi^+\pi^-\pi^+\pi^-$ system is being developed. The COMPASS experiment at CERN uses the diffractive dissociation of a 190 GeV pion beam as a source of meson resonances up to masses of about $3\,\mathrm{GeV}/c^2$. A partial wave decomposition of the 5π system is presented here which for the first time allows to search for mesonic 5-body resonances. A novel technique based on an evolutionary algorithm is developed to solve the problem of finding a reliable truncation of the partial wave expansion of the hadronic amplitude. The method for the first time allows the investigation of systematic uncertainties introduced by the use truncated isobar model amplitudes. The well known $\pi_2(1670)$ and $\pi(1800)$ states are found with good agreement to measurements in other channels. In addition there is evidence for several other resonant contributions, among them the controversial $\pi_2(1880)$ which is being discussed as a hybrid-meson candidate. In the course of the analysis a new software-framework for amplitude analysis has been developed, which is now being used by the COMPASS collaboration for the analysis of several hadronic channels.

Future experiments in particle physics will have to collect large amounts of data in order to search for the subtle effects that would indicate new physics beyond the standard model or to be able to apply sophisticated analysis methods like the amplitude analysis presented in the first part of this thesis. Therefore, modern detectors have to operate at extremely high signal rates. A high-rate capable Time Projection Chamber (TPC) would be an ideal, large-volume charged-particle tracking detector. In order to investigate the possibilities to construct such a device a detailed simulation of a TPC has been implemented. With these tools it is demonstrated that the key challenges of event mixing and space-charge accumulation can indeed be solved.

Zusammenfassung

Das Studium hadronischer Streuamplituden und insbesondere die Spektroskopie leichter Mesonen stellt ein einzigartiges Werkzeug zur Untersuchung der Starken Wechselwirkung dar. Bei sehr kleinen Energien wird das Mesonenspektrum von der spontanen Brechung der chiralen Symmetrie des QCD-Vacuums bestimmt. Bei höheren Massen erscheint eine Serie von Resonanzen. Deren Ursprung und ihre Beziehung zur chiralen Symmetriebrechung sind nur teilweise verstanden. Insbesondere wurden bei Massen über $\sim 1.6\,\mathrm{GeV}/c^2$ Hinweise auf eine große Anzahl an Zuständen beobachtet deren Eigenschaften experimentell noch schlecht bekannt sind. Eine Komplikation bei solchen Messungen sind Mehrteilchen-Endzustände in welche diese schweren Mesonen zerfallen können.
In dieser Arbeit wird eine Methode für die Amplituden-Analyse des $\pi^-\pi^+\pi^-\pi^+\pi^-$ Systems entwickelt. Das COMPASS Experiment am CERN nutzt die diffraktive Dissoziation von Pionen mit einer Energie von $190\,\mathrm{GeV}$ als Quelle von mesonischen Resonanzen mit Massen bis zu etwa $3\,\mathrm{GeV}/c^2$. In dieser Arbeit wird eine Partialwellenzerlegung des 5π-Systems präsentiert, die es zum ersten Mal erlaubt nach 5-Körper Meson-Resonanzen zu suchen. Eine neuartige Technik, basierend auf einem evolutionären Algorithmus wird entwickelt, um das Problem der Suche nach einem verlässlichen Abbruchkriterium für die Partialwellenentwicklung der hadronischen Amplitude zu lösen. Mit Hilfe dieser Methode können zum ersten Mal systematische Messunsicherheiten, die aus der Wahl des Abbruchkriteriums folgen, abgeschätzt werden. Die wohlbekannten Zuständen $\pi_2(1670)$ und $\pi(1800)$ werden in guter Übereinstimmung mit Messungen in anderen Kanälen gefunden. Zudem gibt es Hinweise auf mehrere weitere resonante Beiträge, darunter das als Kandidaten für ein Hybrid-Meson kontrovers diskutierte $\pi_2(1880)$.
Im Verlauf der Analyse wurde eine neue Software für Amplituden-Analysen entwickelt, welche nun von der COMPASS Kollaboration für die Analyse weiterer hadronischer Kanäle verwendet wird.
Zukünftige Experimente in der Teilchenphysik werden große Datenmengen sammeln müssen um nach den subtilen Effekten suchen zu können, die auf neue Physik jenseits des Standardmodels hinweisen könnten, oder um ausgefeilte Analysemethoden wie die Amplitudenanalyse, die im ersten Teil der Arbeit präsentiert wird, anwenden zu können. Aus diesem Grund müssen moderne Detektoren bei hohen Signalraten betrieben werden. Eine hochratenfähige Zeit-Projektions-Kammer (Time Projection Chamber, TPC) wäre ein idealer Spurdetektor für geladene Teilchen, der große Volumen abdecken kann. Um die Möglichkeiten für die Konstruktion eines solchen Gerätes zu untersuchen wurde eine detailierte Computersimulation geschrieben. Mit diesem Werkzeug wurde demonstriert, dass Schlüsselprobleme, wie das Event-Mixing und die Akkumulation von Raumladung in der Kammer lösbar sind.

Acknowledgements

I want to thank Prof. Stephan Paul for giving me the opportunity to work as a member of the E18 group. Especially I would like to thank him for the confidence he has placed in me as I choose the more risky topic, twice. I am grateful for his constant support and all the opportunities I could enjoy during the past years. Sincerest thanks to Bernhard Ketzer, who always was guidance and example for me. From him I learned never to forget the passion for nature despite all the hardships of the daily science grind. I would like to thank Jan Friedrich for introducing me to the COMPASS community and teaching me programming as well as physics. Prof. Suh-Urk Chung's enthusiasm for hadron physics kept me going through many months. I am grateful for everything he taught me. Dima Ryabchikov always had an open ear for analysis problems and most of the time even the solution. It was a great pleasure to work with him. I cannot thank Boris Grube enough. We had a great collaboration on `rootpwa` and I owe him more than one discovered bug. Also many thanks for proof-reading many pages of this thesis. For her advice and kind support I would like to thank Prof. Laura Fabietti. I am indebted to the COMPASS collaboration and the CERN SPS team, who built and operated a marvelous machine and took beautiful data. The results in this thesis would not have been possible without all this work. The tools of the programming trade I learned in earnest from Matthias Steinke, Marc Pelizäus and Bertram Kopf from the BaBar/PANDA computing group. Without the excellent computing support at E18, in particular the work by Thiemo Nagel, Markus Krämer and Felix Böhmer this thesis would not have been possible. Karin Frank was always there when administration was about to get the better of the physicist. I thank her for her patience and support.
Sincerest thanks to all my colleagues at E18. Quirin Weitzel, for a wonderful time as TPC- and PWA-pioneers. Christian Höppner, for an incredibly fruitful train-trip and the PANDA-Bingo. Steffi Grabmüller, for pulling off an amazing analysis. Florian Haas, for his enthusiasm and long discussions at CERN. Thiemo Nagel, for sharing the "Politbüro" with me, fair coffee and companionship. Sebastian Uhl, Alex Austregesilo and the many students in the COMPASS group have been great colleagues. Markus Ball, Maxence Vandenbroucke, Sverre Dørheim, Martin Berger, Jia-Chii Berger-Chen and Johannes Rauch — you are such a cool TPC-Crew. Special thanks to Felix Böhmer, for nerd-adventures, for spoiling me and for his friendship. It has been a privilege working with you all.

My parents have made it possible to fulfill my dream of becoming a scientist. Their support and their love is immeasurable. To my sister I say thank you for simply being there for me.
The one person who was always with me through all ups and downs was Bettina. She endured many a physicist's quirks and kept my coming from the ivory tower to our vegetable garden. I thank her for keeping my feet on the ground, for challenging my assumptions and for her compassion.

Contents

Chapter 1

Introduction: Light–Meson Spectroscopy

> In her [Nature's] inventions nothing is lacking, and nothing is superfluous.
>
> Leonardo da Vinci

Spectroscopy has been an experimental tool for quantum physics since the early beginnings of its development. The study of the bound states of atomic and nuclear systems and the transitions between those states has been one of the cornerstones of the development of modern physics and of particle physics in particular. Today the frontier of spectroscopy in this field lies in the investigation of bound or resonant systems of strongly interacting particles. In this introductory chapter an overview of this topic will be given in order to provide background and context for the data analysis presented in this thesis. This introduction is not meant to be an exhaustive discussion on strong interaction physics but rather an outline of important concepts and a collection of references that have been useful for the author.

Hadron physics — the study of strongly interacting particles, the *hadrons* — is a wide field spanning from the interactions of the elementary fields that carry the charges of the strong force, the *quarks* and the *gluons*, to the nuclei of atoms which build up the baryonic matter our environment consists of.

There are 6 known quarks which are organized into three families as shown in table 1.1. The u-type quarks have electric charge $q_{u,c,t} = +\frac{2}{3}e$ and the d-type quarks have $q_{d,s,b} = -\frac{1}{3}e$, where e is the absolute value of the electric charge of the electron.

up ***u***	charm ***c***	top ***t***
$m_u = 1.7 - 3.3\,\mathrm{MeV}/c^2$	$m_c = 1.27^{+0.07}_{-0.09}\,\mathrm{GeV}/c^2$	$m_t = 172.0 \pm 0.9 \pm 1.6\,\mathrm{GeV}/c^2$
down ***d***	strange ***s***	bottom ***b***
$m_d = 4.1 - 5.8\,\mathrm{MeV}/c^2$	$m_s = 101^{29}_{-21}\,\mathrm{MeV}/c^2$	$m_b = 4.19^{0.18}_{-0.06}\,\mathrm{GeV}/c^2$

Table 1.1: Quark masses. From [1], for the precise definition of the quark masses see there.

From the quark masses listed here the special role of the light quarks — the *up* and *down* quarks — (and to some extend the strange quark s) is apparent. Indeed due to this scale separation between light and heavy quark flavors the phenomena encountered in respective hadronic systems are quite distinct. In addition both light quarks have rather similar masses, at least when viewed on a typical hadronic scale and the resulting symmetry is quite well realized in nature. It can be described by an $SU(2)$ *isospin* symmetry which first was used to describe the proton and the neutron as an isospin-doublet of the nucleon. In most parts of this thesis isospin symmetry will be assumed to hold exactly.

Quarks have never been observed as free particles but are *confined* inside the hadrons of which two classes are known, the *baryons* containing three valence-quarks and the *mesons*, which contain quarks and antiquarks in equal proportions. While the lightest baryon, the proton, appears to be stable on the timescale of the age of the universe, the mesons are very short-lived and ultimately decay into particles (leptons, photons) that do not experience the strong interaction. This classification can be understood from the global $U(1)$ symmetry of the underlying theory — *quantum chromodynamics* (QCD) — which leads to the conservation of the baryon number, while there is no such rule for the mesons.

Predicted already in 1935 in order to explain the short range of nuclear forces [2] the lightest meson — the *pion* — was discovered in 1947 in photo-emulsion experiments studying cosmic rays [3]. As will be discussed below, the pion is now understood as the result of the spontaneous breakdown of a fundamental symmetry of the strong interaction. While the consequences of this symmetry breakdown are being more and more understood its ultimate origin remains an open question. It is believed to be an emergent phenomenon arising from the intricate structure of the strong interaction. The study of these forces on scales where bound systems are formed is the regime of hadron spectroscopy.

Atomic spectra can be understood to great precision in the context of *quantum electrodynamics* (QED). In contrast the situation with the spectrum of hadronic excitations and light mesons in particular is still far from being satisfactory. The difficulties are believed to arise from the astonishingly more complex phenomena that emerge from the gauge-symmetry structures of QCD as compared to its so successful older sister QED. The fact that the energy scales of typical hadronic systems far exceed the masses of light quarks and thus relativistic quark-antiquark pairs can always be produced further complicates the situation.

In the following some models of mesons will be reviewed and some of the open questions that arise will be discussed. In section 1.2 the focus is then narrowed further on those topics which are relevant for the discussion of the data presented this thesis. The chapter will conclude with a section on the parametrization of resonances in the context of spectroscopic models.

1.1 Models of Mesons

The following discussion on different models that are being used to discuss the meson spectrum will be restricted to the light-meson sector. Only mesons containing u and/or d (and in some cases s) quarks will be considered.

1.1.1 Constituent Quark Model

The description of mesons as bound systems of a fundamental fermion–antifermion pair predates the development of QCD as a gauge field theory of the strong interaction and was first introduced by Murry Gell-Mann and Yuval Ne'Eman in their seminal "Eightfold Way" [4]. Light and strange hadrons are here classified according to the $SU(3)_{\text{flavor}}$ symmetry, which is approximately fulfilled by the hadrons known at that time. Different schemes were discussed how to build up the hadron spectrum from a *fundamental triplet* of fields in a Lagrangian field theory, one of them representing the mesons as fermion-antifermion pairs. A particular elegant way of constructing the lightest meson– as well as baryon multiplets was to allow the fundamental fermions to carry non-integer electric charges. The integer-charge representations that could be built from these *quarks* [5] correspond to the basic $SU(3)$ multiplets: A singlet and an octet for the meson sector and a decuplet for the baryons. Thus a meson could be understood as a quark–antiquark pair and a baryon as a bound system of three quarks.

From the assumption that mesons consist of a bound $q\bar{q}$ pair one can[1] immediately construct some basic rules concerning the possible quantum numbers of such systems (see for example [6]). There are two light *flavors* of quarks which can be represented to a good approximation[2] as a $SU(2)_{\text{isospin}}$ doublet with $I = 1/2$, $I_3(u) = +1/2$ and $I_3(d) = -1/2$. Mesons therefore can according to this model only be formed in either isospin singlet, or isospin triplet states. Although the quarks carry fractional electric charges these assignments indeed lead to integer electric charges for the mesons.

Further degrees of freedom are given by the angular momenta of the fermion-antifermion system. The quark has spin $S = 1/2$ and positive parity by convention — the antiquark has negative parity. There are two possible states the two spins can couple to

$$\begin{aligned} &|\uparrow\downarrow\rangle \quad S = 0 \\ &|\uparrow\uparrow\rangle \quad S = 1 \end{aligned}$$

In addition there can by orbital angular momentum ℓ between the two constituents and the total angular momentum of the two-fermion system J can take the values

$$J \in [|\ell - S|, \ell + S].$$

The parity of the meson is then given by

$$P = (-1)^{1+\ell}.$$

In the case when quark and antiquark have the same flavor, i. e. the 3rd component of the meson–isospin of the meson is zero, $I_3 = 0$, then the meson is in a C-parity eigenstate with the eigenvalue

$$C = (-1)^{\ell+S}.$$

Charged mesons ($I_3 \neq 0$) are obviously not in an eigenstate of C. By convention the $I_3 = \pm 1$ elements of an $I = 1$ isospin triplet are assigned the same C-parity as the $I_3 = 0$ element of that triplet. An alternative construction is the G-parity that is defined as a charge-conjugation operation followed by a rotation in isospin-space. This operator flips the I_3 axis and thus the electric charge of the meson and one can construct a good quantum number for all light mesons with

$$G = (-1)^{I+\ell+S}$$

---

[1] in a non-relativistic approximation.

[2] Indeed isospin symmetry is broken by the different electric charges as well as the slightly different masses of the u and d quarks. Since the electromagnetic interaction is much weaker than the strong force at the scales we are interested in and since the mass–splitting between u- and d-quarks is small compared to typical hadronic scales for the purpose of the spectroscopy of excited mesons it is a good approximation to neglect these effects.

From these rules the possible spin/isospin/parity (often abbreviated as spin-parity) states of the $q\bar{q}$ system are readily constructed:

ℓ	S	J	$P=(-1)^{1+\ell}$	I	$G=(-1)^{I+\ell+S}$	$C=(-1)^{\ell+S}$	$I^G J^{PC}$	nomenclature
0	0	0	-1	0	$+1$	$+1$	0^+0^{-+}	η
0	0	0	-1	1	-1	$+1$	1^-0^{-+}	π
0	1	1	-1	0	-1	-1	0^-1^{--}	ω
0	1	1	-1	1	$+1$	-1	1^+1^{--}	ρ
1	1	0	$+1$	0	$+1$	$+1$	0^+0^{++}	f_0
1	1	0	$+1$	1	-1	$+1$	1^-0^{++}	a_0
1	0	1	$+1$	0	-1	-1	0^-1^{++}	h_1
1	0	1	$+1$	1	$+1$	-1	1^+1^{+-}	b_1
1	1	1	$+1$	0	$+1$	$+1$	0^+1^{++}	f_1
1	1	1	$+1$	1	-1	$+1$	1^-1^{++}	a_1
1	1	2	$+1$	0	$+1$	$+1$	0^+2^{++}	f_2
1	1	2	$+1$	1	-1	$+1$	1^-2^{++}	a_2
2	0	2	-1	0	$+1$	$+1$	0^+2^{-+}	η_2
2	0	2	-1	1	-1	$+1$	1^-2^{-+}	π_2

(1.1)

The nomenclature of these mesonic states is completed by adding the mass (in units of MeV/c^2) of a particular state in brackets behind the symbol, such as

$$\rho(770), a_1(1260)\,\mathrm{or}\,\pi_2(1670)$$

for example.

It turns out that there are certain spin-party combinations which are not allowed in a $q\bar{q}$ system. Some examples are

$$J^{PC}=0^{--},0^{+-},1^{-+},2^{+-},3^{-+}...$$

Such states are called *spin-exotic* and they play a central role in current experimental efforts of meson spectroscopy. If a meson with such quantum numbers would be identified it could not be accommodated in the constituent quark model. At the moment there are a few known candidates for a $J^{PC}=1^{-+}$ resonance. The most intensively studied is the $\pi_1(1600)$, for which observations of the decays into $\eta\pi$ and $f_1\pi$ have been reported (see [**?**, PDG10]nd references therein) and which recently has been observed by the COMPASS experiment [7] in the decay to $\pi^-\rho^0(770)$. A recent review on the status of spin-exotic systems can be found in [8].

Indeed it is known that there is much more to systems of strongly interacting particles than the naive constituent-quark picture described so far suggests, as will be seen in the following sections. Consequently the investigation of the so called *exotic* systems might yield insight into the structure of mesons *beyond the naive quark model.* Nevertheless, the systematization scheme that is provided by the quark model is very valuable in classifying the observed hadronic states.

The constituent quark model can be completed with a quark-antiquark potential and relativistic corrections in order to provide the means to calculate the mass spectrum of mesons [9]. For the iso-vector mesons the agreement with experimental data is quite impressive. The iso-scalar resonances, however, are purely described in this model.

To this date the iso-scalar resonances and in particular the scalars are not well understood and it is widely believed that the naive quark-antiquark picture is far too simplistic to describe these states. Carrying the quantum numbers of the vacuum, scalar systems are readily produced in inelastic hadronic scattering processes and an intimate connection to the structure of the strong–interaction vacuum is anticipated. Recent reviews of this topic are available in [10, 11, 12]. Iso-scalar scalar resonances have extensively been studied in $\pi\pi$ and KK interactions. However, there is no reasons why at higher masses the 4π system should not strongly couple to these quantum numbers. It is in this context that scalar systems will play a role in later parts of this thesis.

1.1.2 Quantum Chromodynamics

From the proposition of the quark-concept by Murray Gell-Mann it took another decade of experimental efforts discovering the existence of point-like, spin 1/2 *partons* [13] inside the nucleon and the development of **Q**uantum **C**hromo**d**ynamics (QCD) [14, 15] as the correct quantum field theory of the strong interaction to establish the quarks as physical fields which interact through $SU(3)_{\text{color}}$ gauge fields whose quanta are called *gluons*.

QCD is a renormalizable quantum gauge field theory [16] with a running coupling that strongly depends on the scale at which a system is investigated. Renormalization therefore breaks the classical scale-invariance of QCD and introduces a single scale $\Lambda_{QCD} \sim 1\,\text{GeV}/c$. The running coupling vanishes at small (large) spatial (momentum) scales — the theory exhibits *asymptotic freedom* [17, 18]. In this regime a perturbative expansion of QCD is justified and the theory has been tested to high precision against experiments.

The basic reason for this behavior — radically different from quantum electrodynamics — is the non-abelian nature of the $SU(3)$ gauge group which leads to a self-interaction of the gauge-fields. The gluons provide an additional contribution to the vacuum polarization which differs in character from the quark-antiquark contribution and leads to anti-screening of the gauge charges and thus to asymptotic freedom.

At small momentum scales $q^2 < \Lambda_{QCD}^2$, however, the same cause leads to the running coupling becoming large and a perturbative treatment in terms of quark-gluon interactions is not possible anymore. This is commonly called the *non-perturbative* regime of QCD and it includes the spectrum of bound states of the theory as well as long-range strong interaction, such as the scattering of hadrons at small momentum transfer.

Depending on temperature and density QCD exhibits several phases. For the purpose of this thesis we will focus on low temperatures and densities. In this regime the vacuum contains a quark-antiquark condensate and quarks are not observed as free particles. They are said to be *confined* inside the hadrons and the only configurations that are realized as hadronic particles are color singlets. The detailed mechanism of confinement cannot be understood in perturbation theory and is by many thought of as one of the biggest challenges in particle physics today. Confinement even plays an important role for studies of QCD in the perturbative regime, since although there might be a small scale involved in the microscopic scattering process, in the end there will be hadrons that are detected in the experiment. Perturbative calculations in QCD rely on the assumption that this *hadronization* can be *factorized* from the hard scattering process.

Even in the pre-QCD era, symmetries in the hadron spectrum haven been used to deduce that the light-quark masses are much smaller — $\mathcal{O}(\text{few}\,\text{MeV}/c^2)$ — than typical hadron masses as shown in table 1.1 (a detailed review on this topic is given in [19]). So the situation in the hadron spectrum is quite different from atomic or even nuclear physics where the masses of particles are given to a good approximation by the masses of the constituents (electron/positron for the positronium system, electrons and nucleus for an atom, nucleons inside a nucleus) and the binding energy for most cases is just a small correction. In contrast, it is now understood that the hadron masses are dominated by the non-perturbative dynamics of the gluonic fields and the bare quark masses are essentially negligible[3]. Indeed the small quark masses invalidate attempts to define a potential for light mesons, because of the highly relativistic nature of the problem.

1.1.3 Spontaneous Chiral Symmetry Breaking

In the limit of vanishing quark masses QCD exhibits some remarkable global symmetries, most importantly *chiral symmetry*, which means that the left- and the right-handed parts of the fermion spinors decouple and that they can be transformed independently of each other. However, if this symmetry would be realized in nature, then the hadron spectrum would show a characteristic pattern of pairs of degenerate states with opposite parity. Actually such *parity doubling* is not observed for the ground states of the baryon- as well as the meson spectrum. Chiral symmetry is spontaneously broken. The vacuum of QCD is not chirally symmetric. For $SU(2)$ flavor symmetry the pion triplet is interpreted as the Goldstone-bosons of the spontaneous breaking of chiral symmetry and thus the small pion mass of $m_\pi \sim 140\,\mathrm{MeV}/c^2$ can be explained. The finite value of the pion mass is attributed to the fact that the small current-quark masses explicitly break chiral symmetry.

It is believed that the mechanism for the symmetry breaking emerges from the non-abelian structure of QCD, however its details are not fully understood. In the framework of *QCD sum rules* it can be shown that in the hadronic phase, at low temperatures and low densities, the vacuum contains a *condensate* of quark-antiquark pairs (for a recent review on the topic see [20]). Such a condensate breaks chiral symmetry. Modern applications of QCD Dyson-Schwinger equations also study dynamical symmetry breaking in a non-perturbative framework (see for example [21] and references therein.). On important effect is the dynamical generation of constituent-quark masses. From this perspective the constituent-quarks encountered in the naive quark model above are understood as quasi-particles which derive their mass from the propagation through the QCD condensates.

As Pseudo-Goldstone bosons the pions at rest experience only a faint residual of the strong force. This property has lead to the development of *chiral perturbation theory* [22] or more generally *chiral dynamics* which now are established tools to study interactions of hadrons at small momentum scales. Modern reviews on chiral dynamics can be found for example in [23, 24]. One interesting result, which is of relevance for the discussions in this thesis, is the determination of the $\pi\pi$ scattering amplitude at small masses[25]. Another example is the calculation of the $\pi^-\gamma \to \pi^-\pi^+\pi^-$ cross-section to first order in chiral perturbation theory [26] which has recently been measured by the COMPASS experiment [27] confirming the theoretical result.

Unfortunately as soon as larger (pion-)momenta are involved, the tools mentioned above can not be used anymore. Therefore the excited states of the hadron spectrum still pose a considerable challenge. One important question is, how does the spontaneously broken chiral symmetry, which is so important for the understanding of the low-energy part of the spectrum relate to the excited states? Before this question can be attacked another successful model of excited mesons should be mentioned.

---

[3] The mass of the pion is strongly affected by the small but finite quark masses, since being a Goldstone boson in the limit of vanishing quark masses the pion would also be mass-less

1.1.4 The QCD String — Old and Modern Pictures

Inspired from the Hamiltonian formulation of lattice QCD Nathan Isgur and Jack Paton already in 1985 proposed the *flux-tube model for hadrons* [28, 29]. The basic idea of the model is, that the gluonic field forms a tube-like configuration with constant energy density connecting the quark and the antiquark in a meson. Also configurations would be thinkable in which the flux-tube is closed onto itself and forms a bound state without valence quarks — so called *glueballs*. Indeed in lattice QCD calculation with infinitely heavy quarks the formation of a gluonic flux-tube has been demonstrated [30, 31]. The model is expected to work rather well for the heavy quarkonia.

Despite some remarkable success the model is not derived from first principles and carries some serious deficiencies. In particular the effect of virtual quark-antiquark pairs is neglected. Especially in the light-quark sector it has to be considered as a phenomenological approximation.

Nevertheless, the flux-tube model has been of special interest, since it allows the calculation of decay branching ratios for excited mesons by modeling the decay as a breaking of the flux tube with simultaneous creation of a quark-antiquark pair (to implement confinement) at the breaking point [32]. Especially for field configurations which correspond to *excited flux-tubes*[4] the model can provide interesting predictions by taking into account the overlap of the flux-tube wavefunctions [33, 34]. We will come back to some examples of flux-tube model predictions below.

The idea that hadrons possess *stringy* properties is actually even older than the QCD inspired flux-tube model and was first proposed in the context of high energy hadronic scattering phenomenology for scattering processes with small momentum transfer[5], which can be described by the so called *Regge theory* [35].

Much more will be said about the Regge formalism in chapter 2. One important concept in the discussion of stringy models of hadrons are *Regge trajectories*. As shown in Figure 1.1 there is, to quite good approximation, a *linear* relationship between the spin of excited mesons (or baryons) and their squared mass. This relation is exactly what one would expect from a straight, rotating string with constant, universal energy density (the string tension) along it's length. The picture is supported by the fact that all observed Regge trajectories corresponding to ordinary mesons (and also Baryons) have the same universal slope. The Pomeron trajectory has a special role in the description of high energy scattering processes and will be discussed in section 2.2.2.

The flux-tube model as such makes no reference to chiral symmetry breaking. However, if quarks are indeed confined by a mechanism as implied by the flux-tube model, then there might be a close connection between the two concepts, since confinement is a sufficient (but maybe not necessary) condition for spontaneous chiral-symmetry breaking [36].

The connection between the seemingly stringy character of the excited mesons and the spontaneous breaking of chiral symmetry is one of the most interesting questions in hadron spectroscopy. In recent years there has been a controversy on whether there are global symmetry patterns emerging in the highly excited meson spectrum [37, 38, 39, 40, 41]. Mesons with masses above about $1.5\mathrm{GeV}/c^2$ show a pattern of degeneracies that has been interpreted as the

---

[4] Such states would be called *hybrid mesons* and evidently could possess quantum numbers which are forbidden in the constituent quark model (see section 1.1.1).

[5] At large momentum transfer the hard scattering processes now described in perturbative QCD are becoming relevant and Regge theory cannot explain the observed data.

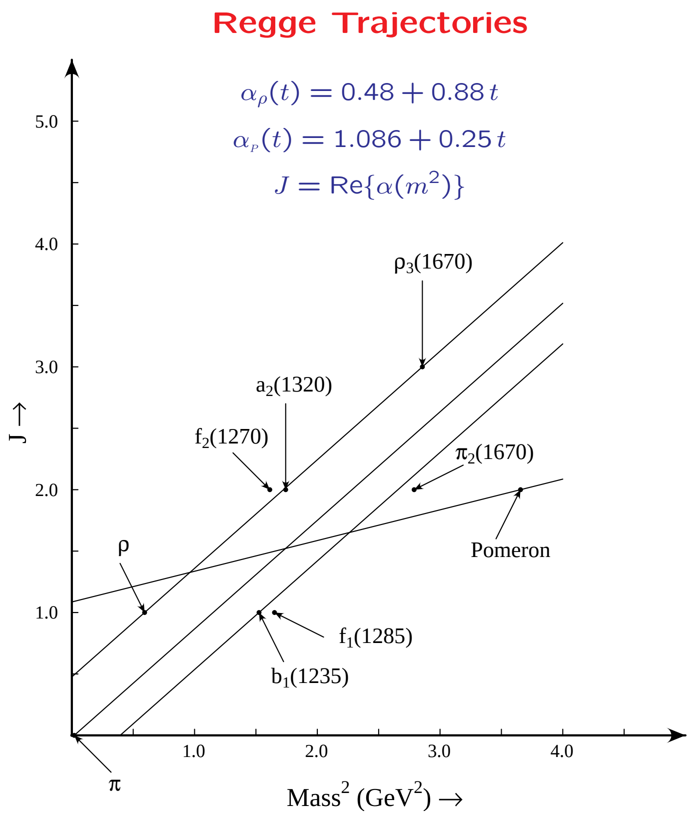

Figure 1.1: Mesonic Regge trajectories. There is a linear relationship between the spin J of a meson and its squared mass. The Pomeron trajectory will be discussed in section 2.2.2. (Plot by courtesy of Suh-Urk Chung)

existence of meson regge trajectories (see Figure 1.2). The interpretation of the observed degeneracies as a sign for an effective restoration of chiral symmetry in the high-lying part of the spectrum is, however, debated.

The measurements which lead to these interpretations have almost exclusively been extracted from the data of only one experiment — the Crystal Barrel experiment [42, 43, 44] at LEAR. Many of the high-lying resonances found there are still awaiting confirmation by independent groups [1]. In order to illustrate this point Figure 1.3 shows the mass distribution of meson states with $I^G = 1^-$ listed by the Particle Data Group [1]. The different colors correspond to the level of confidence assigned to the respective states. It ranges from established states (green), states that have been clearly seen but need confirmation by another experiment (blue) and states which are barely known, mostly from a single publication (red). From this picture it is immediately clear that there is a need for clarification of the light-meson spectrum in the mass range around and above 2 GeV/c^2.

One would also like to compare the data from different production mechanisms. At LEAR the production of mesons through antiproton-nucleon annihilation (at rest) has been studied. The data which will be discussed in this thesis has been obtained from diffractive pion dissociation (for details see chapter 2).

It should be pointed out that the search for resonances in the region above 2 GeV/c^2 is a difficult

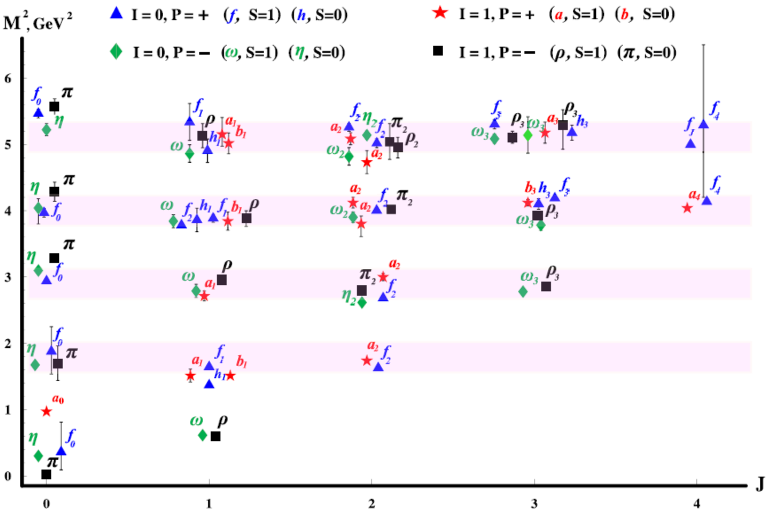

Figure 1.2: Regge trajectories of excited mesons. There is an ongoing debate, whether the observed degeneracies can be interpreted as an effective restoration of chiral symmetry for high-lying states. Plot reproduced from [41].

task since any possible mesonic state will be embedded in a continuum of scattering states, which depends on the production process. Furthermore, at these high masses there are many open channels that a resonant state can couple to, many of which leading to multi-body final states, which further complicates the analyses. The large phase-space that is available for such an excited state to decay into leads to very short lived resonances with large decay widths. This can lead to an overlap of several states and to mixing of states with equal quantum numbers. Experimentally some techniques to deal with these difficulties have been developed and we will discuss some of those below.

Making progress on the understanding of the excited meson spectrum will require not only the precise measurement of the masses of resonances up to high spins in order to reconstruct the Regge trajectories, but even more important the determination of the decay patterns, viz. the hadronic transition matrix elements for as many (coupled) channels as possible. This thesis is attempting to make a contribution to this endeavor, developing methods to deal with multi-particle decays.

An interesting recent development is the reappearance of the hadronic string picture in a new framework. Rather than treating the gluonic flux tube as a semi-classical object, developments in string theory, in particular the conjecture by Maldazena on the duality between string theories and conformal field theories [45] lead to the development of a new class of hadronic models. The conjecture allows to re-interpret the solutions to a weakly coupled gravity theory in a curved, higher dimensional space as the solutions of a strongly coupled $SU(N)$ gauge theory. A recent review on the topic can be found in [46]. The main drawback of these methods is that as far as is known the duality only holds for large N far from the physical value of $N = 3$.

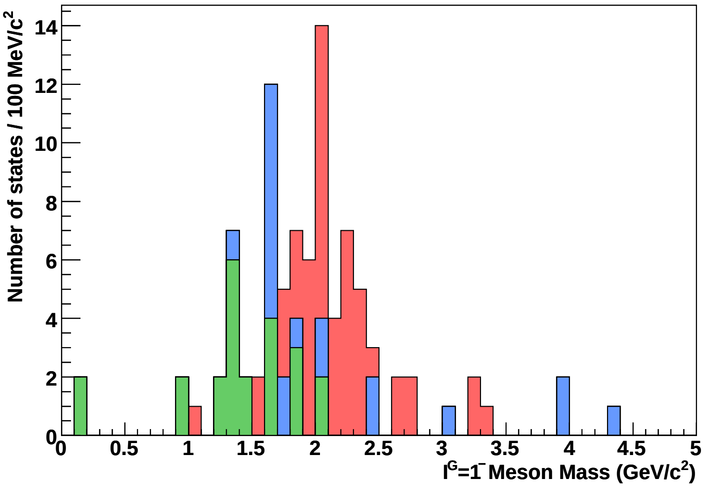

Figure 1.3: Meson states with $I^G = 1^-$ listed in the PDG [1]. Green are established states, blue are states that need confirmation and red are further states that have so far only been seen by one group or for which only limited information on the quantum numbers is available. The histogram is stacked.

1.1.5 Dynamically Generated Mesons

One approach to expand the application of the techniques of chiral dynamics to higher-mass meson states is the construction of so called *dynamically generated mesons*. Any theory of the strong interaction should obey two fundamental constraints which — because their relevance is independent of the underlying dynamics — have also played a major role in the early days of strong interaction physics[6]: they are *analyticity* and *unitarity* of the scattering and transition amplitudes. The requirement that amplitudes can be described by analytic functions which can be continued into the complex plane of its kinematic variables (like the square of an invariant mass s) and which conserve probability, i. e. unitary of the scattering matrix, poses stringent constraints. These constraints allow to extrapolate amplitudes, which are rigorously defined in the region where chiral perturbation theory is valid (i. e. at small meson masses), to higher masses (see [49, 50, 51, 52]). Models like these are known as *chiral-unitary* approaches. The application of the unitarity relation, however, involves sums over all open channels that a state can couple to. The different decay modes of the mesons play a central role in the formation of the spectrum. As a consequence it is important not only to measure the masses and the quantum numbers of hadronic states but also their coupling to all possible decay channels.

An open question is, how the inner substructure of mesons and the symmetries of QCD are reflected in those couplings. There are attempts to set up effective field theories which include not only the pions but also other low-lying mesons, such as the $\rho(770)$, as degrees of freedom (see for example the review [53]). Applying the chiral-unitary framework then allows for example to describe several iso-scalar resonances with masses above $1\,\mathrm{GeV}/c^2$, among them the $f_2(1270)$ with $J^{PC} = 2^{++}$, as a bound system of two (or more) vector states like $\rho\rho$ [54, 55]. In the face of the data that will be presented in this thesis, it would be certainly interesting to

---

[6] For historical text-books see for example [47, 48].

extend such calculations to the three-body system $\rho\rho\pi$.

1.1.6 Lattice-QCD Results on the Light-Meson Spectrum

The explicit numerical evaluation of QCD problems on a space-time *lattice* is another approach to understand the strong interaction [56, 57]. A complete numerical solution of QCD is still not feasible today, however, dramatic progress to overcome some of the technical difficulties in recent years has made it possible to perform first studies of the light-meson spectrum. Among the challenges[7] is the inclusion of quark-antiquark loops, which for light quarks obviously are very important but computationally expensive. Another important issue for the study of angular-momentum eigenstates is, that on a (hyper-)cubic lattice the rotational symmetry is broken down to a set of discrete groups. The correspondence of states found in such a world to the physical world has to be established by the projection of rotation operators onto the elements of the discreet groups.

First calculations along these lines have recently been published for the spectrum of highly excited iso-vector [58] and also iso-scalar states [59]. The study of different operators evaluated on the lattice allows to identify their contributions to the different bound states. In simple words this provides a means to systematically study contributions like $q\bar{q}$, multiquark, gluonic field configurations and so on for each state. Interestingly also bound states with the aforementioned *spin-exotic* quantum numbers $J^{PC} = 1^{-+}, 0^{+-}$ and 2^{+-} have been found. Although the effective pion mass of $m_\pi \sim 400\,\mathrm{MeV}/c^2$ that has been used in these calculations is still far from the physical value there are indications that the lightest multiplet of *hybrid* states is seen in these calculations [60] in the mass-range around $1.8\,\mathrm{GeV}/c^2$. A hybrid meson is a state that has excitations of the gluonic field contribute to the quantum numbers of the object. In the flux-tube model described above this would for example correspond to a vibrational excitation of the flux-tube.

The final, ambitious goal of these such calculations is the computation of the full hadronic spectrum, including scattering and transition amplitudes. However, due to the use of an Euclidean space-time grid in lattice calculations it is not straight forward to extract information on the time-development of bound states, viz. their decays. For a recent review on proposed methods to this end see [61].

1.2 Physics Potential of the 5π Channel

In this thesis a partial-wave analysis of the diffractively produced 5-pion system will be presented. The following section summarizes the most important motivations for this analysis and presents some of the physics questions that arise in the context of the different perspectives on light-meson spectroscopy that have been discussed above.

The $\pi^-\pi^+\pi^-\pi^+\pi^-$ system has negative G-parity and, since it has electric charge, cannot be in an isoscalar state. For the isovector 5π system the C-parity is even. Similar arguments hold for the $\pi^+\pi^-\pi^+$ subsystem. The even G-parity system of four pions, however, can be either in an isoscalar as well as in an isovector state[8].

---

[7] Further problems include effects from the finite size of the simulated lattice and quark masses which have to be chosen larger than the physical values in order to keep the computational efforts manageable.

[8] Isospin $I > 1$ will not be considered for the search for resonant states here.

Search for Hybrid Mesons

As explained in section 1.1.1 spin-exotic states are a promising signature for the search for hybrid mesons because in this case a resonance could not be explained by a $q\bar{q}$ pair. The lightest spin-exotic hybrid state is predicted by lattice QCD to be an isovector with the quantum numbers $J^{PC} = 1^{-+}$ and with a mass of approximately $1.6\,\mathrm{GeV}/c^2$ [8, 60]. A candidate state which would fit these characteristics is the above mentioned $\pi_1(1600)$ for which observations in the decay modes $\rho\pi$, $\eta'\pi$ and $f_1(1285)\pi$ have been reported [1, 7]. However all these analyses have some drawbacks and the nature of the state is still debated [8, 10]. Apart from the fundamental question on the resonant nature of the observed signals, an important question is, whether the couplings of the state to different decay channels can be understood in a model of hybrid mesons.

The lightest spin-exotic hybrid state described by the flux-tube model is predicted to couple strongly to the $f_1\pi$ and $b_1\pi$ decay modes[34] both of which can in principle couple to the 5π final state, with the f_1 having been seen in $\pi^-\pi^+\pi^-\pi^+$.

m_{π_1}	$b_1\pi$		$f_1\pi$		$\eta'\pi$		$\rho(1450)\pi$
1.6 GeV	24	:	5	:	2		
2.0 GeV	43	:	10	:	27	:	12

Table 1.2: Predictions of 1^{-+} hybrid meson relative branching ratios from [34].

Table 1.2 shows flux-tube model calculations for the branching fractions of the $J^{PC} = 1^{-+}$ hybrid meson [34]. A distinct feature of these calculations is the $b_1\pi$ to $f_1\pi$ partial width ratio which also is in very good agreement with studies on the lattice [62]:

$$\frac{\Gamma(\pi_1 \to b_1\pi)}{\Gamma(\pi_1 \to f_1\pi)} = 4 \tag{1.2}$$

An investigation of the $f_1(1285)\pi$ system in the decay channel $f_1(1285) \to \eta\pi\pi$ been carried out at BNL by [63] and indeed they find a contribution of the spin-exotic 1^{-+} wave. In order to establish the resonant nature of the spin-exotic partial wave the authors of that analysis examine its interference with the $J^{PC} = 1^{++}$ $f_1(1285)\pi$ system for which an amplitude with two resonances has been fitted to the data. However, since in that analysis no attempt has been made to clarify this picture by studying interferences with further partial waves, it is still unclear if there is a single $a_1(1700)$ state or if one can confirm the indications that there might actually be several states with these quantum numbers in the mass range from 1.6 to $2\,\mathrm{GeV}/c^2$.

All of the isobars in table 1.2 are allowed to decay into 4 charged pions. The f_1 and the $\rho(1450)$ have been seen in $\pi^+\pi^-\pi^+\pi^-$ decays. The b_1^+ is known to decay to $\pi^+\omega \to \pi^+\pi^-\pi^+\pi^0$ so the analog decay of the b_0^0 into four charged pions can in principle also be expected. The heavy $\eta'(1405)$ has been reported in this channel as well [1]. This means they all can be expected to contribute as a subsystem to the 5π final state, opening the possibility to study their interference patterns and relative branching ratios in the same final state.

However, in diffractive pion dissociation — the mode of production of mesonic systems used at the COMPASS experiment — due to parity conservation in strong interaction processes and for kinematic reasons the excitation of a pion into a spin-exotic state with $J^{PC} = 1^{-+}$ requires a significant momentum transfer t' as will be explained in detail in sections 2.2 and 3.1.1.

There are, however, also hybrid meson candidates which do not carry spin-exotic quantum numbers. For example the aforementioned $a_1(1700)$ state has been discussed in the framework of the flux-tube model and its decay properties have been calculated within this model for the hybrid as well as the conventional meson scenarios [34]. For the hybrid meson a rather narrow width of 100 to 200 MeV/c^2 and a sizable branching into $\rho'(1450)\pi$ is predicted. The experimental situation in this wave is unclear, however, since so far experiments have not been able to convincingly separate resonant contributions from non-resonant background and unambiguously determine the number of resonances contributing.
A similar situation is encountered in the $J^{PC} = 2^{-+}$ sector. In addition to the very well known $\pi_2(1670)$ resonance there are indications for a couple of further resonances (see [1]). Especially the $\pi_2(1880)$ is an interesting candidate since it is so close in mass to the $\pi_2(1670)$ that it seems unlikely to be a radial excitation of that state. A recent investigation of the expected decay patterns of this state in the frameworks of both a quark model as well as the flux-tube model is presented in [64] indicating a dominant quark-antiquark structure of the state. Conversely, in lattice calculations [60] a large hybrid-like component is found for the second $J^{PC} = 2^{-+}$ state.
A further interesting option is to study the 4-pion subsystem in order to search for spin-exotic states with positive G-parity. The four pions can couple both to isoscalar as well as to isovector states and is in itself an extremely interesting object of study as will be discussed in some more detail in sections 3.2.2 and 5.3. The primary candidate of interest would be the isoscalar partner to the $\pi_1(1600)$ with the quantum numbers $I^G J^{PC} = 0^+1^{-+}$, which would be called the $\eta_1(1600)$. Indeed in lattice simulations there are now indications that such a state might exist at a slightly larger mass than its isovector counterpart [60]. The experimental establishment of further parts of a spin-exotic meson multiplet would be a tremendous step forward in the understanding of the light meson spectrum.
Table 1.3 lists three possible spin-exotic even G-parity states with spin 0, 1 and 2. These states have been studied in the flux-tube model indicating significant coupling to the 4π final state [34]. Lattice calculations indicate that both the 0^+0^{+-} and the 0^+2^{+-} states are significantly heavier than the 0^-1^{-+} state [60]. An interesting outcome of these calculations is the prediction of a rather narrow width of 60 to 160 MeV/c^2 for the latter state, making it an interesting object for experimental searches.

J^{PC}	Topic	Status
0^+1^{-+}	η_1	Width $60-160$ MeV/c^2 Decays to $a_1\pi$ and $\pi(1300)\pi$
1^+0^{+-}	b_0	Can be close to lowest 1^{-+} state Decays to $a_1\pi$ and $\pi(1300)\pi$
1^+2^{+-}	b_2	Could be very narrow $\sim$ 10MeV Decays to $a_2\pi$ and $a_1\pi$

Table 1.3: Spin-exotic G-parity even meson candidates. Decay calculations in the flux-tube model [34].

Another topic is the study of scalar resonances in the 4π system. In the mass region between 1.2 GeV/c^2 and 2 GeV/c^2 several isoscalar scalar states have been found. The precise number is still being debated[65, 66]. Although these discussions have been guided mainly by results obtained for the 2-pion system, also the 4π system has been studied already by the Crystal Barrel collaboration [67] in $\bar{p}n$ annihilation. Complimentary data could potentially yield very valuable insights into the coupling of scalar resonances to multibody final states, especially since in diffractive dissociation the mass of the 4π subsystem is not as stringently limited by phase-space as in the case of $\bar{p}n$ annihilation.

The Light-Meson Frontier — Highly Excited States

The spectrum of highly excited light mesons with masses above $\sim 2\,\mathrm{GeV}/c^2$ is only purely known. Nevertheless there are ongoing debates about the interpretation of the general structure of the spectrum in terms of large symmetries as has been discussed in section 1.1.4. One open question in this regard is the possible existence of a parity partner to the well known $J^{PC} = 4^{++} a_4(2040)$ resonance. Is there a $J^{PC} = 4^{-+} \pi_4(2040)$ resonance at roughly $2\,\mathrm{GeV}/c^2$ as predicted by some of the models which imply effective restoration of chiral symmetry in the high-lying meson spectrum [68]? Crystal Barrel has not seen such a state, the lightest 4^{-+} meson being listed in the PDG at a mass of $2250 \pm 15\,\mathrm{MeV}/c^2$[1]. However, it has been argued[69] that such a state might just not be efficiently produced in the Crystal Barrel experiments, since for the production of a spin 4 resonance in $\bar{p}n$ annihilation an $F-$wave is required which should be strongly suppressed for $\bar{p}n$ at rest or even in flight as it has been the case at the LEAR setup. No such limitations exist for the diffractive production of resonances and if the state exists it should be detectable and might couple strongly to the 5π final state.

Dynamically Generated Resonances

Another field where the data presented here could potentially be very valuable input is the extension of the unitarized chiral models for dynamical generated mesons (see section 1.1.5) from the vector-vector case to more complicated configurations. Indeed the $\rho\rho\pi$ system is found to be one of the main components of the 5π final state as will be discussed in this thesis.

1.3 Resonances

Mesons — except for the relatively long-lived ground-states — are not observed directly in common particle detectors due to their extremely short life-times. The time scale on which a typical hadron exists is of the order of $\Delta t = \mathcal{O}(10^{-23}\mathrm{s})$. The corresponding typical uncertainty in the energy of these states is $\Delta E = \hbar/\Delta t = \mathcal{O}(100\,\mathrm{MeV})$. Such *resonances* are most commonly observed as peaks in production cross-sections as a function of the invariant mass of the system under study. For example the differential cross-section for electron-positron annihilation into hadrons

$$\frac{\partial}{\partial s}\sigma(e^+e^- \to \mathrm{hadrons})$$

as a function of the invariant mass of the e^+e^- system $\sqrt{s}$ is dominated by a peak at $\sim 0.8\,\mathrm{GeV}/c^2$ with a width of roughly $150\,\mathrm{MeV}/c^2$. This enhancement on closer inspection is composed of the broad isovector $\rho(770)$ and the much narrower isoscalar $\omega(782)$ resonances.

A basic assumption in the study of hadronic resonances is that resonances are not fundamentally different from stable particles and as such they are described by poles of the scattering amplitude as a function of the squared invariant mass s of the resonant system. The main difference between a stable particle and a short-lived resonance is that in the latter case the amplitude has no pole for real s but instead there exists a pole in the analytic continuation of the amplitude into the complex s-plane. The existence of such an analytic continuation is required in order for the amplitude to respect causality. It is easy to see from the time-development

$$|X(t)\rangle \sim \exp(-iE_X t)\,|X\rangle$$

that a state X which decays as the time t progresses requires a negative imaginary part of E_X. The resonance pole lies in the complex s-plane, below the real axis. The scattering amplitude $\mathscr{A}(s)$ can be examined in the vicinity of this pole by expanding the product [48]

$$g(s) = (s - s_P)\mathscr{A}(s)$$

where $s_P = s_X - i\gamma$ is the position of the pole with $s_X, \gamma \in \mathbb{R}^+$. The expansion around s_P can be written as

$$g(s) = g(s_P) + (s - s_P)g'(s_P) + \ldots$$

The most primitive approximation of the amplitude in the vicinity of the pole can then be obtained by only keeping the first term in the expansion:

$$(s - s_P)\mathscr{A}(s) \approx g(s_P)$$

or

$$\mathscr{A}(s) = \frac{-g(s_P)}{s_X - s - i\gamma}$$

which is the well known form of the Breit-Wigner resonance amplitude.

For convenience this amplitude is often written in the following form, which introduces the width $\Gamma = \gamma/m$ of the resonance as the width of the Breit-Wigner peak at half maximum

$$\mathscr{A}_{BW}(s) = \frac{m\Gamma}{m^2 - s - im\Gamma} \tag{1.3}$$

and the mass of the resonance $m = \sqrt{s_X}$.

In general the width Γ of a resonance depends on the available phase-space for the decay channels. This is a consequence of the unitarity property of the scattering matrix and (in the case of elastic scattering through a resonance) can already be seen from the optical theorem

$$\mathrm{Im}\mathscr{A} \propto \sigma_{\mathrm{tot}}$$

(see for example [48]). For narrow resonances setting $\Gamma = \text{const}$ is a valid approximation. Yet, for a detailed investigation of the shape of a broad resonance the dynamical width has to be taken into account

$$\mathscr{A}_{BW}(s) = \frac{m\Gamma(s)}{m^2 - s + im\Gamma(s)}. \tag{1.4}$$

As more complicated systems are studied, it turns out that the detailed form of the amplitudes can be greatly distorted by the coupling to channels with thresholds close to the resonances mass where $\Gamma(s)$ is a strongly varying function. Furthermore unitarity puts stringent constraints on the amplitude as mentioned before. The mixing of several overlapping resonant states further complicates the picture. In such cases it is indeed the positions of the poles of the analytically continued transition or scattering amplitudes and the residuals at the poles that are the defining characteristics. In the following we summarize a formalism that deals with these issues, especially the mixing of several resonances with the same quantum numbers.

1.3.1 Mixing of Resonances in the Propagator Matrix Formalism

The propagator matrix formalism as reviewed here traces back to Nils Törnqvist's *Unitarized Quark Model* [70]. Based on these ideas and motivated by the data measured at the Crystal Barrel experiment at LEAR, a formalism for the analysis of the scalar meson spectrum has been developed in [71]. Pragmatic applications for phenomenology have been extensively described by David Bugg in [65].

The basic concept that will be spelled out here is the correct generalization of the Breit-Wigner amplitude to the case of several (overlapping) resonances. The formalism is being described for the case of spin 0 resonances. However, the generalization to higher spins will be self evident. It should be noted that the fully dispersive D-matrix formalism is closely related to the manifestly unitary K-Matrix formalism as is explained in [71].

Anisovich et al. write the elastic scattering amplitude in a channel[9] n is in the presence of several resonant states as (cf. [71], eqn.(27))

$$\mathscr{A}^n(s) = g_a^n(s) D_{ab}^n(s) g_b^n(s) \tag{1.5}$$

Here D_{ab} is called the *propagator matrix* and the vertex functions $g_a^n(s)$ and $g_b^n(s)$ describe the coupling of the different resonances to the scattering channel n. A summation over a and b is understood. The vertex functions are in general s-dependent and in particular can contain form factors describing the finite range of interaction between hadrons (see [70]).

For an arbitrary number of resonances the propagator matrix is most conveniently defined through its *inverse* which takes the following form:

$$D^{-1} = \begin{pmatrix} M_1^2 - s & -B_{12}(s) & -B_{13}(s) & \cdots \\ -B_{21}(s) & M_2^2 - s & -B_{23}(s) & \cdots \\ -B_{31}(s) & -B_{32}(s) & M_3^2 - s & \cdots \\ \cdots & \cdots & \cdots & \cdots \end{pmatrix} \tag{1.6}$$

with the definition

$$M_a^2 \equiv m_a^2 - B_{aa}(s). \tag{1.7}$$

Here the real valued m_a are called the *bare* masses of the different states while the complex functions $B_{ab}(s)$ parametrize the dynamics of resonance formation and mixing. The imaginary parts of B_{aa} are determined by the coupling of a state a to its decay channels and are related to the resonance width Γ_{tot} through

$$\text{Im} B_{aa}(s) = m_a \Gamma_{\text{tot}}(s) \tag{1.8}$$

The real part $\text{Re} B_{aa}(s)$ can be obtained from a dispersion relation by imposing analyticity on the propagator functions.

$$\text{Re} B_{aa}(s) = \int_{\text{thr}}^{\infty} \frac{ds'}{\pi} \frac{\text{Im} B_{aa}(s')}{s' - s} \tag{1.9}$$

---

[9] The term *channel* refers to a specific initial and/or final state such as $\pi\pi$, $K\pi$ or $\pi^+\pi^-\pi^+\pi^-$ for example. Of course a state can only couple to a channel with the same quantum numbers.

Here $⨍_{\mathrm{thr}}^{\infty}$ is the Cauchy principle value integral. In the idealized case when $\mathrm{Im}B_{aa}(s)$ does not depend on s then through the dispersion integral also $\mathrm{Re}B_{aa}$ will be a constant which can be absorbed by a redefinition of m_a. In general, however, this *dispersive contribution* will modify the shape of the resonance, especially if it is close to channel thresholds where the respective contribution to $\mathrm{Im}B_{aa}(s)$ is a rapidly varying function of s. For simplicity such effects will be neglected for the further discussion.

Putting the formulas given above together

$$M_a^2 - s = m_a^2 - s - B_{aa}(s) = m_a^2 - s - i m_a \Gamma_{\mathrm{tot}}(s) \tag{1.10}$$

the well-known Breit-Wigner denominator is constructed.

The off-diagonal terms $B_{ab}(s)$ in equation 1.6 describe the mixing between the different states. They in general also depend on s, can in principle also be obtained through dispersion relations and are related to the couplings of the bare states to the scattering channels. In practical fits, where not all open channels are known, the mixing terms may be treated as another set of phenomenological constants (c. f. [65]).

In order to illustrate the difference between the formalism described here and a simple sum of Breit-Wigner amplitudes 1.4 we consider the case of two resonances:

$$D^{-1} = \begin{pmatrix} M_1^2 - s & -B_{12} \\ -B_{21} & M_2^2 - s \end{pmatrix} \tag{1.11}$$

Inverting this matrix gives

$$D = \frac{1}{\det D^{-1}} \begin{pmatrix} M_2^2 - s & B_{12} \\ B_{21} & M_1^2 - s \end{pmatrix} \tag{1.12}$$

which is

$$D = \frac{1}{(M_1^2 - s)(M_2^2 - s) - B_{12}B_{21}} \begin{pmatrix} M_2^2 - s & B_{12} \\ B_{21} & M_1^2 - s \end{pmatrix} \tag{1.13}$$

For the first element D_{11}

$$D_{11} = \frac{(M_2^2 - s)}{(M_1^2 - s)(M_2^2 - s) - B_{12}B_{21}} = \frac{1}{(M_1^2 - s) - \frac{B_{12}B_{21}}{(M_2^2 - s)}} \tag{1.14}$$

with equation (1.10) one arrives at

$$D = \frac{1}{m_1^2 - s - i m_1 \Gamma_1(s) - \frac{B_{12}B_{21}}{m_2^2 - s - i m_2 \Gamma_2(s)}} \tag{1.15}$$

Without mixing $B_{12} = B_{21} = 0$ this expression turns into the Breit-Wigner formula. For the realistic case with mixing it is significant that the last term in the denominator makes a contribution to both the real and imaginary part of the amplitude. As has been shown in [65] the effect of this term to first order is an additional phase by which the two resonances are rotated against each other. Consequently, if mixing effects are not taken into account explicitly but instead parametrizations based on the simple Breit-Wigner formula are used then one has to allow additional (constant) phases between the Breit-Wigner terms. This argument is the justification for the simplified parametrization that will be used in chapter 6 to explore the resonant structure of the 5π system.

Before the complete amplitude can be assembled according to equation 1.5, the vector of vertex functions $g(s)$ has to be defined. Törnqvist in addition to the coupling constants allows for a so called *formfactor* $F(s)$ in the vertex functions, which according to him "one expects [...] to be smooth functions of s, which include angular momentum barriers, radial nodes, and in principle the left hand cuts."[70]. For practical applications and keeping in mind that here the formalism should be applied not to elastic scattering but to a production process, the following assumptions are made:

- The main s-dependence of $g(s)$ is given by the form factors $F(s)$. The coupling itself is assumed to be a smooth and in particular non-singular function of mass (in the physical region). This will be approximated by a simple mass-independent coupling constant. We will use one universal form factor and not distinguish between states and channels here. The couplings g_a^n to the decay channels will be taken as real-valued.
- For diffraction experiments the production coupling constants g_b will be allowed to be complex and denoted as $\hat{g}_b$. This allows for free phases in the production of the different states. Here we divert from the scheme described in [71]. In particular we require the production vertices to be independent of the decay channel in order to allow the decoupling of width of the resonance from the observed intensity, which in production experiments is determined by the source. In order to fix the (unmeasurable) overall phase, one of the production couplings has to be restricted to real values.

The decay couplings are related to the partial widths of the individual resonances. For the case without mixing we have

$$\left(g_a^n\right)^2 \rho_n(m_a^2)/m_a = \Gamma_a^n \tag{1.16}$$

Here m_a is the mass of the resonance a while $\rho_n(s)$ is the invariant phase space of channel n which for a decay into two stable particles with masses μ_1 and μ_2 reads

$$\rho_{(12)}(s) = \frac{1}{16\pi s}\sqrt{[s-(\mu_1+\mu_2)^2][s-(\mu_1-\mu_2)^2]} \tag{1.17}$$

Γ_a^n is the partial width into that channel. It is useful to normalize $\rho(s)$ such that $\rho_n(m_a^2) = 1$. Then the total width of the resonance is defined through

$$\sum_n \left(g_a^n\right)^2 = m_a \Gamma_{\text{tot}} \tag{1.18}$$

and

$$\sum_n \left(g_a^n\right)^2 \rho_n(s) = m_a \Gamma_{\text{tot}}(s) \tag{1.19}$$

For several mixed states decaying into many channels the definition of partial widths and resonance mass becomes difficult. An unambiguous specification can only be given in terms of the poles in the complex s-plane of the proper analytical continuation of the amplitude and its residuals at the poles. However, one can still identify the width that a resonance would have if there would be no mixing by using the equations above.

The full amplitude for two mixed resonances (setting $B_{12} = B_{21}$) in a certain channel n given by equation 1.5 is

$$\begin{aligned} g^n D\hat{g} \quad = \quad & \frac{g_1^n \hat{g}_1}{(M_1^2 - s) - \frac{B_{12}^2}{(M_2^2 - s)}} + \\ & \frac{g_2^n \hat{g}_2}{(M_2^2 - s) - \frac{B_{12}^2}{(M_1^2 - s)}} + \\ & \frac{(g_1^n \hat{g}_2 + g_2^n \hat{g}_1) B_{12}}{(M_2^2 - s)(M_1^2 - s) - B_{12}^2} \end{aligned}$$

From this formula it is obvious that for non-zero mixing the Breit-Wigner-like denominators in the first two terms are modified and there appears a third term containing a product of both poles. Only for zero mixing ($B_{12} = 0$) one recovers an amplitude that takes the shape of a sum of two Breit-Wigners with complex coefficients.

This neglect of the mixing terms has often been employed in phenomenological analyses with good successes in describing the data. For broad resonances exhibiting a strong overlap this simplification should, however, be used with great care since the results will be misleading in the presence of strong mixing. In order to gain a first understanding of 5π system the fit presented in this thesis will employ the simplified model. Attempts to explicitly include mixing in the parametrization are left for future research.

A simple method for the treatment of nonresonant, coherent background has been suggested by Törnqvist [70]. To this end one adds another row into the propagator matrix, which instead of the pole term $(M_x^2 - s)$ contains a constant chosen in the right dimension GeV^2/c^2, thus making the following replacement in (an additional row in) equation 1.6

$$(M_x^2 - s) \rightarrow M_{\mathrm{bkg}}^2 \tag{1.20}$$

The above model allows the parametrization of amplitudes containing several resonances which decay into many channels. The exact line shape of a resonance is determined by all open decay channels as expressed in equation 1.19 and by the dispersive effects. Thus all channels that a resonance is decaying into are tied together. For a full understanding of all the mentioned effects it is therefore necessary to measure a system of resonances in all possible decay channels. Unfortunately such information is not readily available, especially for the mass range above $2\,\mathrm{GeV}/c^2$ with a larger number of open channels.

Still, it is possible to perform a parametrization of the limited data which are available using a simplified model. For this, equation 1.19 can be rewritten:

$$m_a \Gamma_{\mathrm{tot}}(s) = m_a \Gamma_{\mathrm{tot}} \sum_n \gamma_n \rho_n(s) \tag{1.21}$$

where the branching fractions $\gamma_n = \Gamma^n / \Gamma_{\mathrm{tot}}$ have been introduced such that

$$\sum_n \gamma_n = 1 \tag{1.22}$$

Now, a (possibly large) fraction of the contributing decay channels have not been measured. Thus one might split the expression for the width in two pieces

$$m_a \Gamma_{\mathrm{tot}}(s) = m_a \Gamma_{\mathrm{tot}} \left[\sum_n^{\mathrm{measured}} \gamma_n \rho_n(s) + \gamma_{\mathrm{unobserved}} \right] \tag{1.23}$$

Where the mass dependence of $\gamma_{\text{unobs.}}$ has already been neglected. Note that the relative branching fractions of the observed channels are fixed by the different decay strengths into different channels through the g_a^n (c. f. equation 1.16). In addition there is the constraint equation

$$\sum_{n}^{\text{measured}} \gamma_n \rho_n(s) + \gamma_{\text{unobserved}} = 1 \tag{1.24}$$

In summary the effect of several unobserved channels can be approximated by an s-independent contribution to the dynamic width, neglecting the detailed shape of the different phase space factors. This will of course not work properly in the vicinity of sharp thresholds where ρ_n varies strongly with s. A prominent case where this effect cannot be neglected is the $f_2(1565)$ which sits right at the $\omega\omega$ threshold (for a discussion see for example [65]).
For the case of the 5π channel the following thresholds have been identified for the $I^g = 1^-$ quantum numbers:

Channel	Threshold (GeV/c^2)
$\omega\omega\pi$	1.71
$\phi\omega\pi$	1.94
$\eta'\eta'\pi$	2.06
$\phi\phi\pi$	2.18

Table 1.4: Thresholds of $I^G = 1^-$ channels in the region around 2 GeV/c^2 involving narrow secondary states.

For none of these channels reliable information is available. In principle one could try to infer the couplings of the resonances to all possible decay modes by measuring the line shapes with high precision. However, without any direct observation such attempts would be prone to ambiguous solutions. Because of this, threshold effects in unobserved channels have been neglected in the analysis presented below.
From the discussion above it is clear that the approximations made — notably the simplified treatment of the dynamic width and the neglect of dispersive effects — are especially problematic in the vicinity of a threshold when there are few open channels, such as the $K\bar{K}$ threshold, which consequently has attracted much discussion in the literature (some recent examples are given in [72, 73] and references therein). In this case unitarity imposes rigorous constraints on the structure of the amplitude and thus correlations between the participating channels. The situation with many open channels is remarkably different. Here dispersive effects are distributed over many contributions, the detailed influence of a single channel on the shape of the resonance in general becoming quite subtle, depending on its branching ratio. On these grounds the aforementioned approximations may well be justified.
For the implementation in a fitting program, a convenient choice is to use the partial widths Γ_a^n as free parameters (including one for the unobserved channels) and to calculate the decay coupling constants as

$$g_a^n = \sqrt{m_a \Gamma_a^n} \tag{1.25}$$

The total width is then computed through

$$\sum_n \Gamma_a^n = \Gamma_{\text{tot}}^a \tag{1.26}$$

and does not appear as an explicit fitting parameter. The production couplings $\hat{g}_b$, the bare masses m_a and a possible form-factor are additional free parameters of the model. For a model which takes into account mixing between the different states there are the mixing parameters B_{ij} which in the simplest case can be approximated by constants [65].

Chapter 2

Diffractive Pion Dissociation at COMPASS

DIFFRACTIVE pion dissociation is the main mechanism used for the production of mesons at the COMPASS experiment at CERN. This chapter describes the measurement of diffractive processes with this apparatus. In particular the diffractive dissociation of pions into the $\pi^-\pi^+\pi^-\pi^+\pi^-$ final state is discussed. After a brief overview of the experimental setup that has been used during the year 2004 run the main part of the chapter deals with the selection of exclusive 5-pion events from the recorded data and their interpretation in terms of diffractive dissociation.

2.1 The COMPASS Experiment

A very detailed description of the **C**ommon **M**uon and **P**roton **A**pparatus for **S**tructure and **S**pectroscopy (COMPASS) is given in the paper [74] which explains the experimental setup that has been used in the year 2004. In the following, only the main features that are important for the measurement of the diffractive pion dissociation into 5 charged pions will be briefly summarized. COMPASS is also equipped with large-acceptance photon-detection capabilities, but the focus of this thesis is placed on the fully charged final state and so a description of the calorimetry will be left aside.

COMPASS has been designed to study strong interactions in the non-perturbative regime of QCD. Three types of measurements were foreseen in the initial design of the experiment. The first is deep inelastic scattering of polarized muons off a polarized target to study the polarization of the gluonic content of the nucleon. The second type is hadron-hadron scattering at small scattering angles — in the so called diffractive regime — to study hadronic resonances. The third is hadron-photon scattering in Primakoff kinematics [75] which gives access to pion and kaon polarizabilities. In fact the latter two experiments can be performed in parallel using heavy nuclear targets as sources of strong electromagnetic fields (due to their high Z) as well as providing a hadronic medium on which scattering through the strong interaction may happen.

The general requirements that are demanded from the spectrometer in order to perform the envisioned physics measurements are large and uniform angular and momentum acceptance, good kinematic reconstruction capabilities and the ability to measure extremely small scattering angles. Furthermore in order to gather the large data sets that are essential to study rare processes or to perform partial-wave analyses, the experiment is designed to handle high luminosities of up to $5 \cdot 10^{32}\mathrm{cm}^{-2}\mathrm{s}^{-1}$ for the muon beam and to record large data volumes (8 TB/d during the 2004 hadron pilot run).

2.1.1 Hadron Beam at the M2 SPS Beamline

A key feature of the experiment is the M2 beamline at the CERN **S**uper **P**roton **S**ynchrotron (SPS). The intense primary 400 GeV/c proton beam of the SPS is focused onto a Beryllium target of variable length (up to 500 mm) in order to create a secondary beam containing mainly pions as well as some kaons and protons. A system of six quadrupole and three dipole magnets is used to select a secondary beam with up to 225 GeV/c momentum[1]. At this stage the contribution of kaons to the negative beam is $\sim 3.6\%$. The following beamline, which is about 1 km long, is used to collimate the beam, to filter the desired momentum range and (if so desired) to separate muons — which are created in pion decays — from the hadrons by sending the beam through a series of thick hadron absorbers made from Beryllium. While for the muon beam there is a dedicated dipole magnet and detector system to measure the momentum of each individual beam particle, the system is not usable for the hadron beam because of its prohibitively large interaction length. Thus for the hadron beam only the direction of the beam particles is measured by a silicon tracking telescope in front of the target, but not its momentum.

The acceleration cycle of the SPS dictates a *spill structure* of the extracted beam. That means that there is a period where the proton beam is inserted into the SPS and accelerated to the nominal energy, followed by a series of extraction phases (called spills) when the beam is steered out of the SPS ring and delivered to the various experiments. The proton flux that was available to COMPASS in 2004 was $1.2 \cdot 10^{13}$ protons during a 4.8 s spill. The SPS cycle had a length of 16.8 s. The allowed hadron flux at the COMPASS experiment is limited to 10^8 hadrons per SPS cycle by radiation protection regulations.

2.1.2 Target and Luminosity

For the 2004 hadron run the hadron beam impinged on disks made of lead with a total thickness of 3 mm. The total integrated luminosity collected in this run has been determined [76] from decays of kaons in the beamline to be

$$\int \mathscr{L}\, dt = 9.55 \cdot 10^4\,\mathrm{mbarn}^{-1}$$

. The analysis presented in this thesis only uses about 80% of the total data set, which was recorded with a split target of $2+1$ mm thickness. Only during the data taking on this target the Online Filter described below was in stable operation.

2.1.3 Spectrometer Setup

Figure 2.1 shows an overview sketch of the spectrometer from the year 2004 hadron pilot run. Here the

---

[1] The maximum reachable beam momentum with a modified acceptance optics of the beamline is 280GeV/c

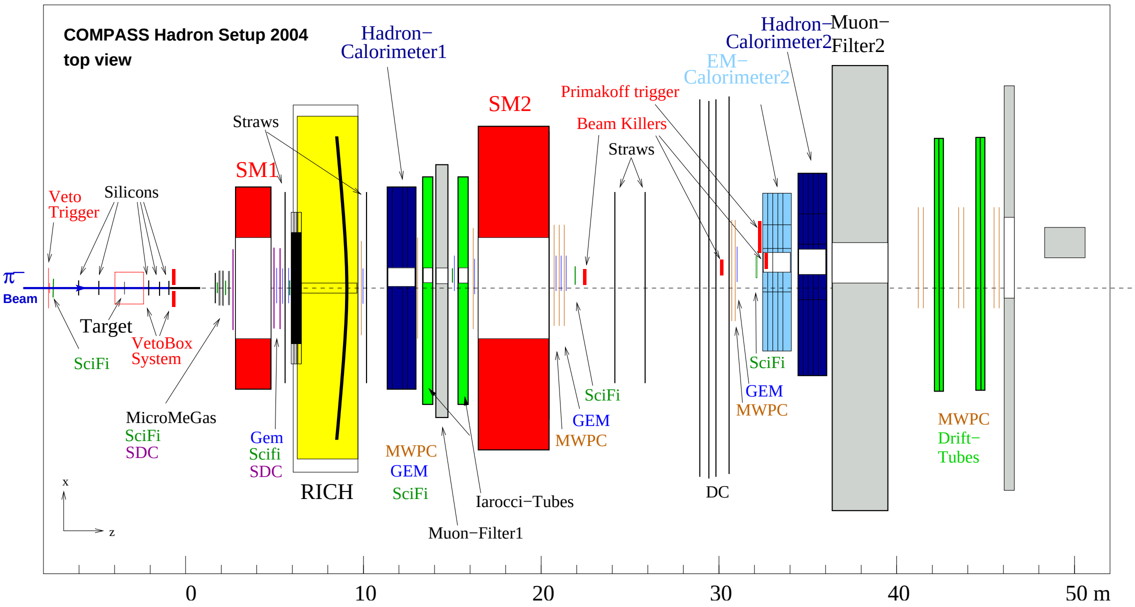

Figure 2.1: Overview of the COMPASS spectrometer setup in the year 2004.

A special feature of COMPASS is its setup as a two-stage magnetic spectrometer. In order to provide optimal tracking capabilities for both particles entering the spectrometer under large angles and/or slow momenta as well as for high momentum particles with very small scattering angles the experiment employs two large dipole magnets which are surrounded by tracking detectors to measure the trajectories of charged particles. The first spectrometer contains a **R**ing **I**maging **C**herenkov **C**ounter (RICH) for charged particle identification. For the 2004 hadron run this detector was filled with N_2 gas in order to reduce the amount of material in the spectrometer for the Primakoff Compton measurement, which was running in parallel. This gas choice severely limits the kinematic domain where effective particle ID can be performed and for this reason no RHICH information has been used in the analysis presented here. In addition each spectrometer stage is also equipped with electromagnetic and hadronic calorimeters. In the following the charged tracking system is described in some more detail, since it is crucial for the measurement of the $\pi^-\pi^+\pi^-\pi^+\pi^-$ final state.

Tracking System

The target region In order to precisely reconstruct the position where an interaction occurred in the target and to measure the scattering angles of outgoing particles with respect to the beam the target has been surrounded by double-sided silicon micro-strip detectors which are capable of measuring points on the trajectories of charged particles with a spatial resolution of $\sim 10\,\mu$m[2] in two projections and a time resolution of 2.5 ns [74]. In the 2004 setup there were two silicon stations in front of the target and three stations downstream. Each station contains two double-sided detectors, thus providing four point measurements on the beam track and up to six point measurements on each outgoing track. The downstream silicon detectors also

---

[2] The double sided silicon strip detectors have an average resolution of 8 μm on the p-doted-side and 11 μm on the n-side.

play a central role in the online-filter that has been used to reject background events and enhance the fraction of usable and interesting data in real-time during data taking. This will be discussed in some detail below.

Another crucial component of the experiment has been a scintillating *multiplicity counter*. Installed directly behind the target this device has been operated in a threshold counter mode as an active element of the trigger system. Details will be given below in section 2.1.3.

The first spectrometer stage — also called the **L**arge **A**ngle **S**pectrometer LAS — is built around a dipole magnet (**s**pectrometer **m**agnet 1, SM1) placed about 4 m downstream of the target area and covering ±180 mrad polar acceptance with a field integral of 1.0 Tm. It is surrounded by several detectors for charged particle tracking. COMPASS employs high luminosities and the detectors close to the beam have to operate and be able to reconstruct particle tracks in a high rate environment. Therefore the tracking system is subdivided into two parts. The **S**mall **A**rea **T**rackers (SAT) cover the region close to the beam (~ 2.5 to 20 cm radial distance) with high granularity and detector technology that can withstand the high ionization rates. The outer regions of the acceptance are covered by the more conventional **L**arge **A**rea **T**trackers (LAT).

COMPASS was the first large-scale particle-physics experiment to make use of **M**icro **P**attern **G**as **D**etectors. Two detectors of this class, the Micromegas[77, 78] and the GEM[79, 80, 81, 82, 83] detectors, have been installed as the SAT system, both offering a rate capability of up to $10^4\,\mathrm{s}^{-1}\mathrm{mm}^{-2}$ and a spatial resolution of the order of $100\,\mu$m[83]. There are three stations of Micromegas detectors — measuring 4 spatial projections each — installed in front of SM1. Downstream of SM1 there are in total eleven GEM detector stations installed. Each of those stations also measured four spatial projections. Further details on these tracking detectors are available in [74] and references therein. The most central regions up to a distance of 2.5 cm from thee beam of the SAT detectors are penetrated by the beam and thus are usually switched off during full intensity data taking. During runs with the muon beam this innermost region is covered with **Sci**ntillating **Fi**ber detectors. However, these detectors have a significant thickness of up to 2.79% of a radiation length and therefore stations 4,6 and 7 were removed[84] for the measurements with the hadron beam. In order to retain sufficient redundancy for charged particle tracking close to the beam in the region between SM1 and SM2 the center-areas of the GEM detectors were activated. This has to be taken into account in the reconstruction software and also in the Monte Carlo model of the detector (see section 3.6) when analyzing data from that period.

The LAT system of COMPASS is comprised of several large drift chambers (DC), multi-wire proportional chambers (MWPC) and straw-tube trackers (see Figure 2.1). In front of SM1 there is one of three identical drift chambers (DCs), the other two being installed downstream of the magnet. With a spatial resolution of $270\,\mu$m and an active size of $180 \times 127\,\mathrm{cm}^2$ these detectors provide tracking information for low-momentum particles. Downstream of SM1 there are also 15 straw-tube detectors and eleven MWPC stations (containing 3 wire layers each) for the tracking of particles which traverse the spectrometer under large angles in the range of $15-200$ mrad. All these detectors have an inactive area to accommodate the beam and the high-rate region which is covered by the SAT.

In total there are 47 tracking detectors (including the micro-strip silicon and the SciFi detectors downstream of the target) in the first spectrometer stage. For further details the interested reader should consult [74].

The second spectrometer stage uses a dipole magnet with 4.4 Tm field integral, located 18 m downstream of the target and offering a polar acceptance of ±30 mrad (hence the abbreviation SAS for **S**mall **A**ngle **S**pectrometer) to detect particles with momenta larger than 5 GeV/c. This magnet is sandwiched by similar detectors as used in the LAS. In addition 6 stations of large-area drift chambers are used here. The total number of tracking detectors in the SAS is 42.

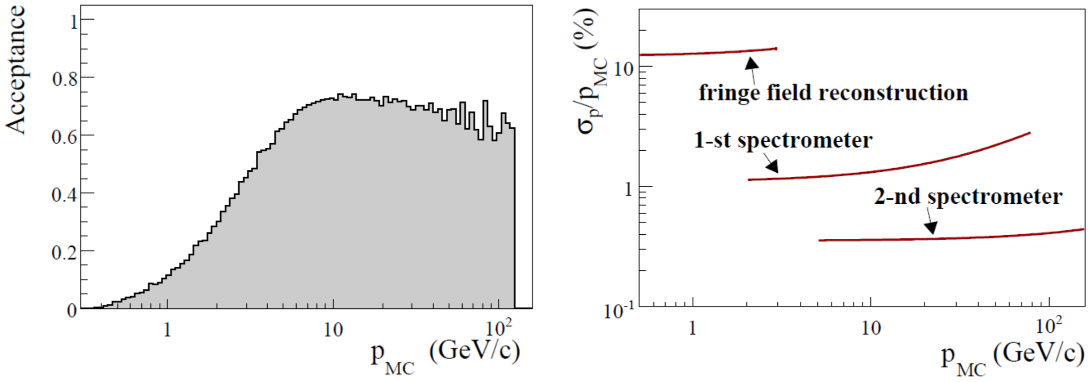

(a) Single track acceptance (b) Momentum Resolution

Figure 2.2: Reconstruction performance for single, charged tracks. (a) Acceptance of the apparatus as a function of the momentum (note the double-logarithmic axes). (b) Momentum resolution of charged track reconstructed in the fringe-field upstream of SM1, in SM1 only or in both spectrometer magnets. Both plots from [74]. For details on the simulated data sample see there.

Charged particle tracking performance of the COMPASS spectrometer is summarized in Figure 2.2, which has been taken from [74]. The single track reconstruction acceptance is shown in Figure 2.2(a). It lies between 60 and 80% over much of the relevant kinematic range. Only for particles blow $p \sim 10\,\mathrm{GeV}/c$ the acceptance drops to roughly 10% at $p \sim 1\,\mathrm{GeV}/c$.
Figure 2.2(b) shows the momentum resolution which is achieved using different parts of the spectrometer. Even slow particles, which do not even reach through the first dipole magnet can be reconstructed by following their trajectory in the fringe field of SM1. For charged particles that are reconstructed using only the first spectrometer stage a resolution in the %-range is achieved over a large kinematic range. The full reconstruction with both dipoles, which is possible for tracks with $p > 5\,\mathrm{GeV}/c$ can achieve an excellent momentum resolution of $\frac{\delta p}{p} \sim 0.4\%$. This performance, which translates to an excellent coverage of even multi-particle phase spaces is an essential prerequisite for partial-wave analyses that depend on the complete reconstruction of exclusive events.

Diffractive Trigger and Online Filter

Figure 2.3 shows an overview of the detector elements that have been used to setup the trigger for the 2004 hadron run. The beam is defined by a beam counter and a veto hodoscope upstream of the target. The upstream veto rejects particles that do not hit the target material. The beam counter is operated in anti-coincidence with three *beam-killer* scintillators to suppress

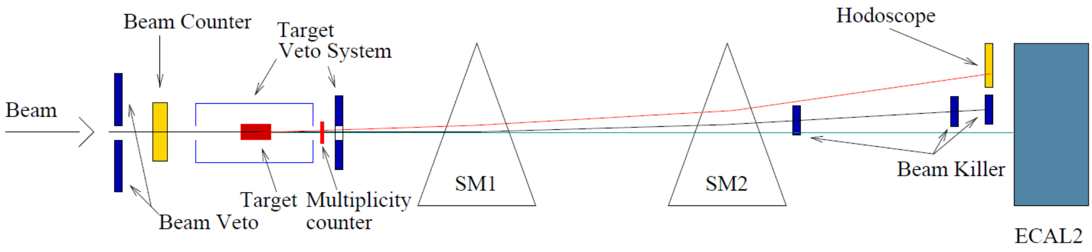

Figure 2.3: Sketch of the trigger elements for the Primakoff/Diffractive Trigger.

pions which do not interact in the target. The downstream hodoscope in front of the second electromagnetic calorimeter (ECAL2) has been used for the Primakoff trigger and will not be needed for the following discussion.

In order to enhance the fraction of diffractive events during the 2004 hadron run a special trigger was set up. Its main active element was a scintillating multiplicity counter (MPC), which covered the complete angular acceptance of the COMPASS spectrometer. A scintillator disk of 49 mm diameter and 3 mm thickness was used to measure the amplitude of the scintillation signal produced by traversing charged particles. By requiring this signal to pass a certain threshold a trigger signal was constructed which implemented the requirement that *at least* two charged tracks were going in coincidence through the counter. For a 5-pion event the probability that two out of five charged particles hit the MPC is very close to 1. An additional element of the trigger logic was the *online filter*. This software-filter improved the selectivity of the trigger by a fast examination of the data stream. Only interesting events have been tagged for tape-recording. This filter was requiring a minimum track multiplicity in the silicon stations downstream of the target. The applied algorithm [85] determines the number of hits in each of the twelve detector planes. The four planes with highest and the four planes with lowest hit multiplicities are discarded. In the remaining four planes a minimum of five hits is required for the event to be accepted. It can be easily shown with Monte Carlo studies (see also section 3.6) that this condition is practically always fulfilled for 5-pion events.

A further element in the diffractive trigger were two veto counters which were supposed to reject particles emitted under large angles, outside the spectrometer acceptance (see Figure 2.4). Especially due to the the second station, which was placed about 4 m behind the target and had a circular central opening of 290 mm, events containing a pion which was emitted under a larger angle of $\theta > 35$ mrad were suppressed. This effect has to be accounted for in the acceptance corrections as it has — for high invariant masses of the 5-pion system — a significant effect on the measured angular distributions as will be discussed in section 3.6.

2.2 Exclusive Production of 5 Pions

The reaction studied in this thesis is the production of five charged pions through the diffraction of a high energy π^- on a nuclear target

$$\pi^- + A \rightarrow \pi^-\pi^+\pi^-\pi^+\pi^- + A$$

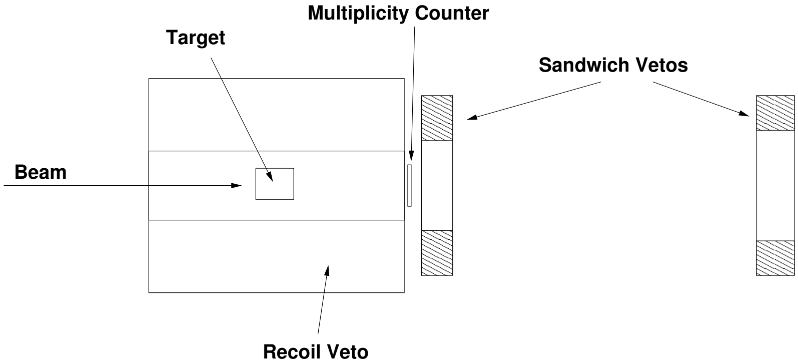

Figure 2.4: Sketch of the trigger elements around the target region.

.
A is the target nucleus which is assumed to act as a source of the strong force and takes up recoil momentum without being destroyed. This assumption will be justified in the following.

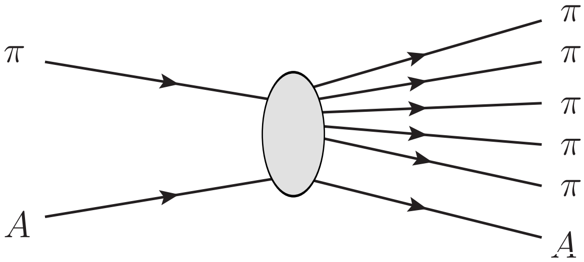

Figure 2.5: A high energy pion beam impinging on a nuclear target and producing five outgoing pions.

Figure 2.5 shows a pictorial illustration of the aforementioned process. In the following the 4-momentum of the incoming pion will be written as p_{beam}. The target nucleus has a 4-momentum p_A (p'_A) before (after) the interaction and $p_X = \sum_{i=1}^{5}(p_\pi)_i$ is the 4-momentum of the multi-pion system in the final state. The most important Lorentz-invariant quantities that describe the process are:

- the squared invariant center of mass energy

$$s = (p_{\mathrm{beam}} + p_A)^2$$

- the squared 4-momentum transfer to the target

$$t = (p_{\mathrm{beam}} - p_X)^2$$

- the invariant mass of the produced multi-pion system

$$m_X^2 = p_X^2$$

Another important quantity that will be used in the discussion is the energy of the multi-pion system in the laboratory frame $E_X = p_X^0$.
In this section the selection of exclusive 5π production events at COMPASS is discussed. The observed momentum transfer distribution is interpreted as diffractive pion dissociation.

2.2.1 Data Set and $\pi^-\pi^+\pi^-\pi^+\pi^-$ Event Selection

The analyzed data sample was recorded during the 2004 COMPASS pilot hadron run. During that run a pion beam with an energy of 189 GeV was impinging on a target made of two stacked lead discs of 2 mm and 1 mm thickness which were suspended with a distance of 100 mm between them. In total data from 56 runs (run numbers 43191-43323) from the *hprod_nov05_1* data-production have been analyzed. The data selection was done in several steps with increasingly tightened kinematic cuts in order to select exclusive 5-body events. For further analysis the data has been partitioned into three momentum transfer intervals as explained below.

5π Final State from Primary Vertex

PHAST [86] is the COMPASS analysis software which provides access to the reconstructed particle candidates. For the present analysis version 7.072 of this program has been used. The first basic steps of data selection were done using this tool and the resulting pre-selected event data was written to a custom ROOT tree in order to facilitate a fast turnaround for further refinements in the analysis. The applied cuts are summarized in Table 2.2.1. Only events with exactly one reconstructed vertex in the target region have been considered. Valid vertices consist of one incoming and five outgoing charged tracks. This definition is motivated by the picture of diffraction (see section 2.2.2). According to this hypothesis the target nucleus only receives a small recoil momentum. Most of the recoiling nuclei will not even leave the target material and thus must remain undetected. Therefore, in the 2004 detector setup no means of detecting slow recoil particles has been foreseen. As a final requirement to define an exclusive 5-pion event, the total charge of the outgoing particles is required to be negative, corresponding to the charge of the beam pions. This requirement excludes charge transfer reactions.

Description	Range	Yield
Exactly one primary vertex	$z_{\text{PV}} \in [-330, 290]$ cm	
Number of outgoing tracks	5	3678937
5π system total charge	$q = -1$	
Refined vertex position	$z_{\text{vertex}} \in [-322, -298]$ cm	2356747
Exclusivity	$E_{5\pi} \in [189-6; 189+6]$ GeV	
Refined vertex position	$z_{\text{vertex}} \in [-319, -299]$ cm	384235

Table 2.1: List of cuts applied in order to select exclusive 5π production events.

Figure 2.6 shows the vertex distribution after these cuts. The two target discs of the $2+1$ mm lead target appear as clearly visible peaks in the histogram.

Pion Hypothesis and Kaonic Background: The selected final state is analyzed under the assumption that all outgoing particles are pions. The final state particle 4-momenta are calculated under this pion hypothesis. The inclusive production cross section for kaons is ex-

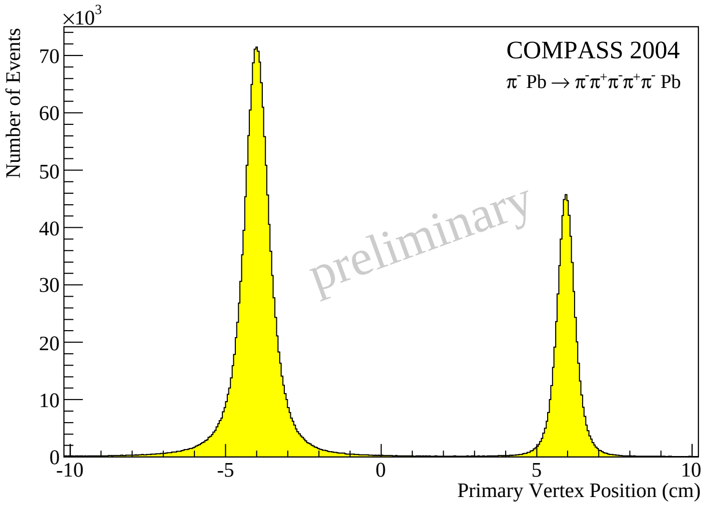

Figure 2.6: Primary vertex distribution along z in the laboratory reference frame of COMPASS. The origin of the ordinate corresponds to $z_0 = -310.5\,\mathrm{cm}$. The two target discs of the $2+1\,\mathrm{mm}$ target are clearly resolved.

pected to be about 5% of the pion cross section. Unfortunately no particle identification was available in 2004 so a background of kaons (which are assigned the wrong mass hypothesis) has to be expected in our data sample. Note, however, that for an incident pion because of strangeness conservation only pairs of kaons will be produced. In that case the reaction $\pi + \mathrm{Pb} \rightarrow \pi^-\pi^+\pi^- K^+ K^- + \mathrm{Pb}$ would be misinterpreted as $\pi + \mathrm{Pb} \rightarrow \pi^-\pi^+\pi^-\pi^+\pi^- + \mathrm{Pb}$.
Furthermore the pion beam contains a $\sim 3\%$ kaon contamination. Since not particle identification for the beam particle has been used, diffractive kaon dissociation $K^- + \mathrm{Pb} \rightarrow \pi^-\pi^+\pi^-\pi^+ K^- + \mathrm{Pb}$ is another background to the 5π final state. The impact of this kaonic background may be studied with Monte Carlo simulations in the future. Improvements in the COMPASS apparatus (CEDARS and RICH) will open the possibility for closer cross checks using data from the 2008 and 2009 runs.

Since the expected background contributions to the cross section are on the few percent level, the pion hypothesis is adopted for the rest of this thesis unless stated otherwise.

There have been no offline selection criteria on the diffractive trigger or the online filter (c. f. section 2.1.3). The diffractive trigger bit has been found to be set for all recorded 5π events. The online filter is 100% efficient for these events. Both effects can be understood by looking at the threshold criteria for the multiplicity counter and the online filter, which had originally been tuned to capture events with 3 charged pions in the final state. Events with even more charged tracks obviously will fulfill these trigger criteria with high probability. Thus the trigger that has been used acts like a minimum-bias trigger for the case of the $\pi^-\pi^+\pi^-\pi^+\pi^-$ final state.

Selection of Exclusive Events

Figure 2.7 shows the total reconstructed energy of the 5π system. A clear exclusive peak is observed at the nominal beam energy of $E = 189\,\mathrm{GeV}$. Since neither the energy of the impinging pion has been measured precisely with the 2004 setup, nor has the recoil particle been observed, the kinematics is under-determined. The exclusivity peak serves as the only criterion to define exclusive events. Excitations of the target nuclei can therefore not be completely excluded. However, for the small momentum transfer reactions that will be studied (see below) any particles from the decay of a nuclear excitation will have very low momentum ($\lesssim 1\,\text{GeV}$) in the laboratory frame and will with high probability not be detected in the apparatus. Such processes are therefore unlikely to contaminate the amplitude analysis of the 5π system described in chapter 3.

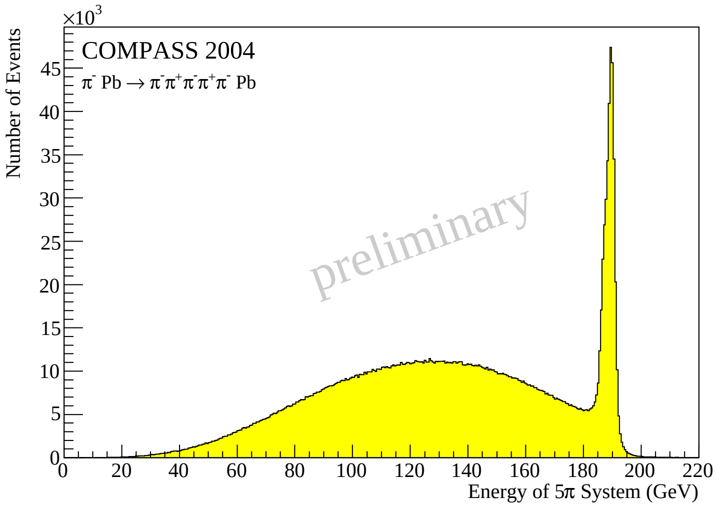

Figure 2.7: Total Energy of the 5π system with a clear peak for exclusive events at 189 GeV.

There is a considerable tail of non-exclusive background events extending below the exclusivity peak. Presumably this distribution originates from events, where one or more particles have not been reconstructed. Candidate background reactions are for example

$$\pi^- + \text{Pb} \rightarrow \pi^-\pi^+\pi^-\pi^+\pi^-\pi^0\pi^0 + \text{Pb}$$

or

$$\pi^- + \text{Pb} \rightarrow \pi^-\pi^+\pi^-\eta' + \text{Pb} \quad \text{with} \quad \eta' \rightarrow \pi^+\pi^-\pi^0$$

where the π^0s remain unobserved.

In order to isolate exclusive 5π production it is required that the five outgoing pions carry the full beam energy. Thus the final cuts for the event selection are:

- Exclusivity: $E_{5\pi} \in [189-6; 189+6]\,\text{GeV}$
- $z_{\text{vertex}} \in [-319, -299]\,\text{cm}$
- Final yield: 384235 events

Figure 2.8 illustrates the effect of the exclusivity cut on the vertex distribution. The gray histogram shows the same distribution as Fig. 2.6 on a logarithmic scale. In yellow the distribution after the exclusivity cut is shown. No background outside the two target cells of the 2+1mm target remains. Therefore the cut on the vertex position can be left relatively loose in the following.

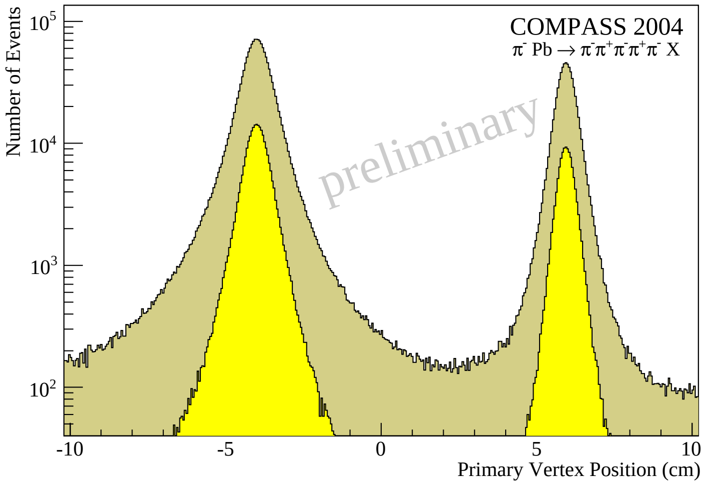

Figure 2.8: Primary vertex distribution along z in the laboratory frame (in gray all 5π events). The yellow histogram shows the effect of the exclusivity cut $E_{5\pi} \in [183, 195]$ GeV on the vertex distribution.

2.2.2 Diffractive Production Mechanisms

Momentum Transfer Distribution

Since only the direction of the beam has been measured with high precision, its 4-momentum is reconstructed from the energy of the outgoing 5-body system under the assumption of an elastic nuclear recoil.

For the case when the mass of the recoiling target particle remains constant during the scattering process, an approximate formula for the beam-energy can be derived [87] which is valid for small scattering angles θ:

$$E_{\text{beam}} = E_X + \frac{1}{2m_0(1-\epsilon)} \left[(E_X\theta)^2 + (m_\pi\epsilon) \right] \quad \text{with} \quad \epsilon \equiv \frac{m_X^2 - m_\pi^2}{2m_0 E_X} \tag{2.1}$$

Here E_X is the energy and m_X the invariant mass of the 5π system and m_0 the recoil mass. The formula takes into account the momentum transfer that is needed to scatter the incoming pion into the massive multi-pion final state.

The minimum value for $|t|$ depends on the invariant mass $m_{5\pi}$ reflecting the fact that a minimal longitudinal momentum transfer is necessary to provide the energy for the production of four additional pions. It is convenient to define

$$t' = |t| - |t|_{\text{min}} \geq 0 \tag{2.2}$$

In the laboratory system for high beam energies the following approximation [87] is useful to calculate t':

$$|t|_{\text{min}} \approx \frac{\left(m_X^2 - m_{\text{beam}}^2\right)^2}{4|\vec{p}_{\text{beam}}|^2_{\text{lab}}} \tag{2.3}$$

Figure 2.9 shows the momentum transfer distribution of the exclusive event sample on a logarithmic scale. The spectrum shows a characteristic peak in the forward direction $t' \sim 0$. This phenomenon is well known in high-energy hadron scattering and is understood in the framework of diffractive hadron scattering.

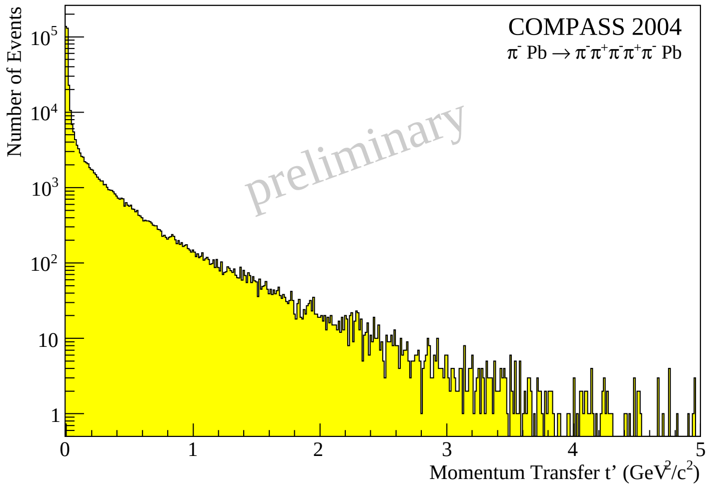

Figure 2.9: Overall t' distribution; logarithmic scale.

Diffraction and Regge theory

The term *diffraction* in high-energy hadron scattering refers to a situation where the center-of-mass energy $\sqrt{s}$ is much larger than the squared momentum transfer. The scattering amplitudes in this regime have been successfully explored in the framework of *Regge theory* [88, 89, 90]. The basic idea of Regge theory is the analytical continuation of the partial wave helicity amplitudes for the scattering process into the complex angular momentum plane and the subsequent application of dispersion relations in order to constrain their possible structure — the so called *Sommerfeld-Watson transform.*

The advantage, but also one limitation of this approach is that it does rely only on very general properties of the scattering amplitudes, such as analyticity and unitarity, while the underlying hadron dynamics is absorbed into phenomenological constants, like the residuals of Regge poles. Extensive reviews on Regge theory are available in [91, 35, 92, 48]. The validity of Regge theory is limited to a specific — yet phenomenologically important — kinematic region characterized by

$$s \gg \Lambda_{\mathrm{QCD}}^2 > |t|$$

The complete derivation of Regge theory from QCD in this kinematic limit is still an open theoretical challenge[3].

For the purpose of the present analysis, however, the Regge picture of diffractive scattering provides a very nice starting point, as it allows to represent the scattering of a high-energy pion

---

[3] There are, however, attempts to explore the issue of Regge behavior in simplified versions of QCD. For a modern example see [93].

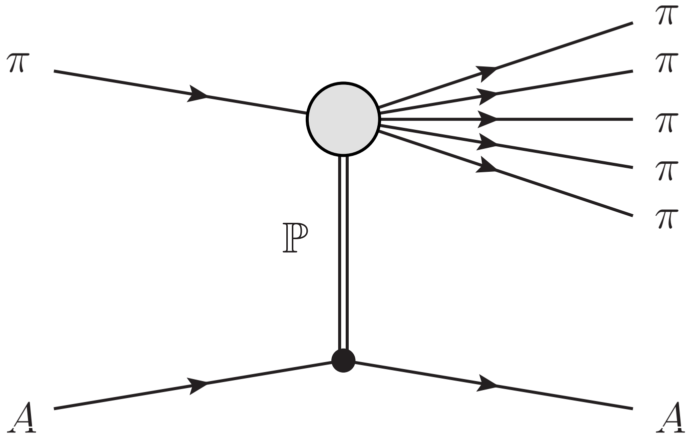

Figure 2.10: Diffractive pion dissociation on a nucleus.

on a nucleus into a five pion state with a graph as shown in Fig. 2.10. The situation where one of the initial hadrons stays intact while the other one scatters into a multi-particle final state is called *single-diffractive dissociation*. Diffractive dissociation events are characterized by large rapidity gaps between the different groups of particles. Here the 5π system is scattered into the forward direction, while the target nucleus only receives a small recoil. This scattering process can be described by the exchange of a quasi-particle in the t-channel which is called a *Reggeon*. Originally Regge theory was developed to understand the properties of elastic hadron scattering. The corresponding amplitude is visualized in Figure 2.11. This relatively simple case shall serve here as a preparation for the description of the inelastic multi-particle production amplitude following later.

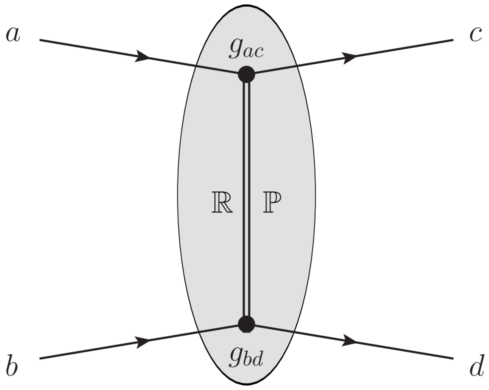

Figure 2.11: Elastic scattering amplitude in the Regge picture.

The elastic scattering amplitude for a single Reggeon exchange (in the limit $s \gg t$) takes the following form [92]:

$$A(s,t) \propto g_{\lambda_a\lambda_c}(t) \cdot \left(\frac{s}{s_0}\right)^{\alpha(t)} \frac{S + \exp(-i\pi\alpha(t))}{2\sin\pi\alpha(t)} \cdot g_{\lambda_b\lambda_d}(t) \tag{2.4}$$

where S is the *signature*[4] of the exchanged Reggeon and $\alpha(t)$ is the corresponding Regge trajectory. The $g_{\lambda_i\lambda_f}$ are (real valued) effective coupling constants associated to the Regge vertices. They contain the regge pole residue as well as kinematic singularities. These latter factors arise from angular momentum conservation and lead to a t-dependence of the vertex functions that is sensitive to the helicity flip $|\lambda_f - \lambda_i|$ at the respective vertex [91]:

$$g_{\lambda_i\lambda_f}(t) \propto (t)^{|\lambda_f-\lambda_i|/2} \tag{2.5}$$

Thus helicity flip amplitudes (i. e. $\lambda_f \neq \lambda_i$) are suppressed for small values of t.

The prediction for the asymptotic behavior of the total hadronic cross section can be obtained by realizing that the amplitude for elastic forward scattering at $t = 0$ is essentially given by equation 2.4 as

$$A(s, t=0) \propto s^{\alpha(0)}. \tag{2.6}$$

With the optical theorem

$$\sigma_{\text{tot}} \propto \frac{1}{s} \text{Im} A(s, t=0) \tag{2.7}$$

the total cross section has to exhibit the asymptotic s-dependence

$$\sigma_{\text{tot}} \propto s^{\alpha(0)-1}. \tag{2.8}$$

It is well known that the Regge trajectories derived from the meson spectrum are to a good approximation linear [89, 91]

$$\alpha(t) = \alpha_0 + \alpha' \cdot t \tag{2.9}$$

as shown in Figure 1.1. The intercept of these trajectories is smaller than one $\alpha(t=0) = \alpha_0 < 1$, which means that the total cross section should drop with rising s. Indeed the contrasting observation is a slow rise of $\sigma_{\text{tot}}(s)$ with increased center of mass energy. This problem is resolved by the introduction of a Regge trajectory with an intercept close to one. The name of this object is the *Pomeron* [94, 95]. It was shown by Foldy and Peierls [96] that the Pomeron has to carry the quantum numbers of the vacuum, in particular its parity and its G-parity are even, and the Pomeron is an isospin-singlet. Another important feature of the Pomeron is its positive *naturality*[5].

The extend to which the total cross section is dominated by Pomeron exchange can be inferred from fitting Regge parametrizations to total cross section measurements obtained from elastic scattering data via the optical theorem. The COMPAS (sic.) working group is fitting the total $\pi^- p$ and $\pi^+ p$ cross sections using models with the exchange of two Regge trajectories and a Pomeron contribution [97]. Figure 2.12 shows their parametrizations in the intermediate energy range. For higher and higher energies the cross sections for the charged pions increasingly coincide indicating an even C-parity process — Pomeron exchange — is dominating for large energies. For a 190 GeV pion beam scattering off a proton, the center of mass energy is

---

[4] As one constructs an analytic continuation of helicity amplitudes into the complex angular momentum plane it turns out that this can not be done in a general way. Instead one has to distinguish explicitly between odd/even J (for integer angular momentum J) contributions. The two cases lead to a different factor ±1 in the amplitude, called *the signature*. For details see [35].

[5] In order to construct helicity amplitudes which describe the scattering of parity eigenstates it turns out that one needs to form linear combinations of amplitudes with the same spin but opposite helicity. The remaining degree of freedom in this construction is described by the so called naturality (compare to the discussion on reflectivity in section 3.1.1).

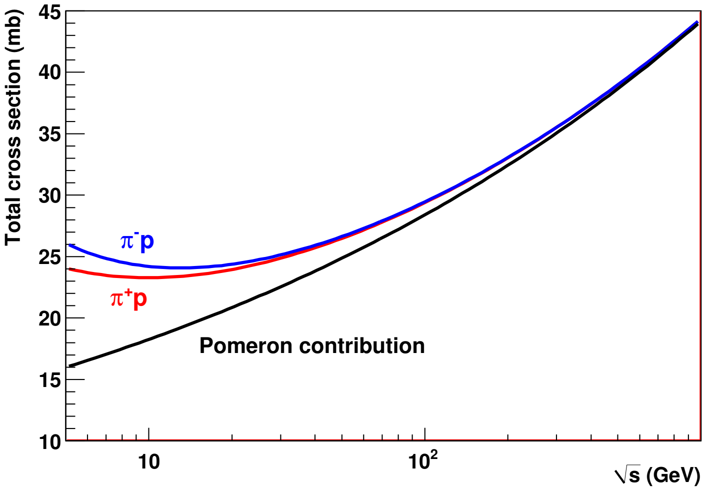

Figure 2.12: Reggeon-Pomeron parametrization of pion-proton total scattering cross sections as a function of the center of mass energy $\sqrt{s}$. Fit parameters from [97].

$\sqrt{s} = 18.9\,\text{GeV}$. From the parametrization of [97] (using the RRE$_{nf}$ model described therein) the ratio of Pomeron / Regge-exchange contributions to the total cross section is 85%. It is important to keep in mind that this number refers to the total cross section as a function only of $\sqrt{s}$, integrating out the $t-$dependence. Indeed for low-t reactions the Pomeron contribution can be much larger. The reason behind this is the different slopes of the Pomeron trajectory ($\alpha'_{\mathbb{P}} = 0.25\,\text{GeV}^{-2}$) [98] and the ordinary meson trajectories ($\alpha'_{\mathbb{R}} = 0.88\,\text{GeV}^{-2}$) [91] (see also Figure 1.1), which implies that their relative contributions to the scattering amplitude (at fixed s) do depend strongly on t.

There are two important expectations that follow for diffractive reactions at COMPASS energies. First, since the Pomeron does not carry isospin and has even G-parity these quantities will be conserved in the reaction and thee incoming pion beam will dominantly dissociate into $I^G = 1^-$ final states. This is the reason why the exclusive production of five pions is favored above the 4-pion final state in COMPASS data. The second conclusion is related to the arguments on naturality discussed above. Parity conservation will lead to a strong constraint on the helicity states of the produced multi-particle system. This topic will be discussed in detail in section 3.1.1.

Historically there are two important approaches how to generalize Regge theory to multi particle production (see e. g. chapter 11 of [92]): the *diffractive excitation* or *nova* model and the *multiperipheral* models. Figure 2.13 shows graphical illustrations of these models.

The diffractive excitation model (Fig. 2.13(a)) is based on the idea, that the incoming pion is excited into an intermediate state X via Pomeron exchange. This state, sometimes called a *fireball* or a *nova*, subsequently decays into the final-state particles. For a small number of decay products it is obvious that X can be a mixture of different spin-parity Eigenstates. The individual partial waves can contain resonant contributions and indeed for the 3π final state it is well known that these resonances are responsible for a significant part of the cross section, in particular for relatively low invariant masses of X in the region of $m_X = 1$ to $2\,\text{GeV}/c^2$. Resonances show up as poles of the production amplitude of the multi-body state in the complex m_X^2-plane. For physical $m_X^2 \in \mathbb{R}$, these poles result in characteristic phase shifts of the amplitudes as a function of m_X. The structure of the production amplitudes can be reconstructed through interference effects in the angular distributions of the decay products as will be explained in chapter 3.

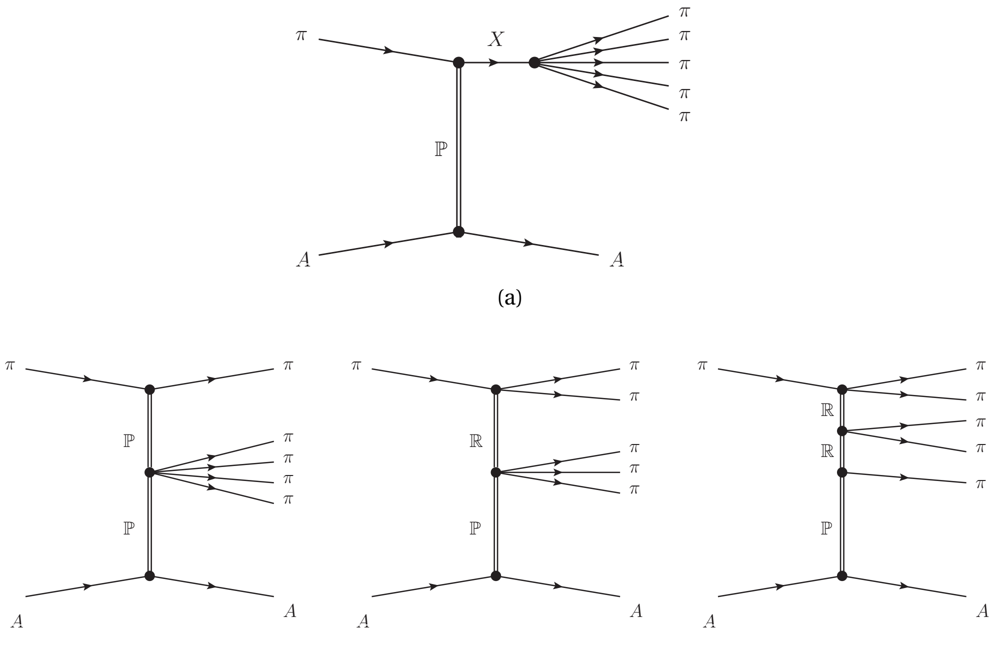

(a)

(b) (c) (d)

Figure 2.13: Multi particle production mechanisms. (a) is the diffractive excitation model in which the incoming pion is excited into an intermediate state X, which subsequently decays into the final state pions. (b-d) are Regge exchange diagrams which appear in the multiperipheral model.

The multiperipheral models involve multiple Regge exchanges. Some example diagrams are shown in Figures 2.13(b-d). A prediction of the multiperipheral model, which has been used in the past to distinguish between the different production mechanisms are the rapidity distributions of the final-state particles. The multiperipheral models predict gaps in rapidity between the different clusters of particles. Harris et al. [99, 100] compared rapidity distributions in the exclusive $\pi^- d \to 3\pi^- 2\pi^+ d$ reaction at 15 GeV/c with model predictions from a multiperipheral and a nova model. They were lead to the conclusion, that the simpler nova model was sufficient to describe the data. Giving the limited statistics of only about 170 events that was available to them it was not possible to study the details of the nova decay such as its spin-parity content.

Figure 2.14(a) shows the rapidity distribution for negative pions out of the exclusive 5-pion final state. There are no pronounced structures in this distribution. Note, however, the limited acceptance of the COMPASS setup in 2004 as shown in Figure 2.14(b). While in the range $4 < y_{\pi^-} < 7$ the distribution is rather flat, there is practically no acceptance for $y_{\pi^-} < 4$. The reason for this is the veto counter which imposes an angular cut of ~ 35 mrad in the laboratory frame. Therefore one can not exclude additional structures at low rapidities and thus an estimation

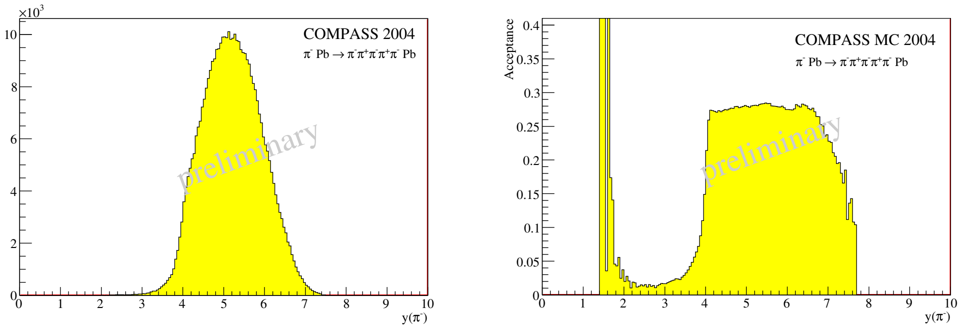

(a) (b)

Figure 2.14: (a) Rapidity distribution for negative pions out of the $3\pi^-2\pi^+$ system. (b) COMPASS acceptance in rapidity. The overshoot of the acceptance below $y = 2$ is an artifact of the Monte Carlo simulation.

of multiperipheral contributions to the 5π production cross section on this grounds is very difficult.

In the future, this issue could be studied in greater detail using the data from the 2008 COMPASS run, for which the angular acceptance of the spectrometer has been greatly improved with a new detector setup.

The present analysis concentrates on production mechanisms of the diffractive excitation type. We will employ amplitude analysis methods to search for resonances with different quantum numbers, decaying into five pions. Figure 2.13(a) will therefore be the guiding picture for setting up the partial-wave analysis formalism in the next chapter. Multiperipheral contributions will not be treated explicitly in the amplitude analysis and will be expected to show up as non-resonant background.

Momentum Transfer Ranges

For further studies the data sample is divided into three bins in the momentum transfer t'. The chosen ranges in t' roughly correspond to a region of coherent scattering on the complete lead nucleus for low t', a high t' range where the scattering is off quasi-free nucleons inside the lead nuclei and an intermediate range between those two cases. The t' bins have been chosen as shown in table 2.2

Low-t':	$t' \in [0, 0.005]\,\text{GeV}^2/c^2$	202578 events
Medium-t':	$t' \in (0.005, 0.1]\,\text{GeV}^2/c^2$	121885 events
High-t':	$t' \in (0.1, 2]\,\text{GeV}^2/c^2$	58672 events

Table 2.2: Momentum transfer ranges.

Figures 2.15(a), 2.15(b) and 2.15(c) show the t' distributions in the low-t', medium-t' and high-t' ranges respectively. Note that these distributions include only events within the exclusivity cut $E_{5\pi} \in [189-6; 189+6]\,\text{GeV}$. The low-$t'$ distribution has a single exponential slope as expected for coherent diffractive scattering off the lead nucleus. The slope for high-t' is considerably smaller and could be due to a scattering off individual nucleons. In the intermediate region the picture is complicated by the occurrence of diffraction patterns.

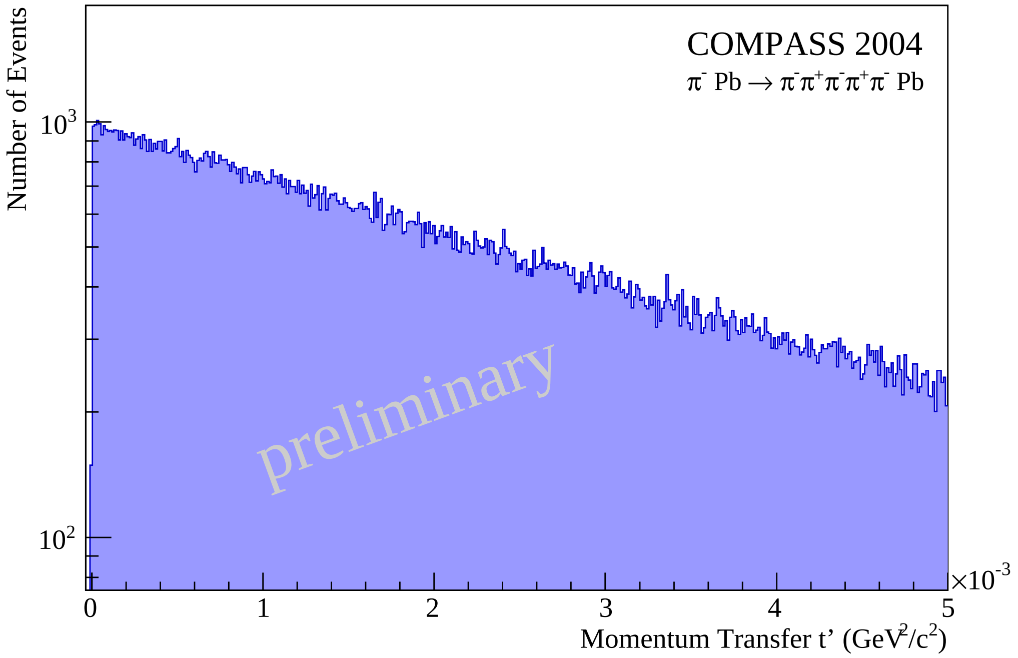

(a) low-t'

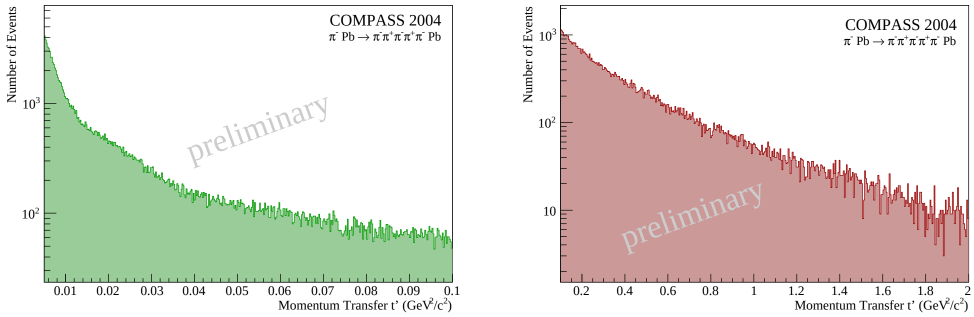

(b) medium-t' (c) high-t'

Figure 2.15: t' distributions for different t' bins (a) low-t': 0 <t'≤ 0.005GeV$^2/c^2$; (b) medium-t': 0.005 <t'≤ 0.1GeV$^2/c^2$; (c) high-t': 0.1 <t'≤ 2GeV$^2/c^2$; logarithmic scale;

The slope of the t'-spectrum $\frac{d\sigma}{dt'} \propto e^{-b_0 t'}$ in the low-t' bin has been fitted to

$$b_0 = 292.8 \pm 1.6 (\mathrm{GeV}^2/c^2)^{-1}.$$

This corresponds to a black disc scattering radius fxfatal[101] of

$$R_{\mathrm{Pb}}^{5\pi} = 0.3\sqrt{b_0}\,\mathrm{fm} = 5.1\mathrm{fm}$$

This is considerably smaller than the value calculated through the approximate formula

$$R_A \sim r_0 A^{\frac{1}{3}} \qquad r_0 = 1.25\,\mathrm{fm}.$$

$$R_{\mathrm{Pb}} \sim 7.4\,\mathrm{fm}$$

Indeed monte carlo studies of the apparatus show that the measured t' spectrum for forward scattering (low-t') is completely dominated by resolution effects. In particular the measured slope in that region can be completely explained with the limited resolution in that variable. The reason for this is the multiple scattering of the charged final state pions inside the target material and in the structures of the detectors themselves. The effect is more pronounced in the $\pi^-\pi^+\pi^-\pi^+\pi^-$ final state than in the $\pi^-\pi^+\pi^-$ where a black disk scattering radius of

$$R^{3\pi}_{\mathrm{Pb}} = 5.92 \pm 0.02\,\mathrm{fm}$$

has been measured using the data from the same period [102].
Because of this limited resolution the choice of the low-t' interval has to be understood only as a means of selecting events in which the 5-pion system is produced in forward direction, without implying a detailed analysis of the shape of the $t'-$distribution.
It is quite instructive to look at the distributions of energy E_X of the 5-pion system for the three t'-ranges separately as shown by the three differently colored distributions in Figure 2.16. For all t'-bins there is an exclusive peak. However, it becomes obvious that the non-exclusive background tail correlates strongly with the momentum transfer and is prominent in the high-t' and even the medium-t' samples, while it is much smaller for the low-t' sample. Actually this is to be expected since for a non-exclusive event the calculated t' will actually only refer to a sub-event. This miscalculation will typically shift the t' to higher values since due to missing particles the transverse momentum balance does not work out.
It is for this reason that the following partial-wave analysis has only been applied to the low-t' data where the assumptions of exclusivity as well as the diffractive picture are much better justified.

5π Invariant Mass Spectrum

Having established the extend to which the exclusive production of 5 charged pions can be understood in terms of diffractive excitation of the incoming pion one can examine the invariant mass spectrum of the 5π system. A spectrum integrated over the whole t'-range is shown in Figure 2.17. There is a distinct structure visible around 1.8 GeV/c^2. The questions to be explored are

- What is the partial-wave decomposition of this spectrum? Which spin-parity states contribute?
- Are there resonant contributions? How many resonances can be identified and what are there parameters?

In the 1.8 GeV/c^2 mass region the $J^{PC} = 0^{-+}\,\pi(1800)$ and $2^{-+}\,\pi_2(1670)$ resonances are known through their decays for example into 3π [1]. In the $J^{PC} = 1^{++}$ sector resonances such as the $a_1'(1700)$ are expected to show up from model calculations [34] which also indicate that these states to contain hybrid meson contributions. Several experiments have measured this partial

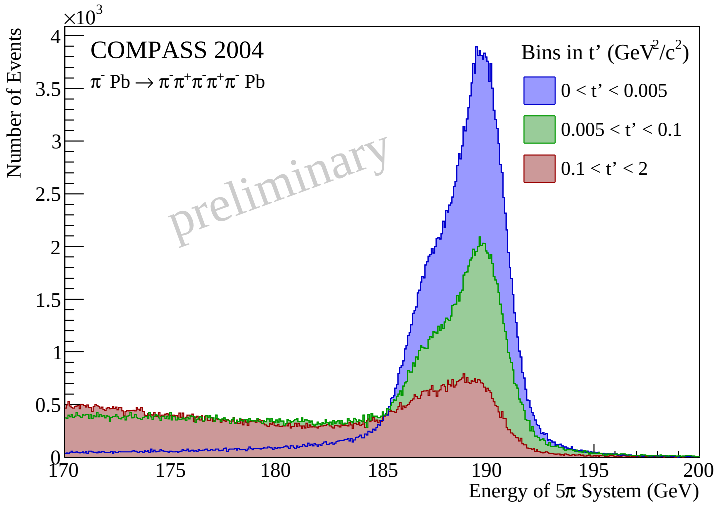

Figure 2.16: Exclusivity peak for three different t' bins.

wave in different final states, but no conclusive picture has emerged yet and it is suspected that actually several overlapping resonant states with $J^{PC} = 1^{++}$ exist in the relevant mass range. Finally Figure 2.18 shows the invariant mass spectra for the 5π final state systems in the different momentum transfer bins. A comparison of the peaking structure at $1.8\,\mathrm{GeV}/c^2$ shows a clear t'-dependence. While at low-t' the peak is quite prominent it tends to decrease in intensity (with respect to the higher mass part of the spectrum) for higher momentum transfer.

In order to learn more about what the diffractively produced 5-pion system is composed of, the full information of correlations in all kinematic variables of the final state have to be taken into account. To achieve this, an amplitude-analysis formalism is developed in the following chapters which enables a decomposition of the spectrum into definite spin and parity eigenstates. Interferences between the different partial-wave amplitudes are accessible through the observed angular distributions and allow the measurement of relative phases between the partial waves. This phase information will be the basis for the search for resonant contributions, which will be described in chapter 6.

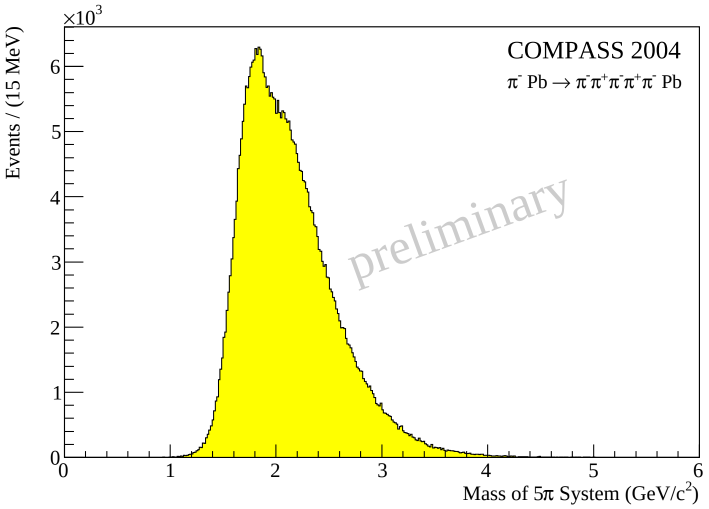

Figure 2.17: Invariant mass of the 5π system. Exclusivity cut applied $E_{5\pi} \in [183, 195]$GeV.

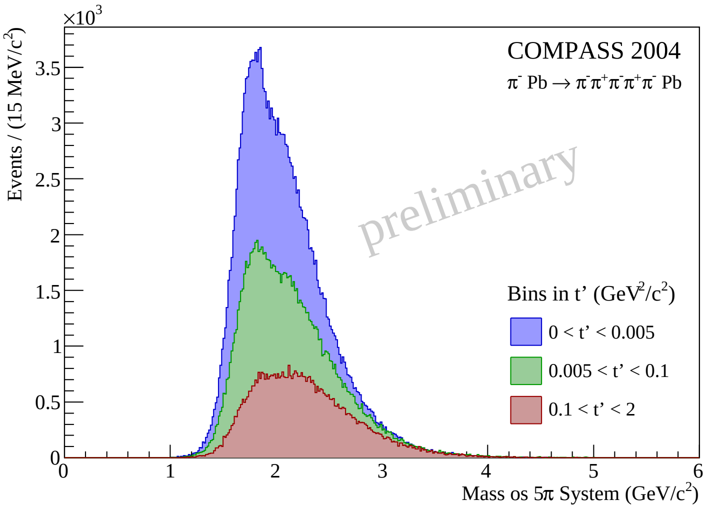

Figure 2.18: Invariant mass of the 5π system for different t' bins.

Chapter 3

Amplitude Analysis for Fixed 5-Body Mass

> To try to make a model of an atom by studying its spectrum is like trying to make a model of a grand piano by listening to the noise it makes when thrown downstairs.
>
> Anonymous

THE goal of the amplitude analysis employed here is the identification of possible resonant contributions to the diffractively produced 5-pion system and the determination of the spin parity quantum numbers of the corresponding states. In order to achieve this, a two-step approach is chosen. In the first analysis step, described in detail in this chapter, the data is partitioned into bins of definite 5-pion mass $m_X = m_{5\pi}$. Based on the observed angular correlations between the pions the intensity in each bin is then decomposed into different partial waves with definite spin-parity. The result of this first step is a measurement of the spin density matrix of the intermediate state X in each mass bin. This first step is often called the *mass-independent partial wave analysis.* I will also use the term *fixed-$m_{5\pi}$ amplitude analysis* instead, in order to emphasize which invariant mass quantity is really kept fixed during the procedure.

In a second analysis step the dependence of the spin density matrix elements on the 5-body mass is investigated. From intensity distributions and relative phase motions between different partial waves possible resonant contributions are inferred. Since absolute phases are not measurable by definition, the strategy will be to use well-known resonances as interferometers in order to construct amplitudes which describe the data. This step is called the *mass-dependent* analysis or *resonance extraction* step and will be explained in chapter 6.1.

3.1 General Structure of the Amplitude

The invariant mass of the 5-pion system m_X is a direct observable in the diffraction experiment. This allows to analyze events with different m_X independently of each other. Since the signature of a resonance is encoded in the phase of the respective amplitude as a function of the invariant mass, the binning of the data allows to conduct the analysis without any prior assumptions on the shape of the amplitude in this variable.

For the present analysis the low-t' data set described in section 2.2 is partitioned into 28 mass bins of 60 MeV/c^2 width each, spanning the mass range 1.36 GeV/$c^2 \leq m_X \leq 3.04 GeV/c^2$. The formalism developed below is applied independently to each of these mass bins in order to measure the spin-density matrix at different masses m_X.

In this section the general structure of the amplitude describing a diffractive excitation process as depicted in Figure 2.13(a) is constructed for the case of fixed 5-body mass m_X and fixed total center-of-momentum energy $\sqrt{s}$. The appropriate quantum numbers are summarized and general conservation laws are used to restrict the structure of the transition amplitude.

3.1.1 Isospin and Parity Conservation

In strong interactions parity is a conserved quantum number. For systems containing only light quarks, isospin and G-parity are also good quantum numbers.

The dominance of Pomeron exchange — the exchange of vacuum quantum numbers $I^G = 0^+$ in the t-channel (c. f. section 2.2.2) — means that isospin and G-parity of the initial pion $I^G = 1^-$ are carried over to the final state. Indeed the 5-pion system has negative G-parity and for a fully charged system $\pi^-\pi^+\pi^-\pi^+\pi^-$ the 3-component of the isospin has to be $I_3 = -1$ as can be seen from the Gell-Mann–Nishijima formula [103, 104]

$$Q = I_3 + \frac{1}{2}Y$$

recalling that the hypercharge $Y = S + C + B' + T + B$ for light mesons (Baryon-Number $B = 0$) without strangeness, charm, bottomness and topness ($S = C = B' = T = 0$) is zero. Consequently the isospin I has to be 1 (or larger). Since no $I = 2$ resonances are known, we will restrict the analysis to the production of $I = 1$ systems. Indeed it is observed that at COMPASS energies in exclusive, single-diffractive processes mainly systems with $I^G = 1^-$ like $\pi^-\eta$, $\pi^-\pi^+\pi^-$, $\pi^-\pi^0\pi^0$ or $\pi^-\pi^+\pi^-\pi^+\pi^-$ are produced.

While the incoming pion has zero spin, the Pomeron, being a Regge-trajectory has a more complicated spin structure which contains scalar as well as tensor components. Furthermore there can be orbital angular momentum between the beam pion and the Pomeron which allows the excitation of higher-spin states for X. However, as will be shown below, there are still some restrictions on the spin-parity states that can be produced in pion diffraction, which can be deduced from the fact that this process is dominated by Pomeron exchange.

The intermediate states X are characterized by the quantum numbers $I^G(J^{PC})M$ where $M \in [-J, J]$ is the z-component of the spin J in a suitable coordinate system. Here the z-direction will be measured along the momentum-vector of the incoming beam-pion in the laboratory system. The corresponding reference frame where X is at rest is the *Gottfried-Jackson frame* which will be explained in detail in section 3.2.1. From the discussion above it is clear that $I^G = 1^-$ for the $3\pi^-2\pi^+$ system. Since per definition the charge-conjugation quantum number is

$$C = G \cdot (-1)^I$$

it follows that the $\pi^-\pi^+\pi^-\pi^+\pi^-$ system is being assigned even charge conjugation $C = +1$. It should be noted, however, that the charged system is not an eigenstate of **C**.

An important issue are the consequences of parity conservation on the polarization of X. It has been shown (c. f. [105]) that under the premise of parity conservation at the pion-Pomeron vertex one can find a basis for the $|JM\rangle$ states in which the spin density matrix assumes a block-diagonal form. This is achieved by forming linear combinations of states with opposite spin projection M. Let ψ_{JM} denote a state with spin J and $J_3 = M$. The parity eigenstate amplitude can the be constructed in the following way:

$$\begin{gathered}\psi^{\epsilon}_{JM} = c(M)\left[\psi_{JM} - \epsilon P(-1)^{J-M}\psi_{J(-M)}\right] \\ \text{with} \quad \epsilon = \pm 1, \quad M \geq 0, \quad c(M>0) = \tfrac{1}{\sqrt{2}} \quad \text{and} \quad c(M=0) = \tfrac{1}{2}\end{gathered} \tag{3.1}$$

where P is the parity quantum number and ϵ is a newly introduced quantum number called *reflectivity*, which for mesons (bosons) can take on the values $\epsilon \in \pm 1$ and by construction corresponds to the naturality of the exchanged reggeon (c. f. [48]). Since the Pomeron has positive naturality it is expected that dominantly states with positive reflectivity are produced at high energies while the contribution of amplitudes with negative reflectivity should be suppressed. The $\sim 15\%$ Reggeon contribution to the total $\pi^- p$ cross section at COMPASS energies (see section 2.2.2) gives a first estimate of the magnitude of this effect.

It can be easily shown from the formulas above, that indeed for positive reflectivity $\epsilon = +1$ only states with

$$P = (-1)^{J-M+1}$$

such as

$$J^P M \in \{0^- 0, 1^+ 0, 1^- 1, 2^- 0, 2^+ 1, \ldots\}$$

contribute. Note that scalar states cannot be produced at all in diffractive pion dissociation with Pomeron exchange.

The kinematic selection of the small momentum transfer region implies a further restriction on the possible states. As can best be seen from equation 2.4 at low t' there is a penalty for helicity flip transitions with $\Delta\lambda = |\lambda_f - \lambda_i| > 0$ of the form

$$A \propto t'^{\Delta\lambda}$$

This applies in principle to both vertices of the diffraction diagram 2.11. A spin flip at the lower "target vertex" g_{bd} would induce the same penalty as a spin flip at the upper "beam vertex" g_{ac}. If the target particle has nonzero spin, the two contributions for spin flip an spin non-flip have to be treated incoherently.

Since the incoming pion has no spin, here $\Delta\lambda = M$. Thus, summarizing, in the limit $t' \to 0$ only $M = 0$ states will be produced and there will be no spin flip at the target vertex. This kinematic constraint limits the list of important contributions to

$$J^{PC} \in \{0^{-+}, 1^{++}, 2^{-+}, 3^{++}, \ldots\} \qquad M = 0$$

The suppression of target spin flip contributions motivates the fully coherent[1] treatment of the diffractive amplitude below.

3.1.2 Amplitude Parametrization

The amplitude for the diffractive dissociation of a pion into $2\pi^+3\pi^-$ through an intermediate state X is constructed by multiplying the production amplitude $\hat{T}$, which describes the transition $\pi + \mathbb{P} \to X$ with an amplitude $\hat{\psi}$ describing the decay of X into five pions as illustrated in

---

[1] apart from background contributions

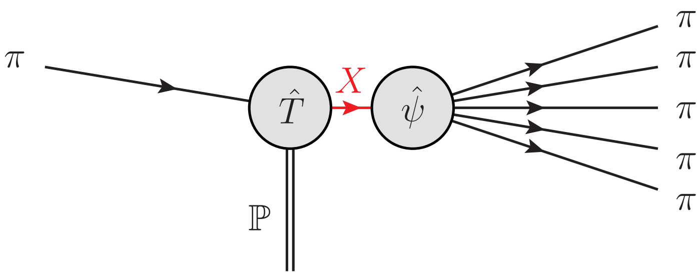

Figure 3.1: Factorization of the partial wave amplitude into production amplitude T and decay amplitude ψ. For fixed 5-body-mass m_X the phase from the propagator of X is absorbed into T.

Figure 3.1. There also is a propagator-like amplitude that describes the intermediate state X carrying a phase and only depending on m_X^2. However, since the constructed amplitude will be applied only in a small range of m_X this propagator can be assumed to by approximately constant in this mass bin and it will be absorbed into the production amplitude. $\hat{T}$ is thus defined at[2] m_x and depends on the quantum numbers of X, the center of mass energy $\sqrt{s}$ and the momentum transfer t'. The $\sqrt{s}$ dependence, which is of the form given in equation 2.4 will be neglected in the following since only data at one value of $\sqrt{s}$ will be analyzed. The t' dependence is assumed to be universal for all partial-wave amplitudes with the same M and will also be integrated over the chosen range.

The full amplitude for pion diffraction into the 5π final state with a given reflectivity ϵ at fixed 5-body-mass m_X is expanded in the following way:

$$\mathscr{A}^{\epsilon} \propto \sum_{\hat{\alpha}\delta} \hat{T}^{\epsilon}_{\hat{\alpha}} \hat{\psi}^{\epsilon}_{\hat{\alpha}\delta}(\tau) \tag{3.2}$$

The index $\hat{\alpha}$ summarizes the possible combinations of quantum numbers $I^G(J^{PC})M$ for the state X, while δ stands for the possible decay channels through which the 5-pion final state is reached (see also section 3.2). τ represents a suitable set of independent kinematic variables which span the phase space of the 5π system at fixed m_X and is the experimental input for the analysis, measured for each event in the data sample. $\hat{\psi}^{\epsilon}_{\hat{\alpha}\delta}(\tau)$ is the amplitude for the decay of the state $\hat{\alpha}$ in the decay channel δ and $\hat{T}^{\epsilon}_{\hat{\alpha}}$ represents the amplitude for the production of that state with reflectivity ϵ. The sum $\sum_{\hat{\alpha}\delta}$ runs over all possible quantum numbers of X and over all possible decay modes δ. It is a generalization of the well known partial wave expansion of elastic scattering and thus the amplitudes $\hat{T}^{\epsilon}_{\hat{\alpha}}\hat{\psi}^{\epsilon}_{\hat{\alpha}\delta}(\tau)$ are also often called *partial waves*. Of course, just as the partial-wave expansion has to be truncated in practical applications, also the number of components in the above parametrization has to be finite. The set of partial waves which is used in a particular application is called the *waveset*. The choice of a particular waveset might introduce an important systematic uncertainty in the analysis. This problem will be explored in depth in chapter 4.

From the general form of the amplitude the multi-differential cross section is parametrized in

---

[2] Indeed the definition of a small mass bin implies that the $\hat{T}$ defined here are actually amplitudes integrated over the respective mass range.

the following way:

$$\frac{d\sigma_{5\pi}}{d\tau} = \sigma_0 \cdot \sum_{\epsilon} \sum_{r} \left| \sum_{\hat{\alpha}\delta} \hat{T}^{\epsilon}_{\hat{\alpha}r} \hat{\psi}^{\epsilon}_{\hat{\alpha}\delta}(\tau) \right|^2 \equiv \sigma_0 \cdot \mathscr{I} \tag{3.3}$$

Here σ_0 is a constant that is left undetermined. All relevant structures which will be explored are encoded in the *intensity* $\mathscr{I}$. Only relative measures, such as relative intensities or phase-differences will be used to perform and interpret the amplitude analysis. There are two incoherent sums in the above parametrizations: States with different reflectivity are produced incoherently as explained above. The *rank r* takes into account further sources of incoherence in the production process. The index therefore only appears in the production amplitudes. In the analysis presented here a rank $r = 1$ has been used for full coherence as mentioned above and we will drop the sum over the rank for brevity in later chapters.

The spin density matrix elements can be written in terms of these amplitudes as

$$\hat{\rho}^{\epsilon}_{\hat{\alpha}\hat{\beta}} \propto \sum_{r} \hat{T}^{\epsilon}_{\hat{\alpha}r} \hat{T}^{*\epsilon}_{\hat{\beta}r} \tag{3.4}$$

3.1.3 Positivity Constraints

Apart from the constraints from parity conservation on the spin density matrix $\hat{\rho}$ discussed in section 3.1.1, there are additional important constraints [105]. In particular the eigenvalues of $\hat{\rho}$ — since they represent probability densities — should be real and positive. This requirement is called the *positivity constraint* and has another important practical implication for the parametrization of the spin density matrix in the reflectivity basis: In order to avoid unphysical phases some of the production amplitudes have to be constrained to the real axis. For higher rank spin density matrices spurious parameters have to be eliminated. In each rank the vector of production amplitudes thus starts with a real-valued entry. For each additional rank one more parameter is set to zero as explained in detail in [105].

The partial waves which occur with real-valued production amplitudes $\hat{T}^{\epsilon}_{\hat{\alpha}r} \in \mathbb{R}$ fix the (unphysical) absolute phase for their rank to 0. Because of this special role, they are called *anchor waves*. Mathematically the choice of anchor waves is arbitrary, however for numerical reasons it is advantageous to choose anchor waves that are stable and have a significant intensity in order to provide a clear reference phase.

3.2 Decay Parametrization — The Isobar Model

In this section the parametrization of the decay amplitude ψ in terms of the so called *isobar model* is discussed. In order to understand its assumptions and to clarify the terms used it is instructive to briefly review the origins of this model before we apply a modern version to our problem.

In hadron physics the isobar model was first introduced in the context of pion-nucleon reactions [106, 107, 108]. The basic idea was that the production of a 2-body system $N\pi$ dominantly proceeds through the formation of an intermediate state called the *isobar R* which then decays into the two final state particles as indicated in Figure 3.2. In that sense the diffractive excitation model described above could already be seen as an instance of the isobar model with the intermediate state X being the first isobar. In modern applications, however, there is a clear

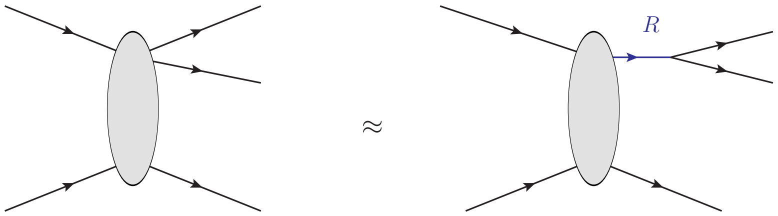

Figure 3.2: Basic idea of the isobar model. The production of a 2-body system is dominated by an intermediate state R which decays into the two final state particles.

distinction made between the diffractively produced system X and the isobars occurring in the decay as explained in the following.

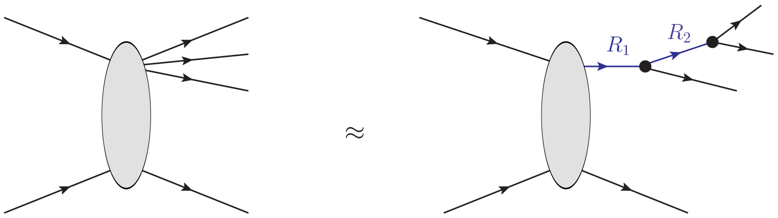

Figure 3.3: Extension of the isobar model to the 3-body system.

The model was soon extended to the description of 3-body systems (see Figure 3.3), notably the $p\pi^+\pi^-$ system [109] and also its short comings in terms of unitarity and analyticity constraints were realized [110]. A vast program to restore proper mathematical properties of the resulting amplitudes via the application of dispersion relation techniques was launched which finally provided “a retrospective justification of the use of the non-unitary isobar model in the $N\pi\pi$ system...” [111]. In recent years, mainly through the availability of large data samples, questions on unitarity effects reemerged (see e. g. [112]). A considerable problem for the exploitation of unitarity arguments to constrain amplitudes in the region above $1.5\,\mathrm{GeV}/c^2$ is the presence of many open channels and partial waves with higher spin content. This problem has not been solved in a general way yet. In the present analysis unitarity effects have not been taken into account explicitly. The development of the corresponding corrections might be a fruitful endeavor for future, improved analyses.

Motivated by the successful application to the three pion system [113, 114, 115, 7] and by recent extensions of the model to diffractively produced 4-body system[116] and the 5-body system in $\bar{p}n$ annihilation at rest[67, 117] the analysis presented in this thesis develops the isobar formalism for the diffractively produced 5-body system. Although the basic building blocks of the amplitudes are essentially the same as for the 3-body isobar model, due to the larger number of final state particles a few additional effects emerge in the 5-body amplitude that play no role in simpler systems. In particular the isospin symmetrization as well as the slightly more complex spin-orbit coupling will be discussed in the following.

For a 5-body system there are 3 possible distinct isobar decay tree topologies which are depicted in Figure 3.4. In case (a) the system X decays into a 3-body and a 2-body subsystem. In cases (b) and (c) the first decay proceeds via the emission of a pion. The remaining 4-pion

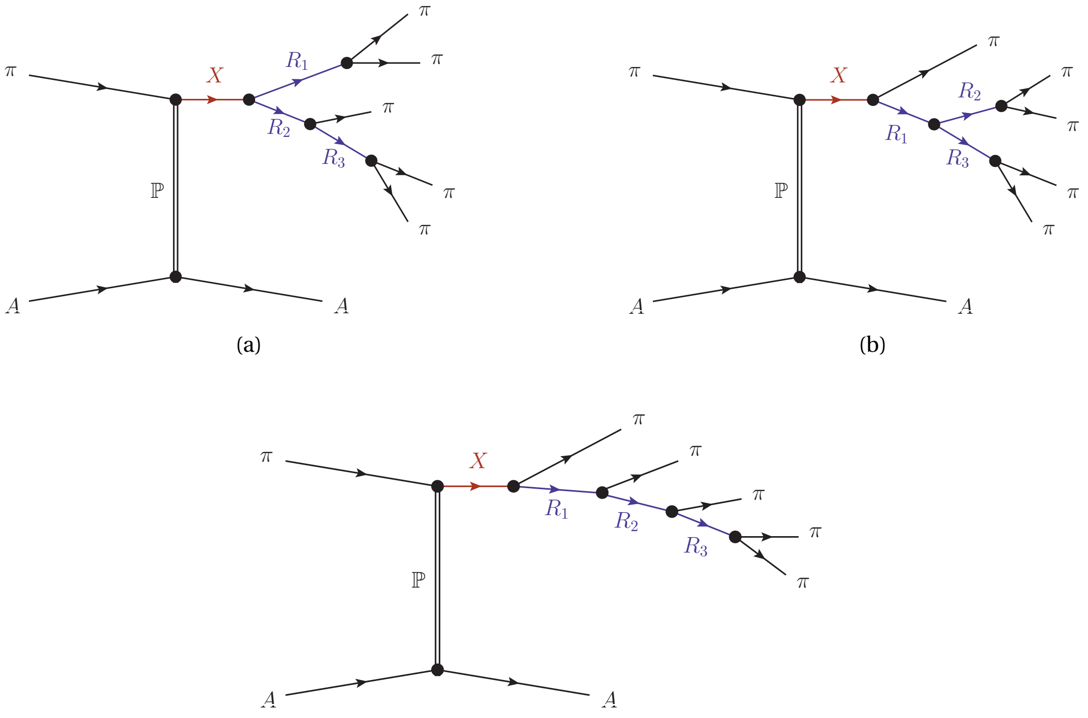

(a)

(b)

(c)

Figure 3.4: The 5-body isobar model. There are three different basic decay topologies. See text.

system can decay into two $(2\pi)^0$ systems as in (b) or it can emit another pion as in (c). The implied dynamics is encapsulated in the parametrization of the propagators for the intermediate isobars. Underlying the three decay topologies for the 5-pion system are in fact the different possible isospin-decompositions of the $3\pi^-2\pi^+$ system which will be discussed in more detail in section 3.2.3.

3.2.1 Helicity Formalism

The helicity formalism [118] provides a very general way of implementing the transition amplitude of complicated decay chains. Each node in the decay tree represents a 2-body decay of a state $I^G(J^{PC})M$ into two isobars $I_1^{G_1}(J_1^{P_1C_1})\lambda_1$ and $I_2^{G_2}(J_2^{P_2C_2})\lambda_2$. Each 2-body decay amplitude depends on the helicities of the decay products λ_1, λ_2 coupling to a total spin S with helicity λ. The orbital angular momentum ℓ between the decay products couples to the spin S yielding the spin of the decaying state J with spin projection M. Note that there is a slight difference in the choice of quantization axes between the decay of the diffractively produced state X and the isobars in the decay tree as will be discussed below.

Of course for the two-body decay all conservation laws have to be fulfilled, such that $G = G_1 \cdot G_2$, $P = P_1 \cdot P_2 \cdot (-1)^\ell$ and the usual spin coupling rules are respected for the isospins $I \in [|I_1 - I_2|, I_1 + I_2]$ and the angular momenta $J \in [|s-\ell|, s+\ell]$.

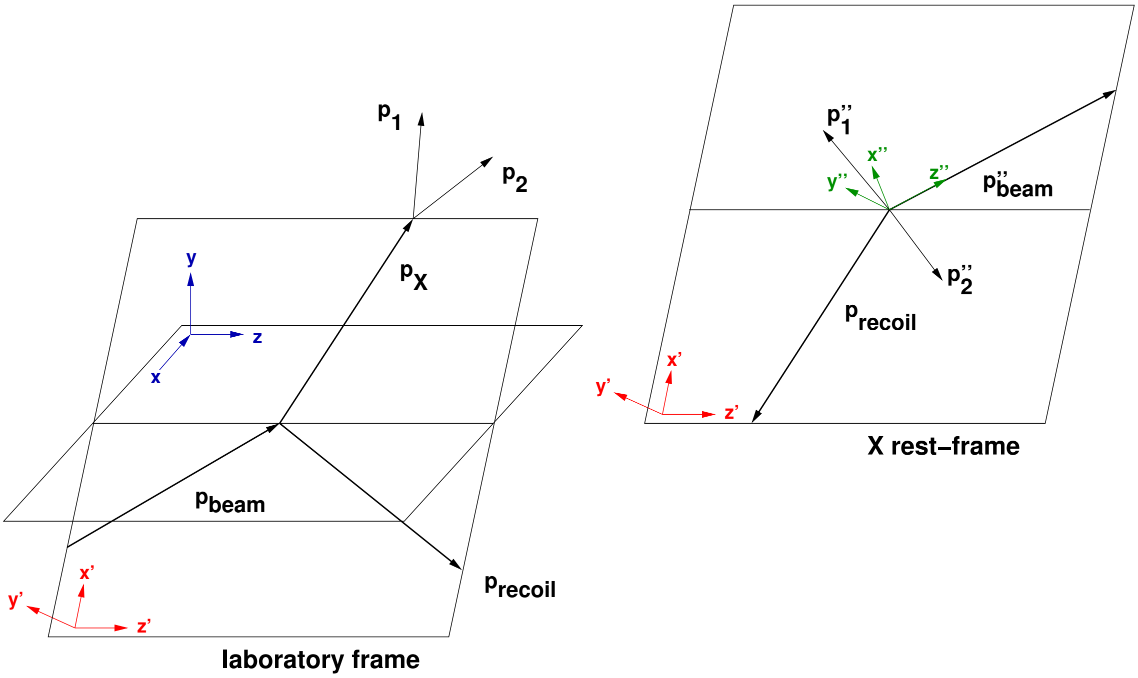

Figure 3.5: Construction of the Gottfried-Jackson frame. For details see text.

The 2-body amplitude can be written as:

$$A(\tau) = \sum_{\lambda_1\lambda_2} D^J_{M\lambda}(\theta,\phi,0) f_\lambda(m_R, m_1, m_2) \quad \text{with} \quad \lambda \equiv \lambda_1 - \lambda_2 \tag{3.5}$$

An important feature of this amplitude is the factorization into an angular part, described by the Wigner-D-functions $D^J_{M\lambda}(\alpha,\beta,\gamma)$ and a dynamical part f.

Angular structure: The D-functions describe the rotation $U[R(\alpha,\beta,\gamma)]$[3] of a state $|JM\rangle$ with spin J and spin-projection M through the Euler angles (α,β,γ) [118]

$$U[R(\alpha,\beta,\gamma)]\,|JM\rangle = \sum_{M'} |JM'\rangle D^J_{MM'}(\alpha,\beta,\gamma)$$

The angular structure of a 2-body decay can be completely described by the orientation of the breakup momentum in a suitable coordinate system. This is the reason why in the amplitude formula only the two angles θ and ϕ appear[4]. The two decay angles are defined in the *Gottfried-Jackson* frame for the decay of the 5-body state X and in so called *helicity frames* for the isobar decays. The main difference between these coordinate systems is the choice of the quantization axis as will be explained in the following.

Figure 3.5 illustrates the construction of the Gottfried-Jackson frame which is used to parametrize the decay of a diffractively produced state X into two decay products p_1 and p_2. As a first step

---

[3] $U[R]$ is the unitary rotation operator acting on the state $|JM\rangle$.

[4] It is possible to write the amplitude in a different convention with $D^J_{M\lambda}(\theta,\phi,-\theta)$. The number of independent angles for a 2-body decay, however, is always two.

the coordinate system in the laboratory frame is rotated from $(x, y, z) \to (x', y', z')$ such that the scattering plane, spanned by the momentum vectors of the beam, the 5-pion system X and (redundantly) the recoil momentum come to lie in the (x', z') plane. The y' axis is then perpendicular to the scattering plane. For the helicity frames a similar construction is made such that the y'-axis is defined by the production plane of the isobar in question. Keeping the y' direction fixed a boost is performed into the rest frame of X. A rotation around the y' direction is then applied such that the z'' axis is aligned with the boosted beam-momentum p'_{beam}. It serves as the quantization axis for the Gottfried-Jackson frame. The 3-momenta of the decay products p''_1 and p''_2 are of course back to back and of equal magnitude in this frame and the breakup momentum is uniquely defined $q = p''_1$. The angles θ_{GF} (Gottfried-Jackson-θ) and ϕ_{TY} (ϕ-Treiman-Young) are the polar and azimuthal angles of the direction defined by q. For the helicity frames the z''-axis is aligned with the direction of flight of the decaying isobar in its production frame before the boost into the isobar rest-frame is being applied.
Experimental results for the angular distribution in these variables, from which the information on the contributing partial waves can be extracted will be discussed in section 5.1.

Dynamics of the intermediate states: The function

$$f_\lambda(m_R, m_1, m_2) = \sqrt{2\ell+1}\,(\ell 0 S\lambda|J\lambda)\,(J_1\lambda_1\, J_2\, -\lambda_2|S\lambda)\, Q_{\ell S}(m_R, m_1, m_2)\, g_{\ell S} \tag{3.6}$$

contains the Clebsch Gordan coefficients of the helicity couplings. Note that the projection of the orbital angular momentum ℓ onto the quantization axis is always 0, as made explicit in the first Clebsch Gordan coefficient. This is so, because the orbital angular momentum vector has to be orthogonal to the breakup momentum of the 2-body system. However, in the helicity frame the breakup momentum has exactly been chosen as the quantization axis. The relative minus sign for the two helicities λ_1 and λ_2 in the second Clebsch Gordan coefficient comes from the fact that they are both measured on the same quantization axis whereas the directions of flight of the decay products are of course back-to-back.
Q is a dynamical function, parametrizing the dependence of the amplitude on the mass of the decaying state m_R. In the most simple case it is given by a relativistic Breit-Wigner propagator and appropriate angular-momentum barrier factors [119]. The choice of a reasonable dynamical function Q to describe the intermediate isobar states is an important input to the model and will be discussed in section 3.2.2. In the case of the first decay node - the decay of the state of interest X - the factor Q contains only the angular-momentum barrier factors. The propagator function is absorbed into the production amplitude as mentioned above.
$g_{\ell S}$ is the ℓS-coupling constant which represents the overlap of the wave function of the mother particle with the two-body wave function of the daughter particles in the state with orbital angular momentum ℓ and total spin S. It can also be understood as the branching fraction of a resonant state into the specific decay channel. As such it could be calculated if a reliable model of mesons would be available and $g_{\ell S}$ would be independent of the masses of the participating particles. Unitarity corrections to the isobar model may lead to an effective dependence of $g_{\ell S}$ on the breakup momentum and the masses of the daughter particles. In principle also additional phases can be generated [120]. However, since no consistent framework for the treatment of such rescattering effects exists, the $g_{\ell S}$ will be approximated as constants and thus can also be absorbed into the model parameters T. For this reason there will be independent production amplitudes $T_{\hat{\alpha}\delta}$ for each decay mode and formula 3.3 has to be rewritten

$$\boxed{\mathscr{I} = \sum_{\epsilon}\sum_{r}\left|\sum_{\alpha} T^{\epsilon}_{\alpha r}\psi^{\epsilon}_{\alpha}\right|^{2}} \tag{3.7}$$

where the index $\alpha = \hat{\alpha}\delta$ now summarizes all quantities needed for the definition of a complete 5-body decay amplitude ψ^{ϵ}_{α}:

- A set of quantum numbers $I^{G}(J^{PC})M^{\epsilon}$ for the system X;
- A decay topology;
- The intermediate systems R_1, R_2 and R_3, with quantum numbers $I_k^{G_k}(J_k^{P_k C_k}) \quad k = 1..3$, taking into account isospin coupling and $G-$parity conservation.
- At each 2-body decay node: the spin s and the orbital angular momentum ℓ between the decay products, taking into account parity conservation such that orbital angular momentum contributes $(-1)^{\ell}$ to the overall parity.

These quantities and their relation to an isobar decay tree are illustrated in Figure 3.6.

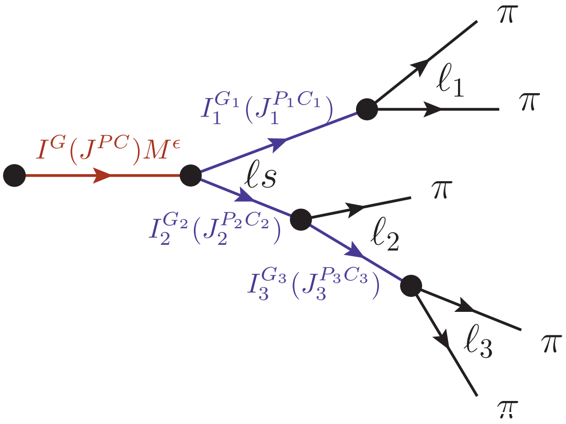

Figure 3.6: Specification of a 5-pion isobar model decay amplitude. In addition to all the spin parity and orbital angular momentum quantum numbers one has to specify propagator functions for the intermediate isobar states (in blue).

Once the 2-body decay amplitudes have been defined for each node in the decay tree, the final amplitude is obtained as a product of these sub-amplitudes, where appropriate sums over all possible helicity states have to be taken into account. Note that each two-body sub-amplitude is defined in its own coordinate system or *helicity frame*. Thus the complete isobar-model amplitude is not formulated in terms of invariant quantities and has to be evaluated algorithmically. For details see [118].

At this point another remark on the generality of the model is in order. The ℓs-coupling structure used in formulas 3.5 and 3.6 is valid only for the non-relativistic case. As long as the breakup momentum of the decay products is small it can be applied as a good approximation. More general expressions have been developed for example in [121]. The implementation of this fully relativistic formalism is an interesting option for future improvements of the present analysis.

3.2.2 Isobar Parametrizations

In the isobar model parametrizations for the isobar subsystems have to be specified in the form of the dynamical functions $Q_{\ell s}(m_R, m_1, m_2)$. In most analyses that are known to the author only the resonant contributions to the amplitudes are used to construct these functions, usually by exploiting results from other experiments where the relevant two-body decay of the state R has been studied in detail.

At this point a problem arises that has often been criticized. As long as in each $I^G(J^{PC})$ channel there is only one (narrow) resonance the approach taken so far is consistent. However, if there are two or more overlapping resonances in the same channel, then unitarity imposes strong constraints on the amplitudes. It can easily be shown that a sum of two Breit-Wigner amplitudes violates (elastic) unitarity. On the other hand it is also well known that the shape of the spectrum of a particular system (say the $\pi^+\pi^-$-system) strongly depends on its source. This makes it difficult to propagate information on the amplitude from one process to another (e. g. $\pi\pi$ scattering to $\pi\pi$ production from different sources). Only the pole positions of resonances in the complex m_R^2-plane and the residuals of these poles are universal and do not depend on the production process. The presence of other particles in addition to the isobar and inelastic contributions invalidate the straightforward application of unitarity constraints. For a discussion on this issue see for example [122] and references therein.

The standard procedure that has been adopted by most analysts so far, is to treat each resonant state independently, which effectively amounts to a sum of Breit-Wigner propagators with *complex* coupling coefficients. Models of this type have been quite successful phenomenologically, which can be understood from the arguments presented in section 1.3.1. The isobar model neglects mixing between the intermediate states. The freedom allowed by complex coupling coefficients is often sufficient to construct an amplitude that gives a decent description of the data. The following analysis will also adopt this strategy, however, it is understood that here we have identified a point which should be better understood for future improvements of the model. One possible approach to this problem is presented in section 5.3.

In this section the two-, three- and four-pion systems are briefly discussed and the parametrizations used for their description are described. Most of the information has been taken from the particle data summary tables [1] and only Isospin 0 and 1 have been taken into account.

The $(\pi^+\pi^-)$ Subsystem

The dominant $I = 1$ state in the $(2\pi)^0$ system is the $\rho(770)$ with $J^{PC} = 1^{--}$ which is showing up as a peak in the $\pi^+\pi^-$ invariant mass distribution in Figure 3.7. The 2-pion p-wave has been parametrized with a fixed-width relativistic Breit Wigner for the $\rho(770)$. The author is aware of more advanced parametrizations of the $\pi\pi$ P-wave[123, 112]. The implementation of these parametrizations would be an interesting option for future improvements of the present analysis.

In the isoscalar $\pi\pi$ S-wave the low mass region is dominated by the σ pole with $J^{PC} = 0^{++}$. The parametrization of the 0^{++} amplitude including also the $f_0(980)$ and possible further contributions has been subject to vigorous discussions. Recent developments include the so called

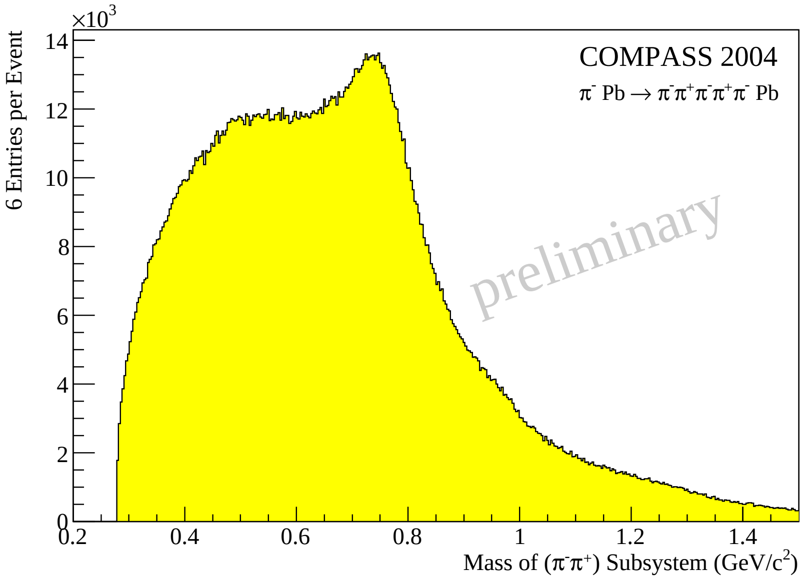

Figure 3.7: Invariant mass of $\pi^+\pi^-$ pairs out of the 5 charged pions in the final state. There are 6 entries per event in this plot. The $\rho(770)$ is clearly visible on top of a large (combinatorial) background.

inverse amplitude method which uses dispersion relation techniques to construct an analytical continuation of the amplitude from the threshold region where constraints from chiral perturbation theory provide a valuable anchor point [124, 125, 126, 123].
In the present analysis these recent parametrizations have not yet been taken into account. Instead an older, phenomenological approach has been taken over which goes back to the K-Matrix parametrization presented in [127]. In particular we use the "M-solution" parametrization described there with all parameters f^i_j set to zero and with parameters $c^4_{00} = c^4_{11} = 0$. This modification has been introduced since the $f_0(980)$ appears as a dip in $\pi\pi$ scattering data — for which the original "M-solution" model has been fitted — while in production processes it is seen as a clear peak and its production strength depends strongly on its source. Therefore the $f_0(980)$ is treated as a separate resonance with a free overall phase shift relative to the modified $(\pi\pi)_{S\text{-wave}}$ "M-solution" parametrization. In the following the symbol σ will be also used to identify the phenomenological $(\pi\pi)_{s\text{-wave}}$, although this amplitude encompasses more than only the σ meson. Intensity and phase are reproduced in Figure 3.8.
A further important resonance is the $f_2(1270)$ with $J^{PC} = 2^{++}$. Although not visible by eye in the 2π spectrum the state has been considered as a Breit-Wigner isobar in the present analysis.

The $(3\pi)^\pm$ Subsystem

The $\pi^-\pi^+\pi^-$ system (odd G-parity) has been studied extensively in diffractive production [113, 114, 115, 7]. The dominant states observed in that production mechanism are listed in table 3.1 together with their dominant decay modes. Figure 3.9 shows the mass-spectrum of the observed $(3\pi)^-$ subsystems selected from the 5π final state. Around 1 GeV/c^2 the broad $a_1(1260)$ and $\pi(1300)$ likely dominate the spectrum. Note that there is considerable combinatorial back-

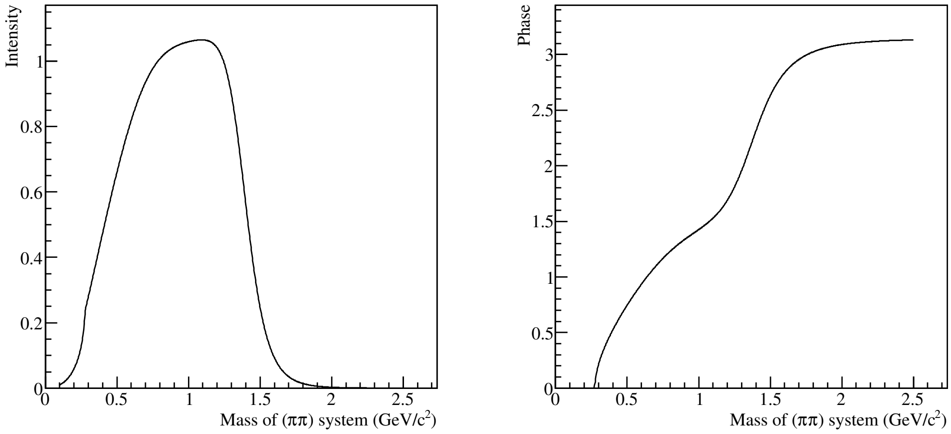

Figure 3.8: $(\pi\pi)$ s-wave parametrization. Modified K-matrix solution from [127] as described in the text.

Name	J^{PC}	Major decay modes
$a_1(1260)$	1^{++}	$\rho\pi, \sigma\pi$
$\pi(1300)$	0^{-+}	$\rho\pi, \sigma\pi$
$a_2(1320)$	2^{++}	$\rho\pi$
$\pi_2(1670)$	2^{-+}	$f_2\pi, \rho\pi$
$\pi(1800)$	0^{-+}	$f_0(980)\pi, \sigma\pi$

Table 3.1: Main resonant contributions to the $\pi^-\pi^+\pi^\pm$ system considered in this analysis.

ground in this plot since it contains six entries per event. In diffractive production the 1^{++} partial wave contains significant contributions from the so called *Deck-effect* [128, 129] which is an example of a multiperipheral process mentioned in section 2.2.2. Only through the observation of the $a_1(1260)$ in τ-decays has its resonant contribution been firmly established [130]. The narrow $a_2(1320)$ is just visible as a slight shoulder in the spectrum, however, it is a well established resonance. The pseudoscalar $\pi(1300)$, which due to its large width is quite hard to pin down experimentally, is included in the analysis as a very broad resonance. $\pi_2(1670)$ and $\pi(1800)$ are both quite well established states. They have been considered in the analysis but due to their large mass they do not yet play a big role in the 5π-mass range and thus the available 3π phase space that has been analyzed.

All these states have been parametrized by relativistic Breit-Wigner amplitudes in their dominant decay modes (see section 1.3).

The $(4\pi)^0$ Subsystem

The $\pi^+\pi^-\pi^+\pi^-$ system is the most challenging to parametrize, even in the simplified approach that is adopted here, because the least reliable information is available and some of the reported states are still controversially discussed. To get an idea in which mass-range those systems fall Figure 3.10 shows the invariant mass spectrum of the neutral 4-pion subsystems (3 entries per event). The sharp peak on the rising edge of the phase space at $m \sim 1.28\,\mathrm{GeV}/c^2$

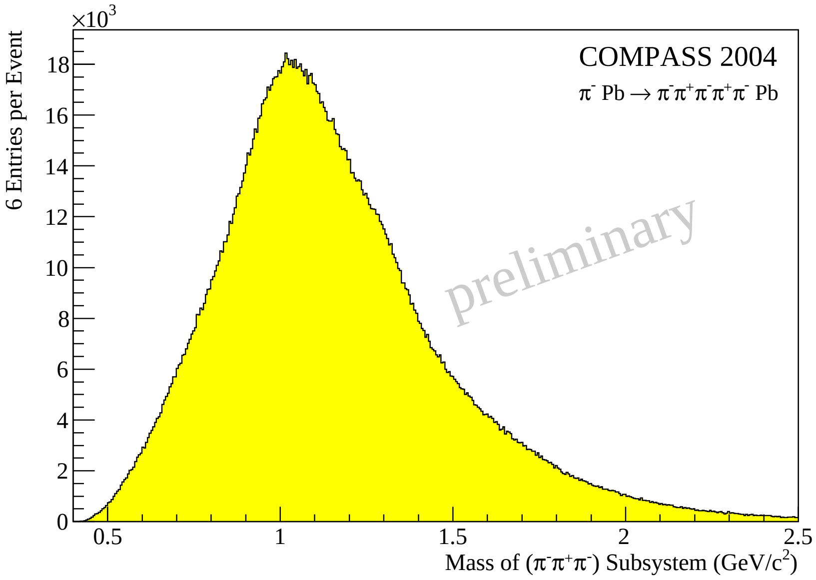

Figure 3.9: Invariant mass of 3π sub-states. There are six entries per event in this plot.

could be explained by the $f_1(1285)$ resonance, which is known to be narrow ($\Gamma = 25\,\mathrm{MeV}/c^2$). In order to investigate this system it is useful to plot the invariant mass of a $(\pi^+\pi^-)$ out of the 4π system against the invariant 4π mass as in Figure 3.11. There is a clear vertical band at $m_{4\pi} \sim 1.28\,\mathrm{GeV}/c^2$ and a broader structure around $m_{4\pi} \sim 1.4\,\mathrm{GeV}/c^2$. At $m_{4\pi} \sim 1.5\,\mathrm{GeV}/c^2$ there are indications of a dominant $\rho\rho$ decomposition of the 4π system. Figure 3.11 has already been studied in [102] and its rich structure was a key motivator for the present work. In order to illustrate the substructure of the 4π system Figure 3.12 shows the invariant mass of one $pi + \pi^-$ subsystem versus the mass of the remaining two pions for different 4π-mass ranges. While for $m_{4\pi} \lesssim 1.6\,\mathrm{GeV}/c^2$ the shape of this distribution is dominated by the limited phase space, for higher 4-pion masses there is a clear $\rho(770)\rho(770)$ correlation visible. For very high masses above $m_{4\pi} \gtrsim 2\,\mathrm{GeV}/c^2$ another structure is becoming visible, which corresponds to an $f_2(1270)\rho(770)$ correlation.

The 4π system can both be realized in an isospin 1 and an isospin 0 state. Its G-parity is even.

Table 3.2 summarizes the resonant states that have been considered for the 4π system. For the resonance parametrizations again relativistic Breit-Wigner amplitudes have been used. It is known that due to coupling effects between different channels the resonance shapes and phase motions can be distorted. The most dramatic known example in this respect is the $f_2(1565)$ which in the 2π decay channel acquires a strongly asymmetric line shape due to the rapid opening of the $\omega\omega$ phase space at roughly the same mass [65]. Apart from this example the effects from dispersion and mixing have been found to produce only mild changes in the line shape [65], justifying the usage of the simplified Breit-Wigner parametrizations used here.

One case in which the parametrization of the dynamical function in the isobar model proved to be difficult was the $1^+(1^{--})$ 4-pion system. There are two known states: the $\rho'(1450)$ and the $\rho'(1700)$ which couple strongly to this decay channel. The resonance parameters listed in [1]

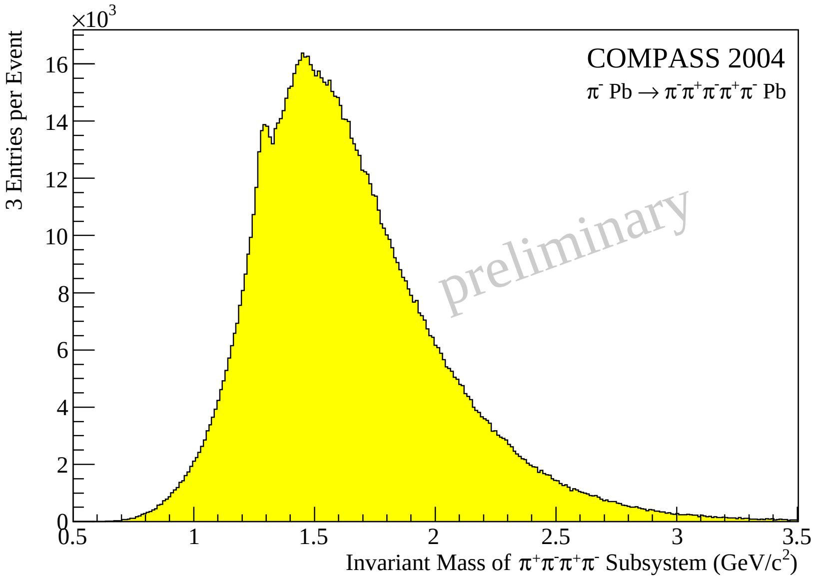

Figure 3.10: Invariant mass of neutral 4 pion subsystem. There are 3 entries per event in this plot. There is a sharp peak at roughly 1.3 GeV/c^2 corresponding to the $f_1(1285)$.

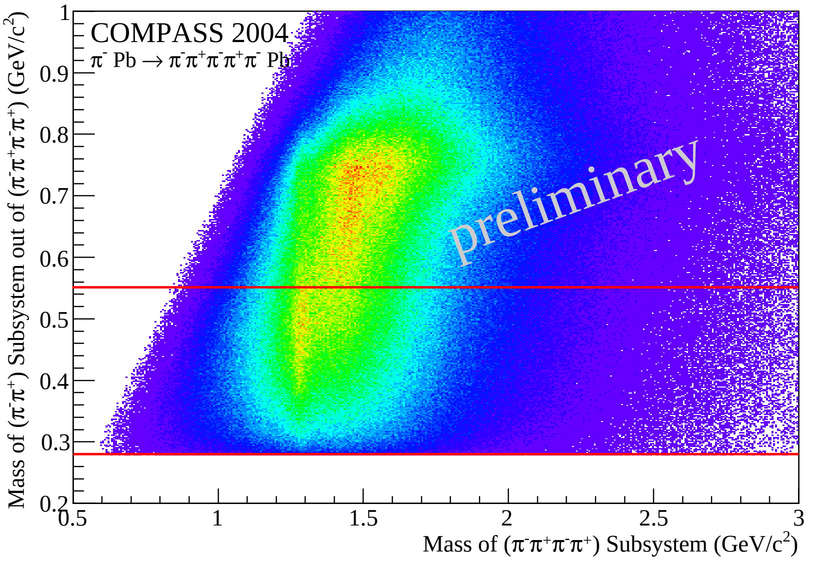

Figure 3.11: Invariant mass of $(\pi^+\pi^-)$ selected out of neutral 4-pion system plotted against the 4π mass.

are:

$$
\begin{array}{lll}
\rho(1450) & m = 1465 \pm 25\,\mathrm{MeV}/c^2 & \Gamma = 400 \pm 60\,\mathrm{MeV}c^2 \\
\rho(1700) & m = 1720 \pm 20\,\mathrm{MeV}c^2 & \Gamma = 250 \pm 100\,\mathrm{MeV}c^2
\end{array}
$$

The $J = 1$ $(4\pi)^0$ system has been studied in electron positron annihilation. In order to fit the

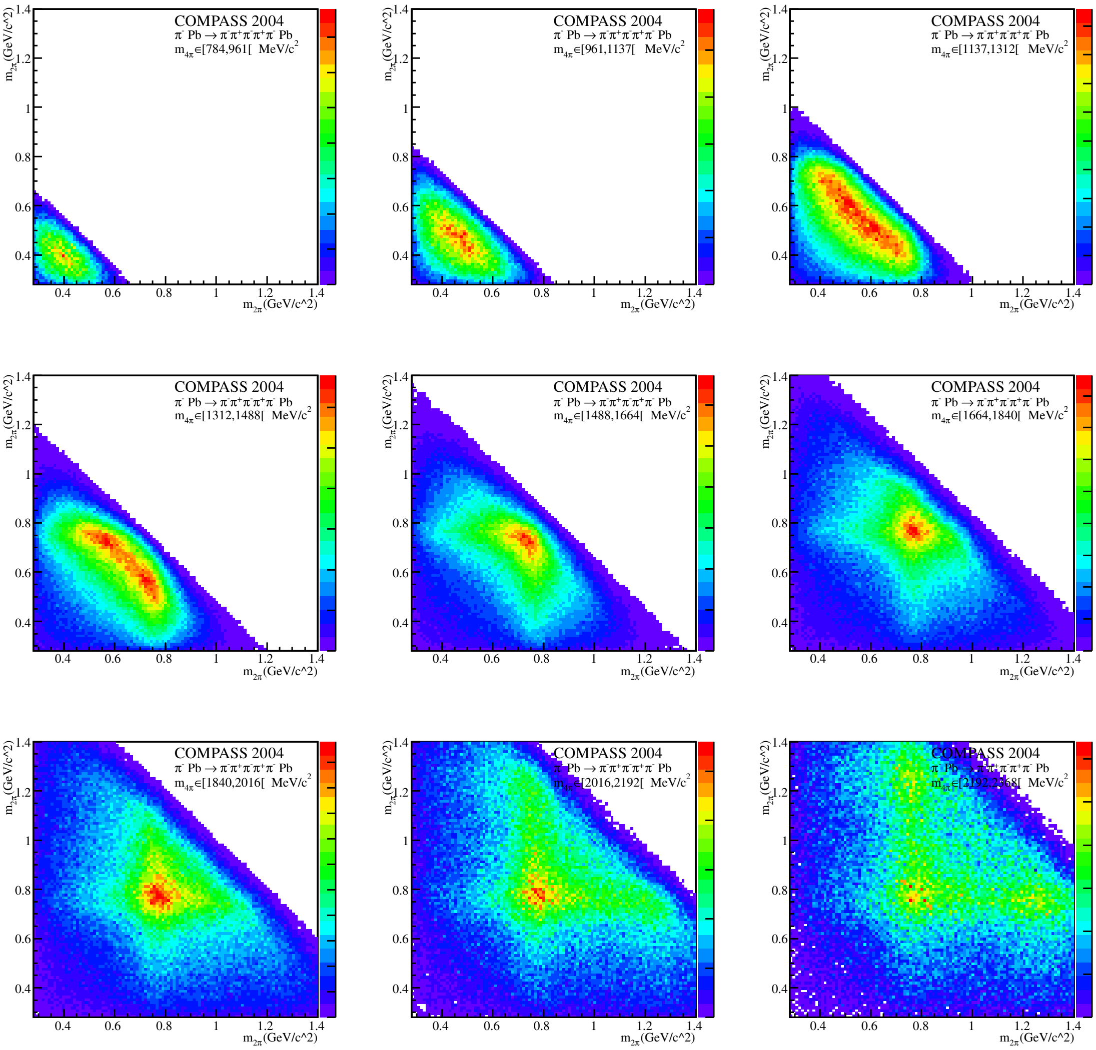

Figure 3.12: Invariant mass of $\pi^+\pi^-$ selected out of neutral 4-pion system plotted against the invariant mass of the remaining $\pi^+\pi^-$ subsystem for different 4π mass ranges.

invariant mass spectrum from $e^+e^- \to 4\pi$ two broad and overlapping resonances have been required [131]. Both states have later also been seen in high-statistics analyses of τ decays [132, 133] and in $\bar{p}n$ annihilation at rest into 5π[117]. A complete review on the status of these states can be found in the particle data book [1].

In order to find a parametrization of this system an attempt was made to treat both states as uncorrelated isobar resonances in the model. However, due to the strong overlap, this approach leads to an unphysical correlation of the respective production amplitudes in the low-mass region. Another approach is to construct a dynamical function containing both resonances. This, however, leads to a function that may be too rigid since it fixes the relative coupling of both states to initial system X. Also it does not allow for different couplings to the various decay

Name	$I^G(J^{PC})$	Candidate Masses (MeV/c^2)
f_0	$0^+(0^{++})$	1370, 1500, 1700
η'	$0^+(0^{-+})$	1295, 1403
ρ'	$1^+(1^{--})$	1450, 1700
b_1	$1^+(1^{+-})$	1235, 1800
f_1	$0^+(1^{++})$	1285, 1450
η_2	$0^+(2^{-+})$	1645
f_2	$0^+(2^{++})$	1270, 1565
ρ_3	$1^+(3^{--})$	1690

Table 3.2: Isobar resonances decaying into $\pi^-\pi^+\pi^-\pi^+$ used in the present analysis. All these resonances except the $b_1(1800)$ have been observed in other experiments. Their parameters are taken from [1]. The $b_1(1800)$ is included based on calculations in the framework of the relativistic quark model of mesons [9].

channels of the two states. The parametrization of reference [131] was used for this purpose:

$$BW_{\rho'} = BW_{1450} - c \cdot BW_{1700} \tag{3.8}$$

The relative phase between the two Breit-Wigner amplitudes is π, the relative coupling is $c = \frac{3}{4}$. As Breit-Wigner parameters the following values from [131] have been used:

$\rho(1450)$ $m = 1465\,\mathrm{MeV}/c^2$ $\Gamma = 235\,\mathrm{MeV}c^2$
$\rho(1700)$ $m = 1720\,\mathrm{MeV}c^2$ $\Gamma = 220\,\mathrm{MeV}c^2$

Intensity and phase of this amplitude are shown in Figure 3.13.

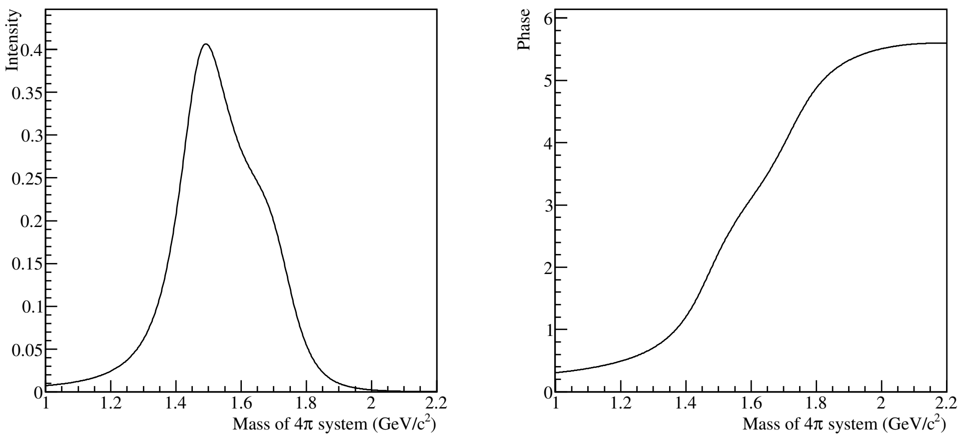

Figure 3.13: Double Breit-Wigner parametrization of $I^G(J^{PC}) = 1^+(1^{--})$ amplitude with two overlapping ρ' states.

It should be noted that this construction violates analyticity and (elastic) unitarity and does not take into account mixing between the two states. It thus can only be a coarse approximation

to the true amplitude. In the future a less model-dependent parametrization is needed here. Indeed a larger sample might allow to extract phase-shift information on the 4π system directly from the data. A prototype attempt on such an analysis is presented in section 5.3.
Also the isoscalar-scalar sector plays a big role in the understanding of the 4π system. While the σ contributes only little to the observed 4π spectrum due to phase space, the higher f_0 resonances all are believed to couple strongly to this system. There are three states that have been allowed in the model-ansatz in the present analysis. While the $f_0(1370)$ is discussed quite controversially [65, 66] the relatively narrow $f_0(1500)$ is a well established state. The $f_0(1700)$ has not been seen in a 4π decay according to [1], nevertheless it has been allowed here.

Decay parametrization of 4π resonances: In the spirit of the isobar model the 4π decay of an isobar R has been modeled by a two-body decay $R \rightarrow R_1 + R_2$. Table 3.3 lists the possible isospin decompositions of the 4π system. Isobars for the description of the respective subsystems are also given. A similar decomposition has also been used in [117]. The two different decay topologies arise because the G-parity even 4π state can decay either into two G-parity even sub-states, for example $\rho^0\rho^0$ or alternatively into two G-parity odd sub-states like πa_1. Note that for an isospin 1 object with $I_3 = 0$ the decay into two states with $I = 1$ and $I_3 = 0$ like $\rho^0\rho^0$ is forbidden since the corresponding isospin Clebsch-Gordan coefficient is zero. Consequently a state which decays into $\rho^0\rho^0$ has to have isospin 0.

I^G	$I_1^{G_1}$	$I_2^{G_2}$	Isobars R_1, R_2
0^+	1^-	1^-	πa_1, $\pi\pi(1300)$,πa_2
	1^+	1^+	$\rho^0\rho^0$
	0^+	0^+	$\sigma\sigma$, $f_2 f_2$
1^+	1^-	1^-	πa_1, $\pi\pi(1300)$, πa_2
	1^+	0^+	$\rho^0\sigma$

Table 3.3: Isospin decomposition of the $2\pi^-2\pi^+$ system. The given isobar decay channels are examples that have been used in the analysis.

Exotic contributions to the 4π system: The $(4\pi)^0$ system itself is an interesting subject that should be studied in depth. Apart from the known contributions that have been discussed so far there is the exciting possibility to find spin-exotic resonances decaying into this final state. A spin-exotic resonances that has been discussed for some time and has been established in a previous analysis of COMPASS data [102, 7] is the $\pi_1(1600)$ with $I^G(J^{PC}) = 1^-(1^{-+})$. If this state truly corresponds to a hybrid meson one would expect by isospin symmetry to find a whole multiplet of partner states. The establishment of such a multiplet of spin exotic resonances would be a very convincing argument for the mesonic nature of these states. The isoscalar partner of the $\pi_1(1600)$ could potentially couple to 4π. It would have the quantum numbers $I^G(J^{PC}) = 0^+(1^{-+})$ and would be called the $\eta_1(1600)$. The mass of this object is expected to be close to the one of the $\pi_1(1600)$. As has been mentioned in section 1.2 recent lattice calculations indicate the existence of a spin-exotic isoscalar state with a mass that is slightly higher than the isovector partner [60].
Indeed there have been experiments looking for such a state in $\bar{p}n$ annihilation at rest into 5

pions [67, 117]. The detailed analysis of the 4π amplitude as a subsystem of 5π is an extremely challenging task since there is no simple way to directly measure the mass dependence of the 4-body spin-density matrix, as the invariant 4-body mass is not well defined for a 5-body event (there are three combinatorial possibilities). In the analysis a Breit-Wigner shape of the amplitude has to be *assumed a priory*, introducing a model dependence that is very hard to specify.
In [117] 30016 events in the final state $\pi^-4\pi^0$ and 19419 events in $\pi^+2\pi^-2\pi^-$ were available for analysis. For the initial antibaryon-baryon state only an $^1S_0$ configuration was taken into account. The 4π systems were modeled by relativistic Breit-Wigner amplitudes. Also a $J^{PC} = 1^{-+}$ resonance was allowed. However, that search has been focused on a mass region around $1.4\,\mathrm{GeV}/c^2$ since at that time the alleged partner state was believed to be the $\pi_1(1400)$. If the η_1 indeed has a higher mass, maybe even slightly above the mass of the $\pi_1(1600)$ which is listed in [1] as $m = 1662^{+15}_{-11}\mathrm{MeV}/c^2$ then the small phase space for the production of the state in $\bar{p}n$ annihilation at rest might disfavor any attempts to find the state there. This argument is even enforced a one realizes that the production of the 1^{-+} 4-pion system together with a bachelor pion from an $^1S_0$ state, requires a P-wave between the η_1 and the π. Thus there is an additional damping of the amplitude for small breakup momenta.
No such restrictions apply in principle to the production of a spin exotic 4-pion resonance as a subsystem in the diffractive 5π production.

Name	$I^G(J^{PC})$	Expected mass range (MeV/c^2)
η_1	$0^+(1^{-+})$	1650 ... 1900
b_0	$1^+(0^{+-})$	> 1600
b_2	$1^+(2^{+-})$	> 1600

Table 3.4: Possible spin-exotic resonances coupling to the $(4\pi)^0$ decay channel. The mass ranges are speculative estimates.

Table 3.4 lists two further spin exotic states that might, if they exist, decay into 4 pions. Since the 4π system can be in an isovector state with positive G-parity the spin exotic quantum numbers $J^{PC} = 0^{+-}$ and 2^{+-} can be realized. A search for resonant states in this sectors would be very interesting. In this respect the diffractively produced 5π system provides an unique environment where these partial waves can be produced with a large phase space. Thus in the present analysis trial amplitudes with exotic quantum numbers have been allowed in the amplitude model. Interestingly there are some hints that a $0^+(1^{-+})$ 4-pion contribution is needed to describe the data. These results will be discussed in chapter 5.2.
A promising way to tackle the problem of the model-dependent amplitudes mentioned above is the usage of a very general parametrization of the 4π amplitude in the fit. This method increases the number of free parameters in the amplitude analysis drastically and is only feasible for larger statistics data samples. A first step in that direction has been taken and will be presented in section 5.3.

3.2.3 Isospin Symmetry

Isospin symmetry relates many of the conceivable isobar-model decompositions of the decay amplitude. For light mesons isospin symmetry is quite well realized. We will here especially use the symmetry between the $I_3 = \pm 1$ states which will be imposed exactly on the amplitudes.

Similar considerations have also been implemented in the analysis of the $\eta\pi^-\pi^+\pi^-$ system [63].

Note again, that only isospin 0 and 1 are taken into account in our isobar-model. An interesting application arises for the decay amplitudes of the $(4\pi)^0$ system into two charged subsystems with $I^G = 1^-$ each (compare table 3.3). In this case there are two possibilities which charge states are realized in the isobars. As an example serves the decay

$$R^0 \to \pi^\pm + a_1^\mp(1260). \tag{3.9}$$

Imposing isospin symmetry one can write the amplitude as a sum

$$\langle \pi^\mp(3\pi)^\pm \,|\, \mathscr{T} \,|\, R^0\rangle = \langle \pi^-(3\pi)^+ \,|\, \mathscr{T} \,|\, R^0\rangle + \eta \cdot \langle \pi^+(3\pi)^- \,|\, \mathscr{T} \,|\, R^0\rangle \tag{3.10}$$

The operator $\mathscr{T}$ is a generic transition operator. The relative sign η between the two amplitudes depends on the isospin I_R of R^0 and can be computed by a careful accounting of the Clebsch-Gordan coefficients that arise in the isospin decomposition which are given in table 3.5. As will be shown below, it turns out that (for a fixed decay mode of the 3-pion system) the relative sign between the two amplitudes is given by the isospin of the 4-pion system. This (anti-)symmetry of the decay amplitudes can be used to disentangle the two possible isospin states.

		J	2	2	1	2	1	0	2	1	2
J_{3a}	J_{3b}	J_3	$+2$	$+1$	$+1$	0	0	0	-1	-1	-2
$+1$	$+1$		1								
$+1$	0			$1/\sqrt{2}$	$1/\sqrt{2}$						
0	$+1$			$1/\sqrt{2}$	$-1/\sqrt{2}$						
$+1$	-1					$1/\sqrt{6}$	$1/\sqrt{2}$	$1/\sqrt{3}$			
0	0					$2/\sqrt{3}$	0	$-1/\sqrt{3}$			
-1	$+1$					$1/\sqrt{6}$	$-1/\sqrt{2}$	$1/\sqrt{3}$			
0	-1								$1/\sqrt{2}$	$1/\sqrt{2}$	
-1	0								$1/\sqrt{2}$	$-1/\sqrt{2}$	
-1	-1										1

Table 3.5: Clebsch-Gordan coefficients for the coupling of two (iso)spin 1 objects.

In order to proof this result one has to construct an explicit isospin decomposition of the 5-pion decay amplitude. Let's define a notation for the isospin part of the decay matrix elements such that

$$\langle I_a{}^{I_{3a}}_{n_a}; I_b{}^{I_{3b}}_{n_b} \,|\, \mathscr{T} \,|\, I^{I_3}_n\rangle$$

denotes the transition matrix element for the decay of an n-pion state with isospin I_n, G-parity $G = (-1)^n$ and isospin 3-component I_3 into two $n_{a,b}$-pion isobars ($n_a + n_b = n$) with isospins $I_{a,b}$ and its 3-components $I_{3a,b}$. Only isospin 0 or 1 are taken into account and I_3 can be either 0, +1 or −1.

For the $(\pi^+\pi^-)$ system the decay amplitude can be written in this notation as

$$\langle 1^\pm_1; 1^\mp_1 \,|\, \mathscr{T} \,|\, I^0_2\rangle. \tag{3.11}$$

Writing the decay in an isospin symmetric way one gets

$$\frac{1}{\sqrt{c}}\left[\langle 1_1^+;1_1^-\,|+(-1)^I\langle 1_1^-;1_1^+\,|\right]\mathscr{T}\,|I_2^0\rangle \tag{3.12}$$

with $c = 3$ for $I = 0$ and $c = 2$ for $I = 1$ from the isospin Clebsch-Gordan coefficients (table 3.5). The factor $(-1)^I$ also can be read off from the isospin Clebsch-Gordan coefficients and for $I = 1$ leads to a relative minus sign between the two terms on the right hand-side of equation 3.12. The 2-pion amplitude can, however, be simplified by applying the parity operation (assuming parity to be a good quantum number) on the second term which leads to another factor $P = (-1)^\ell$ with ℓ being the orbital angular momentum between the two pions.

$$\frac{1}{\sqrt{c}}\left[\langle 1_1^+;1_1^-\,|+(-1)^I(-1)^\ell\langle 1_1^+;1_1^-\,|\right]\mathscr{T}\,|I_2^0\rangle$$

For a system of two spin-less particles the definition of the G-parity leads to

$$G = (-1)^{J+I}$$

Since the 2-pion system has $J = \ell$ and even G-parity this means that

$$\ell + I = \text{even}$$

so that the final isospin-symmetric 2-pion decay amplitude is

$$\langle 1_1^\pm;1_1^\mp\,|\,\mathscr{T}\,|\,I_2^0\rangle = \frac{2}{\sqrt{c}}\langle 1_1^+;1_1^-\,|\,\mathscr{T}\,|\,I_2^0\rangle.$$

For the 3π system this trick is obviously not possible. However, $\pi^-\pi^+\pi^\pm$ will always be in an isospin 1 state[5]. For the decay of the 3-pion system into a pion and an isospin 0 state, such as

$$\langle \pi^\pm\sigma\,|\,\mathscr{T}\,|\,I_3^\pm\rangle$$

the amplitude does not depend on the isospin 3-component of the 3-pion system, while for the case where an $I = 1$ system appears in the decay, like

$$\langle \pi^\pm\rho^0\,|\,\mathscr{T}\,|\,I_3^\pm\rangle$$

an isospin Clebsch-Gordan coefficient is being picked up, which flips the sign between the $\pi^+\pi^-\pi^- \to \pi^-\rho^0$ and the $\pi^+\pi^-\pi^+ \to \pi^+\rho^0$ case. In the following discussion the $\rho\pi$ decay will be used but in general this factor has to be respected in the isospin-symmetrization in order to construct a correct amplitude for a given isospin of the 4-pion system.

The $\pi^+\pi^-\pi^+\pi^-$ system can occur both in $I = 0$ and $I = 1$ states as mentioned above. Let's look at the isospin decomposition for the example of equation 3.9 which in the notation 3.11 can be written

$$\langle 1_1^\pm;1_3^\mp\,|\,\mathscr{T}\,|\,I_4^0\rangle = \frac{1}{\sqrt{c}}\left[\langle 1_1^+;1_3^-\,|+\eta\langle 1_1^-;1_3^+\,|\right]\mathscr{T}\,|I_4^0\rangle.$$

Again from the isospin Clebsch-Gordan coefficients one reads off $\eta = 1$ for $I = 0$ and $\eta = -1$ for $I = 1$. In this case applying parity does not help. There is, however, another factor which arises

---

[5] Recall that $I > 1$ is excluded from the discussion.

from the isospin Clebsch-Gordan coefficients of the subsequent decay of the $\pi^-\pi^+\pi^-$ system (which can only have I=1)

$$\langle 1_1^-;1_2^0\,|\,\mathscr{T}\,|\,1_3^-\rangle = -\langle 1_1^+;1_2^0\,|\,\mathscr{T}\,|\,1_3^+\rangle$$

Putting all this together for the decay of a 4-pion system in an $I=0$ state like

$$f_0(1500) \to \pi^\pm + \pi^\mp(1300) \to \pi^\pm + \pi^\mp + \rho^0$$

one can write:

$$\begin{aligned}\langle 4\pi\,|\,\mathscr{T}\,|\,0_4^0\rangle = &\frac{1}{\sqrt{3}}\langle 1_1^-;1_3^+\,|\,\mathscr{T}\,|\,0_4^0\rangle\cdot\frac{1}{\sqrt{2}}\langle 1_1^+;1_2^0\,|\,\mathscr{T}\,|\,1_3^+\rangle\cdot\frac{2}{\sqrt{2}}\langle 1_1^+;1_1^-\,|\,\mathscr{T}\,|\,1_2^0\rangle\\ +&\frac{1}{\sqrt{3}}\langle 1_1^+;1_3^-\,|\,\mathscr{T}\,|\,0_4^0\rangle\cdot\frac{-1}{\sqrt{2}}\langle 1_1^-;1_2^0\,|\,\mathscr{T}\,|\,1_3^-\rangle\cdot\frac{2}{\sqrt{2}}\langle 1_1^+;1_1^-\,|\,\mathscr{T}\,|\,1_2^0\rangle\end{aligned}$$

with a relative minus sign $\eta=-1$ between the two sub-amplitudes. While for the case where the 4π system is in an $I=1$ state like

$$\rho(1450) \to \pi^\pm + a_1^\mp(1260) \to \pi^\pm + \pi^\mp + \rho^0$$

the resulting symmetrized amplitude is

$$\begin{aligned}\langle 4\pi\,|\,\mathscr{T}\,|\,1_4^0\rangle = &\frac{1}{\sqrt{2}}\langle 1_1^-;1_3^+\,|\,\mathscr{T}\,|\,1_4^0\rangle\cdot\frac{1}{\sqrt{2}}\langle 1_1^+;1_2^0\,|\,\mathscr{T}\,|\,1_3^+\rangle\cdot\frac{2}{\sqrt{2}}\langle 1_1^+;1_1^-\,|\,\mathscr{T}\,|\,1_2^0\rangle\\ +&\frac{-1}{\sqrt{2}}\langle 1_1^+;1_3^-\,|\,\mathscr{T}\,|\,1_4^0\rangle\cdot\frac{-1}{\sqrt{2}}\langle 1_1^-;1_2^0\,|\,\mathscr{T}\,|\,1_3^-\rangle\cdot\frac{2}{\sqrt{2}}\langle 1_1^+;1_1^-\,|\,\mathscr{T}\,|\,1_2^0\rangle\end{aligned}$$

with a relative $\eta=+$ sign between the two sub-amplitudes. Similar decompositions can be done for all three 5π decay topologies, but it turns out that the decay of the 4π system explained above is the only place where the isospin symmetrization has to be done explicitly, taking into account the relative phases obtained above and taking into account the isospin decomposition of the 3-pion subsystem as summarized in table 3.6.

$I(4\pi)$	$I(2\pi)=1$	$I(2\pi)=0$
0	$\eta=-1$	$\eta=+1$
1	$\eta=+1$	$\eta=-1$

Table 3.6: Relative sign η between the two isospin-symmetric amplitudes of the $4\pi \to \pi^\pm(3\pi)^\mp$ decay amplitudes, dependent on the isospin $I(4\pi)$ of the 4-pion system and on the decay-mode of the 3π system, which can be to a $I(2\pi)=1$ isobar (e. g. ρ) plus a pion or a $I(2\pi)=0$ (e. g. σ) plus a pion.

In practice each of the two amplitudes with definite isospin decomposition is calculated individually for a given event and the resulting values are added with the appropriate relative phase according to the isospin of the 4π subsystem. In principle it is possible to check the assumptions by fitting each amplitude individually without imposing isospin symmetry. This cross-check has been done only for a few cases, however, and should be repeated systematically on a larger data sample.

3.2.4 Bose Symmetry

Since the $3\pi^-$ and the $2\pi^+$ in the final state are mutually indistinguishable particles, the decay amplitudes have to be symmetrized with respect to permutations of either π^- or π^+. As spin-zero particles the pions obey the Bose symmetrization rules which prescribes an even-sign summation of the amplitudes evaluated for each permutation of the pion 4-momenta. Consequently in total there are $3! \cdot 2 = 6$ terms in the symmetrized amplitude.

3.2.5 Implementation

Much of the work done for the preparation of this thesis concerned the design and implementation of a new partial wave analysis software called `rootpwa` .

In order to implement the isobar model for the 5-body final state described above the amplitude generator `gamp` developed at BNL [134] has been used as a starting point. The program allows the specification of arbitrary isobar decay chains in a simple scripting language. Resonance parameters and quantum numbers of the intermediate state can be read in from a simple custom text file. For the isobar amplitude parametrizations fixed-width, relativistic Breit-Wigner amplitudes and a $(\pi\pi)_{S-\text{wave}}$ amplitude are available. Further parametrizations can easily be added to the program due to its object oriented design. The amplitudes are calculated using the helicity formalism.

This code has been taken over with only minor modifications into the `rootpwa` package [135]. In addition a small script has been developed to facilitate the construction and testing of the decay amplitudes for the 5-pion final state including the transformation into the reflectivity basis, the Bose- and the isospin symmetrization. Furthermore considerable infrastructure for the visualization and further analyses of the amplitude analysis results has been created including several Monte Carlo generators and a ROOT-based graphical user interface.

The software has been cross-checked against another code [136] verifying all basic functionality in the 3π as well as the 5π final state.

The `rootpwa` program is now being used to analyze COMPASS data in kaon diffraction $K^- + p \to K^-\pi^+\pi^- + p$ [137], the $K^+K^-\pi^+\pi^-$ final state produced in pion diffraction and the 5-pion final state presented in this thesis. The complete code is available from the `sourceforge` open-source repository service [135].

In order to provide the community with a tool that is even more versatile especially when it comes to analyzing data from different production processes, such as muo-production $\mu + A \to \mu + \text{Hadrons} + A$ and central production $p + p = p + \text{Hadrons} + p$ a new framework for amplitude calculation has been designed and implemented [135]. Being more flexible as well as speed-optimized even for complex decay chains, the `rootpwa` amplitude calculator will replace the old `gamp` for future projects. It will allow a simple exchange of the spin-formalism used and will not be limited to isobar-model-like amplitudes. This new calculator has, however, not yet been used for the analysis presented here.

The calculation of the decay amplitudes are done for each event independently and so can be trivially parallelized on a cluster of CPUs with only a small book-keeping overhead. Since the computation of the decay amplitudes is a major effort for a complex case like the 5-body final state this parallelization is essential in order to keep the turnaround times of the analysis at a manageable level. As explained below in section 3.4 for the type of amplitude parametrization used here the decay amplitudes for each event need only be calculated once. If in the future more complex problems are being attacked, with free fitting parameters *inside* the decay amplitudes, then the speed of the amplitude calculation would have to be increased dramatically. An example for such a fast, massively parallel partial wave amplitude calculator has been implemented by N. Berger for the BES III collaboration [138].

Suggestions for future research:

- *Detailed studies of the subsystems, using different parametrization hypothesis or using less model-dependent approaches*
- *Inclusion of dispersive and mixing effects, especially for the* 4π *system*
- *Search for exotic resonances in the* 4π *system*
- *Implementation of fully covariant two-body decay amplitudes*
- *Take into account rescattering effects*
- *Develop fast, parallelizable amplitude calculator, e. g. using GPUs*

3.3 Partial Waves Examples

Having defined the parametrization of the decay amplitudes in terms of the isobar model with the input described in the preceding section, in the following a few examples of decay amplitudes are constructed in order to illustrate the typical considerations and to introduce the reader to some notation used in later chapters.

Let's choose an amplitude of topology (c) in Figure 3.4. After the isobar states have been chosen the amplitude construction is mainly a task of applying the rules of the angular momentum algebra and parity conservation at the 2-body decay nodes. Building up the amplitude from the final to the initial state one starts with a final pion-pair. This system is completely determined by the orbital angular momentum between the two pions which can be $\ell = 0,1,2,...$ or in spectroscopic notation S, P, D-wave and so forth. The $\pi^+\pi^-$ system is known to exhibit a strong resonance in its P-wave, the $\rho(770)$ with quantum numbers $I^G(J^{PC}) = 1^+(1^{--})$. Let's continue by assuming the 2-pion system to be a ρ and the final decay node in the tree is written as

$$\rho(770) \to \pi^+ \begin{bmatrix} \ell = 1 \\ S = 0 \end{bmatrix} \pi^-$$

where the bracket notation $a \begin{bmatrix} \ell \\ S \end{bmatrix} b$ indicates the orbital angular momentum ℓ between isobars (or final state particles) a and b printed above the spin S to which the two isobars are coupled, which in the example is 0 since the pions are spin 0 particles. In later formulas this notation is simplified by leaving away the spin if its choice is unique (when either a or b have spin 0), thus writing

$$\rho(770) \to \pi^+[1]\pi^-$$

In particular for the $\pi^+\pi^-$ system the decay is not written out explicitly and only the 2-body isobar $\rho(770)$ is kept in the notation with its decay into $\pi^+\pi^-$ understood. Note that the parity of the ρ works out correctly. Both pions have intrinsic uneven parity, however, the orbital angular momentum contributes another factor $(-1)^\ell$ to the parity of the system. So the 2-pion system in P-wave has indeed negative parity.

With the same rules it is easy to see what happens if another pion is added to the ρ. For $\ell = 0$ between the pion and the ρ:

$$J^P = 1^+ \to \pi^+ \begin{bmatrix}\ell = 0\\ S = 1\end{bmatrix} \rho(770)$$

For larger ℓ up to D-wave one gets the amplitudes

S-wave	P-wave	D-wave
	$0^- \to \pi^+ \begin{bmatrix}1\\1\end{bmatrix} \rho(770)$	$1^+ \to \pi^+ \begin{bmatrix}2\\1\end{bmatrix} \rho(770)$
$1^+ \to \pi^+ \begin{bmatrix}0\\1\end{bmatrix} \rho(770)$	$1^- \to \pi^+ \begin{bmatrix}1\\1\end{bmatrix} \rho(770)$	$2^+ \to \pi^+ \begin{bmatrix}2\\1\end{bmatrix} \rho(770)$
	$2^- \to \pi^+ \begin{bmatrix}1\\1\end{bmatrix} \rho(770)$	$3^+ \to \pi^+ \begin{bmatrix}2\\1\end{bmatrix} \rho(770)$

For definiteness a suitable isobar is inserted for the 3-pion state and the → might be omitted for brevity as in

$$a_1^+(1260)\pi^+ \begin{bmatrix}0\\1\end{bmatrix} \rho(770)$$

It should be clear how to continue for the remaining pions. The 4-pion state for example may be constructed as

$$2^+ \to \pi^- \begin{bmatrix}1\\1\end{bmatrix} a_1^+(1260) \to \ \pi^+ \begin{bmatrix}0\\1\end{bmatrix} \rho(770)$$

Note that at this stage the isospin of the 2^{++} 4-pion system is undetermined, it could both be 0 and 1. Only the proper symmetrization with the isospin mirror amplitude

$$2^+ \to \pi^+ \begin{bmatrix}1\\1\end{bmatrix} a_1^-(1260) \to \ \pi^- \begin{bmatrix}0\\1\end{bmatrix} \rho(770)$$

will fix the isospin as discussed in section 3.2.3. For the isospin 0 case there is a well known resonance with $I^G(J^{PC}) = 0^+(2^{++})$ – the $f_2(1270)$. The corresponding isospin 1 state with $I^G(J^{PC}) = 1^+(2^{+-})$ would be the spin-exotic b_2. Of course depending on the $\ell - S$ coupling of the a_1 and the fourth pion more states can be constructed. The $f_2(1270)$ shall just serve as an example here.

Finally adding the fifth pion in an S-wave to the f_2 we arrive at an important wave for the analysis of the diffractively produced 5π system:

$$I^G J^{PC} M^\epsilon = 1^- 2^{-+} 0^+ \quad \pi^- \begin{bmatrix}0\\2\end{bmatrix} f_2(1270) \to \pi^\mp[1] a_1(1269) \to \pi^\pm[0]\rho(770)$$

Here the $f_2\pi$ S-wave combines to $J^{PC} = 2^{-+}$, a partial wave where the well studied $\pi2(1670)$ resonance occurs. This decay is a prominent contribution to the 3-pion system with the $f_2(1270)$ decaying into 2π. Here we have constructed the same amplitude but with the f_2 going into a $(4\pi)^0$ final state. The $\pi_2(1670)$ should show up in this wave.

As an alternative example for a 5-pion decay amplitude consider the decay of a 4π system into two $\rho(770)$ resonances which now allows to couple the spins of the two vector-systems in three different ways. This, together with a possible orbital angular momentum between the two ρs gives a wide variety of possible partial waves. As discussed above the $\rho^0\rho^0$ system can only be in an $I = 0$ state. So the S-wave and P-wave amplitudes are

S-wave	P-wave	
$0^{++} \to \rho(770)\begin{bmatrix}0\\0\end{bmatrix}\rho(770)$	$1^{-+} \to \rho(770)\begin{bmatrix}1\\0\end{bmatrix}\rho(770)$	$1^{-+} \to \rho(770)\begin{bmatrix}1\\2\end{bmatrix}\rho(770)$
$1^{++} \to \rho(770)\begin{bmatrix}0\\1\end{bmatrix}\rho(770)$	$0^{-+} \to \rho(770)\begin{bmatrix}1\\1\end{bmatrix}\rho(770)$	$2^{-+} \to \rho(770)\begin{bmatrix}1\\2\end{bmatrix}\rho(770)$
$2^{++} \to \rho(770)\begin{bmatrix}0\\2\end{bmatrix}\rho(770)$	$1^{-+} \to \rho(770)\begin{bmatrix}1\\1\end{bmatrix}\rho(770)$	$3^{-+} \to \rho(770)\begin{bmatrix}1\\2\end{bmatrix}\rho(770)$
	$2^{-+} \to \rho(770)\begin{bmatrix}1\\1\end{bmatrix}\rho(770)$	

These 4-body decays can again be implemented as sub-systems of the 5π decay amplitudes in the topology (b) of Figure 3.4. A prominent example, that will be used later is the partial wave

$$I^G J^{PC} M^\epsilon = 1^- 0^{-+} 0^+ \quad \pi^- \begin{bmatrix} 0 \\ 0 \end{bmatrix} f_0(1500) \to \rho(770)\begin{bmatrix}0\\0\end{bmatrix}\rho(770)$$

In this fashion a very large number of possible 5-body isobar model amplitudes can be constructed. A complete list of amplitudes, that has been used in the present analysis is given in appendix B. The prominent known resonances and their dominant decay modes are an important input not only for the parametrization of the intermediate states but also for the question which amplitudes to consider at all[6]. We will return to the question which of these many amplitudes are required to describe the data later in chapter 4. Before we can answer that question, however, we have to define a procedure to infer the values of the production amplitudes and thus *fit* an amplitude-model to the data.

3.4 Extended Log-Likelihood Fit Formalism

This section describes the algorithm that is used to infer the free parameters of the 5-body isobar model described above from the data. It is based on the maximization of the extended log-likelihood that can be calculated from the data for a given isobar model. In section 4 this algorithm will be extended in order to find a solution to the problem of how to truncate the partial wave expansion on which the isobar model is based.

3.4.1 Derivation of the Log-Likelihood Function

As a starting point the intensity for the diffractive 5-pion production in a fixed 5-body mass bin is parametrized as (compare to 3.7)

$$\mathscr{I}(\tau) = \sum_{\epsilon=\pm 1} \sum_{r=1}^{N_r} \left| \sum_{\alpha} T^{\epsilon}_{\alpha r} \bar{\psi}^{\epsilon}_{\alpha}(\tau) \right|^2 + T^2_{\mathrm{FLAT}} \tag{3.13}$$

The intensity function is an incoherent sum of $2 \cdot N_r$ terms. Each of the terms is a coherent sum of amplitudes squared. N_r is called the *rank* of the fit. Note that only the production amplitudes $T^{\epsilon}_{\alpha r}$ carry the rank-index r. The decay amplitudes do not depend on r. For the analysis of the 5π production at small momentum transfer, coherent scattering off the lead nucleus is assumed

---

[6] For example, apart from a few exceptions, amplitudes which have spin-exotic states occurring as isobars are not considered for the analysis.

and the analysis is restricted to rank 1. However, in order to accommodate phase space like, incoherent background a constant term T_{FLAT} is allowed in the fit. For brevity this term is not written explicitly in the following formulas.

Amplitudes with different reflectivity quantum number ϵ (see section 3.1.3) by construction do not interfere due to parity conservation[105]. They are added incoherently. The coherent sums are taken over all the partial amplitudes α that are included in the fit. Each decay amplitude $\psi_\alpha(\tau)$ is characterized by a full set of quantum numbers and a particular set of intermediate states as explained in section 3.2 on page 56. The $\psi_\alpha(\tau)$ are functions of the measured 5π phase space variables τ such that for each event the amplitude $\psi_\alpha(\tau)$ is represented by a complex number. Recall that in this parametrization the decay amplitudes do not contain any free parameters and can be calculated once for each event.

The following normalization is chosen for the decay amplitudes:

$$\bar{\psi}^{\epsilon}_{\alpha}(\tau) = \frac{\psi^{\epsilon}_{\alpha}(\tau)}{\sqrt{\int |\psi^{\epsilon}_{\alpha}(\tau')|^2 \mathrm{d}\rho(\tau')}} \quad \text{with} \quad \mathrm{d}\rho(\tau) \equiv f(\tau)\mathrm{d}\tau \tag{3.14}$$

Here $f(\tau)\mathrm{d}\tau$ is the phase-space differential and the integration runs over the whole 5-body phase space. In practice integrals like these are calculated by Monte Carlo integration. The general formula for the phase space integrals is

$$I^{\epsilon}_{\alpha\beta} = \int \psi^{\epsilon}_{\alpha}(\tau)\psi^{\epsilon*}_{\beta}(\tau)\mathrm{d}\rho(\tau).$$

The numerical calculation is achieved through summing over a sample of synthesized events which are generated with a flat[7] probability distribution throughout the 5-body phase space using the GENBOD [139] algorithm. Calculating the decay amplitudes for this sample of phase space events and summing over all N_{MC} events yields the phase space integrals

$$I^{\epsilon}_{\alpha\beta} \cong \frac{1}{N_{\mathrm{MC}}} \sum_{i}^{N_{\mathrm{MC}}} \psi^{\epsilon}_{\alpha}(\tau_i)\psi^{\epsilon*}_{\beta}(\tau_i) \tag{3.15}$$

Note that all internal 5-body kinematic variables τ are integrated out, but the $I^{\epsilon}_{\alpha\beta}$ still depend on the 5-body invariant mass. They have to be calculated in each m_X bin separately. Due to the orthonormality of the $D-$functions which appear in the partial-wave expansion (see equation 3.5) only off-diagonal terms with α, β belonging to the same $J^{PC}M^{\epsilon}$ survive the integration over all angles in equation 3.15. The total phase space available for the 5-body final state of course grows strongly with higher 5-body mass. This opening of the phase space is absorbed as an overall factor into the production amplitudes at this stage and in each mass-bin an equal number of Monte Carlo events is generated (see section 6.1 for further discussion).

The numerical approximation requires a certain amount of Monte Carlo events to achieve a satisfying degree of convergence. For the present analysis 100 000 Monte Carlo events have been generated in each 60 MeV/c^2 mass bin.

---

[7] A flat phase space distribution means equal probability density over all phase space elements. In particular this results in flat angular distributions. However, of course the available phase space for the 2,3 or 4-body subsystems will not be flat.

The diagonal elements of the matrix of phase space integrals are used to perform the normalization in equation 3.14. The normalized phase space integrals are defined through

$$\bar{I}^{\epsilon}_{\alpha\beta} = \int \bar{\psi}^{\epsilon}_{\alpha}(\tau)\bar{\psi}^{\epsilon *}_{\beta}(\tau)\mathrm{d}\rho(\tau) = \frac{I^{\epsilon}_{\alpha\beta}}{\sqrt{I^{\epsilon}_{\alpha\alpha}I^{\epsilon}_{\beta\beta}}}.$$

The normalization procedure described above stabilizes the fit numerically by establishing a common scale for all terms of the model. This proves to be especially useful with regards to the stability of the calculation of the covariance matrix. It has the further advantage that in this case the production amplitudes T^{ϵ}_{ar} have a straight forward interpretation. Namely the spin density matrix (which has a block-diagonal structure according to the reflectivities) is given by the production amplitudes as

$$\rho^{\epsilon}_{\alpha\beta} = \sum_{r} T^{\epsilon}_{ar} T^{\epsilon *}_{\beta r} \tag{3.16}$$

The diagonal elements of the spin density matrix are the intensities of the individual partial waves while the off-diagonal elements describe interferences. Note that the intensities are simply given by the square of the production amplitudes summed over the rank.

With this definition of the spin-density matrix the intensity can be written as:

$$\mathscr{I}(\tau) = \sum_{\epsilon}\sum_{\alpha,\beta} \rho^{\epsilon}_{\alpha\beta}\bar{\psi}^{\epsilon}_{\alpha}(\tau)\bar{\psi}^{\epsilon *}_{\beta}(\tau) \tag{3.17}$$

The likelihood $\mathscr{L}$, which is the probability P to observe (a specific set of) N events in a bin with finite acceptance $\eta(\tau)$ assuming that the data is distributed according to a model M with parameters T^{ϵ}_{ar} is:

$$P(\mathrm{Data}|T^{\epsilon}_{ar}, M) = \mathscr{L} = \left[\frac{\overline{N}^{N}}{N!}e^{-\overline{N}}\right] \prod_{i}^{N} \frac{\mathscr{I}(\tau_i)\eta(\tau_i)f(\tau_i)}{\underbrace{\int \mathscr{I}(\tau)\eta(\tau)\mathrm{d}\rho(\tau)}_{=\overline{N}}} \tag{3.18}$$

The product $\prod_i$ runs over all N events in the data sample and the τ_i are the measured kinematics of the individual events. The inclusion of the Poisson probability to find N events in equation 3.18 is necessary to implement a finite normalization of the production amplitudes in the inference procedure (while the decay amplitudes have been normalized according to equation 3.14). It acts as a constraint to ensure that the average number of events predicted by the model $\overline{N}$ is equal to the number of events that have actually been observed. This method is known under the name of *extended* likelihood [140].

The notation $P(\mathrm{Data}|T^{\epsilon}_{ar}, M)$ for the likelihood has been introduced here in preparation of chapter 4 to emphasize that any result obtained in an inference procedure, for example the measurement of the spin-density matrix elements, depends on the model M that is being applied for the inference. In the present analysis M will always be chosen from the class of isobar-models. However, there is still the freedom of choosing a specific waveset. In subsequent sections, when the text refers to a specific model, then an isobar-model with a specific choice of waveset is meant.

Noting that the integral of the intensity over the acceptance corrected phase space $\eta(\tau)\mathrm{d}\rho(\tau)$ equals the expected number of events $\overline{N}$, the expression for the likelihood can be rewritten as follows.

$$\mathscr{L} = \left[\frac{\overline{N}^N}{N!} e^{-\overline{N}}\right] \prod_i^N \frac{\mathscr{I}(\tau_i)}{\overline{N}} \eta(\tau_i) f(\tau_i) = \frac{1}{N!} \prod_i^N \mathscr{I}(\tau_i) \cdot \prod_i^N \eta(\tau_i) f(\tau_i) \cdot e^{-\overline{N}} \tag{3.19}$$

In order to make this expression more manageable for numeric calculations it is useful to take the logarithm using Stirling's approximation for $\ln N!$ and to insert the phase-space integral for $\overline{N}$ in the last factor of equation 3.19:

$$\ln\mathscr{L} = -N\ln N + N + \sum_i^N \ln\eta(\tau_i) f(\tau_i) + \sum_i^N \ln\mathscr{I}(\tau_i) - \int \mathscr{I}(\tau)\eta(\tau) d\rho(\tau) \tag{3.20}$$

Since the first three terms do not depend on the free parameters in the model, it is possible to drop $\left[-N\ln N + N + \sum_i^N \ln\eta(\tau_i) f(\tau_i)\right]$. If one then inserts the intensity parametrization the extended log-likelihood function is given by

$$\ln\mathscr{L} = \sum_{i=1}^{N_{\text{events}}} \ln\left[\sum_{\epsilon,r} \sum_{\alpha,\beta\in M} T^{\epsilon}_{\alpha r} T^{\epsilon *}_{\beta r} \bar{\psi}^{\epsilon}_{\alpha}(\tau_i) \bar{\psi}^{\epsilon *}_{\beta}(\tau_i)\right] - \sum_{\epsilon,r} \sum_{\alpha,\beta\in M} T^{\epsilon}_{\alpha r} T^{\epsilon *}_{\beta r} IA^{\epsilon}_{\alpha\beta} \tag{3.21}$$

with the acceptance-corrected phase space integral

$$IA^{\epsilon}_{\alpha\beta} = \int \bar{\psi}^{\epsilon}_{\alpha}(\tau) \bar{\psi}^{\epsilon *}_{\beta}(\tau) \eta(\tau) \mathrm{d}\rho.$$

These integrals include the acceptance effects through the factor $\eta(\tau)$ which is the probability density to reconstruct an event in the apparatus at the phase space point τ including all applied data selection cuts. They are calculated with a Monte Carlo integration similar to the raw phase-space integrals (c. f. equation 3.15)

$$IA^{\epsilon}_{\alpha\beta} = \frac{1}{N_{\text{MC}}} \sum_i^{\substack{\text{accepted}\\\text{events}}} \bar{\psi}^{\epsilon}_{\alpha}(\tau_i) \bar{\psi}^{\epsilon *}_{\beta}(\tau_i) \tag{3.22}$$

To take the finite acceptance η into account the sum in equation 3.22 runs over all Monte Carlo events that, according to the detector simulation, would be reconstructed and that have survived all data selection cuts as described in sections 3.6 and 2.2.

The construction of the log-likelihood function as described here offers a clear view onto a special feature of the chosen parametrization of the partial wave amplitudes. Note that the decay amplitudes and thus the phase-space integrals do not depend on any free parameters of the model. They can be computed once in advance and do not have to be recalculated at any time during the inference procedure which maximizes $\ln\mathscr{L}$ by varying the production amplitudes $T^{\epsilon}_{\alpha r}$. This property is of considerable computational value since the calculation of the decay amplitudes for the complex 5-body final state is quite expensive in terms of computing resources.

For the maximization of the extended log-likelihood function the program MINUIT2 [141] has been used. This program offers several minimization algorithms from which the steepest descent method MIGRAD is the most widely used. The numerical calculations can be greatly sped up and improved in accuracy if the gradient of the log-likelihood function $\nabla \ln \mathscr{L}$ can be supplied explicitly. Indeed the form of $\ln \mathscr{L}$ in 3.21 allows a straight forward analytical computation of the gradient. For the real parts of the production amplitudes the gradient function reads

$$\frac{\partial \ln \mathscr{L}}{\partial \operatorname{Re} T^{\epsilon}_{\alpha r}} = \sum_{i=1}^{N} \frac{\sum_{\beta \in M} T^{\epsilon *}_{\beta r} \bar{\psi}^{\epsilon}_{\alpha}(\tau_i) \bar{\psi}^{\epsilon *}_{\beta}(\tau_i) + \text{c.c.}}{\sum_{\epsilon, r} \sum_{\alpha, \beta \in M} T^{\epsilon}_{\alpha r} T^{\epsilon *}_{\beta r} \bar{\psi}^{\epsilon}_{\alpha}(\tau_i) \bar{\psi}^{\epsilon *}_{\beta}(\tau_i)} - \sum_{\beta \in M} T^{\epsilon *}_{\beta r} I A^{\epsilon}_{\alpha\beta} + \text{c.c.} \tag{3.23}$$

The expression for the imaginary parts is obtained analogously.

In terms of computational speed it is obvious from equation 3.21 that the sum over all events $i = 1..N$ will dominate execution time. However, since this is the same sum for all elements of the gradient, it has to be run only once and $\nabla \ln \mathscr{L}$ can be computed in parallel to the value of $\ln \mathscr{L}$ itself. Especially since the denominator in the first term of equation 3.23 has to be calculated only once per event.

For the implementation of log-likelihood function and its gradient in the form described here the programming interface of ROOT [142] has been used. The object oriented code takes advantage of the `ROOT::Math::IGradientFunctionMultiDim` function interface which allows to easily exchange the minimization algorithms for future developments.

In many cases the minimization of a complicated log-likelihood function such as the one constructed here is a quite difficult task and gradient search algorithms are known to be prone to yielding solutions that correspond to local minima rather than the true optimum. For the partial-wave analysis of the 5π system extensive tests have been performed to ensure proper behavior of the optimization. In particular it has been tested if fits with different starting parameters give consistent results. Interestingly, no significant problem with multiple solutions has been found. This result has also been confirmed in an independent cross-check of the analysis, which utilized a minimizer that also takes into account the 2nd derivatives of the log-likelihood function.

3.5 Observable Quantities

The physical content embodied in the production amplitudes is conveniently expressed in terms of the spin-density matrix defined in equation 3.16 which by construction has real valued diagonal entries and complex off-diagonal elements.

The intensity of the individual partial-wave amplitudes is given by the diagonal elements:

$$\text{Intens}^{\epsilon}_{\alpha} = \rho^{\epsilon}_{\alpha\alpha} \tag{3.24}$$

The off-diagonal entries are the interference terms between two partial waves α and β. They can be either represented by their real and imaginary parts or by a magnitude $N^{\epsilon}_{\text{overlap}\,\alpha\beta} = 2\text{Re}(\rho^{\epsilon}_{\alpha\beta} \bar{I}^{\epsilon}_{\alpha\beta})$ and the phase difference between the two waves

$$\Delta\phi^{\epsilon}_{\alpha\beta} = \arg(\rho^{\epsilon}_{\alpha\beta}). \tag{3.25}$$

Through the interference effects one has access to the phase shifts of the individual waves. Resonant contributions can be identified through characteristic phase shift patterns.

The total acceptance-corrected intensity is given by the sum of the intensities in all channels plus the interference terms:

$$\text{Intens} = \sum_{\epsilon}\sum_{\alpha\beta} \rho^{\epsilon}_{\alpha\beta} \bar{I}^{\epsilon}_{\alpha\beta} \tag{3.26}$$

In addition to the observables described so far for rank $r > 1$ the *coherence* can be defined as

$$\text{Coh}^{\epsilon}_{\alpha\beta} = \frac{\sqrt{(\text{Re}\rho^{\epsilon}_{\alpha\beta})^2 + (\text{Im}\rho^{\epsilon}_{\alpha\beta})^2}}{\sqrt{\rho^{\epsilon}_{\alpha\alpha} \cdot \rho^{\epsilon}_{\beta\beta}}} \tag{3.27}$$

which by construction is a number between 0 and 1. For rank $r = 1$ the coherence is 1 by definition.

Rules for the calculation of the uncertainties on these observables are given in appendix C.

3.6 Acceptance Corrections

In order to take into account the acceptance effects of the spectrometer in the partial wave analysis a Monte Carlo simulation is used. We generate 5π events uniformly distributed in phase space and pass them through the COMGEANT simulation[143] with the 2004 COMPASS spectrometer geometry and the CORAL reconstruction[144] software (see section 2.1).

For the event generator the `TGenPhaseSpace` class of ROOT[142] is used which is a C++ implementation of the well known GENBOD [139] algorithm. We use the measured scattering angle distribution and the beam and target characteristics (beam spread, slopes) as determined from the 3π data (cf. [102]). For each 5π mass bin 100 000 events have been generated uniformly distributed in mass.

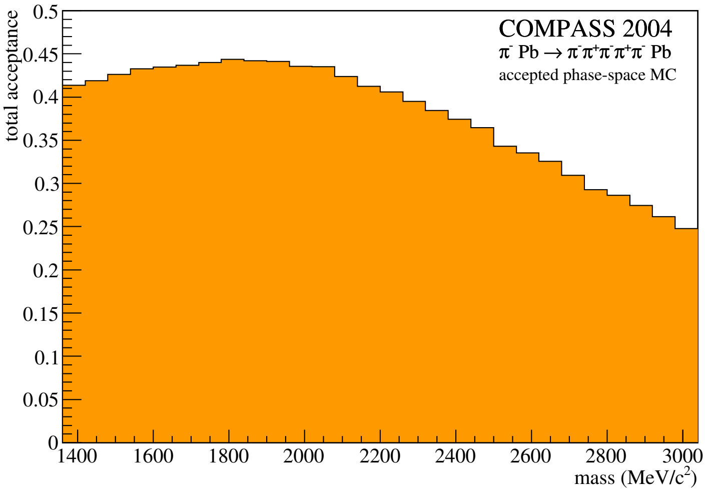

Figure 3.14: Total acceptance for low-t' events ($t' < 0.005\,\text{GeV}^2/c^2$) as determined by phase-space Monte Carlo simulation.

On the simulated and reconstructed pseudo-data the same cuts are applied as to the real data. It is found that the multiplicity counter and online filter accept conditions are met for every event in the sample.

Figure 3.14 shows the overall acceptance for the low-t' range as determined from the Monte Carlo simulation in 28 mass bins. Around a mass of $2\,\mathrm{GeV}/c^2$ the value of $\sim 40\%$ is essentially determined by the single track reconstruction efficiency of COMPASS and scales accordingly with respect to the 3π data set, for which an acceptance of $\sim 60\%$ has been determined [102]. At higher 5π-masses, however there are significant acceptance losses down to a value of $\sim 25\%$ at $3\,\mathrm{GeV}/c^2$ which are mainly due to the second veto counter (see section 2.1.3) limiting the angular acceptance as will be discussed in more detail in the following.

For the partial wave analysis the angular distributions of the different subsystems contain the information about spin-parity quantum numbers as has been discussed in section 3.2.1. The acceptance corrections have to take into account any structures in these variables that originate from the imperfections of the measurement apparatus and the data reconstruction procedure or that might be introduced by the data selection.

Figure 3.15 shows the projection of Monte Carlo pseudo-data that has been passed through the apparatus simulation, the reconstruction software and the data selection procedure onto the different relevant kinematic variables for the interval $m_{5\pi} \in [1.84, 2.08]\,\mathrm{GeV}/c^2$. Similar acceptance plots covering the other 5-body mass regions are provided in appendix A. Since the pseudo-data shown here were generated flat in phase-space, acceptance effects show up as deviations from a flat distributions in the angles.

The first row of figures shows angular distributions in the Gottfried-Jackson frame. Figure 3.15(a) shows the cosine of the Gottfried-Jackson angle θ_{GJ} of the $(\pi^-\pi^+\pi^-\pi^+)$ subsystem. In this variable the acceptance effects are visible most dramatically. When the 4π subsystem is going forward in the 5π rest-frame a single pion has to be emitted in backward direction. In the laboratory frame this single pion will appear relatively slow and under a large angle with a non-negligible probability to fall out of the acceptance of the spectrometer. The effect becomes more pronounced at larger 5π masses and leads to the pronounced dip at large $\cos\theta_{\mathrm{GJ}}^{4\pi}$. Figure 3.16 shows the development of this acceptance dip for the different 5-body mass regions.

A similar effect appears in Figure 3.15 (c) which shows the corresponding angle for the $\pi^-\pi^+\pi^-$ subsystem. However, in this case, due to the distribution of momentum onto a 3π and a 2π system the effect on the angular spectrum is washed out. Figure (b) is the Treiman-Young angle ϕ_{TY} of the 4π subsystem and appears essentially flat (as is the case for the corresponding angle of the 3π subsystem, which has been omitted from the plots). This behavior is of course expected for the low-t' data, since in this case the scattering plane, against which the azimuthal angle is measured, is not well defined or at least not measured with enough precision to allow a reliable determination of ϕ_{TY}.

The bottom two rows show distributions which have been constructed in the helicity frames of the respective isobar systems. Figures (d),(e) and (f) show the cosine of the polar angle θ_{Hel} for the cases of a 4π system decaying into $\pi^-\pi^+ + \pi^+\pi^-$ ($\cos\theta_{\mathrm{Hel}}^{22}$), a 4π system decaying into $\pi^-\pi^+\pi^+ + \pi^-$ ($\cos\theta_{\mathrm{Hel}}^{31}$) and a 3π system decaying into $\pi^-\pi^+ + \pi^-$ ($\cos\theta_{\mathrm{Hel}}^{21}$) respectively. The last row of figures shows – for the same subsystems – the distributions of the azimuthal angles ϕ_{Hel}.

The acceptance correction is performed according to the prescription given in equation 3.21 with the accepted phase-space integrals defined in equation 3.22. Note that this form of acceptance correction takes into account the full correlations of the acceptance effects (which are not visible in projections like those shown in Figure 3.15) for each partial wave separately.

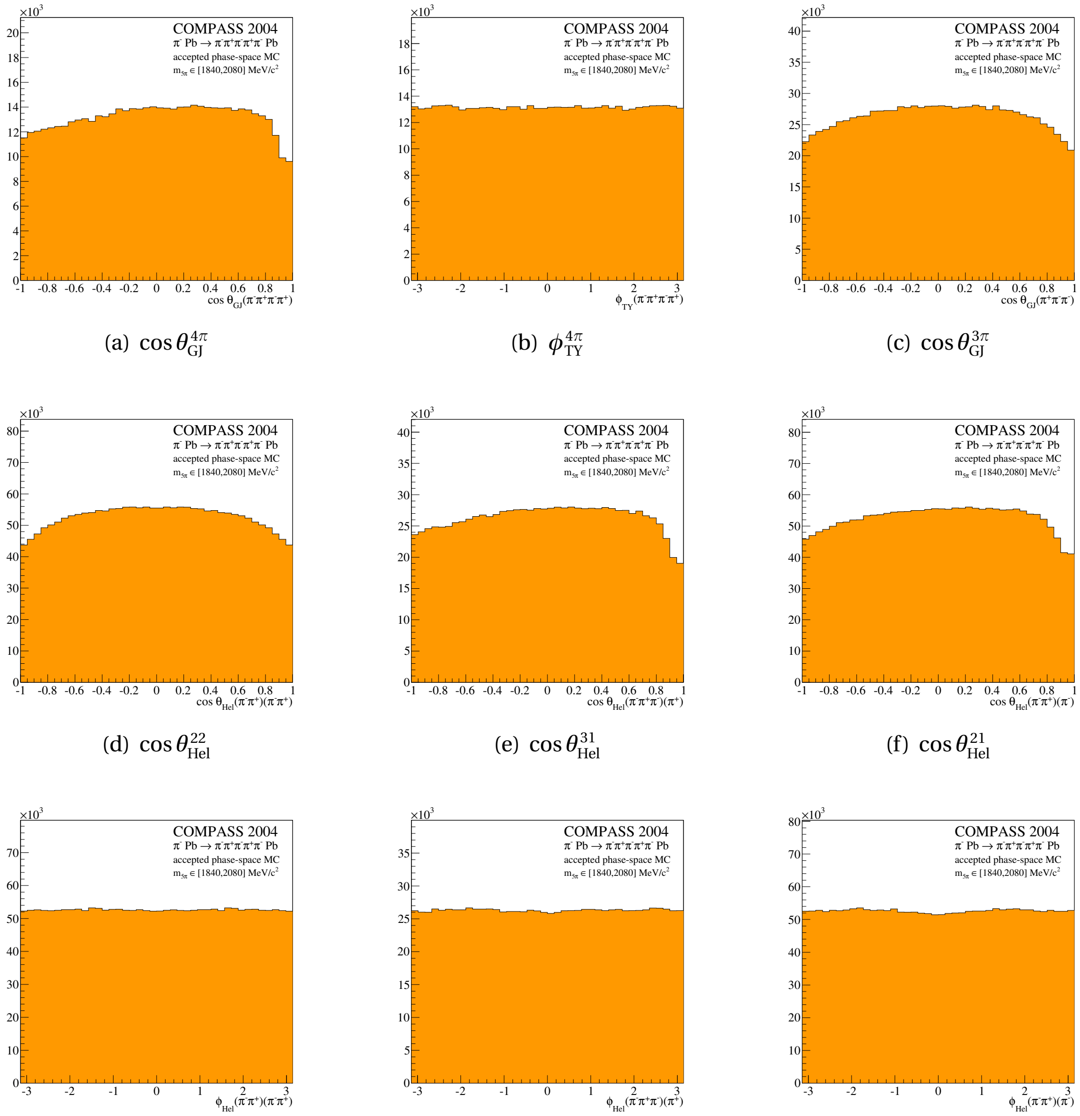

(a) $\cos\theta_{\mathrm{GJ}}^{4\pi}$ (b) $\phi_{\mathrm{TY}}^{4\pi}$ (c) $\cos\theta_{\mathrm{GJ}}^{3\pi}$

(d) $\cos\theta_{\mathrm{Hel}}^{22}$ (e) $\cos\theta_{\mathrm{Hel}}^{31}$ (f) $\cos\theta_{\mathrm{Hel}}^{21}$

(g) ϕ_{Hel}^{22} (h) ϕ_{Hel}^{31} (i) ϕ_{Hel}^{21}

Figure 3.15: Angular acceptance for the 5-pion final state as determined by Monte Carlo simulation. The distributions shown are projections of accepted phase-space events. Unmodified phase-space distributions would be flat in all variables. See text for a detailed description of the kinematic variables shown. $m_{5\pi} \in [1.84, 2.08]\,\mathrm{GeV}/c^2$

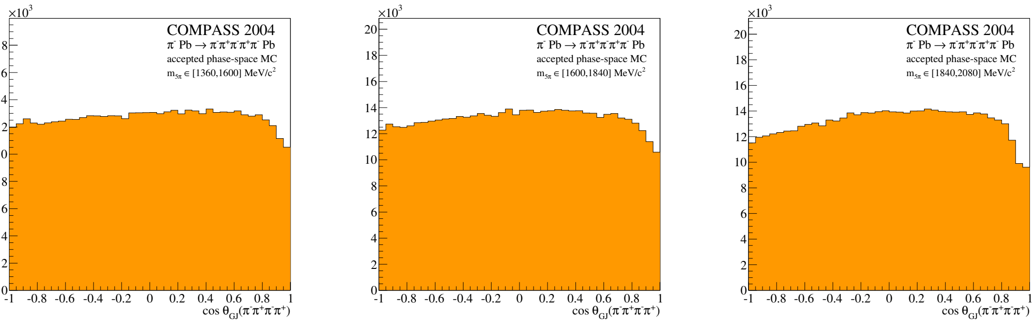

(a) $m_{5\pi} \in [1360, 1600]\mathrm{MeV}/c^2$ (b) $m_{5\pi} \in [1360, 1600]\,\mathrm{MeV}/c^2$ (c) $m_{5\pi} \in [1360, 1600]\,\mathrm{MeV}/c^2$

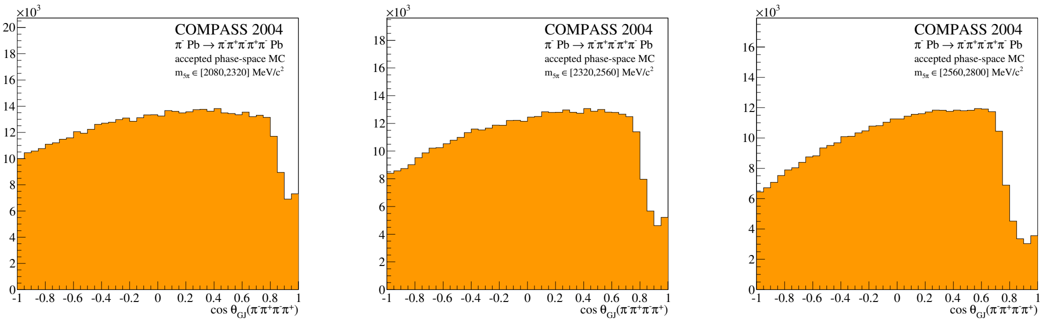

(d) $m_{5\pi} \in [1360, 1600]\,\mathrm{MeV}/c^2$ (e) $m_{5\pi} \in [1360, 1600]\,\mathrm{MeV}/c^2$ (f) $m_{5\pi} \in [1360, 1600]\,\mathrm{MeV}/c^2$

Figure 3.16: Angular acceptance for low-t' events ($0\,\mathrm{GeV}^2/c^2 < t' < 5 \cdot 10^{-3}\,\mathrm{GeV}^2/c^2$) as determined by phase space Monte Carlo simulation in different mass bins between 1 and $3\,\mathrm{GeV}/c^2$. Shown are distributions of $\cos\theta_{\mathrm{GJ}}$ – the angle between the beam-axis and the $(4\pi)^0$ subsystem in the rest frame of the decaying 5π resonance (see section 3.2.1 for a definition of the Gottfried-Jackson frame). There are 3 entries per event in each plot.

Chapter 4

Model Selection

> They say that Understanding ought to work by the rules of right reason. These rules are, or ought to be, contained in Logic; but the actual science of logic is conversant at present only with things either certain, impossible or entirely doubtful, none of which (fortunately) we have to reason on. Therefore the true logic of this world is the calculus of Probabilities, which takes account of the magnitude of the probability which is, or should be, in a reasonable man's mind.
>
> J. C. Maxwell

It has already been mentioned in section 3.1.2 that the expansion of the 5-pion amplitude into its partial waves has to be truncated at some point. Already from the point of view of statistics the number of waves ψ_α that can be included in a partial-wave fit (equation (3.21)) is limited. It is a well-known problem in statistical inference of model parameters from a finite sample of measurements that in the presence of imperfect measurements it is always possible to trade predictive power of the model for a better description of the data by including more free parameters. A trivial example is the fit of a polynomial curve to a set of n points $\{(x, y)\}$. One can obtain a perfect description of the data by using a polynomial of order n. However, it is highly unlikely that the true distribution from which the sample was drawn really is governed by the such inferred curve. This problem is known as *over-fitting*.

Working with the isobar-model fits described in the previous chapter one is tempted to further maximize the log-likelihood by including more and more partial-wave amplitudes. From log-likelihood arguments alone it is not possible to judge in a straight-forward manner whether the data provide significant support for a specific partial wave.

On the other hand the addition or removal of a component to the waveset can indeed have significant influence on the results. Thus the decision which waveset should be used is a delicate one. A prominent example where this issue led to some confusion are the two analyses of the $\pi^+\pi^-\pi^-$ system presented by the E852 collaboration in [115] and [145]. The use of two different wavesets in the partial-wave analyses (among other things) led to a different conclusion on the critical issue of the existence of an exotic meson — the $\pi_1(1600)$. Without an estimate of the systematic error that is introduced by the choice of a particular waveset it is difficult to draw meaningful conclusions in such cases.

In past analyses the behavior of the log-likelihood when new waves were added has been examined in order to choose the waveset. The selection was supported by physical arguments or pre-knowledge such as the optimization of the signals of well known resonances.
For the 5-body problem the number of possible decay amplitudes becomes very large making it necessary to establish an at least semi-automatic method to determine a suitable set of waves. The following presuppositions are made in order to constrain the choice of a waveset:

1. The model should yield a good description of the data with an optimal log-likelihood result.
2. The number of partial waves should be as small as possible. Components with negligible significance should be dropped from the waveset.
3. Excessive correlations between different waves should be avoided.

In this section a method is developed which fulfills all of these criteria and which can be used as a tool to find the optimal waveset for the partial-wave analysis. The framework of discussion is found in *Bayesian statistics* which formalizes the analysis of the degree to which a model is supported by data in terms of Bayesian probabilities. Bayesian statistics is discussed in most modern textbooks on statistics, data analysis and inference such as [146, 147]. There are also two useful reviews on the topic written by G. Cowan and published in the particle data book [1].
It should be kept in mind that a certain systematic error is being made already with the adoption of the amplitude parametrization in the isobar model (equations 3.2,3.5 and 3.6), which cannot be attacked with the methods presented here. Rather the analysis of this section is limited to the systematics of choosing a particular model out of the class of possible isobar-model expansions of the amplitude.
For simplicity in this section only the case of rank $r = 1$ is discussed and the index r will be skipped from the formulas. Extensions to partial-wave fits with higher rank are straight forward.

4.1 Bayesian Model Evaluation

The free parameters of the isobar partial-wave model are the production amplitudes T^{ϵ}_{ar}. In general these are complex numbers so that the actual parameters on which the fitting algorithm operates are their real and imaginary parts. In this section for ease of notation all free parameters in a fixed n-body-mass partial-wave fit are collected into a tuple A^k such that $A^k = (\mathrm{Re}T^{+}_{00}, \mathrm{Re}T^{+}_{10}, \mathrm{Im}T^{+}_{10}, \mathrm{Re}T^{+}_{20}...)$. The index k labels the specific hypotheses for the waveset M_k which is also called a *model* in this section. The tuples A^k have a dimension d^k which is roughly[1] twice the number of partial waves in the waveset k times the rank of the fit. The maximum likelihood solution for waveset k is written as A^k_{ML}.
The starting point of the discussion is the application of Bayes' theorem to the model probability:

$$P(M_k|\mathrm{Data}) = \frac{P(\mathrm{Data}|M_k)P(M_k)}{\sum_{k'} P(\mathrm{Data}|M_{k'})P(M_{k'})} \tag{4.1}$$

---

[1] Note that due to positivity constraints some of the production amplitudes are real or even zero (cf. section 3.1.3).

Here the *posterior* model probability $P(M_k|\text{Data})$ is a measure for the Bayesian probability of a particular model hypothesis M_k that can be assigned after the specific sample (denoted simply by "Data" in the formulas) has been observed. The sum runs over all models under consideration. Under the premise of equal a-priory model probabilities $P(M_k) = \text{const}$, it is sufficient to compare the *marginal likelihoods* $P(\text{Data}|M_k)$ for different models in order to get a measure for the model quality. It is obtained from the well known likelihood $\mathscr{L} = P(\text{Data}|A^k, M_k)$ (compare equation 3.18) by integrating over the parameter space of the model:

$$P(\text{Data}|M_k) = \int \underbrace{P(\text{Data}|A^k, M_k)}_{=\mathscr{L}} P(A^k|M_k) dA^k \tag{4.2}$$

This marginal likelihood is the probability of observing a specific data set under the assumption that the observed data has been generated by the model M_k without having precise knowledge of the values of the model parameters. It is also called the *evidence* for a model. $P(A^k|M_k)$ is the *prior probability density* of the parameters A^k in the model M_k which explicitly includes any kind of pre-knowledge or boundary conditions on the A^k.

Equation 4.2 provides a measure of the quality of a model which is qualitatively different from the maximum likelihood value $P(\text{Data}|A^k_{\text{ML}}, M_k) = \max$, which is the optimal *point estimate* for the parameters of model M_k but does not make any statement on the model as a whole. The marginal likelihood, though, takes into account model complexity and provides systematic means of avoiding the over-fitting problem.

However, there are some difficulties in the direct application of equation 4.2:

1. The marginalization of the likelihood, i.e. calculation of the integral in equation 4.2 is usually a non-trivial task, especially for high-dimensional problems.

2. In the standard formulation of the amplitude analysis inference problem only the log-likelihood is available (c. f. equation 3.21). Indeed the likelihood itself quickly becomes numerically unstable if there are complex models and a lot of data points.

In the following section a formulation of the evidence will be presented that can cope with these difficulties.

4.1.1 The Occam-Factor Approximation

In the limit of a large data sample Laplace's method can be used to approximate the integral in 4.2 by the value of the integrand at its maximum [148, 146].

$$P(\text{Data}|M_k) \approx P(\text{Data}|A^k_{\text{ML}}, M_k) \cdot \underbrace{P(A^k_{\text{ML}}|M_k) \cdot \sqrt{(2\pi)^d |\mathbf{C}_{A|D}|}}_{\text{Occam factor}} \tag{4.3}$$

where $\mathbf{C}_{A|D}$ is the covariance matrix of the maximum likelihood estimate.

An intuitive interpretation of this formula is given by MacKay [146] as he notes that for a constant prior probability $P(A^k|M_k) = \text{const} = \frac{1}{V^k_A}$ the so called *Occam factor*

$$P(A^k|M_k) \cdot \sqrt{(2\pi)^d |\mathbf{C}_{A|D}|} = \frac{\sqrt{(2\pi)^d |\mathbf{C}_{A^k|D}|}}{V_{A^k}} = \frac{V_{A^k|D}}{V_{A^k}}$$

is simply the ratio of the volumes in parameter space that are available before and after taking the data into account. In other words the Occam factor is the factor by which the allowed parameter space shrinks on observation of the data set. Over-fitting in this picture corresponds to an overly strong shrinkage, i. e. error bars that are too small to be justified by the data (in comparison to another, simpler model). Also the case of strong correlations between two parameters is dealt with since the allowed parameter volume shrinks with stronger correlation even if the individual errors are large.
Bringing equation 4.3 into logarithmic form yields an expression where the maximum log-likelihood is corrected by two terms accounting for the model complexity:

$$\ln P(\mathrm{Data}|M_k) \approx \ln P(\mathrm{Data}|A^k_{\mathrm{ML}}, M_k) + \ln P(A^k|M_k) + \ln\sqrt{(2\pi)^d|\mathbf{C}_{A|D}|} \tag{4.4}$$

The last term penalizes models that require excessive correlations between their parameters while the log–prior-probability $\ln P(A^k|M_k)$ puts a penalty on models containing a large number of parameters. It is thus obvious that the choice of prior distribution is a crucial ingredient to complete the formalism.

4.1.2 Prior Probabilities

In the majority of practical inference problems the selection of a *reference prior* is attempted [149] which avoids any bias towards a certain outcome. As such the reference prior can be thought of as “merely a formal way of expressing ignorance”[150] (also see [151] for a critical analysis and comparison to conventional “frequentist’s” approach to statistics). The simplest “non-informative” prior distributions are those which assign a constant probability density over a closed set of parameter values. For the problem of partial-wave fitting such a prior probability distribution can be constructed at least approximately by the following arguments.
For a constant prior probability density the volume of the allowed parameter space V^k_A acts as the normalization so that the prior can be written as

$$P(A^k|M_k) = \frac{1}{V^k_A} \tag{4.5}$$

Since the total intensity in one n-body-mass bin is fixed, this volume can indeed be specified. By construction (see equation 3.26) the number of reconstructed events (including acceptance effects) is

$$N_{\mathrm{events}} = \sum_{\alpha,\beta} T_\alpha T^*_\beta IA_{\alpha\beta} \tag{4.6}$$

which acts as a constraint on the production amplitudes. Equation 4.6 defines a subset of the parameter space outside of which the prior can safely be set to zero. Due to the mixed terms in equation 4.6 the volume in parameter space of this subset is not immediately obvious though. A simplified choice for the prior can still be constructed by assuming that the off-diagonal elements of the spin-density matrix are small. Thus neglecting interference effects

$$\sum_\alpha |T_\alpha|^2 \approx N_{\mathrm{events}} \tag{4.7}$$

This formula describes a d-dimensional sphere with radius $R = \sqrt{N_{\mathrm{events}}}$. The volume of such a sphere is given by

$$V^k_A = S_{m-1} = m\frac{\pi^{m/2}}{\Gamma\left(\frac{d}{2}+1\right)}R^{d-1}$$

The above expression is conveniently evaluated in its logarithmic form:

$$\ln V_A^k = \ln d + \frac{d}{2}\ln\pi + \frac{1}{2}(d-1)\ln N_{\text{events}} - \ln\Gamma\left(\frac{d}{2}+1\right)$$

where for the logarithm of the Γ-function good approximations based on Stirling's formula are available.

There is one last problem with the formulation of the evidence so far. The choice of the prior probability density as a constant over the whole parameter space neglects the assumption (implicit in specifying a finite waveset) that all the selected waves must make significant contributions to the total intensity. Unfortunately the above formulation of the Occam factor cannot take this into account, because for a wave with an intensity close to 0 but for which the fit predicts a large error the contribution to the Occam factor will not disfavor the inclusion of this wave.

The most general way to deal with this issue is to modify the prior distribution in 4.2 such that the implicit assumption of non-vanishing waves is realized. In the context of partial-wave fitting the resulting distribution is nontrivial in the sense that only those parts of the parameter space have a reduced prior probability which correspond to both real and imaginary part of an amplitude to be close to zero.

Instead of explicitly specifying such a prior and evaluating the evidence integral 4.2 here a more practical way is proposed. For each wave the significance S_i is the probability of the intensity of this wave to be more than 5σ larger than zero. Assuming real and imaginary parts of the production amplitudes have Gaussian errors, then the intensity follows a Rice-distribution. For simplicity this has been approximated again with a Gaussian.

$$S_\alpha = \int\limits_{5\sigma_\alpha}^{\infty} \frac{1}{\sqrt{2\pi}} \exp\left[-\frac{(x-|T_\alpha|^2)}{2\sigma_\alpha^2}\right] dx \tag{4.8}$$

The error that is being made by the Gaussian assumption depends on the actual significance as can be seen in Figure 4.1. The Gaussian approximation will slightly over-suppress small values of intensity. Note that with the lower bound of the integral at $5\sigma_\alpha$ a parameter has been introduced into the prior which in principle allows to tune the degree to which small partial waves should be suppressed. The sum of all logarithmic significances is added to the log–evidence of formula 4.4 in order get the the final form for the Occam factor formula which approximates the evidence for a given partial-wave model as:

$$\ln P(\text{Data}|M_k) \approx \ln P(\text{Data}|A_{\text{ML}}^k, M_k) + \ln\sqrt{(2\pi)^m|\mathbf{C}_{A|D}|} - \ln V_A^k + \sum_\alpha \ln S_\alpha \tag{4.9}$$

It is in this form that the evidence has been coded in the software. For the evaluation of a complete set of partial-wave fits over the whole n-body-mass range the evidences of the fits in the individual mass bins are added up.

Figure 4.2 shows the distribution of evidences for a large number of fits as a function of the respective number of waves in the waveset. Wavesets with more than about 34 waves are penalized in the evidence, suggesting that this is the statistically supportable number of waves for the given data set. The set of fits has been generated with the genetic algorithm described in the following section.

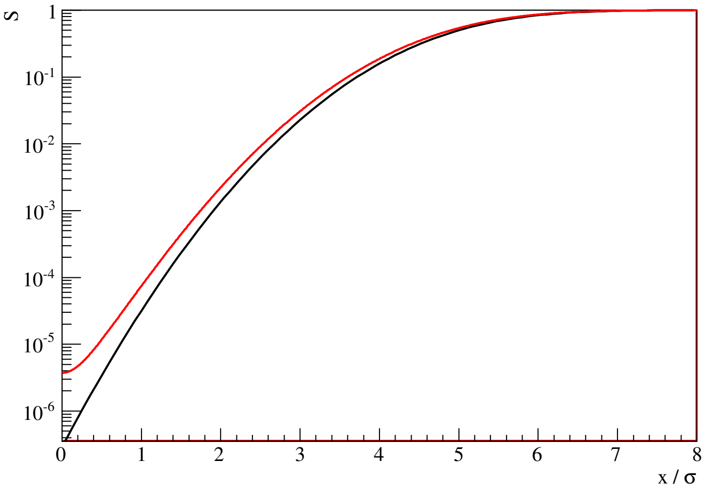

Figure 4.1: Comparison of 5σ significance as a function of the measured value normalized to the measured error in the Gaussian approximation (black) to the correct case of the Rice-Distribution (red).

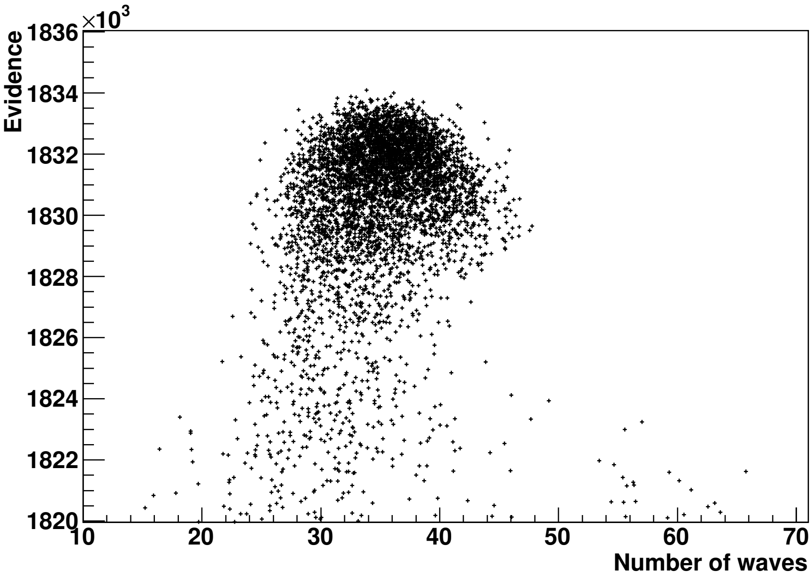

Figure 4.2: Evidences for models with different wavesets. Each entry in the plot corresponds to one model that has been fitted to the data. There is a clear maximum in the evidences around 34 waves. Larger wavesets tend to be penalized in the evidence. The collection of fits was produced in a run of the genetic algorithm described in section 4.2.

4.1.3 Quantitative Interpretation of Evidence

The quantitative interpretation of the evidence unfortunately is not as intuitive as the confidence levels that can be defined for a point measurement. Although, when all involved probability densities are properly normalized, the evidence can in principle be interpreted in terms of a probability, the resulting values usually do not compare well with standard measures. Also note, that in the case discussed here already in the definition of the log-likelihood (equation 3.21) terms which do not depend on the model parameters have been dropped in equation 3.20.

In order to compare two models with each other Kass and Raftery [148] define the Bayes-Factor as the ratio of marginal likelihoods.

$$B_{12} = \frac{P(\text{Data}|M_1)}{P(\text{Data}|M_2)}$$

In the equivalent logarithmic form the difference between the log-evidences has to be taken and all common, model-independent terms cancel.

The following table[148] serves as a rough guideline for the interpretation of the values:

$2\ln B_{12}$	B_{12}	Evidence
0 to 2	1 to 3	Not worth mentioning
2 to 6	3 to 20	Positive
6 to 10	20 to 150	Stong
> 10	> 150	Very strong

Table 4.1: Interpretation of the Bayes Factor [148].

Suggestions for future research:

- *A more rigorous formulation of the prior probability density of the production amplitudes*
- *The marginalization in equation 4.2 can also be done using monte carlo integration methods. This would allow a much more detailed study of the shape of the likelihood function and provide potentially very valuable information on possible correlations of the model parameters.*

4.2 Waveset Evolution

With the tools developed in the previous section it is possible to compare different models, i. e. wavesets, by evaluating the evidence $P(\text{Data}|M_k)$ for each. Equation (4.9) tells how to weigh them against each other. In the following an algorithm for automatic waveset optimization is developed on this basis.

4.2.1 The Genetic Optimization Algorithm

Actually there is a nice analogy between the waveset and a chromosome in a living cell. In this analogy each possible wave ψ_α corresponds to a gene on the chromosome. This analogy suggests the usage of *genetic algorithms* [152] to implement a search for good wavesets. Genetic algorithms are a well studied class of optimization procedures [153, 154, 155] which are especially useful in high-dimensional problems. Inspired by biological evolution they use competitive selection and genetic mutation as a template to implement efficient search and optimization schemes. The basic outline of such an algorithm applied to the search for an optimal waveset is illustrated in Figure 4.3 and can be summarized as follows

1. Specify a *pool* of possible waves from which to choose. This defines and limits the space of possible models in which the algorithm operates. A partial-wave amplitude that is not offered here will not become a part of the final model.
2. Randomly generate a collection of wavesets — the first *generation* — by drawing subsets from the pool.
3. Evaluate the *fitness* of each model:
   (a) For each of the wavesets perform a fixed n-body-mass fit.
   (b) Evaluate each fit by calculating the evidence as defined in equation 4.9.
   (c) Rank the wavesets according to their evidence.
4. Reproduction: Create a new generation out of the previous wavesets such that the highest ranking waves are preferred. Apply cross-over and mutation to explore the space of possible wavesets.
5. Go to step 2 and repeat until a suitable stopping condition is reached.

In the following these individual steps are explained in some more detail.

The Pool of Amplitudes

Ideally the pool of available amplitudes contains all possible partial waves up to high spins. In practice the allowed spin states have to be limited, relying on the convergence of the partial-wave expansion. In the present analysis the majority of partial amplitudes that have been included in the pool only use $\ell \in \{0,1,2\}$ at each node in the decay tree. Only the isobar decays mentioned in section 3.2.2 have been used and often only the most prominent decay mode (such as $a_2(1320) \to \pi\rho$) has been allowed.
For the analysis of the low-t' 5π final state a pool of 284 partial waves has been used. A complete list is given in appendix B. After some tests “by hand” with selected waves have not yielded significant intensities for $M = 1$ amplitudes, as would be expected for the low-t' data set (see section 2.2.2 only waves with $M = 0$ have been included in the pool. Assuming a strong dominance of Pomeron exchange most amplitudes have positive reflectivity. Negative reflectivity has only been allowed for partial waves that by parity conservation cannot be generated without a spin-flip in pomeron exchange processes (c. f. equation 3.1).

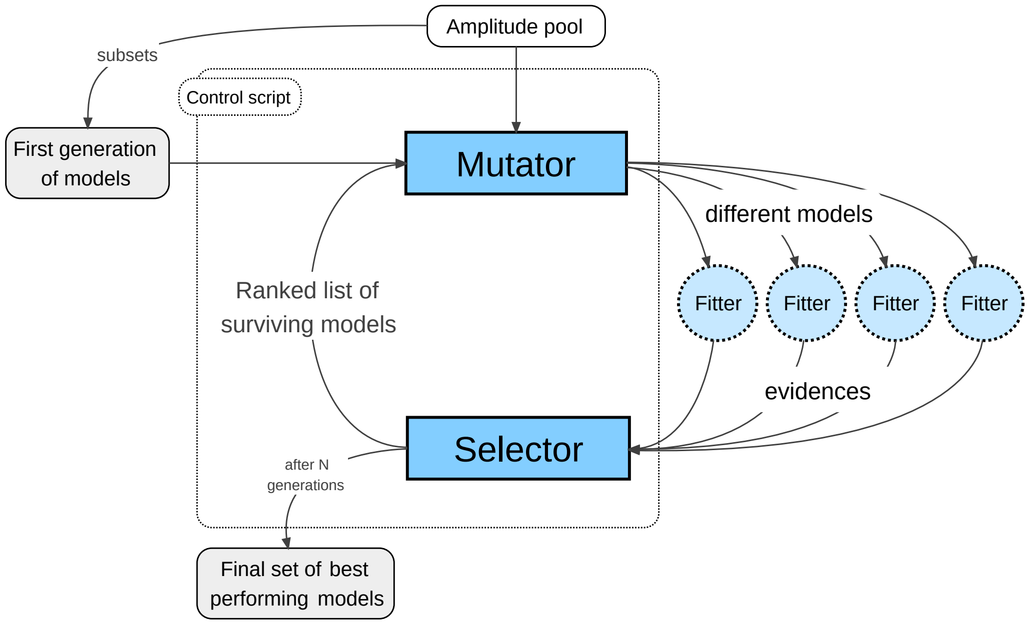

Figure 4.3: Waveset evolution algorithm. For details see text.

The First Generation

From the pool of partial amplitudes a first generation of wavesets is created. Since the algorithm is free to determine the appropriate number of free parameters in the model on its own, important starting parameters which are used in this step are the average number of waves per waveset and the spread of the waveset size.

Two different starting scenarios have been tried out. In one case all initial wavesets have been generated with a low average number of waves per waveset of $\bar{N} \approx 10$ and a relatively small spread which results in a collection of wavesets with $N \in [3,20]$.

In a second setup more diverse starting generation has been created using the result for the expected number of waves from the previous run to set $\overline{N} = 35$ and generate wavesets with very different sizes $N \in [10,70]$. This second scenario was also used for the final run of the algorithm which yielded the solution presented below.

For both scenarios the population size was 50 individuals.

In order to provide a good anchor wave for all fits, the amplitude

$$1^{-}2^{-+}0^{+} \quad \pi^{-} \begin{bmatrix} 0 \\ 2 \end{bmatrix} f_2(1270) \rightarrow \pi^{\mp}[1]a_1(1269) \rightarrow \pi^{\pm}[0]\rho(770)$$

has been included in every initial model. It has also been protected from being removed from a model in the course of the optimization.
Note that it is always possible to restart the genetic search using a (possibly modified) generation from an earlier evolution run.

Fitness Evaluation

For each waveset fixed n-body-mass fits are performed in all mass bins. The goodness of each model is evaluated through the evidence as given by equation 4.9 summed up over all mass bins. Consistency between mass bins is required only insofar as the same waveset is fitted over the whole mass range. In particular at this point no assumptions on the shape of the partial-wave amplitudes as a function of the n-body-mass, other than the requirement of significant intensity (equation 4.8) are being applied.
There are several, widely used methods how to implement the essential element of competition into the genetic algorithm (for a review see [156] and references therein). In the *proportionate reproduction* scheme the probability for an individual — viz. a waveset — to reproduce is determined by its fitness. The scheme of *ranking selection* is a slight variation of proportionate production in the sense that the fitness is not used directly to determine the reproduction probability but it is used to rank the individuals on a scale from zero to one.
In the current application a linear ranking scheme has been used in order to determine the probability of reproduction of each waveset. The wavesets are assigned a rank R_i according to their evidence with the best fit having the highest rank. Only the best $N_{\text{survivors}}$ are allowed to reproduce. In order to exploit the available information at each step in the process in an optimal way all previous fits are included when the ranking is calculated. This means individuals from “old” generations are not dying out but are allowed to further reproduce if they perform well.

Reproduction

For the reproduction step two wavesets are chosen according to the following probability distribution:

$$P(i) = \frac{1}{N_{\text{survivors}}} \left(2 - s + \frac{2(s-1) \cdot R_i}{N_{\text{survivors}}} \right) \tag{4.10}$$

where $s \in [1,2]$ is called the *selective pressure*. It can easily be seen that a selective pressure $s = 1$ corresponds to equal probability (no competition) while for $s > 1$ the reproduction probability is proportional to the rank R_i of the model and the slope of the proportionality grows with s. This linear ranking avoids the dominance of a few very well performing individuals at the beginning of the evolution, which would take over the whole population if the evidence would be used directly as a measure for the reproduction probability.
A new descendant waveset is built from the two ancestors according to the following rules:

- Although in principle from each pair of ancestors a pair of descendants can be constructed only one of them is kept in the program that has been used here in order to simplify the technical implementation of the algorithm.

- It is possible to specify a range of waves that will not be modified and just copied to the descendant from the first ancestor. This allows some manual control over the resulting wavesets and is important to keep the anchor wave in the waveset (cf. section 3.1.3).

- With an adjustable probability p_{x} the descendant can contain components from both ancestors. This is implemented using the scheme of *cross-over*, a concept that is modeled according to how genes are transmitted and mixed in nature. In a cross-over operation a sequence of component waves in one ancestor waveset is selected randomly (position and entries in the wavelist, the wavelists are aligned at the first entries) and swapped for the corresponding sequence in the second ancestor as illustrated in Figure 4.4. Care has to be taken, when the two models have a different length. In that case, segment to be crossed over is shortened according to the length of the smaller model. Further care has to be taken to ensure that every partial amplitude occurs only once per waveset.

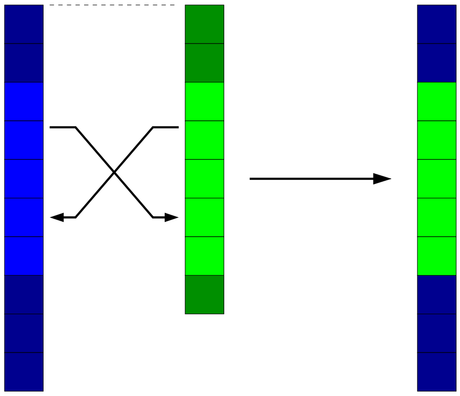

Figure 4.4: Illustration of the cross-over operation. In both models (blue and green) the same randomly chosen sequence is marked (light colors), “cut out” and exchanged. The resulting descendant model contains a mixture of the blue model and the green model.

- *Mutation*: with adjustable probability p_{m} a number of waves can be added, dropped or exchanged from the waveset. This step ensures that all possible waves are tried out during the evolutionary search.

In summary the algorithm has the following meta-parameters:

Name	variable	range
Population size	N_{pop}	> 1
Number of generations to run	N_{Gen}	> 1
Number of survivors	$N_{\mathrm{survivors}}$	$N_{\mathrm{survivors}} \in [2, N]$
Number of fixed waves	N_{fix}	≥ 0
Selective pressure	s	$s \in [1, 2]$
Cross-over probability	p_{x}	$p_{\mathrm{x}} \in [0, 1]$
Mutation probability	p_{m}	$p_{\mathrm{m}} \in [0, 1]$
Exchanged waves	N_{ex}	$N_{\mathrm{ex}} \in [0, N - N_{\mathrm{fix}}]$
Number of waves to add/drop	N_{add}	$N_{\mathrm{add}} \geq -N + 1$

Implementation

The genetic waveset optimization has been implemented as a set of small C++ programs and a control script as a part of the `rootpwa` framework. A flow-diagram of the algorithm is given

in Figure 4.3. The generation of new models from a ranked list of ancestors and a wave pool according to the rules described above is implemented in the `mutator` program. The evaluation of the fitting results and the ranking is implemented in a program called `selector`. This tool also takes care about errors that might occur during the process, such as failed fits etc. The complete algorithm is tied together and controlled through a bash-script `wavegenetics.sh`.
The computational effort of the algorithm is considerable, since in order to explore the space of models a large number of fits has to be performed. The decay amplitudes for all partial waves in the pool as well as the phase-space integrals (with and without acceptance correction) can be pre-calculated once and stored on a server for reuse in the fitting program. The algorithm can be parallelized almost trivially by running the independent fits (different wavesets and independent n-body-mass bins) of one generation in parallel. For the evaluation of a generation all results have to be collected however, and the algorithm has to wait until all fits have finished. It thus is important to use an efficient load-balancing scheduling algorithm to make the best use of the available computing resources. In the implementation used for the analysis presented in this thesis, the Sun$^{\mathrm{TM}}$Grid Engine [157] framework has been used to parallelize the fitting part of the algorithm on the Linux computing farm at TUM E18. Since the details of the parallelization very much depend on the particular infrastructure that is being used, I will not go into more detail here. The interested reader is referred to the source-code for further details, which is available through the `rootpwa` repository [135].

4.2.2 Performance of 5π Waveset Evolution

The algorithm described above has been used to find a waveset that describes the data while at the same time minimizes the number of waves needed. The meta-parameters used to run the genetic search are listed in table 4.2.

Name	variable	value
Population size	N_{pop}	50
Number of generations to run	N_{Gen}	100
Number of survivors	$N_{\mathrm{survivors}}$	50
Number of fixed waves	N_{fix}	1
Selective pressure	s	1.7
Cross-over probability	p_{x}	0.85
Mutation probability	p_{m}	1
Exchanged waves	N_{ex}	1
Number of waves to add/drop	N_{add}	$\in [-5, 5]$

Table 4.2: Meta-parameters of the evolutionary search for a 5π waveset.

A pool of 284 decay amplitudes has been used to draw from. Each generation consisted of 50 wavesets. The fixed-5-body-mass fit was done in 28 bins of (60 MeV/c^2) width. The initial wavesets have been generated randomly from the pool of waves. Only one wave, the $2^{-+}0^{+}\pi f_2(1670)$ S-wave, has been required for all wavesets as an anchor wave, and only rank 1 (full coherence) fits have been used in this analysis.
Figure 4.5 shows the evolution of the evidence as the genetic optimization proceeds through 100 generations. Although the mean evidence that is achieved for a generation is leveling off after about 15 generations, the best fit can be improved far beyond that point.

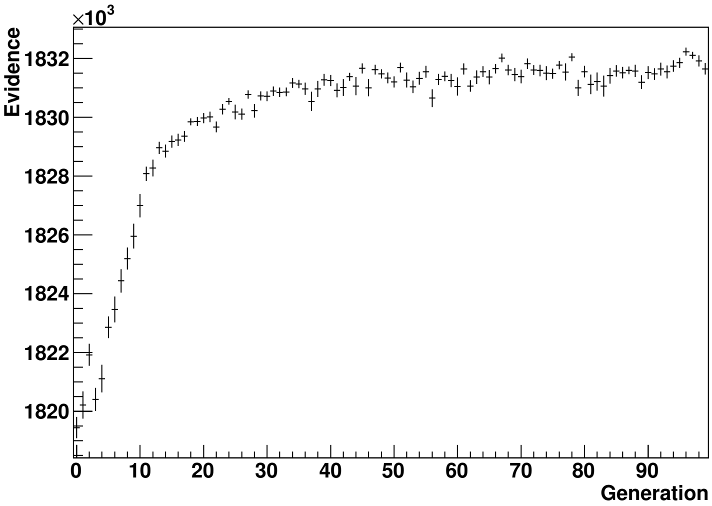

Figure 4.5: Evolution of the evidence. The mean evidence of all 50 fits per generation is shown. The error bar gives the RMS of the evidence distribution.

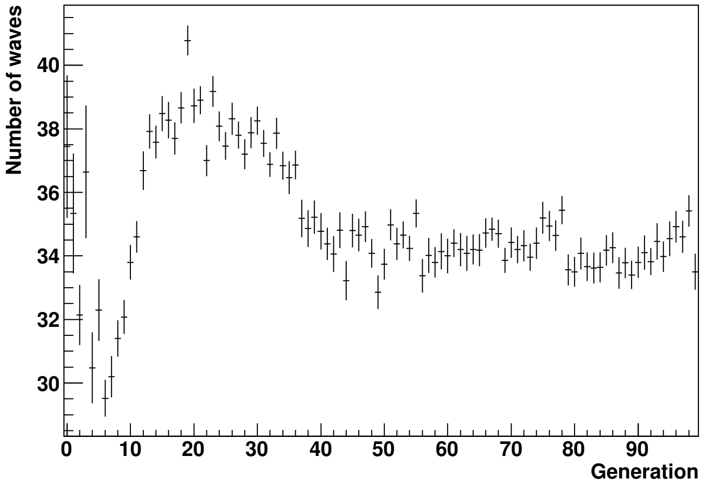

Figure 4.6: Evolution of the size of the waveset. See text for details.

Due to the penalty on the model complexity that was introduced above, the optimal number of waves can be determined by the genetic optimization. For the example presented here the initial generation contained wavesets with a wide variety of sizes from 10 to about 70 waves. Figure 4.6 shows how the mean number of components in the model evolves. The observed behavior can be interpreted in the following way. Due to the penalty on large models, wavesets with excessive size are quickly eliminated. Then the mean number of waves grows to about 40 as the algorithm discovers wavesets with good combinations of waves. Finally, as only those wavesets which contain the necessary components to describe the data survive, the algorithm can further optimize by eliminating unimportant components. Thus the mean size shrinks again and levels off at around 34 waves. This value is driven by the amount of data that is available and the definition of the significance of small waves (equation 4.8).

As a final step in the waveset selection the 20 best fits from the genetic optimization have undergone a closer examination. This corresponds to a range in log-evidence of about 1000 between the best fit and the 20th fit. Table 4.3 shows which waves have been used in those 20 models. The strong coherence of the results shows the level of convergence that the algorithm has reached. The average number of waves used in the top20 selection was 33.9.

A Final Breeding Step

Based on these results from the automatic waveset evolution it appeared that the result could possibly be improved by a dedicated combination of the best performing models. In the metaphor of biological evolution this would be a breeding intervention. Indeed the construction of a new waveset from those waves, that were used in more than half of the top20 fits (see table 4.3) allowed to increase the log-evidence once again by $2.7\cdot10^2$ units from $1.83409\cdot10^6$ to $1.83436\cdot10^6$. This waveset is presented in the next section as the final mass independent partial-wave decomposition of the diffractively produced 5π system.

The large increase in model performance that could be achieved with the breeding step indicates that the reproduction routine used could probably be improved considerably. However, care has to be taken to allow the algorithm to explore the space of possible models and to avoid a premature convergence onto a mediocre solution. How this could be realized optimally remains a question for future research.

4.3 Mini-Conclusion

In the preceding sections an algorithm has been developed that allows to implement a systematic, data-driven way of studying different truncation schemes of partial-wave expansions. The Bayesian formulation of the evidence for a given model, evaluated on the available data, allows to compare and rank different truncation schemes. This is the key for the implementation of an automatic evolution of a model that provides a reasonable balance between a good description of the data and its complexity. For complex problems such as many-body decay processes the framing of the problem in algorithmic terms provides an indispensable tool to the analyzer.

The systematic approach to the problem is seen as the biggest advantage of the proposed scheme as it provides a clear and well-founded recipe for the selection of a waveset. Furthermore the comparison of different models allows to study the systematic uncertainties which are introduced by choosing a specific truncation scheme.

However, it should be kept in mind that the approach ultimately is a statistical one which allows no conclusion on the validity of a certain class of amplitudes, such as the isobar model, other than the level to which they are able to describe the data. There may well be other, physical reasons which could lead to the adoption of a different form of the amplitudes, such as unitarity and analyticity arguments mentioned in section 3.2.2. In this case the Bayesian arguments would still be valid, however, it may be necessary to include more data sets from different processes into the considerations in order to see the virtues of a new model.

At the moment the proposed scheme is seen as a useful tool to facilitate the investigation of complex decay processes and to extract systematic uncertainties introduced by the truncation

Used in 20/20	
	1−0−+0+pi−_00_f01500=rho770_00_rho770.amp
	1−0−+0+pi−_00_f01500=sigma_0_sigma.amp
	1−0−+0+rho770_00_a11269=pi−_0_rho770.amp
	1−0−+0+rho770_22_a11269=pi−_01_rho770.amp
	1−0−+0+sigma_00_pi1300=pi−_00_sigma.amp
	1−1++0+pi−_01_rho1600=rho770_01_sigma.amp
	1−1++0+pi−_10_f01370=rho770_00_rho770.amp
	1−1++0+pi−_10_sigma=sigma_0_sigma.amp
	1−1++0+pi−_11_f11285=pi−+_11_a11269=pi+−_0_rho770.amp
	1−1++0+rho770_01_pi1300=pi−_1_rho770.amp
	1−1++0+sigma_01_a11269=pi−_0_rho770.amp
	1−1++0+sigma_01_a11269=pi−_1_sigma.amp
	1−1++0+sigma_21_a11269=pi−_0_rho770.amp
	1−1++0+sigma_22_a21320=pi−_2_rho770.amp
	1−2−+0+pi−_02_f21270=pi−+_1_a11269=pi+−_0_rho770.amp
	1−2−+0+rho770_02_a11269=pi−_0_rho770.amp
	1−2−+0+rho770_02_a21320=pi−_2_rho770.amp
	1−2−+0+rho770_20_a11269=pi−_0_rho770.amp
	1−2−+0+sigma_20_pi1800=pi−_0_sigma.amp
Used in 19/20	
	1−0−+0+rho770_11_pi1300=pi−_00_sigma.amp
	1−1++0+pi−_01_eta11600=pi−+_01_a11269=pi+−_01_rho770.amp
	1−1++0+rho770_12_a11269=pi−_0_rho770.amp
	1−1−+0−rho770_21_a11269=pi−_0_rho770.amp
Used in 17/20	
	1−1++0+rho770_01_pi1300=pi−_00_sigma.amp
Used in 16/20	
	1−2−+0+pi−_22_f21270=pi−+_11_a11269=pi+−_01_rho770.amp
Used in 15/20	
	1−3++0+sigma_21_a11269=pi−_0_rho770.amp
Used in 13/20	
	1−1++0+rho770_21_pi1300=pi−_1_rho770.amp
	1−2−+0+f21270_02_pi21670=pi−_02_f21270.amp
	1−2−+0+pi−_11_rho1600=rho770_01_sigma.amp
Used in 12/20	
	1−1++0+pi−_01_eta11600=pi−+_10_pi1300=pi+−_00_sigma.amp
Used in 11/20	
	1−1++0+sigma_10_pi1300=pi−_00_sigma.amp

Table 4.3: Usage of partial amplitudes in top20 models from the genetic waveset optimization. Components which have been used less than 10 times are omitted from the table.

of the partial-wave expansion. Future application of these ideas to similar problems should be straight forward.

Suggestions for future research:

- *Enlarge pool of available partial waves*
- *Try to evolve a waveset in each mass bin independently*
- *Optimize the genetic algorithm to achieve faster convergence by experimenting with different starting conditions, population sizes, etc.*
- *Systematic study of meta-parameters and reproduction algorithm*

Chapter 5

Results of the Partial-Wave Decomposition in Fixed 5-Body-Mass Bins

In this chapter the results of the partial-wave decomposition in individual 5-body-mass bins are presented. The waveset used to obtain these results has been constructed with the help of the genetic waveset optimization as explained in chapter 4. It contains the partial-wave amplitudes listed in tables 5.1 and 5.2. It should again be stressed that this list of waves has been determined in a systematic procedure to be the one best supported by the data. Apart from the large pool of available amplitudes (see appendix B) and the definition of the above mentioned anchor wave no assumptions have been imposed on the selection of waves. It is therefore remarkable that the waveset shows a structure as would be expected in diffractive pion dissociation at small momentum transfer, namely that the main occurring quantum numbers are

$$J^{PC}M^{\epsilon} = \{0^{-+}0^{+}, 1^{++}0^{+}, 2^{-+}0^{+}\}$$

There is also one $J^{PC}M^{\epsilon} = 3^{++}0^{+}$ wave. Higher spins might be important for the high mass tail of the spectrum, but recall that the waveset has been optimized for all mass bins together. The dominant contributions to the evidence come from the region with highest statistics around $m_X \approx 1.9\,\mathrm{GeV}/c^2$ and so with the sample-size currently available higher-spin partial waves are not well supported by the data. Recall that the model also contains an incoherently treated amplitude, which is flat in phase space and serves to accommodate structureless background events in the analysis.

There is one $J^{PC}M^{\epsilon} = 1^{-+}0^{-}$ which has survived the genetic optimization. However, it is the only wave with negative reflectivity, a fact that casts doubt on the interpretation of this partial wave as the diffractive production of a resonance. Note, that because of the different reflectivity there are no interferences of this partial wave with the rest of the waveset. This will discussed in some more detail below.

The log-evidence achieved with the rank 1 fit using this waveset is $1.83436 \cdot 10^{6}$.

$J^{PC}M^{\epsilon}$	ℓ	s	Isobar1 Isobar2	Decay Isobar2	
$0^{-+}0^{+}$	S	0	$\pi^{-}f_0(1500)$	$\rho(770)\begin{bmatrix}0\\0\end{bmatrix}\rho(770)$	•
$0^{-+}0^{+}$	S	0	$\pi^{-}f_0(1500)$	$(\pi\pi)_S\begin{bmatrix}0\\0\end{bmatrix}(\pi\pi)_S$	
$0^{-+}0^{+}$	S	0	$\rho(770)a_1(1260)$	$\pi^{-}\begin{bmatrix}0\\1\end{bmatrix}\rho(770)$	•
$0^{-+}0^{+}$	D	2	$\rho(770)a_1(1260)$	$\pi^{-}\begin{bmatrix}0\\1\end{bmatrix}\rho(770)$	
$0^{-+}0^{+}$	S	0	$(\pi\pi)_S\pi(1300)$	$\pi^{-}(\pi\pi)_S$	
$0^{-+}0^{+}$	P	1	$\rho(770)\pi(1300)$	$\pi^{-}\begin{bmatrix}0\\0\end{bmatrix}(\pi\pi)_S$	
$1^{++}0^{+}$	S	1	$\pi^{-}\rho(1600)$	$\rho(770)\begin{bmatrix}0\\1\end{bmatrix}(\pi\pi)_S$	
$1^{++}0^{+}$	P	0	$\pi^{-}f_0(1370)$	$\rho(770)\begin{bmatrix}0\\0\end{bmatrix}\rho(770)$	•
$1^{++}0^{+}$	P	0	$\pi^{-}(4\pi)_{0^{++}}$	$(\pi\pi)_S(\pi\pi)_S$	
$1^{++}0^{+}$	P	1	$\pi^{-}f_1(1285)$	$\pi^{\mp}\begin{bmatrix}1\\1\end{bmatrix}a_1(1260)$	•
$1^{++}0^{+}$	S	1	$\rho(770)\pi(1300)$	$\pi^{-}\begin{bmatrix}1\\1\end{bmatrix}\rho(770)$	•
$1^{++}0^{+}$	S	1	$\rho(770)\pi(1300)$	$\pi^{-}\begin{bmatrix}0\\0\end{bmatrix}(\pi\pi)_S$	
$1^{++}0^{+}$	D	1	$\rho(770)\pi(1300)$	$\pi^{-}\begin{bmatrix}1\\1\end{bmatrix}\rho(770)$	
$1^{++}0^{+}$	S	1	$(\pi\pi)_S a_1(1260)$	$\pi^{-}\begin{bmatrix}0\\1\end{bmatrix}\rho(770)$	
$1^{++}0^{+}$	S	1	$(\pi\pi)_S a_1(1260)$	$\pi^{-}\begin{bmatrix}1\\0\end{bmatrix}(\pi\pi)_S$	
$1^{++}0^{+}$	D	1	$(\pi\pi)_S a_1(1260)$	$\pi^{-}\begin{bmatrix}0\\1\end{bmatrix}\rho(770)$	•
$1^{++}0^{+}$	D	2	$(\pi\pi)_S a_2(1320)$	$\pi^{-}\begin{bmatrix}2\\1\end{bmatrix}\rho(770)$	
$1^{++}0^{+}$	P	0	$(\pi\pi)_S\pi(1300)$	$\pi^{-}\begin{bmatrix}0\\0\end{bmatrix}(\pi\pi)_S$	
$1^{++}0^{+}$	S	1	$\pi^{-}\eta_1(1600)$	$\pi^{\mp}\begin{bmatrix}0\\1\end{bmatrix}a_1(1260)$	
$1^{++}0^{+}$	S	1	$\pi^{-}\rho(1700)$	$\pi^{\mp}\begin{bmatrix}1\\0\end{bmatrix}\pi(1300)$	
$1^{++}0^{+}$	P	2	$\rho(770)a_1(1260)$	$\pi^{-}\begin{bmatrix}0\\1\end{bmatrix}\rho(770)$	

• waves used in mass-dependent fit.

Table 5.1: The final waveset. $J^{PC} = 0^{-+}$ and 1^{++} components. The partial waves used in the mass-dependent fit are marked with a bullet.

5.1 Comparison of Fit Results with the Data

In order to visualize the quality to which the inferred model reproduces the data it is useful to plot the relevant kinematic distributions together with their respective model solutions. While the distributions can be plotted directly from the original data, in order to obtain the model distributions a set of pseudo-data has to be generated. Such a Monte Carlo sample, with all the decay amplitudes used in the model, is already available from the integration of the acceptance-

$J^{PC}M^{\epsilon}$	ℓ	s	Isobar1 Isobar2	Decay Isobar2	
$2^{-+}0^{+}$	S	2	$\pi^{-}f_2(1270)$	$\pi^{\mp}\begin{bmatrix}1\\1\end{bmatrix}a_1(1260)$	•
$2^{-+}0^{+}$	S	2	$\rho(770)a_1(1260)$	$\pi^{-}\begin{bmatrix}0\\1\end{bmatrix}\rho(770)$	•
$2^{-+}0^{+}$	S	2	$\rho(770)a_2(1320)$	$\pi^{-}\begin{bmatrix}2\\1\end{bmatrix}\rho(770)$	•
$2^{-+}0^{+}$	D	0	$\rho(770)a_1(1260)$	$\pi^{-}\begin{bmatrix}0\\1\end{bmatrix}\rho(770)$	•
$2^{-+}0^{+}$	D	0	$(\pi\pi)_S\pi(1800)$	$\pi^{-}\begin{bmatrix}0\\0\end{bmatrix}(\pi\pi)_S$	
$2^{-+}0^{+}$	D	2	$\pi^{-}f_2(1270)$	$\pi^{\mp}\begin{bmatrix}1\\1\end{bmatrix}a_1(1260)$	
$2^{-+}0^{+}$	S	2	$f_2(1270)\pi_2(1670)$	$\pi^{-}\begin{bmatrix}0\\2\end{bmatrix}f_2(1270)$	
$2^{-+}0^{+}$	P	1	$\pi^{-}\rho(1600)$	$\rho(770)\begin{bmatrix}0\\1\end{bmatrix}(\pi\pi)_S$	
$3^{++}0^{+}$	D	1	$(\pi\pi)_S a_1(1260)$	$\pi^{-}\begin{bmatrix}0\\1\end{bmatrix}\rho(770)$	
$1^{-+}0^{-}$	D	1	$\rho(770)a_1(1260)$	$\pi^{-}\begin{bmatrix}0\\1\end{bmatrix}\rho(770)$	
FLAT					

• waves used in mass-dependent fit.

Table 5.2: The final waveset. $J^{PC} = 2^{-+}$, 3^{++} and 1^{-+} components. The partial waves used in the mass-dependent fit are marked with a bullet.

corrected phase space integrals (equation 3.22) and can be reused for this task. For each Monte Carlo event one can calculate a *weight* w_i according to the model prediction for the differential cross section given by equation 3.13 so that

$$w_i = \sum_{\epsilon=\pm1}\sum_{r=1}^{N_r}\left|\sum_{\alpha} T^{\epsilon}_{\alpha r}\bar{\psi}^{\epsilon}_{\alpha}(\tau_i)\right|^2 + T^2_{\mathrm{FLAT}} \tag{5.1}$$

Properly weighted kinematic distributions can then be plotted easily as binned histograms, if the (arbitrary) number of Monte Carlo events is taken into account by an overall normalization factor. A comparison of data and model prediction through a set of such distributions is shown in Figures 5.1–5.7 for different 5-pion-mass ranges. In order to condense the information the plots presented here each aggregate the information of four of the $60\,\mathrm{MeV}/c^2$ mass bins in which the fits have been performed, thus integrating m_X over an interval of $240\,\mathrm{MeV}/c^2$ width. The corresponding 5-pion-mass ranges are indicated in the captions of the plots. For each range the same twelve kinematic distributions are plotted. They correspond to the angular distributions which enter into the isobar-model amplitudes and which have already been discussed in sections 3.2.1 and 3.6. In addition the invariant mass distributions of the 4, 3 and 2-pion systems are presented. The seven sets of plots cover the complete 5π-mass range from $1.36\,\mathrm{GeV}/c^2$ to $3.04\,\mathrm{GeV}/c^2$.

It should be kept in mind, that each histogram represents a projection of an 11-dimensional space onto a one-dimensional variable. Important correlations between the different variables, which are taken into account in the log-likelihood estimator, are not so easily displayed. Nevertheless, a good fit should of course reproduce the projected distributions.

5.1.1 Discussion of Kinematic Distributions

The first row of Figures 5.1–5.7 shows (a) the $\pi^-\pi^+\pi^-\pi^+$, (b) the $\pi^-\pi^+\pi^-$ and (c) the $\pi^-\pi^+$ invariant mass spectra which are quite well reproduced by the model in all mass ranges. Systematic differences show up in the $\rho(770)$ region which is slightly underestimated by the fit relative to the rest of the 2π mass distribution. This could be connected with the oversimplified parametrization of the $(\pi\pi)_{\text{S−wave}}$ that has been used as discussed in section 3.2.2.
The angular distributions are shown in the same variables that have already been discussed in the section 3.6 on acceptance corrections.
The second row shows angular distributions in the Gottfried-Jackson frame. Figure (d) shows the cosine of the Gottfried-Jackson angle θ_{GJ} of the $\pi^-\pi^+\pi^-\pi^+$ subsystem. The shape shows a clear variation in the different mass regions which indicates the origin of the 4π system from different partial waves.
The bottom two rows show distributions which have been constructed in the helicity frames of the respective isobar systems. Figures (g),(h) and (i) show the cosine of the polar angle θ_{Hel} for the cases of a 4π system decaying into $\pi^-\pi^+ + \pi^+\pi^-$, a 4π system decaying into $\pi^-\pi^+\pi^+ + \pi^-$ and a 3π system decaying into $\pi^-\pi^+ + \pi^-$ respectively. The last row of figures shows – for the same subsystems – the distributions of the azimuthal angles ϕ_{Hel}.
In those 6 angles, in particular Figures (h) and (k) the largest discrepancies of the model show up especially for $m_{5\pi} \gtrsim 2\,\text{GeV}/c^2$. The reason could be missing partial waves in this region. The model can not completely reproduce the detailed structure in ϕ^{31}_{Hel}. There seem to be contributions of higher polynomials in this angle, which would indicate the presence of higher helicity states that are not taken into account by the model. Also the $\cos\theta_{\text{Hel}}$ distribution at the edge of the acceptance are not yet completely well described. In order to check for systematic errors in the description of the 4π systems several tests have been done, such as changing the $\rho(1600)$ parametrization to a form with only one resonance, leaving the isospin symmetry relations as free parameters in the fit (c. f. 3.2.3) and completely removing the amplitudes containing $I^G(J^{PC}) = 0^+(1^{-+})$ spin exotic 4π isobars. None of these operations could improve the description of the data.
There remains the possibility that at higher 5π masses new 4π systems are being produced which in turn exhibit more complicated decays involving higher orbital angular momentum and 2 or 3-body isobars with higher spin. The genetic waveset optimization has been run integrating over all 5π mass bins and thus is dominated by those bins with most statistics. It might be worthwhile to perform a waveset optimization in each mass-bin individually. In particular, if there are contributions of multiperipheral processes (see section 2.2.2) the projections of these amplitudes onto the isobaric partial waves are expected to contain higher angular momentum components for higher masses. Alternatively one could attempt to directly fit the observed angular distributions with a multiperipheral model, rather than the diffractive excitation model used here.

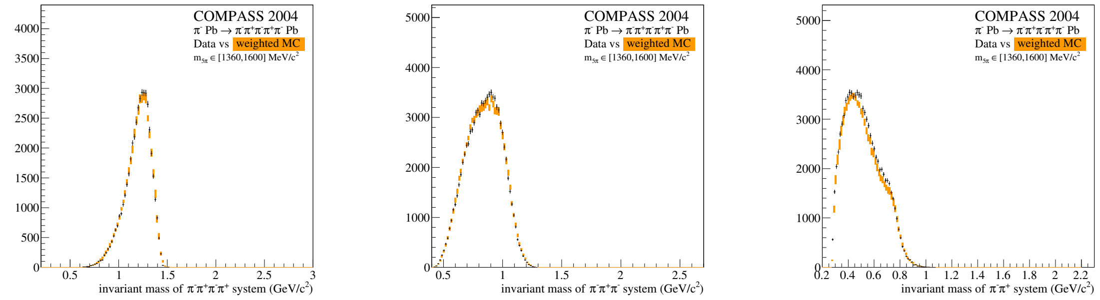

(a) 4π mass (b) 3π mass (c) 2π mass

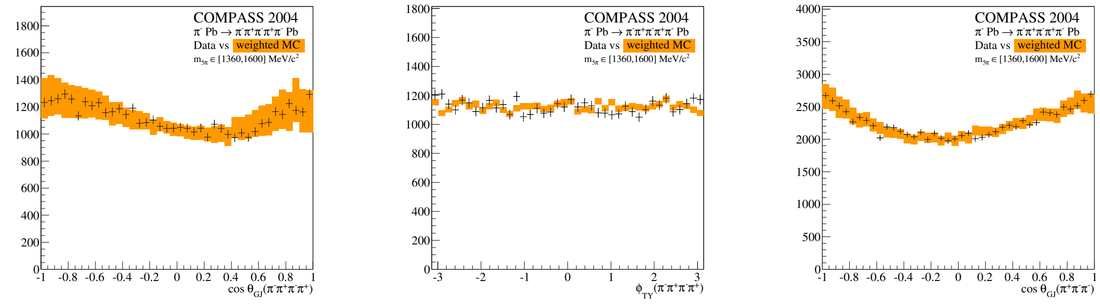

(d) $\cos\theta_{\text{GJ}}^{4\pi}$ (e) $\phi_{\text{TY}}^{4\pi}$ (f) $\cos\theta_{\text{GJ}}^{3\pi}$

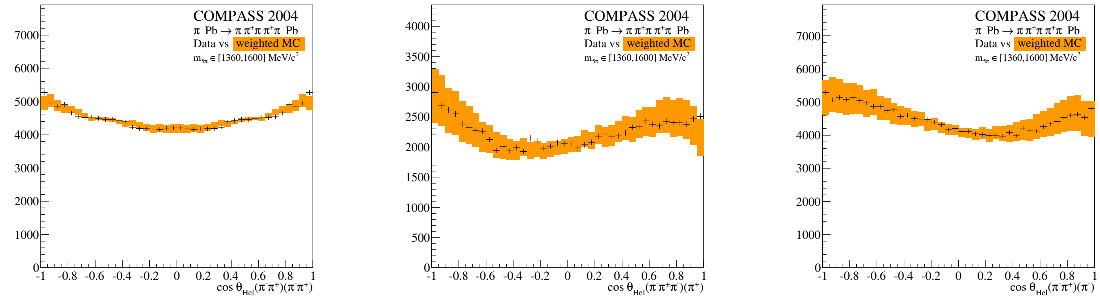

(g) $\cos\theta_{\text{Hel}}^{22}$ (h) $\cos\theta_{\text{Hel}}^{31}$ (i) $\cos\theta_{\text{Hel}}^{21}$

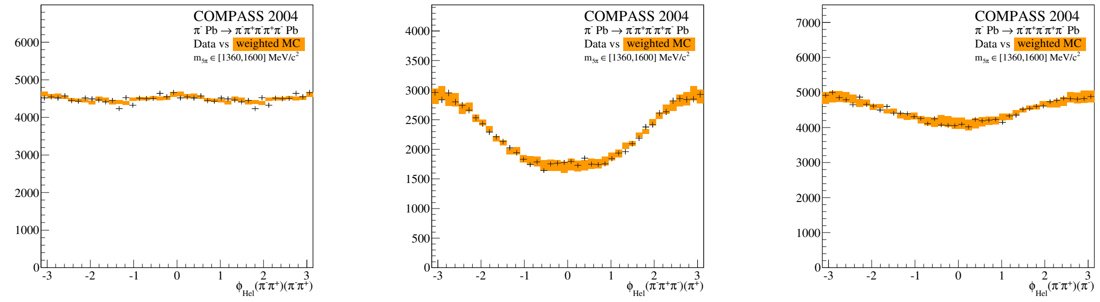

(j) ϕ_{Hel}^{31} (k) ϕ_{Hel}^{31} (l) ϕ_{Hel}^{21}

Figure 5.1: Comparison of the model (orange) with the data (black). For a detailed description of the kinematic variables shown, see text. $m_{5\pi} \in [1.36, 1.60]\,\text{GeV}/c^2$.

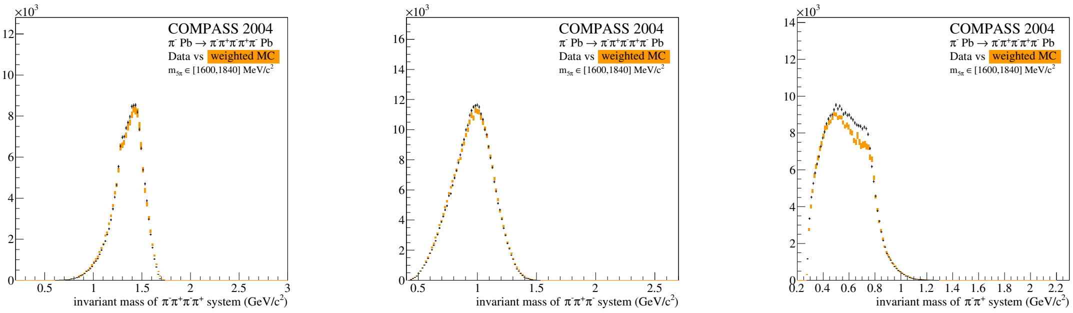

(a) 4π mass (b) 3π mass (c) 2π mass

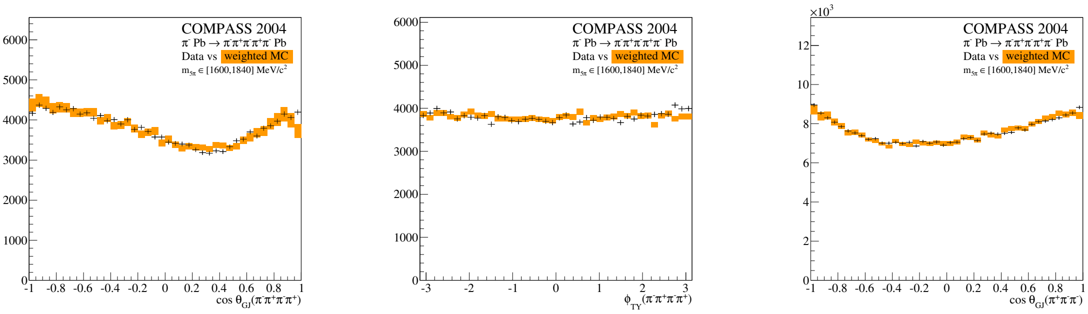

(d) $\cos\theta_{\mathrm{GJ}}^{4\pi}$ (e) $\phi_{\mathrm{TY}}^{4\pi}$ (f) $\cos\theta_{\mathrm{GJ}}^{3\pi}$

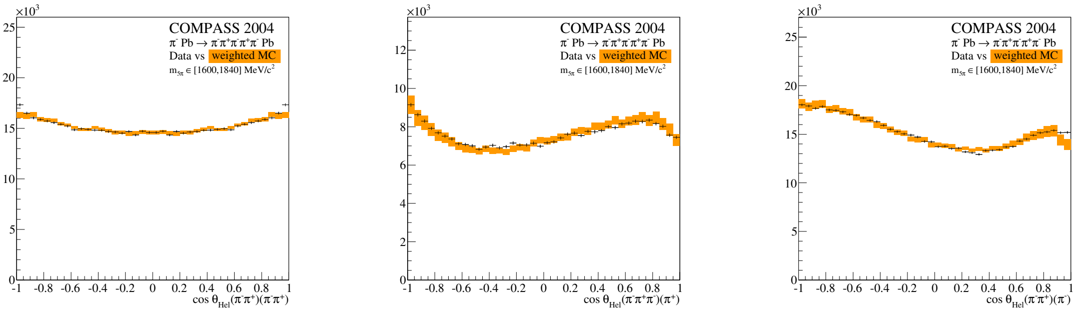

(g) $\cos\theta_{\mathrm{Hel}}^{22}$ (h) $\cos\theta_{\mathrm{Hel}}^{31}$ (i) $\cos\theta_{\mathrm{Hel}}^{21}$

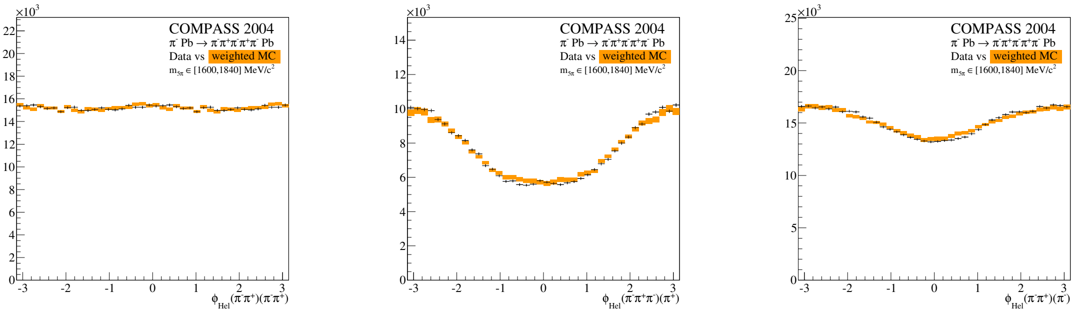

(j) ϕ_{Hel}^{22} (k) ϕ_{Hel}^{31} (l) ϕ_{Hel}^{21}

Figure 5.2: Comparison of the model (orange) with the data (black). For a detailed description of the kinematic variables shown, see text. $m_{5\pi} \in [1.60, 1.84]\,\mathrm{GeV}/c^2$

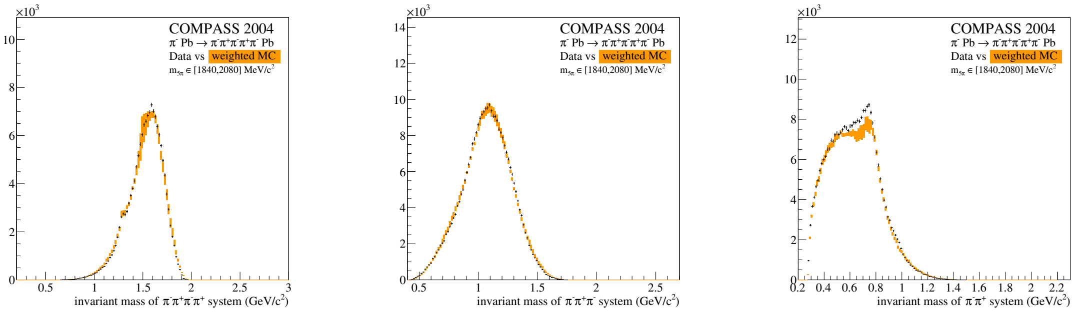

(a) 4π mass (b) 3π mass (c) 2π mass

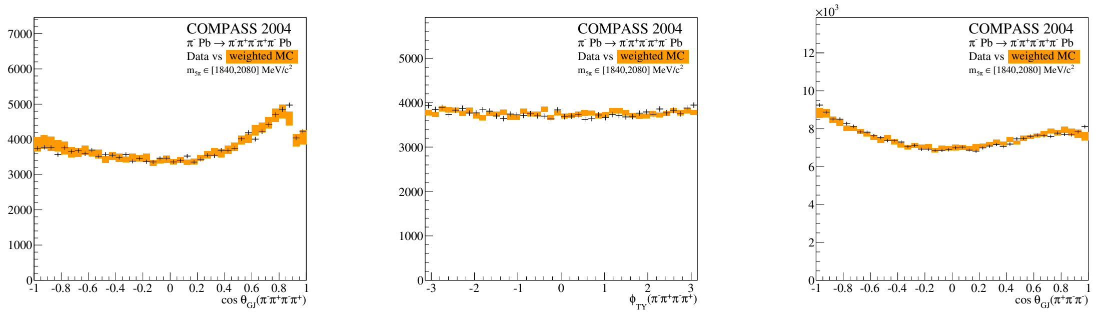

(d) $\cos\theta_{\mathrm{GJ}}^{4\pi}$ (e) $\phi_{\mathrm{TY}}^{4\pi}$ (f) $\cos\theta_{\mathrm{GJ}}^{3\pi}$

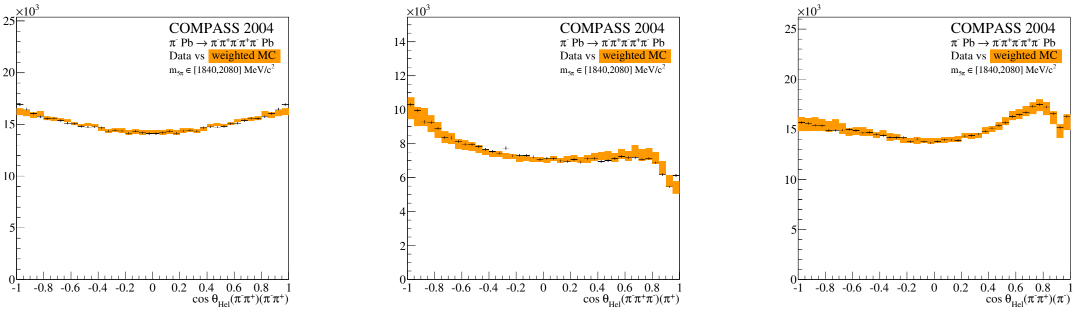

(g) $\cos\theta_{\mathrm{Hel}}^{22}$ (h) $\cos\theta_{\mathrm{Hel}}^{31}$ (i) $\cos\theta_{\mathrm{Hel}}^{21}$

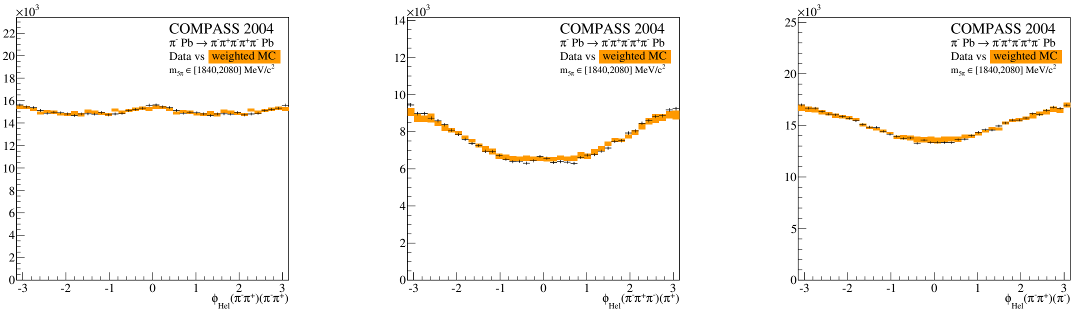

(j) ϕ_{Hel}^{22} (k) ϕ_{Hel}^{31} (l) ϕ_{Hel}^{21}

Figure 5.3: Comparison of the model (orange) with the data (black). For a detailed description of the kinematic variables shown, see text. $m_{5\pi} \in [1.84, 2.08]\,\mathrm{GeV}/c^2$

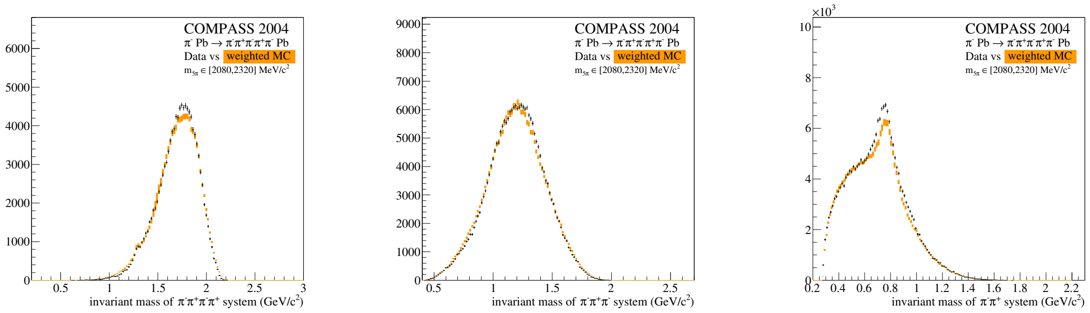

(a) 4π mass

(b) 3π mass

(c) 2π mass

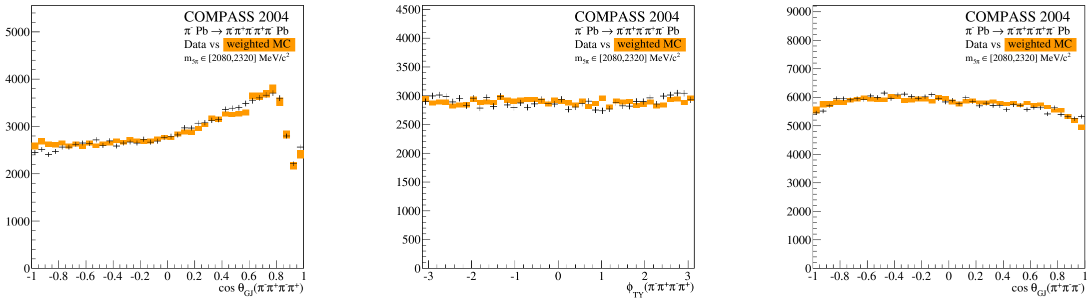

(d) $\cos\theta_{\mathrm{GJ}}^{4\pi}$

(e) $\phi_{\mathrm{TY}}^{4\pi}$

(f) $\cos\theta_{\mathrm{GJ}}^{3\pi}$

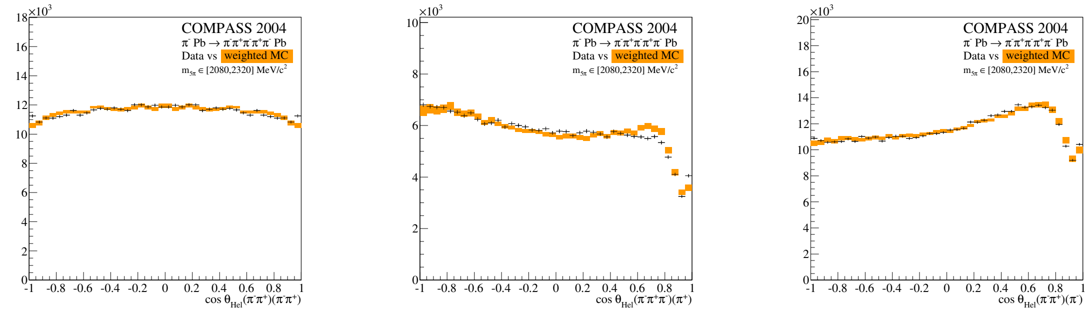

(g) $\cos\theta_{\mathrm{Hel}}^{22}$

(h) $\cos\theta_{\mathrm{Hel}}^{31}$

(i) $\cos\theta_{\mathrm{Hel}}^{21}$

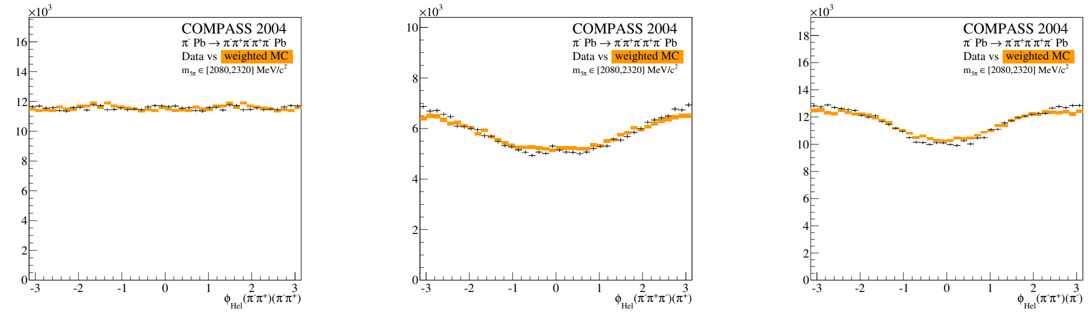

(j) ϕ_{Hel}^{22}

(k) ϕ_{Hel}^{31}

(l) ϕ_{Hel}^{21}

Figure 5.4: Comparison of the model (orange) with the data (black). For a detailed description of the kinematic variables shown, see text. $m_{5\pi} \in [2.08, 2.32]\,\mathrm{GeV}/c^2$

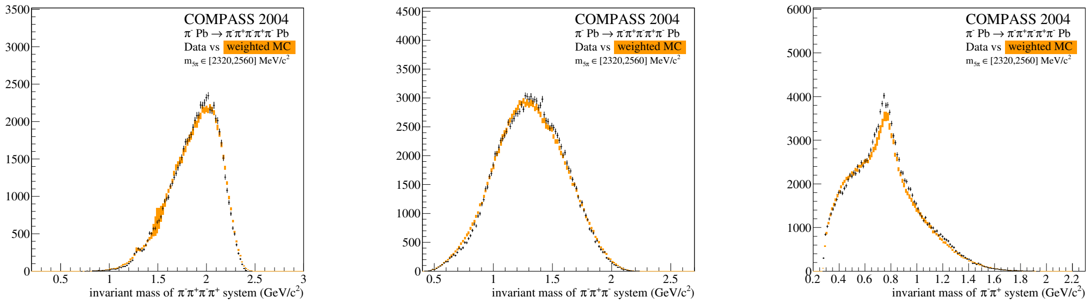

(a) 4π mass (b) 3π mass (c) 2π mass

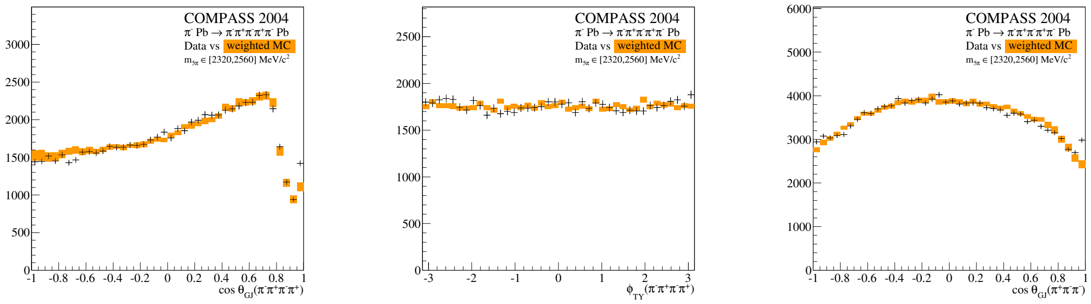

(d) $\cos\theta_{\mathrm{GJ}}^{4\pi}$ (e) $\phi_{\mathrm{TY}}^{4\pi}$ (f) $\cos\theta_{\mathrm{GJ}}^{3\pi}$

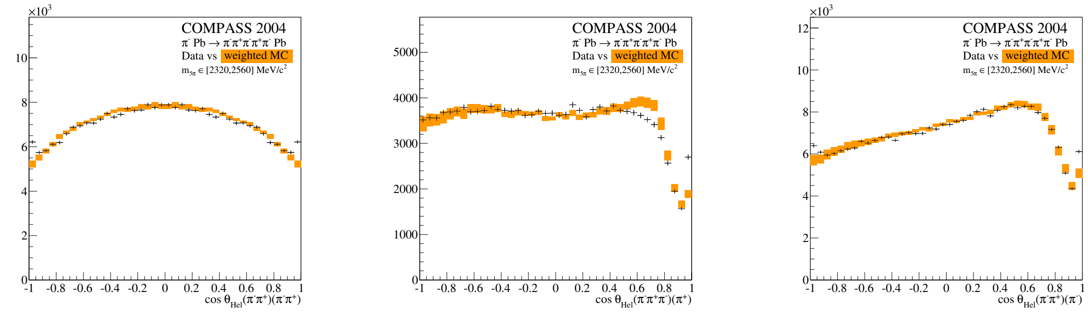

(g) $\cos\theta_{\mathrm{Hel}}^{22}$ (h) $\cos\theta_{\mathrm{Hel}}^{31}$ (i) $\cos\theta_{\mathrm{Hel}}^{21}$

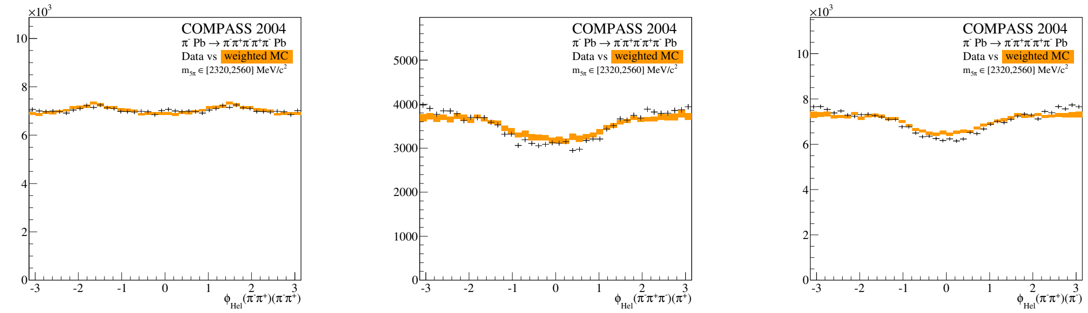

(j) ϕ_{Hel}^{22} (k) ϕ_{Hel}^{31} (l) ϕ_{Hel}^{21}

Figure 5.5: Comparison of the model (orange) with the data (black). For a detailed description of the kinematic variables shown, see text. $m_{5\pi} \in [2.32, 2.56]\,\mathrm{GeV}/c^2$

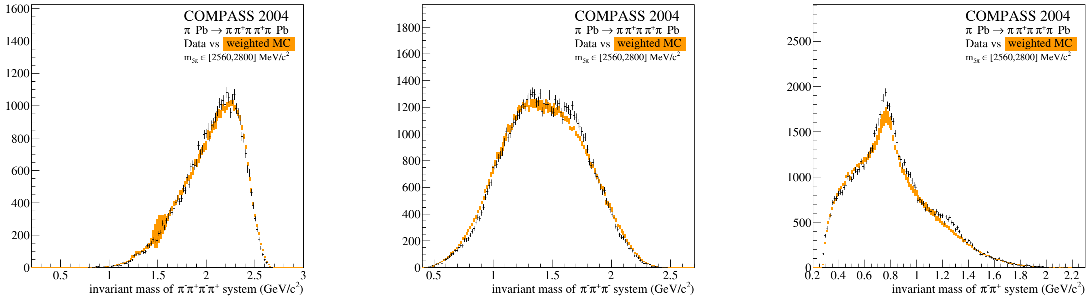

(a) 4π mass (b) 3π mass (c) 2π mass

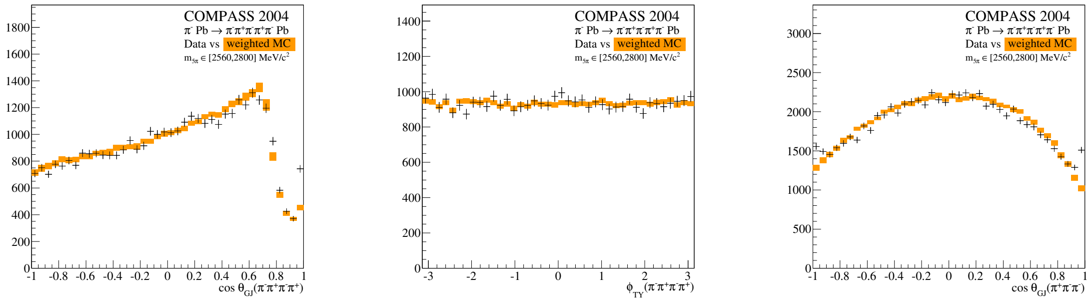

(d) $\cos\theta^{4\pi}_{\mathrm{GJ}}$ (e) $\phi^{4\pi}_{\mathrm{TY}}$ (f) $\cos\theta^{3\pi}_{\mathrm{GJ}}$

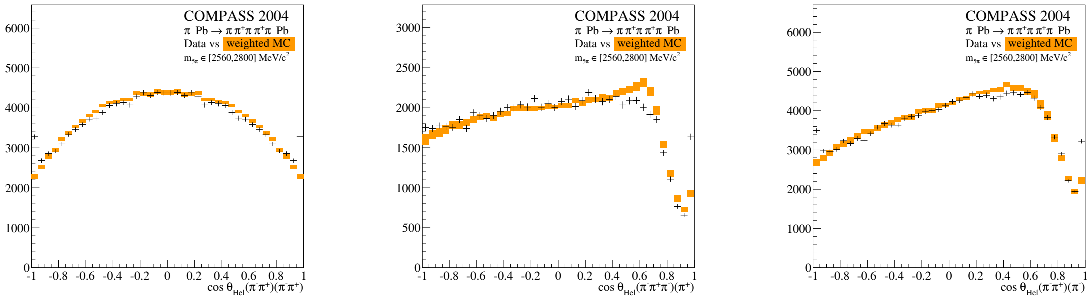

(g) $\cos\theta^{22}_{\mathrm{Hel}}$ (h) $\cos\theta^{31}_{\mathrm{Hel}}$ (i) $\cos\theta^{21}_{\mathrm{Hel}}$

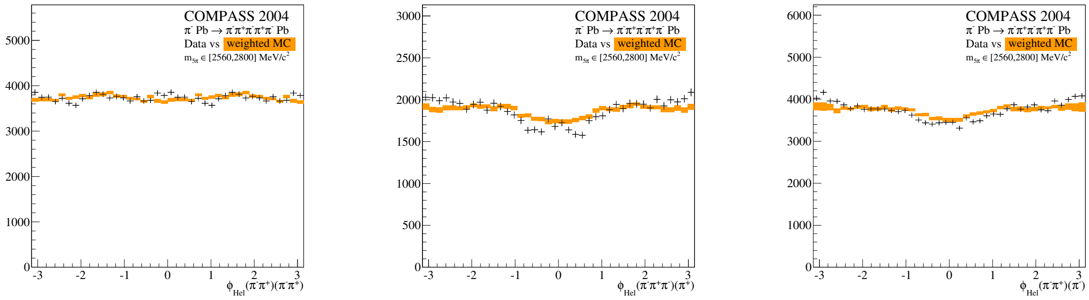

(j) ϕ^{22}_{Hel} (k) ϕ^{31}_{Hel} (l) ϕ^{21}_{Hel}

Figure 5.6: Comparison of the model (orange) with the data (black). For a detailed description of the kinematic variables shown, see text. $m_{5\pi} \in [2.56, 2.80]\,\mathrm{GeV}/c^2$

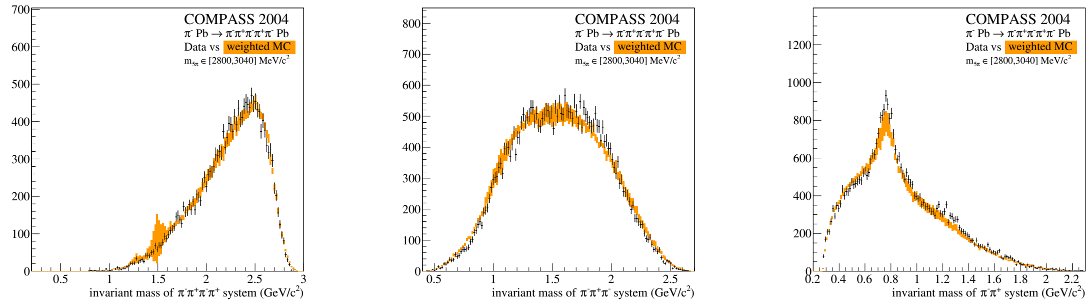

(a) 4π mass (b) 3π mass (c) 2π mass

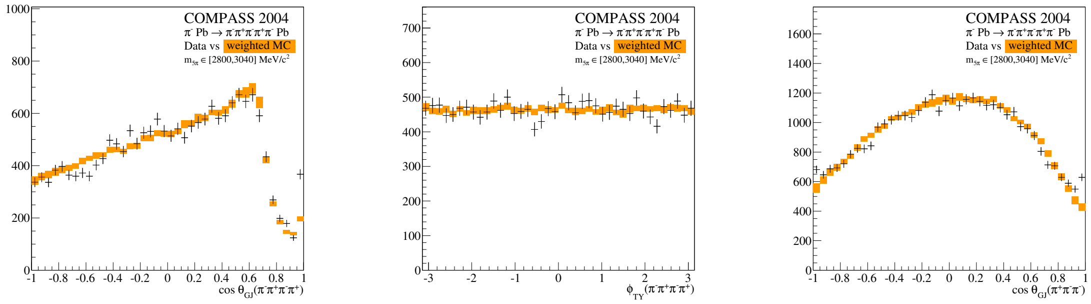

(d) $\cos\theta_{\mathrm{GJ}}^{4\pi}$ (e) $\phi_{\mathrm{TY}}^{4\pi}$ (f) $\cos\theta_{\mathrm{GJ}}^{3\pi}$

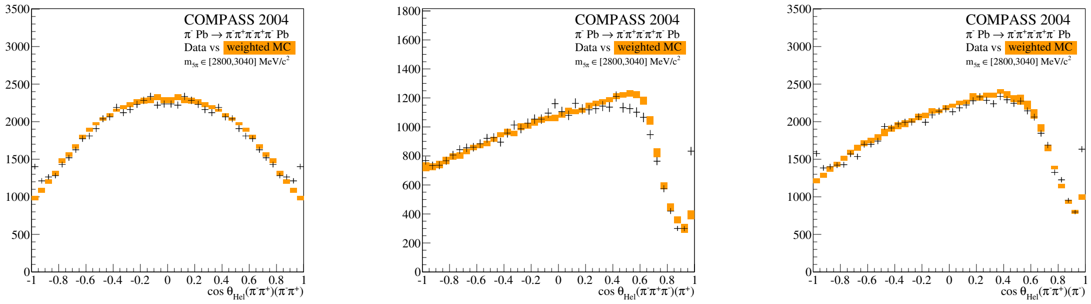

(g) $\cos\theta_{\mathrm{Hel}}^{22}$ (h) $\cos\theta_{\mathrm{Hel}}^{31}$ (i) $\cos\theta_{\mathrm{Hel}}^{21}$

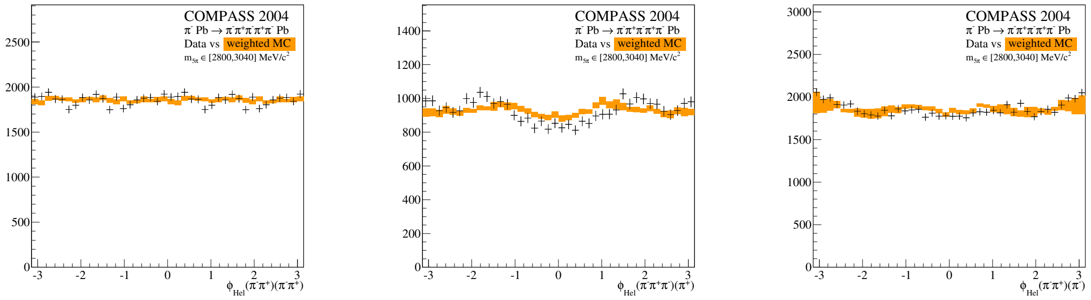

(j) ϕ_{Hel}^{22} (k) ϕ_{Hel}^{31} (l) ϕ_{Hel}^{21}

Figure 5.7: Comparison of the model (orange) with the data (black). For a detailed description of the kinematic variables shown, see text. $m_{5\pi} \in [2.80, 3.04]\,\mathrm{GeV}/c^2$

5.1.2 Calculation of Bands of Uncertainty

Of course the inferred model parameters carry uncertainties which translate into uncertainties for the predictions of the kinematic distributions. Since the latter are generated through the Monte Carlo method described above, it is not possible to apply an analytical error propagation. Instead another Monte Carlo sampling approach has been chosen here.

The covariance matrix of the model parameters describes a multidimensional Gaussian[1] probability distribution. By sampling from this distribution a set of slightly different models can be generated such, that all uncertainties and correlations are preserved. Numerically this problem is solved (see e. g. [158]) by sampling a vector of *uncorrelated* normal distributed variables x with variance $\sigma = 1$ and then performing an affine transformation

$$\bar{x} = \mu + Tx.$$

T is the Cholesky-decomposition of the covariance matrix

$$C = T^T T$$

and μ is the expectation value of the multivariate normal distribution. The samples $\bar{x}$ will then be distributed according to the full covariances of C.

The pseudo-data weighted with the different predictions of the model samples will yield the desired distributions in the kinematic variables and thus allow to construct error bands for the model predictions. The width of an uncertainty band is computed from the variance of the set of sampled model predictions in a given bin. There also is another source of uncertainty which comes from the finite number of pseudo-data events that are used to plot the distributions. The associated error, taking into account the weights of the individual contributions is added quadratically to the model-error. The error bands constructed in that way are centered at the maximum-likelihood solution.

5.2 Spin-Density Matrix Elements

Figure 5.8 shows an overview of the complete spin-density matrix as extracted in the mass independent partial-wave decomposition. Each row and column respectively corresponds to one wave. Each subplot in this matrix shows an element of the spin-density matrix as a function of the 5-pion mass. On the diagonal the intensities are plotted. In the upper right triangle the real parts of the interference terms are plotted and in the lower left triangle the imaginary parts of the interference terms.

Although rich structures show up in the partial-wave decomposition, in contrast to the 3π case for example there are no outstanding “dominant waves” with obvious resonance signals. Also, the phase motions in the interference terms (which are not shown here) are not easily interpreted without further tools. This is not unexpected, since in the mass range under investigation there are several overlapping resonances which lead to complicated interferences patterns. The methods used to understand possible resonant contributions and the interference of several resonances and the results obtained from that analysis are presented in chapter 6. In the present section all the partial amplitudes used in the fit are briefly discussed in order to allow

---

[1] The Gaussian approximation is used here for simplicity. Strictly speaking it only captures the most important features of the curvature of the log-likelihood function in the vicinity of the maximum-likelihood solution.

the reader to get a broad overview over the partial-wave decomposition which serves as the basis for the later search for resonances.

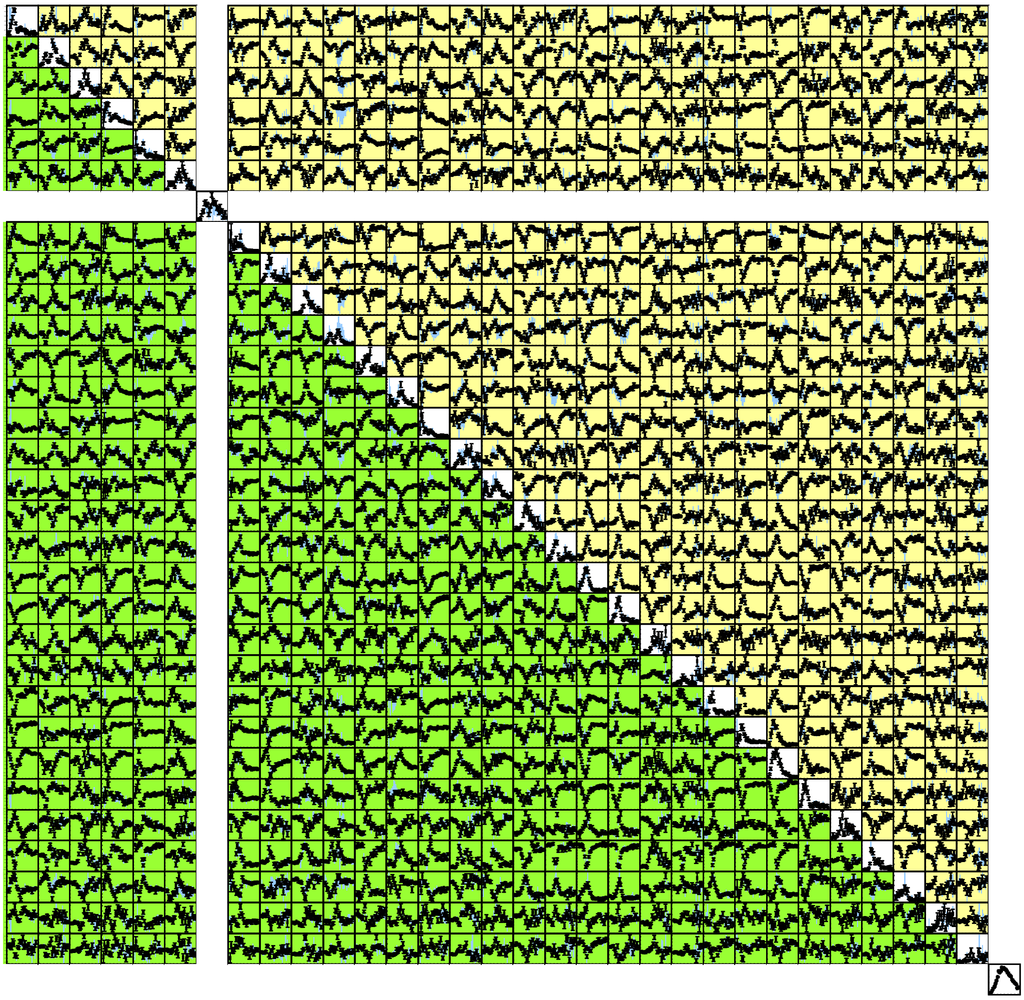

Figure 5.8: Complete overview of the mass independent partial-wave decomposition of the 5π system. On the diagonal the intensities of 32 waves are shown. In the right upper (left lower) triangle the real (imaginary) parts of the corresponding interference terms are plotted. The fits in each mass bin are independent of each other.

In the plots below (Figures 5.9 to 5.16) the intensities of all partial amplitudes in this fit are shown. Like in the 3π case the main contributions come from the $0^{-+}, 1^{++}$ and 2^{-+} waves. As discussed above in section 2.2.2 this is expected due to Pomeron dominance and the suppression of helicity flip amplitudes at low t'. It will become clear from the discussion of the individual intensities, that contrary to what is known from the 3π system here there are no clear *major waves.*

A remark on systematic uncertainties: The necessity to find an objective method to construct the waveset (tables 5.1 and 5.2) was the main motivation to develop the genetic search described above in chapter 4. Since for this purpose a large number (≈ 5000) of different models has been tested on the data, those results can further be used to study the systematic effects that arise from the choice of a particular waveset. For the spin density matrix elements discussed below these systematic uncertainties will be indicated by blue error bars. These error bars show the range of the corresponding observable obtained in the 20 best wavesets found by the genetic algorithm (see also table 4.3). The systematic range in each bin is spanned by the lowest and the highest value found in the top 20 fits. They give an indication of the robustness of the inferred parameter values under small changes in the model. Only the central values have been used to calculate these systematic error bands, statistical uncertainties are only shown for the best fit.

5.2.1 The *FLAT* Amplitude

The *FLAT* amplitude is an incoherent contribution to the intensity, that is isotropic in phase space (see equation 3.13). It is allowed in the fit in order to absorb any contributions that are not projected onto the partial waves. In the present analysis the FLAT wave has been present in all models fitted during the genetic optimization, solutions without this contribution have not been taken into account. It takes about a quarter of the total intensity. Figure 5.9 shows the intensity of the FLAT wave as a function of the 5-pion mass.

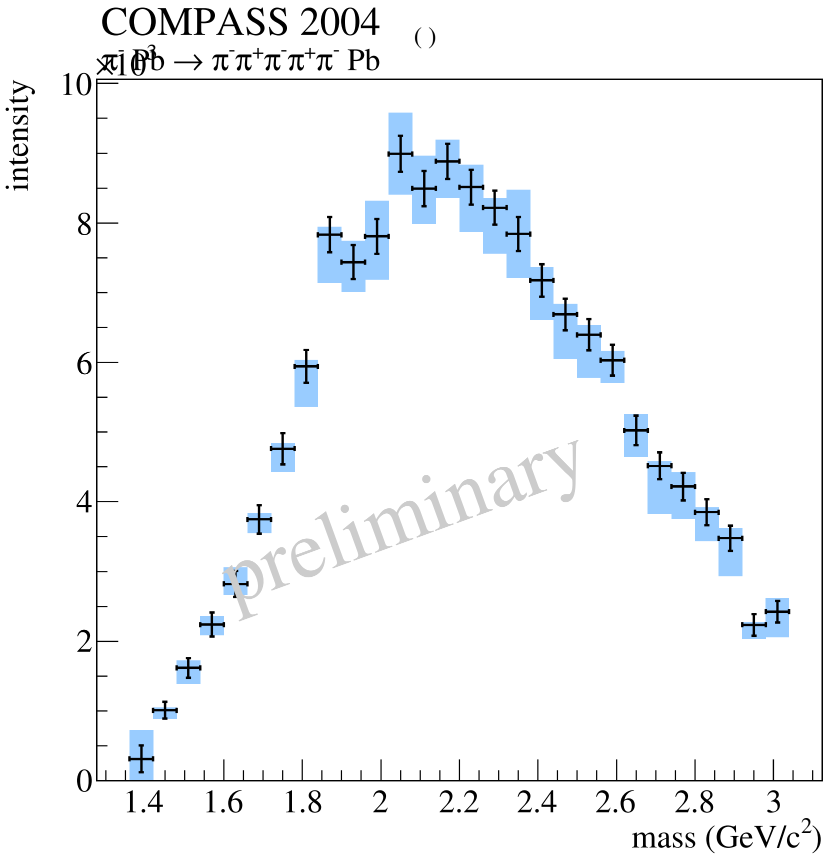

Figure 5.9: The intensity of the incoherent, isotropic FLAT contribution to the intensity.

The FLAT wave still shows some slight structures around $m_{5\pi} \sim 1.9\,\mathrm{GeV}/c^2$ and $2.1\,\mathrm{GeV}/c^2$, which are the regions where resonances are expected and also seen in other waves. That the isotropic background shows such fluctuations here might be an indication that the model is still missing some components. On the other hand it is obvious that partial waves which are mainly built up of S-wave two body decays can experience strong correlations with the FLAT wave making it difficult for the fit to distinguish these components of the model. In general the result obtained here is similar to what has been found in previous multi-body partial wave analyses like [63].

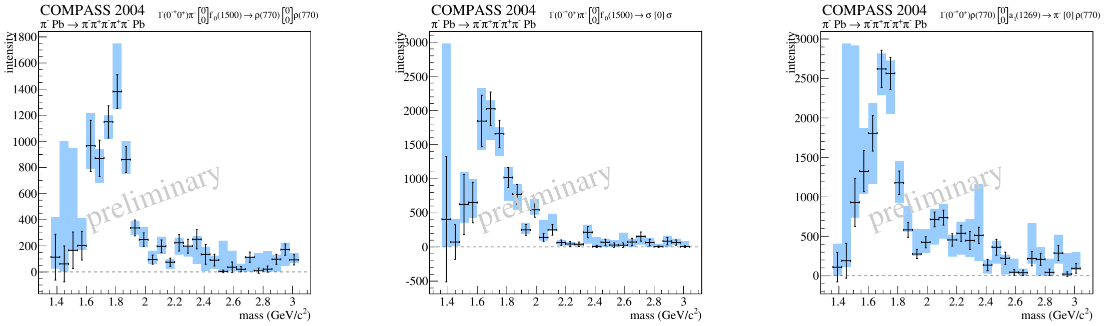

(a) $\pi^- f_0(1500) \to \pi^- \rho\rho$ (b) $\pi^- f_0(1500) \to \pi^- \sigma\sigma$ (c) $\rho a_1(1260)$

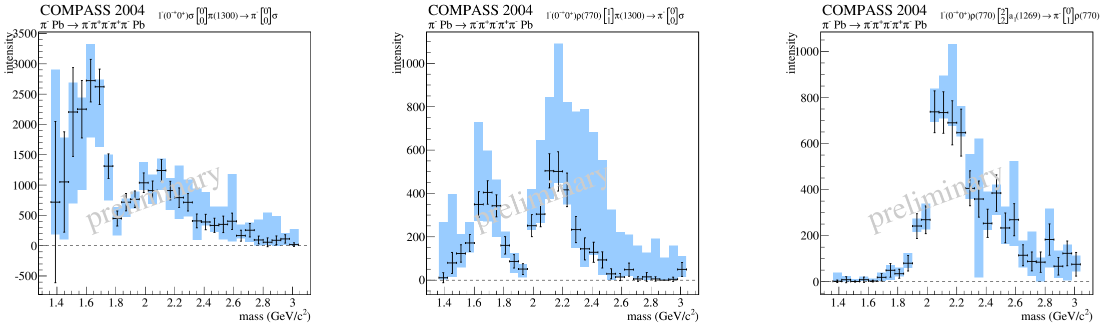

(d) $\sigma\pi(1300)$ (e) $\rho\pi(1300)$ (f) $\rho a_1(1260)$

Figure 5.10: Intensities of partial waves with $J^{PC} = 0^{-+}$. Waves (a–d) are S-wave decay modes, (e) is a P-wave and (f) shows a D-wave. Waves (a) and (c) have been used in the mass-dependent fit.

5.2.2 $J^{PC} = 0^{-+}$ Partial-Wave Amplitudes

Figure 5.10 shows the intensity distributions for the 6 partial amplitudes with $J^{PC} = 0^{-+}$ that have been used in the fit. The first two figures 5.10(a) and 5.10(b) both correspond to an S-wave decay of the $J^{PC} = 0^{-+}$ system into $\pi^- f_0(1500)$. In the former case the f_0 subsequently decays into $\rho^0\rho^0$ while in the latter it goes to $(\pi^+\pi^-)_S(\pi^+\pi^-)_S$. Both intensity plots show a peaking structure around 1.7 GeV/c^2 as does the intensity for the S-wave decay into $\rho^0 a_1(1260)$ which is shown in Figure 5.10(c). In all three spectra there is only a small tail towards higher masses, however in Figure 5.10(c) one might identify a small shoulder around 2.1 GeV/c^2.

A slightly different picture is displayed for the S-wave decay mode $(\pi^+\pi^-)_S\pi(1300)$ in Figure 5.10(d). Here the maximum of the intensity lies at a bit smaller values and after a dip at 1.8 GeV/c^2 there is a clear, broad structure peaking around 2.1 GeV/c^2. A similar picture with a dip around 1.9 GeV/c^2 is obtained for the P-wave decay mode into $\rho\pi(1300)$ (Figure 5.10(e)). Due to the orbital angular momentum barrier here the lower mass structure is less pronounced compared to the S-wave case. It should, however, be noted that these two decay modes, especially for the S-wave decay of the broad $\pi(1300)$ into $\pi^-(\pi^+\pi^-)_S$ which is used here, has no striking signature in the angular correlations and thus carries quite some systematic uncertainty.

The last plot in this series shows the intensity for a D-wave decay of the $J^{PC} = 0^{-+}$ system into $\rho^0 a_1(1260)$ in Figure 5.10(f). Here the low-mass part is strongly suppressed and only a broad structure around 2.1 GeV/c^2 shows up.

For a more detailed interpretation of these results interferences with other waves have to be studied. The peaking structure at 1.8 GeV/c^2 can be hypothesized to come from the well known $\pi(1800)$ resonance. The dip in Figure 5.10(d) might be due to a destructive interference of that resonance with some background. Whether the structure at 2.1 GeV/c^2 is of resonant origin can only be answered by a detailed analysis of the interference terms and the phase-motions encoded there. These hypotheses will be tested in chapter 6 using the two partial amplitudes 5.10(a) and 5.10(c).

5.2.3 $J^{PC} = 1^{++}$ Partial-Wave Amplitudes

The largest portion of partial amplitudes belongs to the $J^{PC} = 1^{++}$ sector.However as will be discussed in this section the 15 partial waves show a quite inconsistent picture and a straight forward interpretation is not possible.

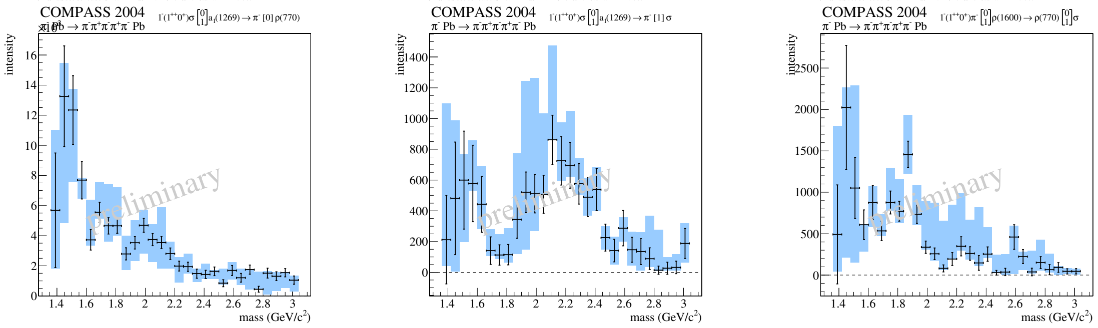

(a) $\sigma a_1 \rightarrow \sigma\rho\pi$ (b) $\sigma a_1 \rightarrow \sigma\sigma\pi$ (c) $\pi\rho' \rightarrow \pi\rho\sigma$

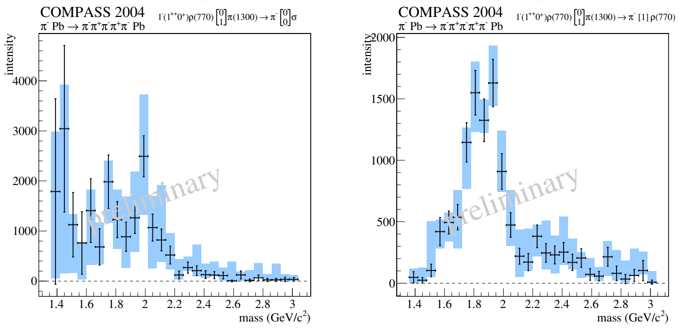

(d) $\rho\pi(1300) \rightarrow \rho\sigma\pi$ (e) $\rho\pi(1300) \rightarrow \rho\rho\pi$

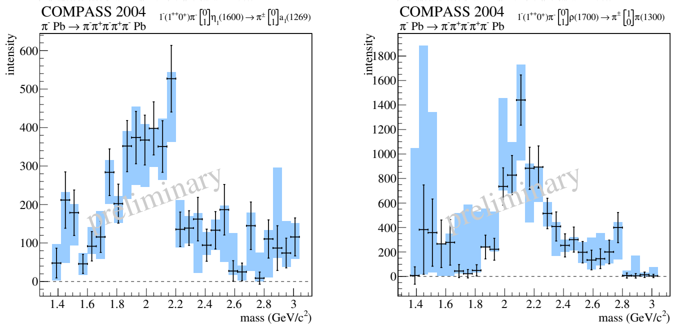

(f) $\pi\eta_1(1600)$ (g) $\pi\rho' \rightarrow \pi a_1\pi$

Figure 5.11: Intensities of partial waves with $J^{PC} = 1^{++}$ and S-wave isobar decays. Wave (e) has been used in the mass-dependent fit.

Figure 5.11 shows the intensities for partial amplitudes which describe the 1^{++} system decaying into two isobars in S-wave. The intensity shapes do not follow a consistent pattern. Only the intensity for the $\rho^0\pi(1300)$ decay mode, with the $\pi(1300)$ decaying into $\rho\pi$, (Figure 5.11(e)) shows a clean peaking structure around 1.9GeV/c^2. This partial wave has been used for the

mass-dependent fit. The similar wave in Figure 5.11(d) where the $\pi(1300)$ decays into $\pi(\pi^-\pi^+)_S$ does not show such a clean peak. This might be due to the smaller coupling of the $\pi(1300)$ to the latter channel, however due to the larger errors on this partial amplitude a conclusion would be difficult here without increased statistics.
It is an interesting detail that there is one partial wave (Figure 5.11(f)), which has been required in the waveset evolution, that contain an $I^G J^{PC} = 0^+1^{-+}$ $\eta_1(1600)$ isobar. It has been parametrized with the same resonance parameters as its possible isospin partner the $\pi_1(1600)$ (c. f. section 3.2.2). Apparently the data supports such a contribution to the 4π subsystem. However, it would be premature to conclude that this isobar is really a resonant state. For this claim it would be necessary to perform more detailed investigations, ideally observing a resonant phase motion of this state. Section 5.3 presents a first attempt at such a study, extracting phases for the 4π system in $I^G J^{PC} = 0^+1^{++}$ and 0^+2^{++} partial waves.

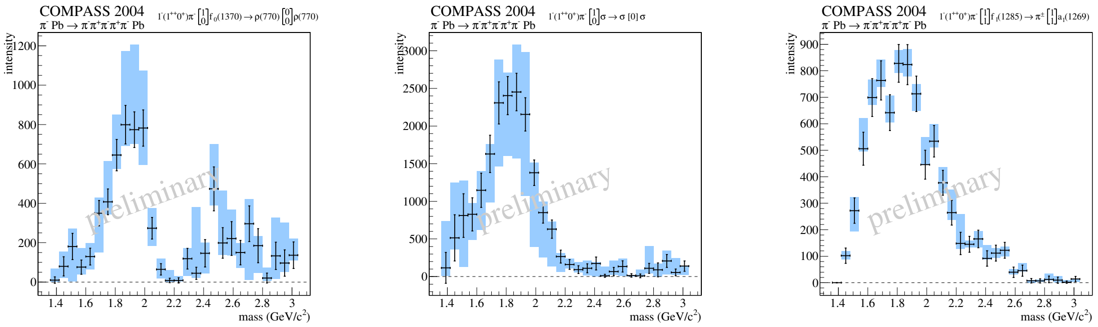

(a) $\pi f_0(1370)$ (b) $\pi(\sigma\sigma)_{S\text{-wave}}$ (c) $\pi f_1(1285)$

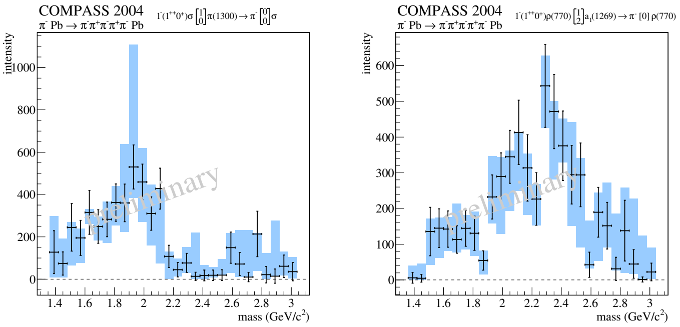

(d) $\sigma\pi(1300)$ (e) $\rho a_1(1260)$

Figure 5.12: Intensities of partial waves with $J^{PC} = 1^{++}$ and P-wave isobar decays. The partial amplitudes (a) and (c) have been used in the mass-dependent fit.

For the 1^{++} P-wave decay modes shown in Figure 5.12 the results are much more consistent compared to the S-wave intensities. Figures 5.12(a) and 5.12(b) both show a P-wave decay into a pion and a isoscalar, scalar 4π system. The only difference being that the former partial amplitude contains a resonant $f_0(1370)$ contribution (which subsequently decays into $\rho\rho$, while in the latter case the 4π system is parametrized through the σ amplitude described in section 3.2.2 and a decay into $(\pi^+\pi^-)_S(\pi^+\pi^-)_S$. Both partial waves show a peak at $1.9\,\mathrm{GeV}/c^2$.
Figure 5.12(c) shows the small, but remarkably stable partial wave with the isobars $f_1(1285)\pi^-$ in a P-wave. Here the intensity is distributed over a quite broad range. A hypothesis, that

has already been advanced by other experimenters [63], is that there are 2 overlapping states decaying into this channel. This hypothesis will be tested in the mass-dependent fit.
The lower row in Figure 5.12 shows to small contributions which so far have not been further analyzed.

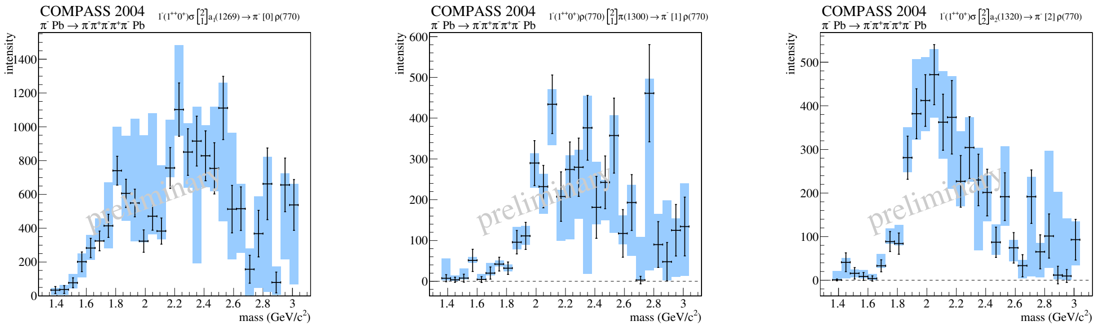

(a) $\sigma a_1(1260)$ (b) $\rho\pi(1300)$ (c) $\sigma a_2(1230)$

Figure 5.13: Intensities of partial waves with $J^{PC} = 1^{++}$ and D-wave isobar decays. Partial amplitude (c) is used in the mass-dependent fit.

The 1^{++} D-wave partial amplitudes are shown in Figure 5.13. they all feature relatively small intensities. Remarkable here is the $(\pi\pi)_S a_2(1320)$ partial wave, presented in Figure 5.13(c). Although strongly damped below $1.9\,\mathrm{GeV}/c^2$ this amplitudes is quite stable at higher masses and will play an important part in the mass-dependent analysis in chapter 6.

5.2.4 $J^{PC} = 2^{-+}$ Partial-Wave Amplitudes

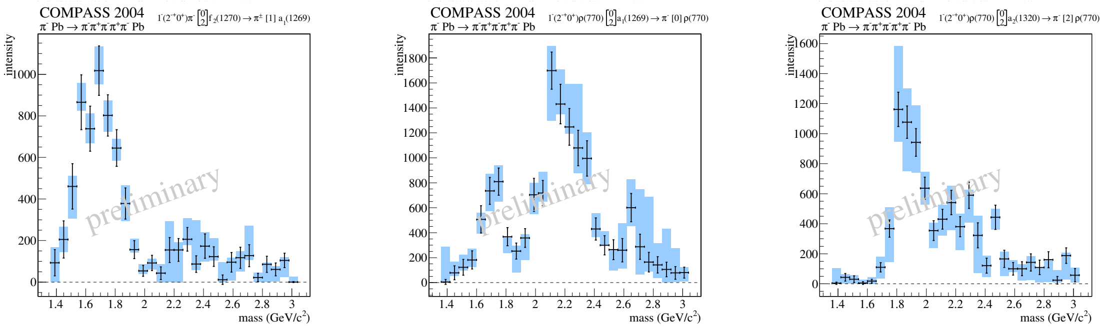

(a) $\pi f_2(1270)$ (b) $\rho a_1(1260)$ (c) $\rho a_2(1320)$

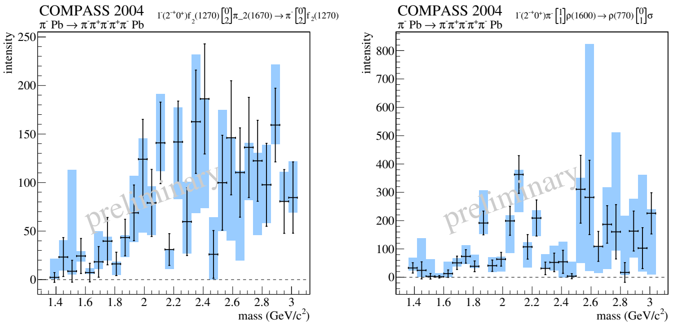

(d) $f_2(1270)\pi_2(1670)$ (e) $\pi\rho'$

Figure 5.14: Intensities of partial waves with $J^{PC} = 2^{-+}$ with S-wave and P-wave (e) decay modes. Partial waves (a)-(c) have been used in the mass dependent fit.

The $J^{PC} = 2^{-+}$ sector shows quite interesting and remarkably clear structures. Especially the S-wave partial amplitudes shown in Figure 5.14 feature small systematic errors (blue). The prominent 2^{-+} $f_2(1270)\pi$ S-wave amplitude, with the 4π decay of the $f_2(1270)$ modeled as an $\pi\, a_1(1260)$ P-wave isobar decay is shown in Figure 5.14(a). It has been used as the anchor wave (c. f. section 3.1.3) in all the fits performed. The intensity of this wave peaks at $1.7\mathrm{GeV}/c^2$ in a region where the well known $\pi_2(1670)$ resonance exists. The decay of the $\pi_2(1670)$ into the $f_2(1270)\pi$ channel is well studied for the 3π final state since $f_2(1270) \to \pi\pi$ is the dominant decay mode with a branching ratio of $84.8^{+2.4}_{-1.2}\%$ [1]. What is observed here in the 5π final state is the decay of the $f_2(1270)$ into 4 charged pions for which the Particle Data Group lists a branching fraction of $2.8 \pm 0.4\%$.

A different picture is obtained for the intensity in the $\rho\, a_1(1260)$ decay channel presented in Figure 5.14(b). There are two peaking structures visible here, separated by a dip at $1.9\,\mathrm{GeV}/c^2$. Yet a different behavior is shown in Figure 5.14(c) for the S-wave decay of the 2^{-+} system into $\rho\, a_2(1320)$. In the latter intensity spectrum there is no sign of the $\pi_2(1670)$ — in agreement with earlier experiments [1]. However a rather sharp peak shows up at $1.9\,\mathrm{GeV}/c^2$ with a small shoulder around $2.2\,\mathrm{GeV}/c^2$. How to interpret these striking patterns will be a major question for the further analysis. A possible solution will be discussed in chapter 6.

The two partial amplitudes in Figures 5.14(d) and 5.14(e) only make small contributions to the spectrum and will not be discussed in more detail here.

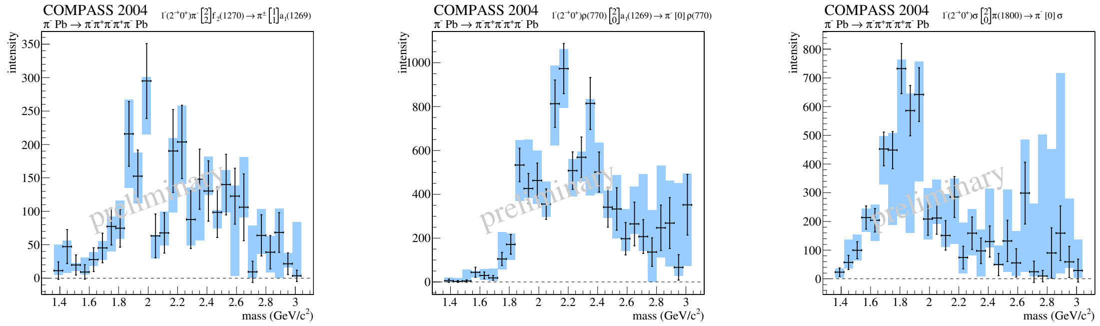

(a) $\pi f_2(1270)$ (b) $\rho a_1(1260)$ (c) $\sigma\pi(1800)$

Figure 5.15: Intensities of partial waves with $J^{PC} = 2^{-+}$ and D-wave isobar decays. Partial amplitude (b) has been used in the mass dependent fit.

Figure 5.15 shows the 2^{-+} D-wave amplitudes. In neither of those intensity spectra a clear signal of the $\pi_2(1670)$ is seen. The $f_2\pi$ and $\rho\, a_1$ D-wave decay modes show a rather broad distribution around $2\,\mathrm{GeV}/c^2$. The latter one, showing the largest intensity and smallest systematic uncertainties, has been included in the mass dependent analysis.

5.2.5 Further Components

The remaining two components in the partial-wave model are shown here for completeness in Figure 5.16. The only $J^{PC} = 3^{++}$ shows a small bump at $2\,\text{GeV}/c^2$. The amount of data seems too little to draw any further conclusions. The only wave with negative reflectivity, that has survived the genetic optimization is shown in Figure 5.16(b). Incidentally it has the quantum numbers 1^{-+}. However, note that negative reflectivities were only allowed in the wave pool for those amplitudes that cannot be produced without spin flip in positive reflectivity exchange (c. f. sections 3.1.1 and 4.2). Since there are no other partial waves interfering with this one, the phase motion cannot be studied. The large systematic uncertainties are another indication that this amplitude should be interpreted with due skepticism.

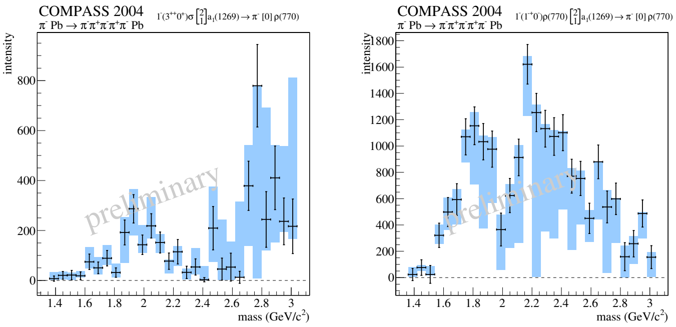

(a) $3^{++}0^{+}\sigma a_1(1260)$ (b) $1^{-+}0^{-}\rho a_1(1260)$

Figure 5.16: Intensities of partial waves with (a) $J^{PC} = 3^{++}$ and (b) $J^{PC}M^{\epsilon} = 1^{-+}0^{-}$. (b) is the only wave with negative reflectivity that has been picked up by the genetic waveset optimization.

5.3 The 4π Subsystem

In section 3.2.2 it has already been discussed that the 4-pion system is as well the least studied as well as the most interesting of the isobaric systems available in the 5π data set. So far we had to make assumptions on the structure of the 4-pion amplitudes, in particular on the resonant contributions. In this section a technique for the extraction of information on these amplitudes directly from the data is introduced. Some results from a first application of these ideas to the available data are presented.

5.3.1 A Technique for the Extraction of Isobar Amplitudes

The basic idea of a semi-model-independent isobar analysis is to find a parametrization for the isobar amplitudes that introduces as little as possible a bias into the analysis. A recent implementation has been presented by the E791 collaboration [159] in order to parametrize the $K^-\pi^+$ system in the reaction $D^+ \rightarrow K^-\pi^+\pi^+$. The method that is being proposed here is quite similar to their approach.

The general structure of the isobar-model decay amplitude as it has been described in section 3.2 is left untouched. The only thing that will be changed is the form of the dynamical function $Q(m_R, m_1, m_2)$ in equation 3.6 for the isobar on which information is going to be extracted. The Breit-Wigner resonance amplitude, which is usually put in this place, is replaced by a complex-valued step-function, which is constant over a small interval in the isobar mass m_R. The complex values of this function in the m_R bins are free parameters to be determined by the fit. In this way it is possible to extract the dependence of the amplitude on the isobar mass.

There are a few caveats to this method, though. First, in order to determine the phase of the isobar-amplitude one needs the interference with another partial wave and here one is required to put an ansatz for the form of the corresponding amplitude. In other words, it is only possible to replace one (or very few) isobar propagators with the flexible representation by a step function — hence the term *semi-model-independent* isobar analysis. Furthermore, the number of fit parameters is considerably increased by adding a free real and imaginary part in each isobar-mass bin. The method will only yield meaningful results if enough data is available to support these additional parameters.

The main advantage of the method is, that it can be integrated quite easily in the present representation of the decay amplitudes as will be explained below. Also the factorization into a set of decay amplitudes which contain no unknowns and a set of production amplitudes which are inferred from the data can be kept. The latter form is computationally very advantageous as has been discussed in section 3.4.

In order to implement the scheme[2] described above one 5-body decay amplitude ψ_α for example

$$\psi_{1^{++}f_1\pi} = 1^-1^{++}0^+ \quad \pi^- \begin{bmatrix} 1 \\ 1 \end{bmatrix} f_1(1285) \rightarrow \pi^\mp[1]a_1(1269) \rightarrow \pi^\pm[0]\rho(770)$$

is replaced by a series of amplitudes $\psi^k_{1^{++}f_1\pi}$ in which the propagator (c. f. equation 3.6) of the

---

[2] The method has only been implemented for rank 1 fits.

$f_1(1285)$ is replaced[3] by

$$Q(m_{4\pi}, m_\pi, m_{3\pi}) = \begin{cases} 1 & : \quad m_{4\pi} \in [m_k, m_k + \delta m[\\ 0 & : \quad \text{else} \end{cases} \tag{5.2}$$

inside a mass interval which starts at $m_{4\pi} = m_k$ and has a width of $\delta m = 50\,\mathrm{MeV}/c^2$ for example.

$$\begin{aligned}
\psi^1_{1^{++}f_1\pi} &= 1^-1^{++}0^+ \quad \pi^- \begin{bmatrix} 1 \\ 1 \end{bmatrix} f_1(700-750) \to \pi^\mp[1]a_1(1269) \to \pi^\pm[0]\rho(770) \\
\psi^2_{1^{++}f_1\pi} &= 1^-1^{++}0^+ \quad \pi^- \begin{bmatrix} 1 \\ 1 \end{bmatrix} f_1(750-800) \to \pi^\mp[1]a_1(1269) \to \pi^\pm[0]\rho(770) \\
\psi^1_{1^{++}f_1\pi} &= 1^-1^{++}0^+ \quad \pi^- \begin{bmatrix} 1 \\ 1 \end{bmatrix} f_1(800-850) \to \pi^\mp[1]a_1(1269) \to \pi^\pm[0]\rho(770) \\
&\vdots
\end{aligned}$$

Here the symbols $f_1(m_\text{low} - m_\text{high})$ indicate the isobar-mass bin that is covered by the amplitude. Note that the whole angular structure of the amplitude is left unchanged. Indeed it is the angular correlations which will allow to extract the correct behavior of the isobar amplitude. Thus the initial amplitude is expanded in the following way:

$$\psi_{1^{++}f_1\pi} \approx \sum_k f_k \psi^k_{1^{++}f_1\pi}$$

Now follows the crucial step: Similar to the treatment of the ℓS-coupling constants $g_{\ell S}$ (see section 3.2.1) the complex f_k are absorbed into the production amplitude $T^k_{1^{++}f_1\pi}$ that is associated with the kth part of the decay amplitude and thus become part of the fitting parameters. Otherwise the fit in fixed bins of the 5-body mass is carried out as usual.

In order to analyze the 4-body system one then can select a certain 5-body-mass bin and plot the results for the production amplitudes $T^k_{1^{++}f_1\pi}$ as a function of the 4-body mass.

5.3.2 Results for Selected 4π Partial Waves

In order to ensure a large-enough data sample all 5π events in the region $m_{5\pi} \in [1780, 1960]\,\mathrm{MeV}/c^2$ have been combined in the fit. The complete final waveset has been used in this fit, with only the $1^-1^{++}0^+$ $f_1(1285)\pi$ P-wave being replaced by the piecewise parametrization.

Figure 5.17 shows the $I^G(J^{PC}) = 0^+(1^{++})$ 4-pion amplitude extracted from the data using the method described above. There is a very clear peak in the intensity at $m_{4\pi} = 1275\,\mathrm{MeV}/c^2$ which is also associated with a clean phase-motion in the same region. The Argand-plot shows the amplitude in the complex plane with the numbers on the markers indicating the mass at which the corresponding measurement has been taken. There is a clear circular, counterclockwise motion. These features are exactly what would be expected for the $f_1(1285)$ resonance decay into four pions. The results thus nicely confirms the initial assumption of the presence of this resonance and justifies its usage as an isobar.

---

[3] Angular momentum barrier factors are taken into account by absorption into the subsystem phase-space factors.

Note that the Argand-plot is rotated away from the origin of the complex plane. The reason is, that the production amplitudes inferred inn the fit also contain the contribution from the 5π system, which has not been factored out. In principle such a factorization is possible using an extension [160] of the techniques of the mass-dependent fit (see chapter 6.1).

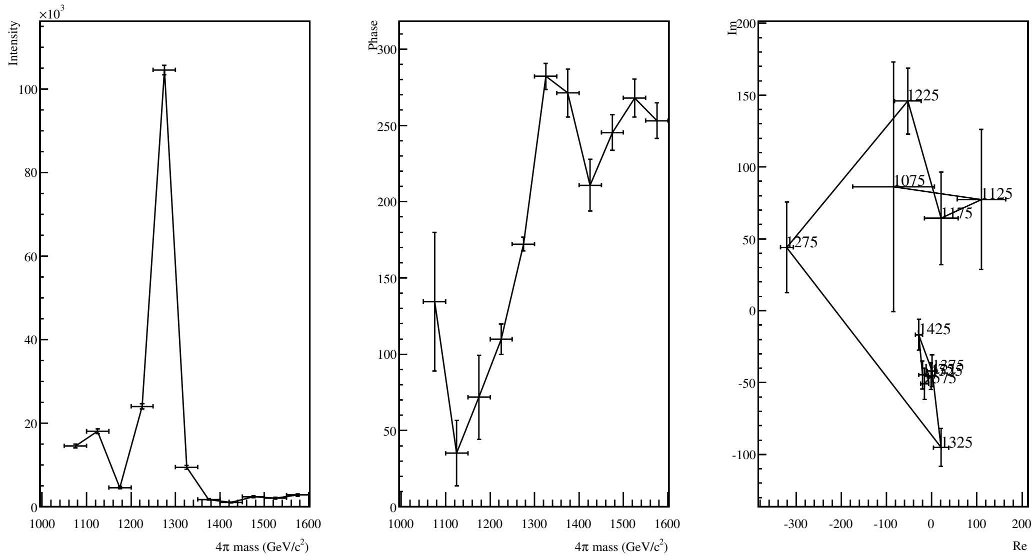

Figure 5.17: The 4π amplitude with $I^G(J^{PC}) = 0^+(1^{++})$ decaying via $\pi\, a_1(1260)$. The $f_1(1285)$ resonance is clearly visible in intensity and phase motion. Also the Argand-plot shows a clear circle.

A second example is displayed in Figure 5.18. Here the $I^G(J^{PC}) = 0^+(2^{++})$ 4-pion subsystem in the $2^{-+} f_2(1270)\pi\, S$-wave has been extracted. The intensity of this 4-pion amplitude also shows a peak at 1275 MeV/c, albeit with a considerably larger width than the $f_1(1285)$ and a long tail to higher masses. There is also a clear phase motion and a clear signature of a resonance in the Argand-plot. These findings are clearly in agreement with the hypothesis that here the decay of the $f_2(1270)$ into four pions is seen. The signal is not as clean as for the $f_1(1285)$, though. Whether this has to do with the broad 5π mass range over which the procedure has effectively integrated here or if there are additional contributions to the $0^+(2^{++}$ system — beyond the $f_2(1270)$ resonance — remains to e investigated. For such studies a larger data set would be extremely valuable.

The preliminary conclusion, which can be drawn from the prototype analyses presented in this section, is that detailed information on the 4-pion amplitude can indeed be extracted if enough data on the 5π system is available to permit the binned-isobar ansatz. The method would allow the investigation of scalar as well as isoscalar 4-pion systems and could be an indispensable tool for the search for isoscalar spin-exotic states. Also the principal method can also be applied to subsystems other than the four pions, for example to perform precision studies of the $(\pi\pi)_{S-\text{wave}}$ in the 3π final state. Another interesting possibility is to study the

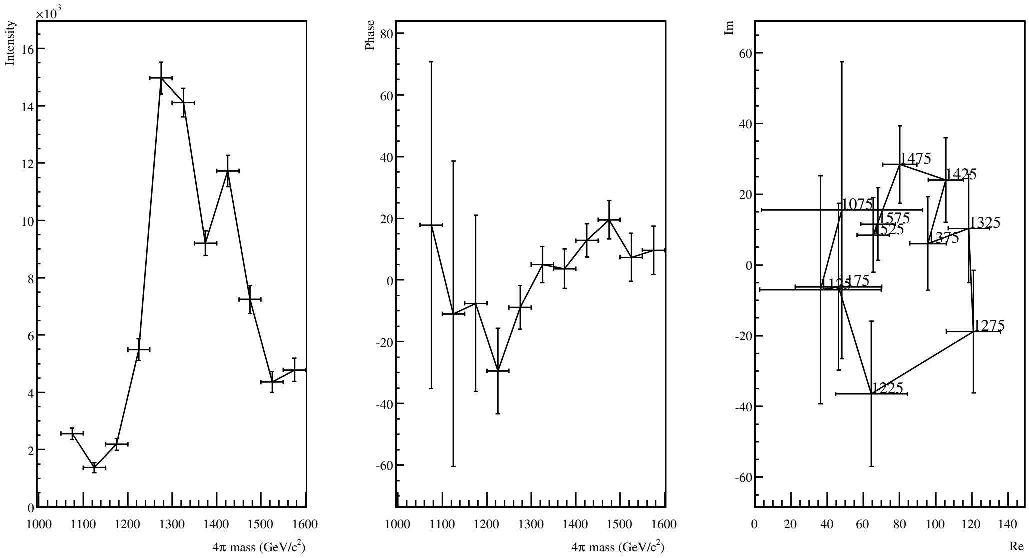

Figure 5.18: The 4π amplitude with $I^G(J^{PC}) = 0^+(2^{++})$ decaying via $\pi\, a_1(1260)$. The $f_2(1270)$ resonance is clearly visible.

dependence of the extracted subsystem amplitudes on the mass of the *source* system.

Suggestions for future research:

- *Run binned-isobar fit on larger data sample.*
- *Perform a mass-dependent parametrization of the extracted isobar amplitudes.*
- *Investigate isobaric systems in other partial waves.*
- *Apply method to study isoscalar scalar, and spin-exotic states.*

Chapter 6

Mass Dependent Parametrization of the Spin Density Matrix

> But a knowledge of the positions and intensities of the spectra does not suffice for the determination of the structure. The phases with which the diffracted waves vibrate relative to one another enter in an essential way.
>
> Max von Laue

THIS chapter describes the techniques employed to parametrize the mass dependence of the spin-density matrix-elements in terms of resonant and non-resonant contributions. Based on the general discussion of resonance parametrizations given in section 1.3 a simplified model and its application to the data are described. Finally the results are discussed.

6.1 Mass Dependent Fit Formalism

According to the arguments presented in section 1.3 the spin density matrix is parametrized as a sum of relativistic Breit-Wigner amplitudes and constant background terms in the following form:

$$T^{\epsilon}_{\alpha} T^{\epsilon *}_{\beta} = \rho^{\epsilon}_{\alpha\beta}(m) = \left(\sum_k C^{\epsilon}_{\alpha k} \mathscr{A}_{\alpha k}(m) \sqrt{\rho_\alpha(m)} \right) \left(\sum_l C^{\epsilon}_{\beta l} \mathscr{A}_{\beta l}(m) \sqrt{\rho_\beta(m)} \right)^{*} \cdot \rho_{5\pi}(m) F(m) \tag{6.1}$$

The $\mathscr{A}_{\alpha k}(m)$ take a specific form representing either resonances or constant background terms. The resonant components are described by relativistic Breit-Wigner amplitudes

$$\mathscr{A}_{\alpha k}(m, M_0, \Gamma_0) = \frac{M_0 \Gamma_0}{m^2 - M_0^2 + i \Gamma_0 M_0} \qquad k = \text{resonance} \tag{6.2}$$

with a fixed width Γ_{tot}. Due to the lack of knowledge about the coupling of the resonances to other channels a dynamic width has not been used in the fits presented here. Thresholds in the region of interest such as those collected in table 1.4 are not yet taken into account in the analysis. Including such information in the future will lead to an improvement of the fits and the extracted resonance parameters. As long as no explicit information on additional open channels is available experimentally the resonance parameters have to be considered as approximate values. In each fitted wave a coherent, constant background term is allowed, such that

$$\mathscr{A}_{\alpha k}(m) = c_\alpha \quad \text{for} \quad k = \text{bkg}. \tag{6.3}$$

The phase space factors

$$\rho_\alpha(m) = \int |\psi_\alpha^\epsilon|^2 d\tau \tag{6.4}$$

are obtained from the phase space integrals used in the mass independent fit (c. f. section 3.4). The phase space integrals used here already contain the angular momentum barrier factors.
The shape of the five-body phase space $\rho_{5\pi}(m)$ as a function of the invariant 5-body mass m is obtained from a Monte-Carlo simulation, using the GENBOD multi-body event generator [139]. For ease of use the resulting distribution is parametrized with a function of the following form:

$$\rho_{5\pi}(m) = a(m - m_{\text{thresh}})^5 \cdot [1 + b(m - m_{\text{thresh}})] \tag{6.5}$$

where $m_{\text{thresh}} = 698\,\text{MeV}/c^2$ is the threshold for the production of five charged pions.

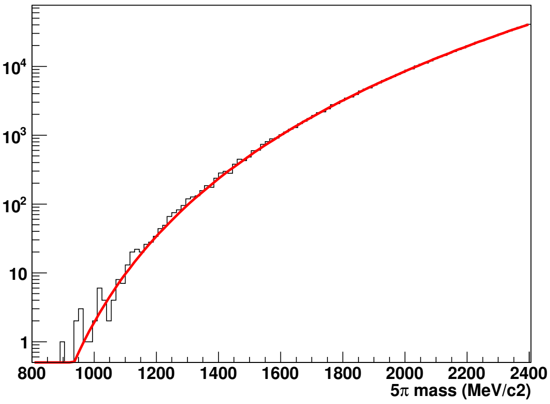

Figure 6.1: 5 pion phase space. The histogram shows the distribution predicted by the GENBOD Monte Carlo generator. The red line is the fit according to equation 6.5.

The form of the function 6.5 can be motivated by examining the behavior of the five-body phase space in the limiting cases close to threshold and for $m \to \infty$ respectively [161]. For the former case $\rho_{5\pi}|_{5m_\pi} \sim m^5$ while for the latter one finds $\rho_{5\pi}|_{m\to\infty} \sim m^6$. The parameters a and b have been determined from a fit to the Monte Carlo pseudo-data shown in Figure 6.1. While a is just an overall normalization to the number of Monte Carlo events, $b = 4.859\,\text{GeV}^{-1}c^2$ determines the shape of this phase space.
In addition it turns out to be necessary to describe the data to include a form factor $F(m)$ as described in section 1.3. The functional form has been chosen as a simple exponential dampening

$$F(m) = \exp(-c_{\text{ff}}(m - m_{\text{thresh}}))$$

where the dampening factor c has been left free in the fit and is extracted from the data to a value of

$$c_{\mathrm{ff}} = 1.742 \pm 0.025\,\mathrm{GeV}^{-1} c^2$$

.
According to the discussion in section 1.3 the coupling constants $C_{\alpha k}$ are allowed to be complex, such that each component of the model has an overall, mass independent phase, the value of which is left floating in the fit. Since absolute phases cannot be measured the coupling for the $2^{-+}0+\pi^- f_2(1270)\,S$-wave is restricted to be real valued. Note that by construction the background is assumed to have no 5-body-mass dependent phase shift. In this model any phase shift, therefore, can only be explained by resonant contributions. Note that if a resonance is introduced in the model, by default it is allowed to couple to each partial-wave with the corresponding quantum numbers that is taken into account for the fit.
With this model for the cross-section the χ^2 function is written in the following way:

$$\chi^2 = \sum_{m}^{\text{bins}} \sum_{\alpha\beta}^{\text{waves}} (\rho^m_{\alpha\beta} - \rho_{\alpha\beta}(m))^T \mathbf{C}^{-1}_{\alpha\beta} (\rho^m_{\alpha\beta} - \rho_{\alpha\beta}(m)) \tag{6.6}$$

Here $\rho^m_{\alpha\beta}$ is the spin density matrix element as measured by the mass independent fit in the mass bin m. The complex number is represented in vector form with the real part being the first component and the imaginary part being the second component. $\mathbf{C}_{\alpha\beta}$ is the 2×2 covariance matrix of the real and imaginary parts of the spin-density matrix element and $\rho_{\alpha\beta}(m)$ represents the mass-dependent parametrization. This formulation of the χ^2 function neglects the covariances between different waves. The minimization is done with the ROOT version of Minuit2 [141]. Each fit is performed in three steps: At the beginning only the coupling constants $C^{\epsilon}_{\alpha k}$ and the damping factor c_{ff} are left free in the fit, the resonance parameters are kept fixed at some reasonably chosen values. In a second step the mass-parameters are released and only the widths are kept fixed. At last also the widths of the Breit-Wigner amplitudes are released and the final optimization is performed using the previous iteration as its set of starting values. This approach has proven useful in order to avoid unphysical solutions, where in the early stages of the optimization the minimizer gets stuck on a solution where one or more parameters reach the limits of their allowed range. If there are more than one resonance with the same J^{PC}, the the corresponding mass-parameters have to be limited to well defined, non-overlapping ranges in order for the parametrization to be uniquely defined. In any given fit it is therefore predefined by the choice of the parameter ranges how the Breit-Wigner amplitudes are ordered from the lightest to the heaviest state. Also for the widths limits have been set.
For each individual fit several attempts have been made in order to test the influence of the choice of starting values and parameter limits.

6.2 Resonance Extraction Results

In order to restrict the problem to a manageable size, only for a subset of the amplitudes presented in section 5 will a mass-dependent parametrization be constructed. In order to facilitate the search for resonances in all three major J^{PC} states that contribute, two 0^{-+} partial waves, four 1^{++} partial waves and four amplitudes with $J^{PC} = 2^{-+}$ have been picked. These partial waves have all been used in all of the top-20 partial-wave decomposition models (see table 4.3) and have been chosen because they display a very good stability with respect to modifications of the waveset. Also to some extend the choice attempts to include representative waves with different orbital angular momenta and different decay topologies. A list of the ten selected amplitudes is given below:

$J^{PC}M^{\epsilon}$	ℓ	s	Isobar1 Isobar2	Decay Isobar2	
$0^{-+}0^{+}$	S	0	$\pi^- f_0(1500)$	$\rho(770)\begin{bmatrix}0\\0\end{bmatrix}\rho(770)$	●
$0^{-+}0^{+}$	S	0	$\rho(770)a_1(1260)$	$\pi^-\begin{bmatrix}0\\1\end{bmatrix}\rho(770)$	●
$1^{++}0^{+}$	P	0	$\pi^- f_0(1370)$	$\rho(770)\begin{bmatrix}0\\0\end{bmatrix}\rho(770)$	●
$1^{++}0^{+}$	P	1	$\pi^- f_1(1285)$	$\pi^{\mp}\begin{bmatrix}1\\1\end{bmatrix}a_1(1260)$	●
$1^{++}0^{+}$	S	1	$\rho(770)\pi(1300)$	$\pi^-\begin{bmatrix}1\\1\end{bmatrix}\rho(770)$	●
$1^{++}0^{+}$	D	1	$(\pi\pi)_S a_1(1260)$	$\pi^-\begin{bmatrix}0\\1\end{bmatrix}\rho(770)$	●
$2^{-+}0^{+}$	S	2	$\pi^- f_2(1270)$	$\pi^{\mp}\begin{bmatrix}1\\1\end{bmatrix}a_1(1260)$	●
$2^{-+}0^{+}$	S	2	$\rho(770)a_1(1260)$	$\pi^-\begin{bmatrix}0\\1\end{bmatrix}\rho(770)$	●
$2^{-+}0^{+}$	S	2	$\rho(770)a_2(1320)$	$\pi^-\begin{bmatrix}2\\1\end{bmatrix}\rho(770)$	●
$2^{-+}0^{+}$	D	0	$\rho(770)a_1(1260)$	$\pi^-\begin{bmatrix}0\\1\end{bmatrix}\rho(770)$	●

Table 6.1: Partial waves used for the mass-dependent analysis.

There are three waves in this list which have also been studied by other experiments in different final states. These are the $0^{-+}\pi^- f_0(1500)S$-wave, the $1^{++}\pi^- f_1(1285)P$-wave and the $2^{-+}\pi^- f_2(1270)S$–wave.

Analysis Strategy The main questions that arises as one tries to describe the partial waves and their interference terms as functions of the 5-body mass is the number of resonances which should be allowed in each J^{PC} channel. The resonance parameters will then be inferred from the data.

Several hypotheses on the number of resonances have been tested. As a basic assumption one resonance for each J^{PC} sector was allowed and the model improved from that basis by adding further resonant terms. It was found that at least 7 resonant terms are needed to achieve a satisfying description of the data. We first present an overview of this fit before each J^{PC} sector is being discussed in detail. In particular the motivations for the inclusion of the different resonant contributions will be explained.

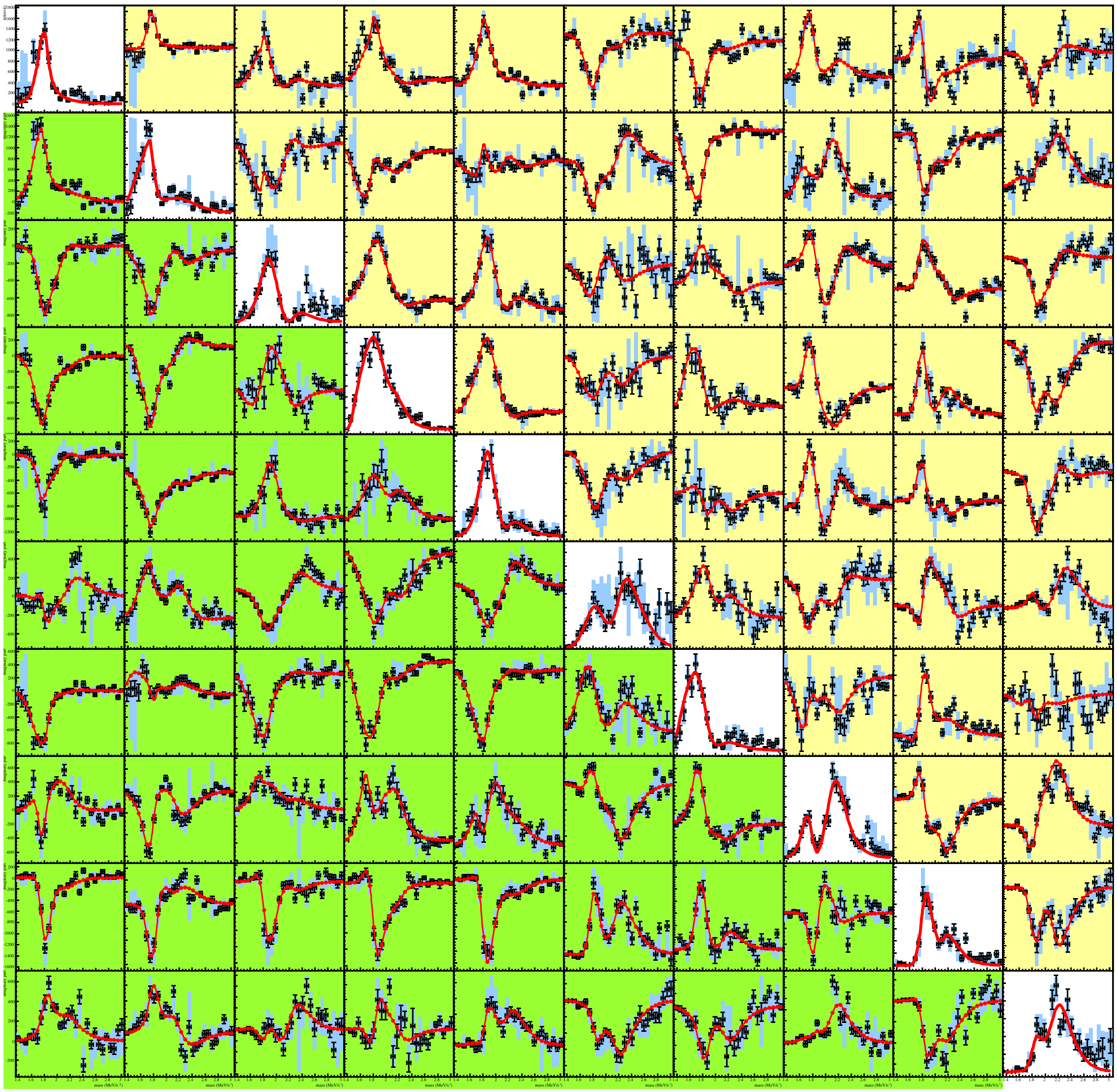

Figure 6.2: Each entry in this matrix of plots shows an element of the spin-density matrix as a function of $m_{5\pi}$ (in black). The light-blue error-bars are the estimates of systematic uncertainties from the choice of waveset for the mass independent partial-wave decomposition. On the diagonal the intensities of the ten selected partial waves are shown. The partial waves are ordered from top-left to bottom-right in the same order as they are listed in table 6.1. In the upper-right (lower-left) triangle the real (imaginary) parts of the corresponding interference terms are plotted. The red curve shows the fit result of the parametrization with 7 resonances as described in the text.

Figure 6.2 shows the result of a mass-dependent fit with seven resonant contributions. This overview-plot is organized such as to resemble the form of the spin-density matrix with the intensities being displayed on the diagonal sub-plots and the real and imaginary parts of the interference terms in the off-diagonal sub-plots in the upper-right and lower-left triangle, respectively. Each graph shows the respective spin-density matrix-element as a function of the 5-body mass. The black data points are the results from the mass-independent partial wave decomposition, the light-blue error bands indicate the systematic uncertainty from the waveset selection (see chapter 5). The mass-dependent fit of the parametrization described in section 6.1, including coherent, phase-space-like background in each wave is shown in red.

	Parameter			Fit	PDG
	Resonance	J^{PC}		(MeV/c^2)	
	$\pi(1300)$	0^{-+}	M	1400^*	1300 ± 100
			Γ	$500^\dagger$	200...600
	$\pi(1800)$	0^{-+}	M	$1781 \pm 5^{+1(+8)}_{-6(-6)}$	1816 ± 14
			Γ	$168 \pm 9^{+5(+62)}_{-14(-15)}$	208 ± 12
○	$a_1(1900)$	1^{++}	M	$1853 \pm 7^{+36(+36)}_{-6(-49)}$	
			Γ	$443 \pm 14^{+12(+98)}_{-45(-65)}$	
○	$a_1(2200)$	1^{++}	M	$2202 \pm 8^{+15(+53)}_{-8(-11)}$	$2096 \pm 17 \pm 121$
			Γ	$402 \pm 17^{+41(+125)}_{-52(-51)}$	$451 \pm 41 \pm 81$
	$\pi_2(1670)$	2^{-+}	M	$1719.0^\dagger$	1672.4 ± 3.2
			Γ	$251.4^\dagger$	259 ± 9
	$\pi_2(1880)$	2^{-+}	M	$1854 \pm 6^{+6(+6)}_{-4(-9)}$	1895 ± 16
			Γ	$259 \pm 13^{+7(+7)}_{-17(-31)}$	235 ± 34
○	$\pi_2(2100)$	2^{-+}	M	$2133 \pm 12^{+7(+43)}_{-18(-18)}$	2090 ± 29
			Γ	$448 \pm 22^{+60(+80)}_{-40(-40)}$	625 ± 50
			M		2245 ± 60
			Γ		320^{+100}_{-40}

○ not established * at limit; † fixed in fit

Table 6.2: Summary of extracted resonance parameters. The first uncertainty is the statistical error. The second, asymmetric uncertainty is the systematical error of the fit to the final waveset. The third uncertainties, listed in brackets, include also the systematic uncertainties from the choice of the final waveset. PDG values are from [1]

All effective coupling constants are taken complex valued except for the coupling of the $\pi_2(1670)$ to the $\pi f_2(1270) S$-wave partial wave, which is real-valued to fix the overall phase of the amplitude. Since the $\pi_2(1670)$ is a very well known resonance it has been used as a sort of prerequisite to stabilize the fit. To achieve this initial fits have been done with the parameters of the $\pi_2(1670)$ fixed to their PDG-values [1]. After a stable fit had been achieved in this fashion the parameters of all other resonances were kept fixed and the $\pi_2(1670)$ parameters were left floating in the fit. For all further fits these parameters have been kept fixed again, which is why no uncertainties on the $\pi_2(1670)$ are given here.

The ability of the relatively simple model to describe even small details in the interference terms is remarkable. The reasoning behind including seven resonant terms will be discussed in the sections below. Table 6.2 summarizes the extracted resonance parameters from this fit. There are two 0^{-+} resonances, two 1^{++} and three 2^{-+} resonances. Of those only the $\pi(1300)$, $\pi(1800)$, and $\pi_2(1670)$ and to some extend the $\pi_2(1880)$ are well established [1]. The $\pi(1300)$ is actually lying below the mass range investigated here, however, even at masses as high as $1.8\,\mathrm{GeV}/c^2$ there still seems to be a contribution from the tail of this broad resonance. There is a clear signal for the $\pi(1800)$ at a mass and width slightly below the PDG average. In section 6.2.1 these findings will be discussed in some more detail.

The 1^{++} sector is not very well understood in the mass region under investigation. We need two very broad and overlapping resonances to fit the data as shown below in section 6.2.2.

In addition to the $\pi_2(1670)$ there are two further 2^{-+} states needed. The $\pi_2(1880)$ has already been mentioned in section 1.2 as a possible hybrid meson candidate. We find Breit-Wigner parameters that compare well to previous findings and a significant coupling especially to the ρa_1 and ρa_2 decay channels. The third resonance is quite heavy and features a large width of $\sim 450\,\mathrm{MeV}/c^2$. There are two states listed in the PDG with similar resonance parameters (see table 6.2). The number of π_2 states which are needed to describe the data will be discussed in section 6.2.3.

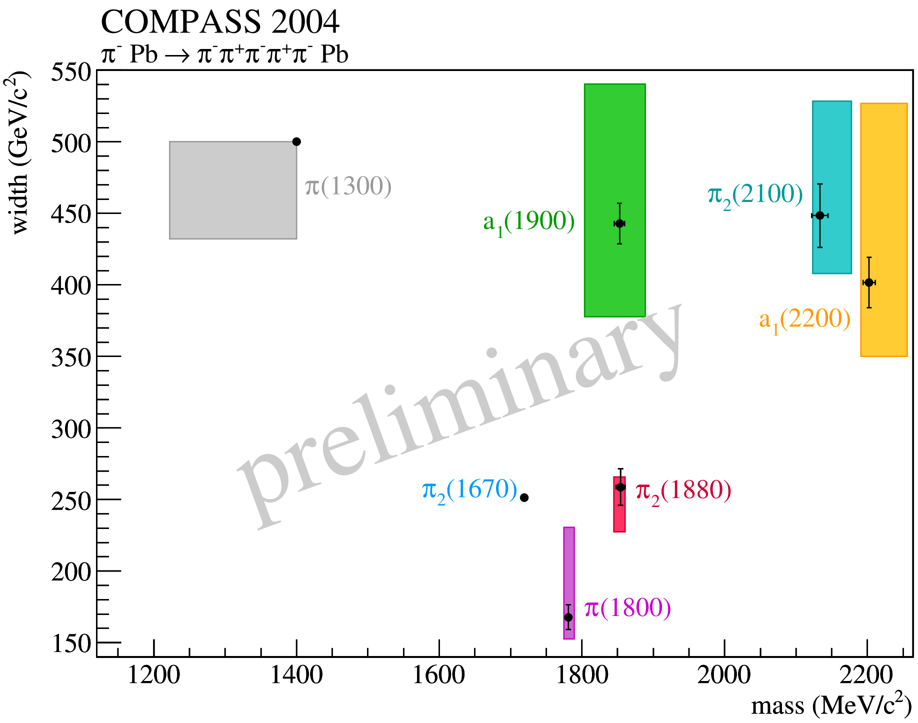

Figure 6.3: Extracted resonance parameters for the 7-resonance fit. The systematic errors shown include the systematics from choosing different fitting-ranges, using or neglecting the covariances between real and imaginary parts of the interference terms and the choice of waveset.

Figure 6.3 collects the extracted resonances in one overview where the width is plotted against the Breit-Wigner mass of the resonances. The black markers indicate the most likely solution with statistical uncertainties. The colored boxes indicate the full systematic uncertainties, which are given in table 6.2. The first set of systematic errors which are listed, are obtained by varying the mass-range over which the fit is performed. This leads only to small systematic changes of the extracted resonance parameters. Furthermore, the similar parametrizations have been obtained by using two different analysis software packages. This cross-check, which differs in the numerical implementation of many intermediate steps, leads to very similar parameters. Any differences found here are also taken into account as systematic uncertainties.
The systematic errors listed in brackets are obtained from studying the sensitivity of the results to variations of the waveset. In addition to the final waveset (tables 5.1 and 5.2) the five best performing wavesets produced by the genetic algorithm (see chapter 4) have been fitted with the 7-resonance model. The systematic uncertainties obtained in this way are much larger in most cases than any other uncertainty in the problem.
The following subsections contain a detailed discussion of the fit results for the different partial waves and comparisons with published results from other experiments. Note that the following plots have all been obtained from a simultaneous fit to the complete 10×10 spin-density matrix shown in figure 6.2. In order to study the finer details we will pick out exemplary elements of the spin-density matrix.

6.2.1 $J^{PC}M^{\epsilon} = 0^{-+}0^{+}$ Partial Waves

In the mass region covered here the dominant state in the $J^{PC} = 0^{-+}$ sector is the well known $\pi(1800)$, which we find clearly in the $f_0(1500)\pi$ decay mode.

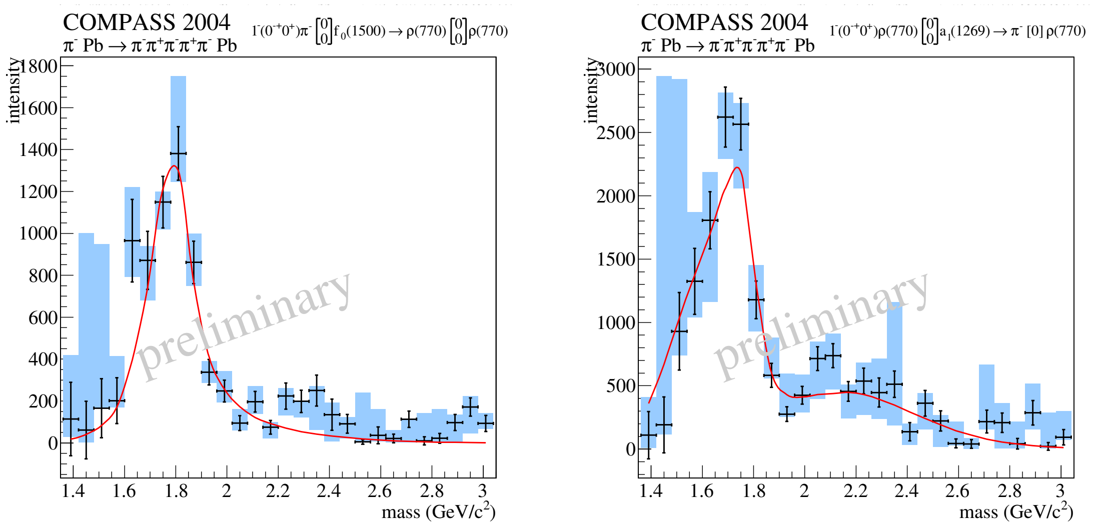

(a) $\pi f_0(1500)$ S-wave

(b) $\rho(770)a_1(1269)$ S-wave

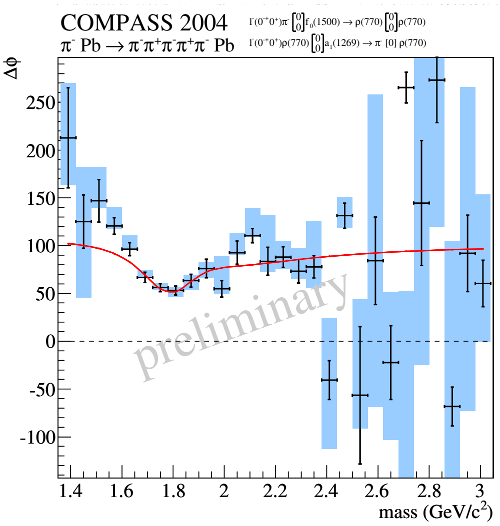

(c) Phase difference.

Figure 6.4: $J^{PC} = 0^{-+}$ waves with mass-dependent parametrization. (a) Intensity of the $\pi f_0(1500)$ S-wave (b) Intensity of the $\rho(770)a_1(1269)$ S-wave (c) Phase difference between these two partial waves. In red the fit containing two resonances and a coherent background.

Figure 6.4(a) shows the intensity of the $0^{-+}\pi f_0(1500)$ S-wave with the $f_0(1500) \to \rho^0\rho^0$ decay mode. This partial wave exhibits a very clear peak at 1.8 GeV/c^2 which can be described reasonably well by the mass-dependent parametrization. The intensity of the $0^{-+}\rho(770)a_1(1260)S$-wave is shown in Figure 6.4(b). The peak in the intensity is at a lower mass than in the $\pi f_0(1500)$ case. Indeed at ~ 1.8 GeV/c^2 there is a rather sharp drop in the intensity. This is explained in the fit as being due to a destructive interference of the $\pi(1800) \to \rho a_1$ decay amplitude with the ρa_1 background. The phase motion of the $0^{-+}\rho(770)a_1(1260)S$-wave relative to $0^{-+}\pi f_0(1500)$ is shown in Figure 6.4(c). At small masses below 1.7 GeV/c^2 there is an additional phase mo-

tion which is not accounted for in the model, although the $\pi(1300)$ has been allowed as an additional contribution coupling to both channels. Note, however, that the threshold for the $f_0(1500)\pi$ decay channel is rather sharp due to the narrow $f_0(1500)$ with $\Gamma_{f_0(1500)} = 109{\pm}7\,\mathrm{MeV}/c^2$ and is located at $m_{\mathrm{thr}} = m_{f_0(1500)} + m_\pi \approx 1645\,\mathrm{MeV}/c^2$. Furthermore although both the ρ as well as the $a_1(1260)$ are rather broad states. The region below $1.65\,\mathrm{GeV}/c^2$ is at the edge of the phase space for a decay into these states with $m_{a_1} + m_\rho - \Gamma_{a_1} - \Gamma_\rho \approx 1.6\,\mathrm{GeV}/c^2$. A more detailed model of possible background contributions, especially from multi-peripheral processes may be needed here to model the behavior at threshold (see also section 2.2.2).
The mass of the $\pi(1800)$ is fitted to a value of $m_{\pi(1800)} = 1827 \pm 6.9\,\mathrm{MeV}/c^2$ that is in good agreement with the PDG average value of $m^{PDG}_{\pi(1800)} = 1816 \pm 14\,\mathrm{MeV}/c^2$ [1]. Also the width of $\Gamma_{\pi(1800)} = 224 \pm 17.6\,\mathrm{MeV}/c^2$ is in agreement within uncertainties to the PDG value of $\Gamma_{\pi(1800)} = 208 \pm 12\,\mathrm{MeV}/c^2$. A closer look at the mass values from different analyzes gathered in the PDG report [1] shows a spread from as low as $\sim 1770\,\mathrm{MeV}/c^2$ to up to $\sim 1870\,\mathrm{MeV}/c^2$. From this compilation it is clear that the extracted resonance parameters strongly depend on the specific method used and analyses of different channels tend to give different answers. The result obtained here is consistent with these previous measurements.

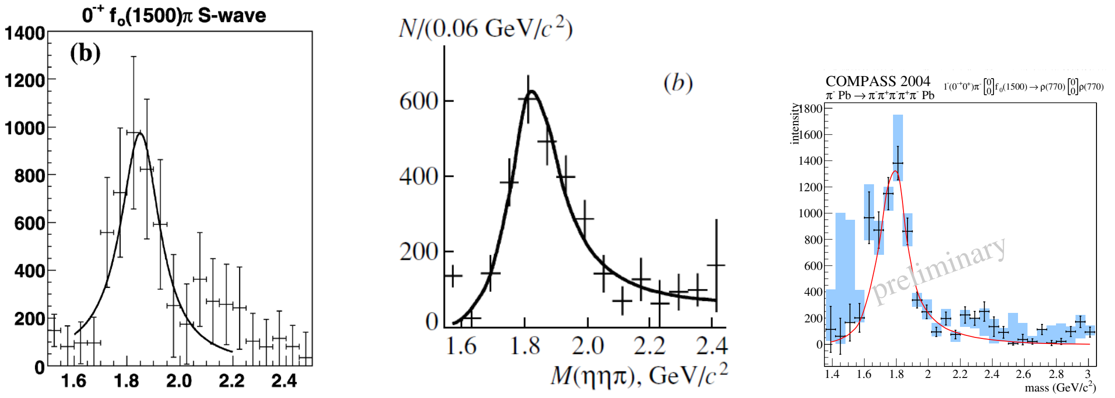

(a) BNL E852 (b) VES (c)

Figure 6.5: Comparison of the $f_0(1500)\pi$ s-wave intensity: a) obtained from an analysis of the $\eta\eta\pi$ system at BNL [162]. b) obtained from an analysis of the $\eta\eta\pi$ system at VES [163] c) COMPASS 5π result. Note the slightly different scaling of the abscissas.

The $\pi f_0(1500)$ decay mode of the $\pi(1800)$ has been of special interest since the narrow isoscalar $f_0(1500)$ is a prime glueball candidate. Both the BNL E852[162] and VES [163] collaborations have studied this partial wave in the $\eta\eta\pi$ final state. The intensities that have been extracted in these 3-body partial wave analyzes are shown in Figure 6.5 in comparison to the COMPASS 5π result. There is a reasonable qualitative agreement between the three results. However, in order to study the details of the resonance shape more data will be required and in particular coupled channel effects will have to be investigated.

$\pi(1300)$ Contribution

The $\pi(1300)$ is a very broad resonance that has been observed in the 3π system [1]. Because of its large width of 200 to $600\,\mathrm{MeV}/c^2$ the state's parameters are not very well determined. Due to the large width the high-mass tail of the resonance might contribute even to the region above 1.6 GeV/c^2 and for that reason it has been included in the fit. The 5π final state with the given amount of data provides too little coverage in the relevant region to get a credible fit of the parameters of this state. Note that the $\pi(1300)$ is also occurring as an isobar in several decay amplitudes. The analysis is not completely self-consistent in the sense that the parameters used for the isobars are not synchronized with the parameters found in the mass-dependent fit to the 5π spin-density matrix.

6.2.2 $J^{PC}M^{\epsilon} = 1^{++}0^{+}$ Partial Waves

The 1^{++} sector is the most difficult one to describe in terms of the model used here. If one uses the ansatz nevertheless, a single resonance is insufficient to describe the observed interference patterns. Also, looking at previous analyzes the situation in the region around 1.8 GeV/c^2, where the 1^{++} partial waves exhibit an intensity peak is especially unclear and so far just a few publications have presented fits to these partial waves in this mass-region (see [63] for example).

In the 5π data we find a good description with two heavy 1^{++} states. A prominent signal is observed in the $\pi f_0(1370)$ decay mode as shown in Figure 6.6(a). An interesting feature of this amplitude is the drop to zero intensity at 2.2 GeV/c^2 which in the mass-dependent fit is interpreted as a strong destructive interference of the background with a resonance. As mentioned in section 1.2, a significant branching fraction into this decay mode according to the flux-tube model contradicts the interpretation of a heavy a_1 resonance as a hybrid meson [34]. Here we confirm findings of earlier analyses.

A well studied amplitude is the $1^{++} f_1(1285)\pi$ partial wave. The results of the mass-dependent fit for this wave is shown in Figure 6.6(b). The intensity distribution is broad around 1.8GeV/c^2 and reaches to unusually low masses for a P-Wave, as has also been noted by other experiments (see for example [63]). Figure 6.6(c) shows the phase difference of the $f_1\pi$ P-wave to the $f_0\pi$ P-wave, which is well reproduced with this parametrization.

Another strong $J^{PC} = 1^{++}$ amplitude is the decay mode $\rho(770)\pi(1300)$ in S-wave. The corresponding intensity is shown in 6.7(a). It resembles the shape of the $\pi f_0(1370)$ P-wave with the dip at 2.2 GeV/c^2 being not quite as expressed.

The relatively small D-wave has a remarkable influence in the fit. It's interference terms help to stabilize the fit in the 1^{++} sector and allow the separation of the two contributing states. Figure 6.7(b) shows the result. Figure 6.7(c) shows the phase difference between the $1^{++}\rho(770)\pi(1300)S$-wave and the $1^{++}(\pi\pi)_S a_1(1260) D$-wave.

Figure 6.8 finally shows the interference between the $1^{++}\pi f_1(125)$ partial wave and the $0^{-+}\pi f_0(1500)$ amplitude. The rising relative phase produced by the $\pi(1800)$ is clearly visible in this plot, although the magnitude of the effect is greatly reduced by the presence of the two a_1 resonances, which create considerable phase motion in their respective channels. The fit again fails to describe the phase at low masses and from this plot we can conclude that this problem has its roots in the representation of the $0^{-+}\pi f_0(1500)$ amplitude (see also discussion in section 6.2.1).

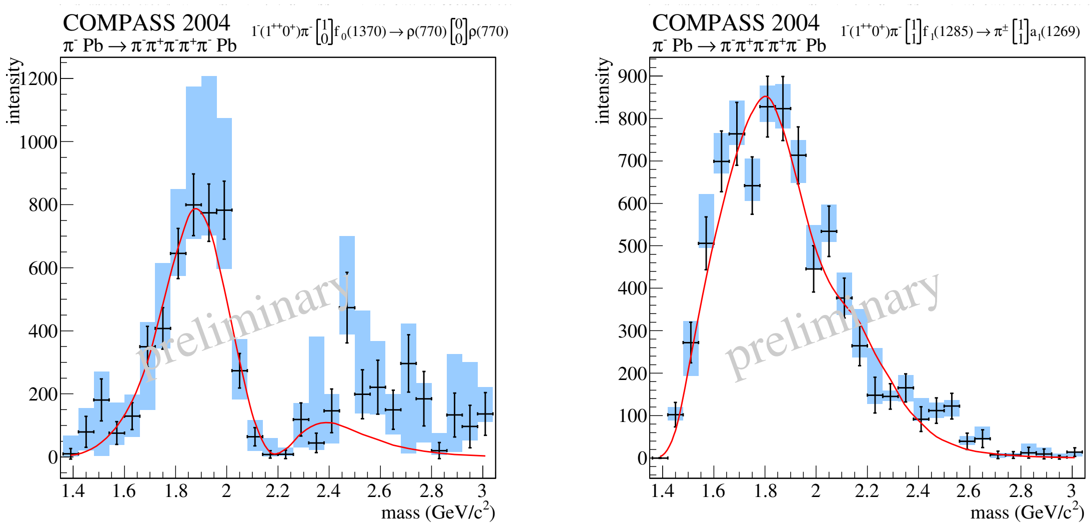

(a) $1^{++}\pi f_0(1370)$ P-wave

(b) $1^{++}\pi f_1(1285)$ P-wave

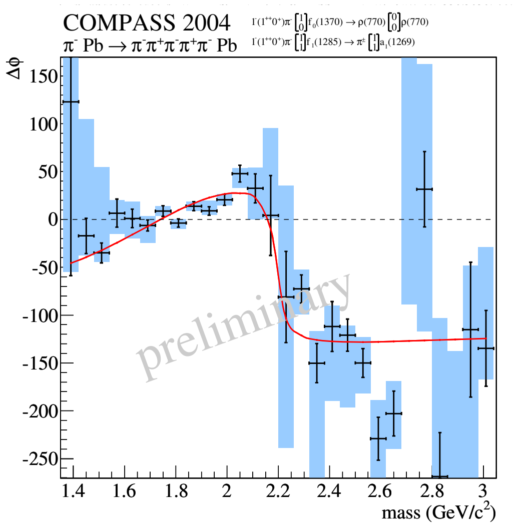

(c) Phase difference.

Figure 6.6: $J^{PC} = 1^{++}$ partial waves with mass-dependent parametrization. (a) $\pi f_0(1370)$ P-wave intensity. Note the drop of this intensity to almost zero around $m_{5\pi} \sim 2.2\,\mathrm{GeV}/c^2$ (b) $\pi f_1(1285)$ P-wave intensity (c) Phase difference. The red line shows the fit with two 1^{++} Breit-Wigner amplitudes and a coherent background in each wave.

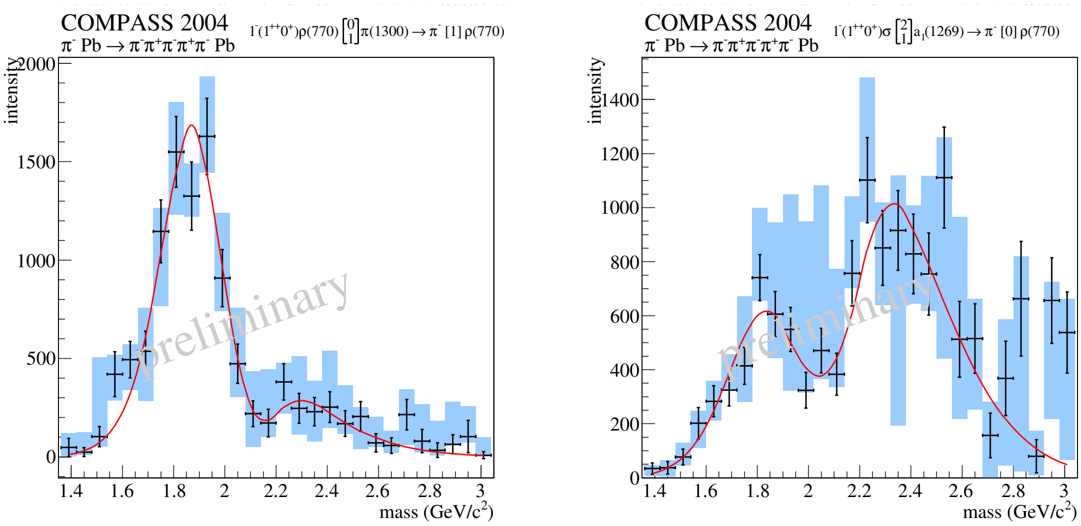

(a) $1^{++}\rho\pi(1300)S$-wave

(b) $1^{++}(\pi\pi)_S a_1(1260)D$-wave

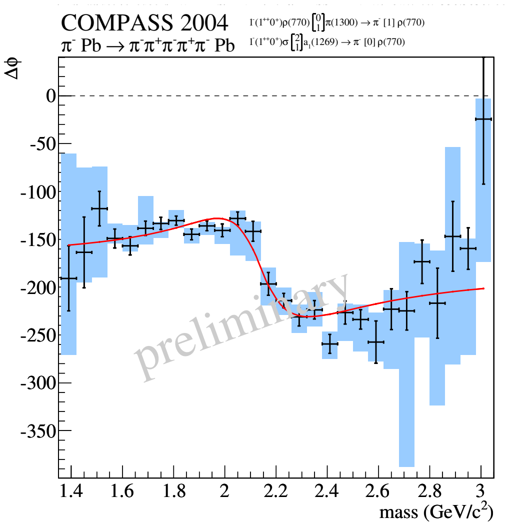

(c) Phase difference

Figure 6.7: (a) $1^{++}\rho\pi(1300)S$-wave intensity (b) $(\pi\pi)_S a_1(1260)D$-wave intensity (c) Phase difference. Note that the rapid phase motion just below $m_{5\pi} \sim 2.2\,\text{GeV}/c^2$ is not due to a single narrow resonance but can be explained with the interference of two broad states.

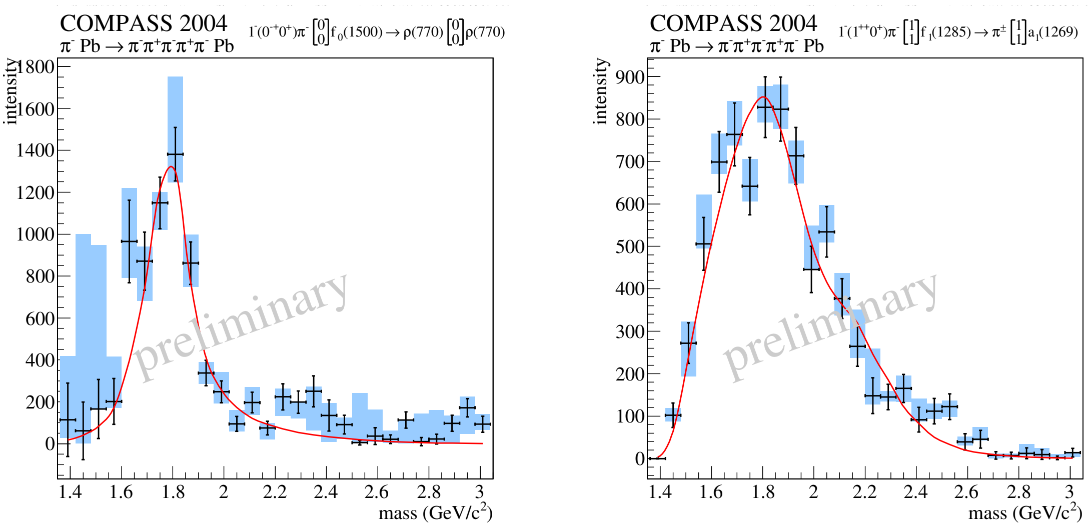

(a) $0^{-+}\pi f_0(1500)$ S-wave

(b) $1^{++}\pi f_1(1285)$ P-wave

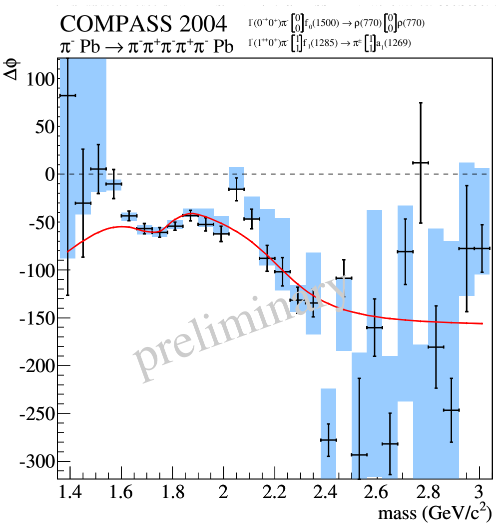

(c) Phase difference.

Figure 6.8: Interference between the $J^{PC} = 0^{-+}\pi f_0(1500)$ S-wave (a) and the $1^{++}\pi f_1(1285)$ P-wave (b). The phase difference is shown in (c). The red line shows the fit with two 1^{++} and two 0^{-+} Breit-Wigner amplitudes and a coherent background in each wave.

Fit With Only One a_1 Resonance

An alternative scenario would be to fit the 1^{++} sector with only one resonance and the non-resonant background. Figure 6.9 shows the fit of such a model to the data. It is apparent that especially above 2.2 GeV/c^2 the phases and especially the $1^{++}(\pi\pi)_S a_1(1260)D$-wave are not well described. This is the main motivation to parametrize the 1^{++} waves with two resonances. However, a valid criticism of this ansatz would be that the neglect of mixing terms as discussed in section 1.3.1 is a problematic simplification in a situation where there is so strong overlap between two resonances as in the case here with the two a_1 states we have used. For a better understanding of the system this will definitely have to be taken into account in future analyses.

Comparison To Other Experiments

Due to the narrow isobar the $f_1\pi$ system is relatively easy to study, especially in decay channels where the contributions from other isobars is small, such as $f_1 \to \eta\pi^+\pi^-$. The comparison of our result to a partial-wave analysis of this final state from the E835 collaboration is shown in Table 6.3.

The BNL fit [63] requires two a_1 resonances with similar parameters as in the 5π case (see table 6.3). However, the parameters of the lighter state at 1714 MeV/c^2 had to be fixed in that analysis in order to get a converging fit.

Resonance	J^{PC}	(MeV/c^2)	COMPASS 5π	E835 $\eta\pi^+\pi^-\pi^-$
○ $a_1(1900)$	1^{++}	M	1853 ± 7	1714(fixed)
		Γ	443 ± 14	308(fixed)
○ $a_1(2160)$	1^{++}	M	2202 ± 8	$2096 \pm 17 \pm 121$
		Γ	402 ± 17	$451 \pm 41 \pm 81$

○ not established

Table 6.3: Comparison of the heavy a_1 resonance parameters extracted in $1^{++}f_1(1285)\pi \to \eta\pi^+\pi^-\pi^-$ [63] and the results obtained in the 5π final state.

It should be noted that the resonant nature of the 1^{++} wave in the $f_1\pi$decay mode is not only interesting in itself. The question is significant because in the above mentioned analysis the two a_1 states have been used as interferometers to claim a spin exotic $1^{-+}\pi_1(2000)$ meson. An independent confirmation of the resonance content of the 1^{++} wave in this mass region would be a very important check of that approach. The results obtained from the 5π state provide further evidence on such resonant contributions to the 1^{++} partial waves, however, mixing between these two broad states as well as more detailed investigations of the non-resonant background should be conducted before final conclusions can be made.

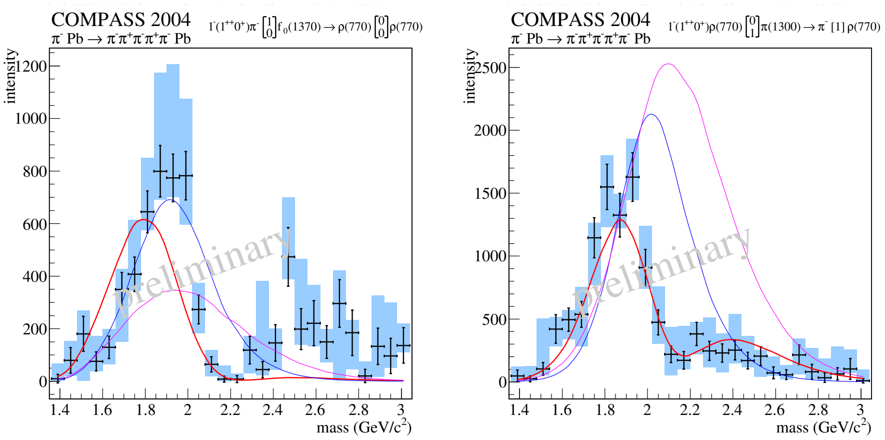

(a) $\pi f_0(1370)$ P-wave

(b) $\rho\pi(1300)$ S-wave

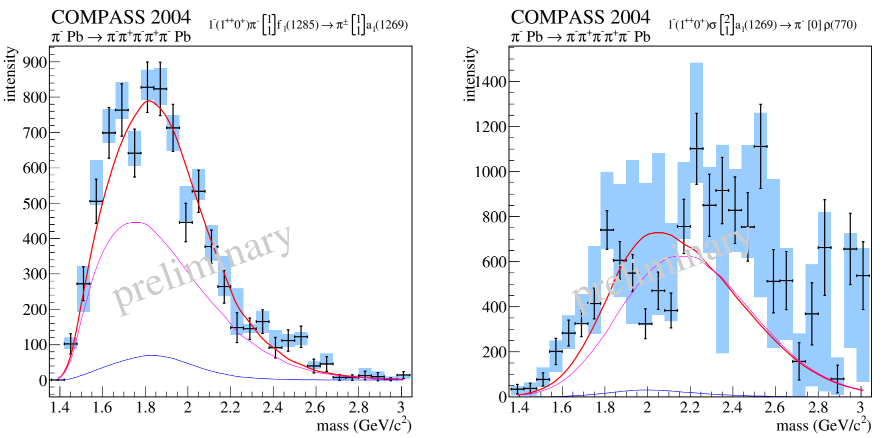

(c) $\pi f_1(1285)$ P-wave

(d) $(\pi\pi)_S a_1(1260)$ D-wave

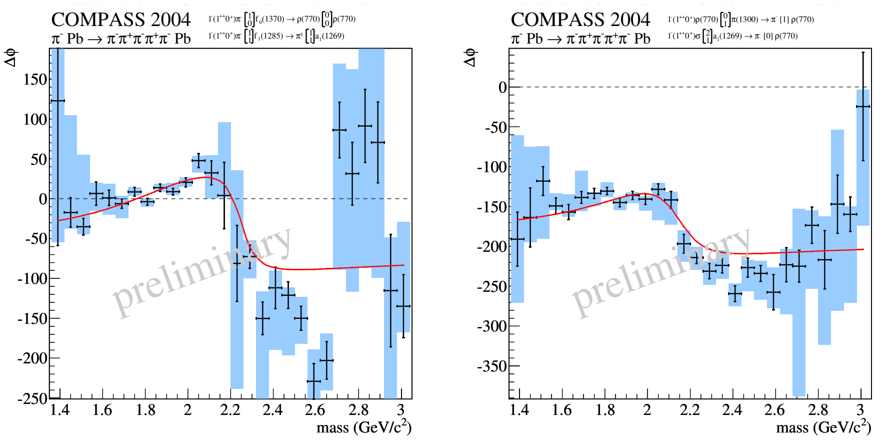

(e) $\pi f_0(1370)$ — $\pi f_1(1285)$ phase difference.

(f) $\rho\pi(1300)$ — $(\pi\pi)_S a_1(1260)$ phase difference

Figure 6.9: $J^{PC} = 1^{++}$ partial waves with mass-dependent parametrization containing only one $J^{PC} = 1^{++}$ resonance.

6.2.3 $J^{PC}M^{\epsilon} = 2^{-+}0^{+}$ Partial Waves

In the 2^{-+} sector three resonances are needed to describe the data. Apart from the very well established $\pi_2(1670)$ we find two more resonances: The $\pi_2(1880)$ and a heavy $\pi_2(2100)$.

The $\pi f_2(1270)$ decay mode of the $\pi_2(1670)$ is well known from the 3π system with the $f_2(1270)$ decaying into $\pi^+\pi^-$. The result of the mass dependent fit for the $2^{-+} f_2(1270)\pi$ S-wave, in the case of a 4-pion decay of the $f_2(1270)$ is shown in Figure 6.10(a). The peak at $m_{5\pi} \sim 1.7\,\mathrm{GeV}/c^2$ is dominated by the $\pi_2(1670)$. In comparison Figure 6.10(b) shows the $2^{-+}\rho a_1$ S-wave, which displays a quite peculiar shape with a prominent dip at $m_{5\pi} \sim 1.9\,\mathrm{GeV}/c^2$. This dip is due to a destructive interference of the $\pi_2(1880)$ with the two neighboring states and the background. The strong second peak in the spectrum can only fully be explained by allowing a third resonance as will be discussed below.

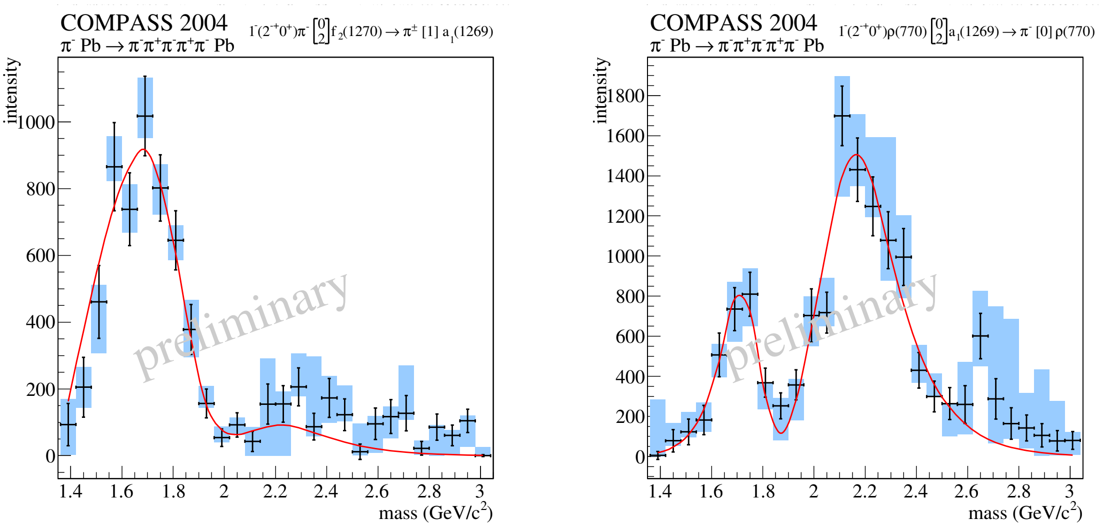

(a) $\pi^- f_2(1270)$ S-wave

(b) $\rho a_1(1269)$ S-wave

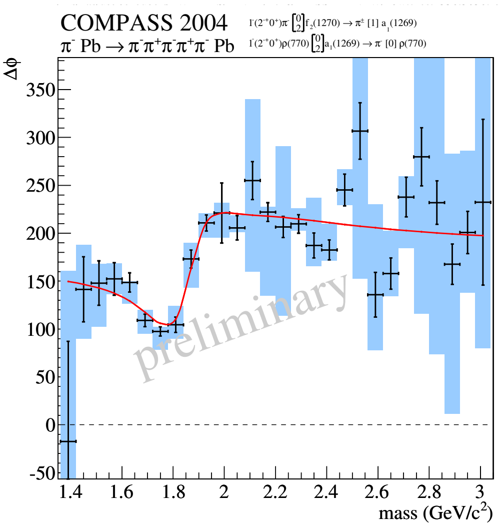

(c) Phase difference

Figure 6.10: $J^{PC} = 2^{-+}$ partial waves. (a) $\pi^- f_2(1270)$ S-wave intensity. (b) $\rho a_1(1269)$ S-wave intensity. (c) Phase difference. The red line shows the fit with three 2^{-+} Breit-Wigner amplitudes and a coherent background in each wave.

The phase difference between these two waves is shown in Figure 6.10(c) and is quite well fit by the parametrization with three Breit-Wigner amplitudes in the 2^{-+} sector. The rapid phase-motion around $m_{5\pi} \sim 1.9\mathrm{GeV}/c^2$ is quite characteristic and is well above the region where the $\pi_2(1670)$ is resonating, lending evidence to the existence of a second resonance — the $\pi_2(1880)$. This picture is consistently repeated in the other 2^{-+} partial waves.

One of the most stable amplitudes in the partial-wave decomposition is the $2^{-+}\rho(770)a_2(1320)S$-wave shown in Figure 6.12(a). Both the peak at $1.9\,\mathrm{GeV}/c^2$ as well as the shoulder around $2.2\,\mathrm{GeV}/c^2$ are successfully described. The $\rho a_1(1269)$ D-wave is shown in Figure 6.12(b). The fit describes the gross features of this intensity, however, above $m_{5\pi} \sim 2\,\mathrm{GeV}/c^2$ there are more sudden intensity fluctuations as can be represented with the parametrization used here. In the phase difference of these two amplitudes shown in Figure 6.12(c), the situation is reverse. While it varies smoothly and rather slow between $m_{5\pi} \sim 1.8\,\mathrm{GeV}/c^2$ and $2.4\,\mathrm{GeV}/c^2$ the fitted parametrization shows a small kink at $m_{5\pi} \sim 2.1\,\mathrm{GeV}/c^2$. We will come back to these features in the discussion on the number of 2^{-+} resonances required.

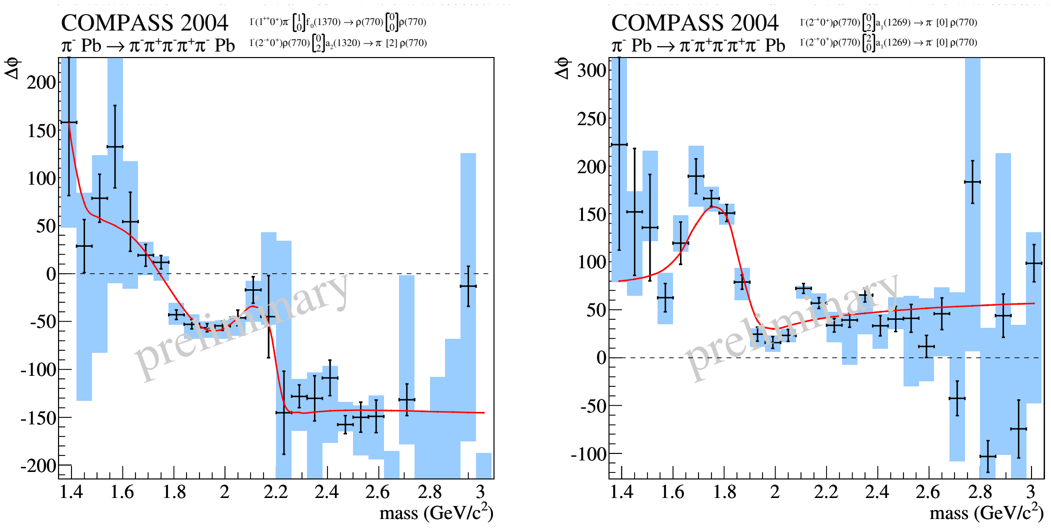

(a)

(b)

Figure 6.11: (a) Phase difference of $1^{++}\pi f_0(1370)P$-wave to $2^{-+}\rho a_2(1320)S$-wave. (b) Phase difference of $2^{-+}\rho a_1(1269)D$-wave to $2^{-+}\rho a_1(1269)S$-wave.

Another set of phases is shown in Figure 6.11 illustrating the quality of the fit for these elements of the spin-density matrix. The interference between the $1^{++}\pi f_0(1370)P$-wave and the $2^{-+}\rho a_2(1320)S$-wave is shown in Figure 6.11(a). A good representation over the whole mass range is achieved here. Figure 6.11(b) shows the phase difference between the $2^{-+}\rho a_1(1269)D$-wave and the corresponding S-wave.

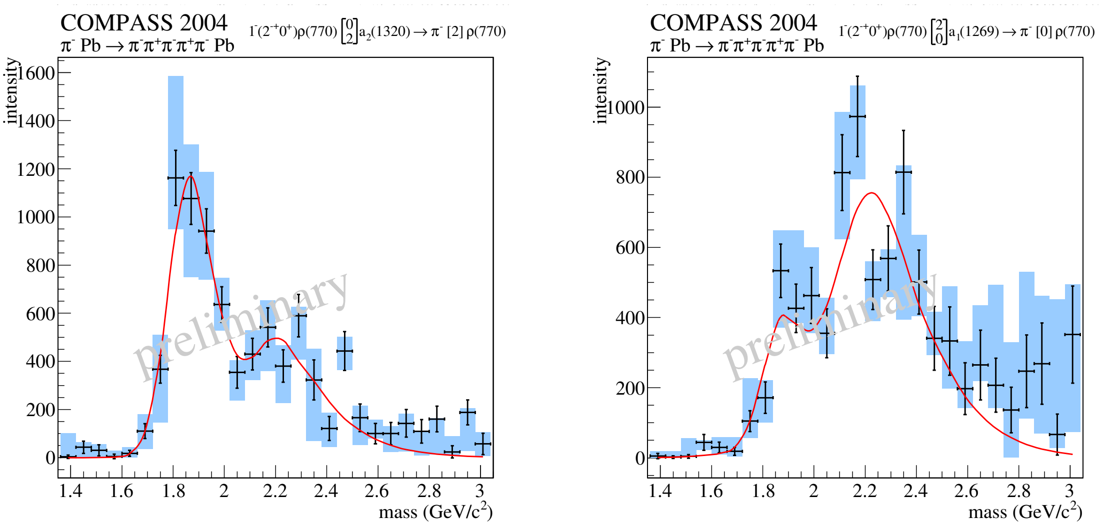

(a) $\rho a_2(1320)$ S-wave

(b) $\rho a_1(1269)$ D-wave

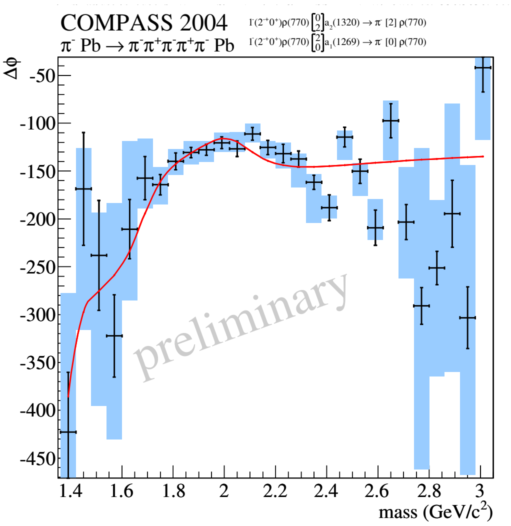

(c) Phase difference

Figure 6.12: $J^{PC} = 2^{-+}$ partial waves. (a) $\rho a_2(1320)$ S-wave intensity. (b) $\rho a_1(1269)$ D-wave intensity. (c) Phase difference

Number of 2^{-+} Resonances

With three Breit-Wigner terms in the parametrization of the 2^{-+} amplitude the natural question arises what is the true number of states required to fit the data. Before discussing the different attempts that have been made to answer this question, a word of caution is in order. As has been discussed in section 1.3.1 overlapping resonances will mix, leading to amplitudes that can differ significantly from the parametrization used here. Furthermore an unambiguous determination of the poles of the amplitude can only be achieved through a proper analytical continuation into the complex s-plane, which is not possible with the simplified amplitude used in our fit. Consequently in this analysis we are only searching for a parametrization of the spin-density matrix elements for physical $s = m_{5\pi}^2 \in \mathbb{R}$.

In order to investigate the number of Breit-Wigner terms needed to fit the 2^{-+} amplitudes fits with up to four resonances have been performed, while the 0^{-+} and 1^{++} sectors of the model have been kept unchanged but their parameters allowed to be re-optimized.

For an illustration of the outcome of this procedure figures 6.13 to 6.16 show the two S-wave amplitudes $2^{-+}\rho a_1$ (a) and $2^{-+}\rho a_2$ (b) with the real (b) and imaginary (d) parts of their interference term. This is of course just a subset of all the amplitudes that have been fitted simultaneously, chosen here because they most clearly show the effect of changing the number of resonances. In red the inferred mass-dependent parametrization is shown. The different fits correspond to the cases with one, two, three or four resonances. Each fit also includes a coherent, phase-space-like background term.

Both the one and two resonance fit give a very bad description of the data. While the peak at $\sim 1.7\,\mathrm{GeV}/c^2$ in the $\rho a_1\,S$-wave can be reproduced reasonably well both fits fail to describe the high-mass part of the amplitude, the intensity in the $\rho a_2\,S$-wave and also the details of the interference term.

By comparison the three resonance model shown in Figure 6.15 results in a nice fit. In particular the intermediate step visible in the real part of the interference term (Figure 6.15(b)) at $m_{5\pi} \sim 1.9 GeV/c^2$ can be reproduced in this model. The resulting heavy $\pi_2(2100)$ state has a fitted mass of $m = 2133 \pm 12\,\mathrm{MeV}/c^2$ and a width of $\Gamma = 448 \pm 22\,\mathrm{MeV}/c^2$. It was this drastic improvement of the fit which led to the conclusion that at least three resonant terms are needed to describe the data.

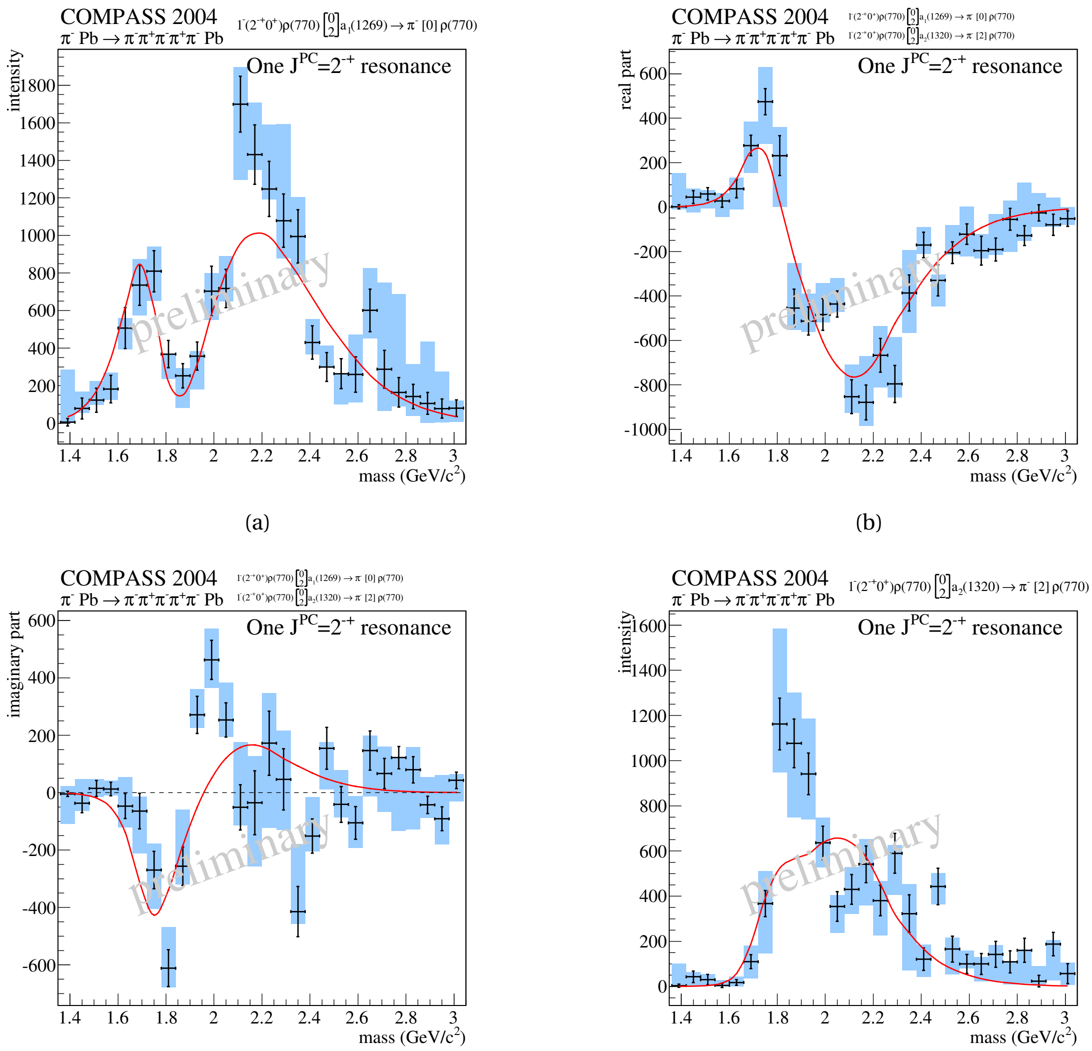

(a) (b) (c) (d)

Figure 6.13: The $2^{-+}\rho\, a_1$ (a) and $2^{-+}\rho\, a_2$ (d) amplitudes and their interference (c,b) as described by fit with only one π_2 resonance.

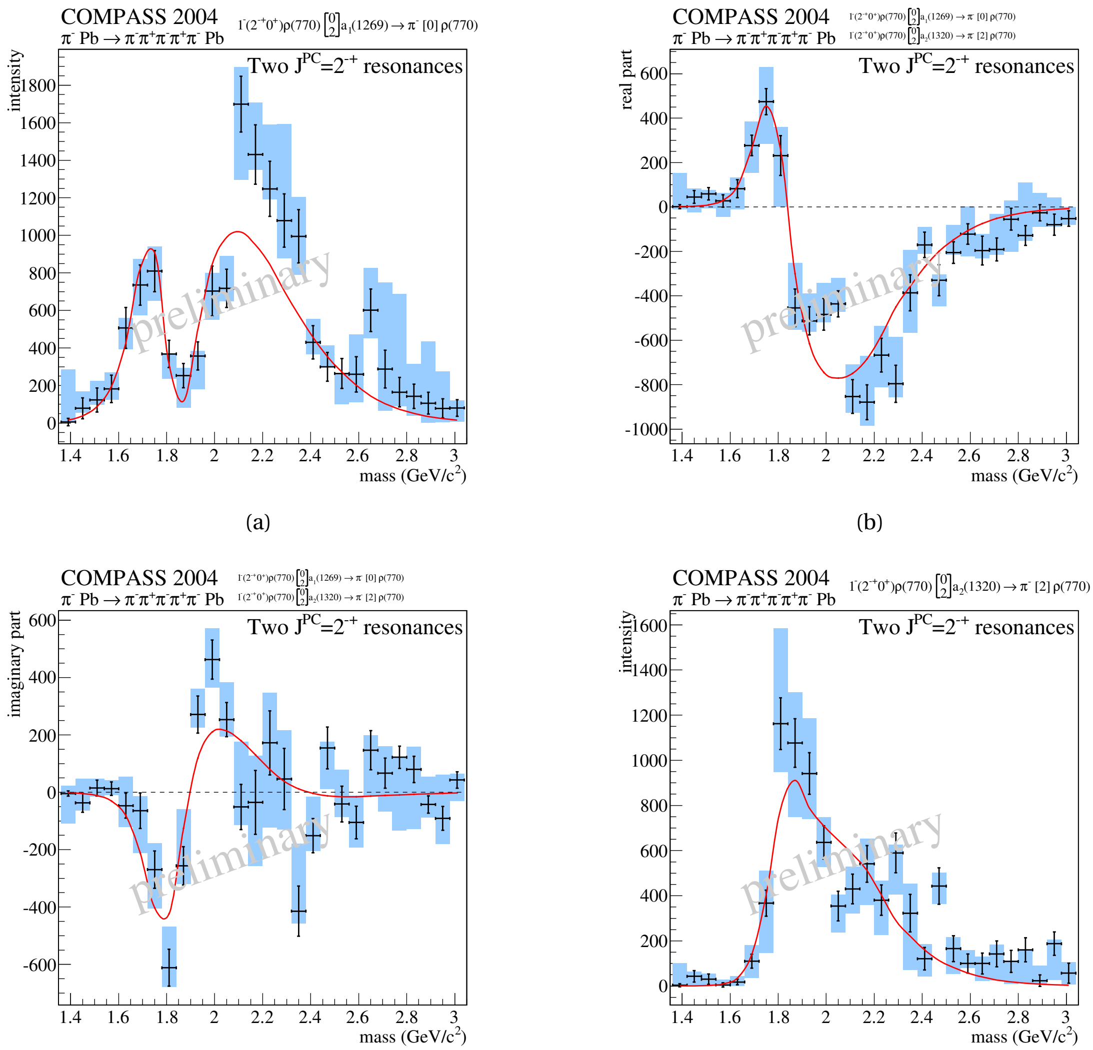

(a) (b) (c) (d)

Figure 6.14: The $2^{-+}\rho\, a_1$ (a) and $2^{-+}\rho\, a_2$ (d) amplitudes and their interference (c,b) as described by fit with two π_2 resonances.

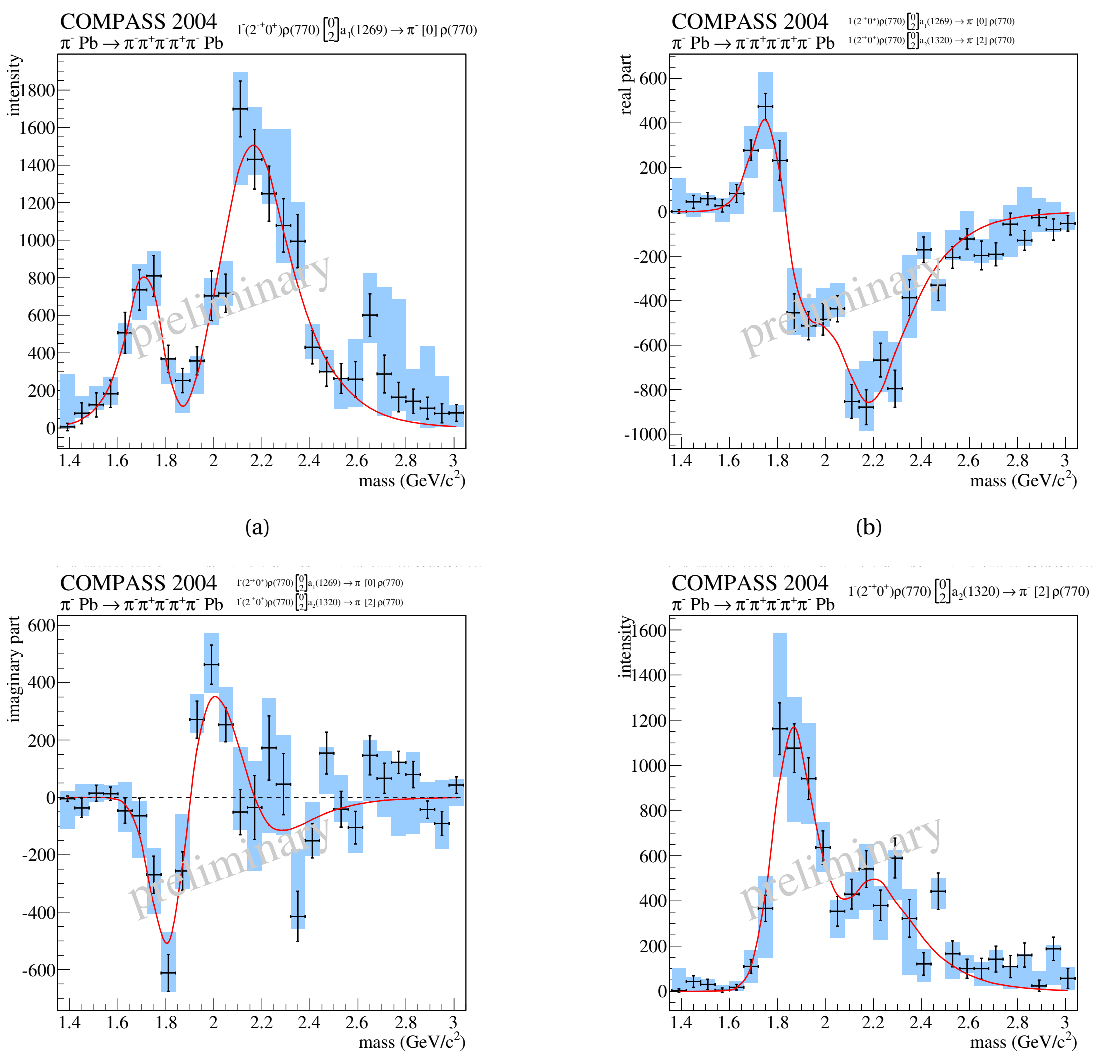

(a) (b)

(c) (d)

Figure 6.15: The $2^{-+}\rho\, a_1$ (a) and $2^{-+}\rho\, a_2$ (d) amplitudes and their interference (c,b) as described by the fit with three π_2 resonances. This is the reference fit.

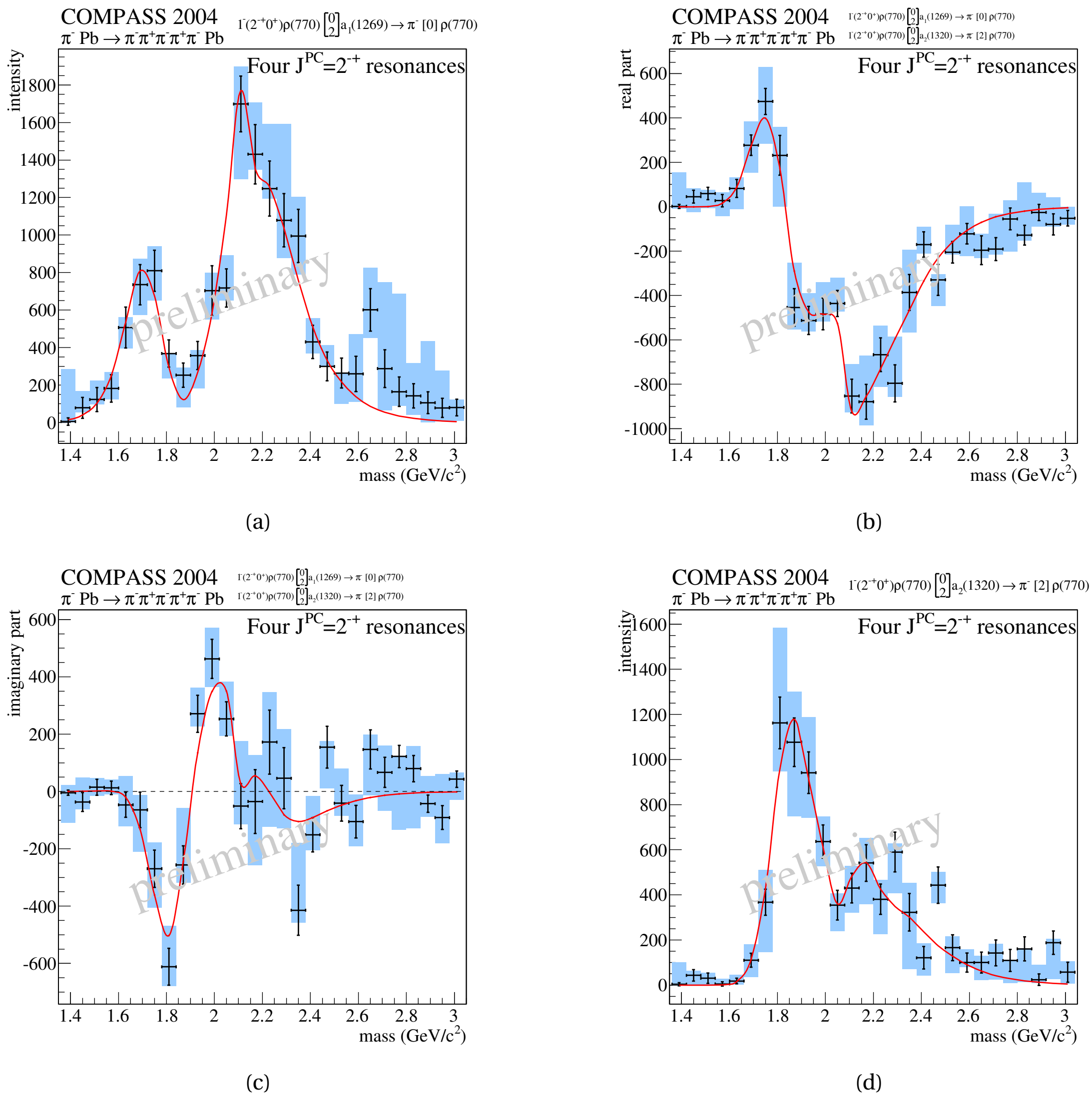

(a) (b) (c) (d)

Figure 6.16: The $2^{-+}\rho\, a_1$ (a) and $2^{-+}\rho\, a_2$ (d) amplitudes and their interference (c,b) as described by the fit with four π_2 resonances. Note that the this fit is unstable if the allowed parameter ranges are changed.

The PDG [1], however, in addition to the $\pi_2(1670)$ and the $\pi_2(1880)$ lists two 2^{-+} candidates with masses higher than $2\,\mathrm{GeV}/c^2$. The third resonant term required in our fit lies in between these values and does not obviously fit any of them (see table 6.4). The $\pi_2(2100)$ is listed in the proper PDG table but omitted from the summary tables and flagged as *needs confirmation*. The $\pi_2(2245)$ is listed under *further states*, which is the least established category of resonances in the PDG. A recent reanalysis of Crystal Barrel data has revised the mass of this state to the value of $2285 \pm 20 \pm 25$ [164].

Therefore, in order to test the PDG scenario a fourth 2^{-+} resonance has been allowed in the fit. The result for the two example waves is shown in Figure 6.16. Indeed there is some improvement in the finer details of the amplitude. The step in the real part of the interference term is

Resonance	J^{PC}	(MeV/c^2)	
∘ $\pi_2(2100)$	2^{-+}	M	2090 ± 29
		Γ	625 ± 50
∘ $\pi_2(2245)$	2^{-+}	M	$2285 \pm 20 \pm 25$
		Γ	$250 \pm 20 \pm 25$

∘ not established

Table 6.4: High mass π_2 candidates listed in the PDG [1] in need of confirmation.

even better described and also for the intensities the parametrization follows the data points very closely. The improvements achieved in this way are even more visible if one compares the phase difference between the $2^{-+}\rho a_2\, S$-wave and the $\rho a_1\, D$-wave as shown in Figure 6.17. The smooth variation of this phase-difference is well reproduced in the fit with four resonant terms. Apparently a peculiar cancellation between the different terms takes place to generate this result.

However, it turns out that the resonance parameters extracted in the model with four Breit-Wigner terms are not stable and it was not possible to achieve a stable fit with this parametrization without any parameter hitting the limits of its allowed range. Probably this shows that using so many terms without taking mixing effects into account really stretches the limitations of the ansatz too far, especially if there indeed would be an extremely wide $\pi_2(2100)$ with a width of over 600MeV/c^2 as the Crystal Barrel results imply. More detailed studies therefore require taking into account mixing effects and also the coupling to other channels as far as possible.

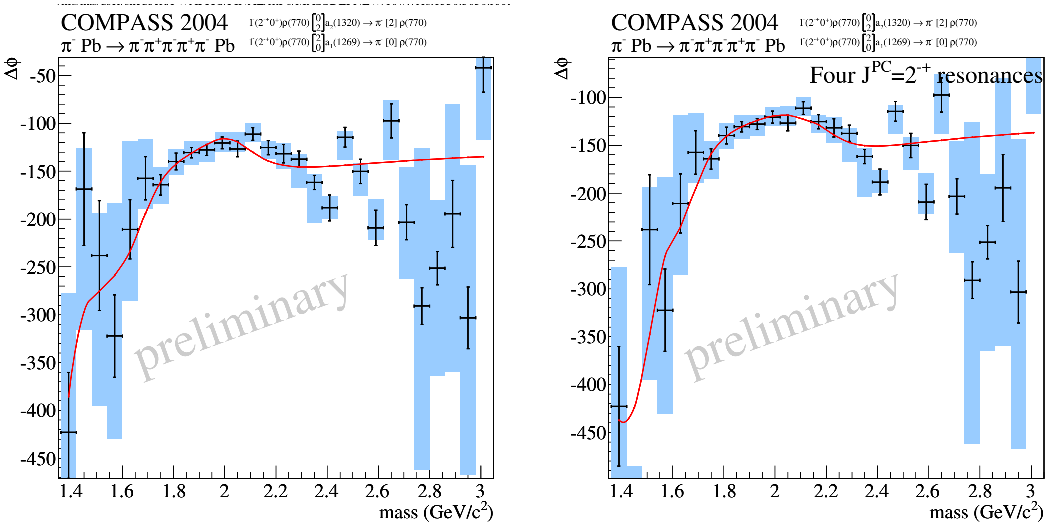

(a) Phase difference

(b) Phase difference

Figure 6.17: Comparison of the parametrization of the phase-difference between the $2^{-+}\rho a_2\, S$-wave and the $\rho a_1\, D$-wave. (a) shows the fit with three π_2 resonances. (b) with four resonances. Note that the latter fit is unstable if the allowed parameter ranges are changed.

Comparison of the results on the 2^{-+} Partial Wave to other Experiments

As has been mentioned in section 1.2 the $\pi_2(1880)$ in particular is a strongly debated state since its mass is so close to the $\pi_2(1670)$ that it seems to be unlikely to be a radial excitation of the latter. The $\pi_2(1880)$ has been, however, observed by several experiments. As an example figure 6.18 (a) shows the intensity of the $2^{-+}\omega\rho$ P–wave obtained in [165] using a partial wave analysis of the $\omega\pi^+\pi^-$ system with $\omega \to \pi^+\pi^-\pi^0$. For comparison the $\rho a_1(1260) S$-wave is shown again in Figure 6.18(b).

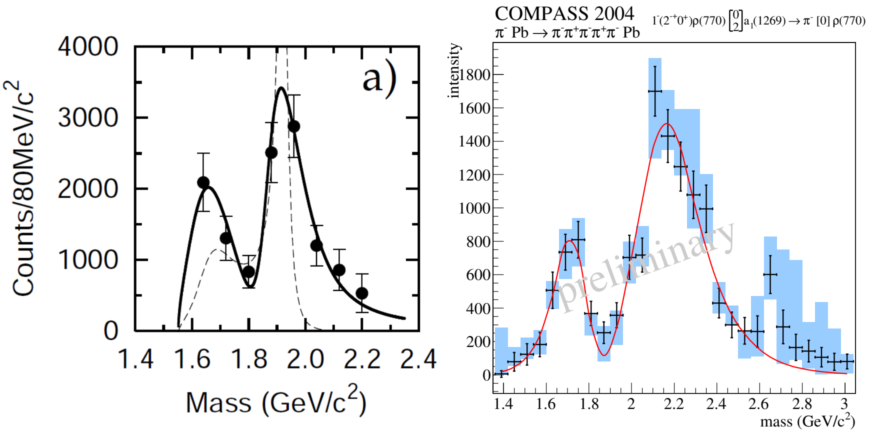

(a) (b)

Figure 6.18: Comparison of the 2^{-+} intensities: (a) $\omega\rho$ P-wave obtained from an analysis of the $\omega\pi^0\pi^-$ system at BNL [165]. (b) COMPASS 5π result: $a_1(1269)\rho$ S-wave. Note the different scales of the abscissas.

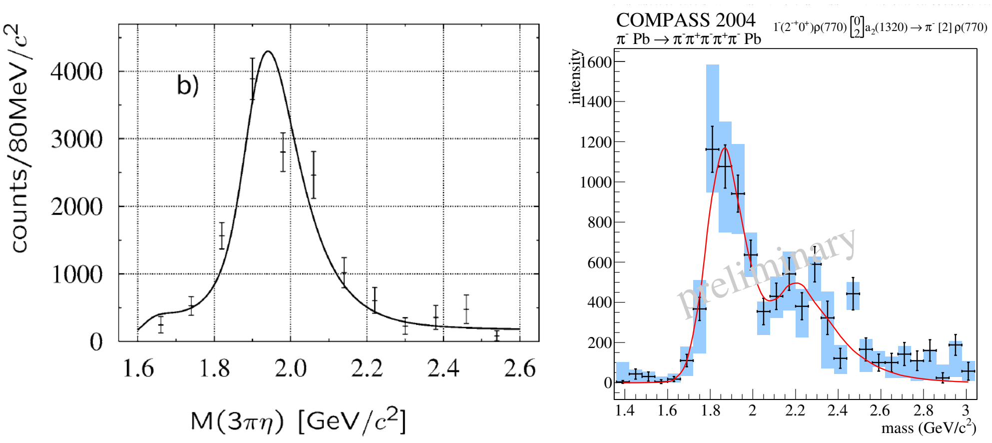

(a) (b)

Figure 6.19: Comparison of the 2^{-+} intensities: (a) $\eta a_2(1320)$ S-wave obtained from an analysis of the $\eta 3\pi$ system at BNL [63].(b) COMPASS 5π result: $a_2(1320)\rho$ S-wave. Note the different scales of the abscissas.

Both intensities display a superficially similar structure. A closer inspection of the respective

mass-scale, however, shows that while the $\pi_2(1880)$ appears as a dip in the 5π final state there it is visible as a peak in the $\omega\rho$ partial wave. An interesting option for future analysis will be a combined fit of data from these two final states.
Another example is the shown in Figure 6.19. Here the 2^{-+} partial waves for $\eta a_2^-(1320)$ in $\eta 3\pi$ [63] and $\rho^0 a_2^-(1320)$ in the 5π final state are compared. The peak at $1.9\,\mathrm{GeV}/c^2$, attributed to the $\pi_2(1880)$ compares quite well in both final states. At higher masses the prominent shoulder in the 5π data is not visible in the $\eta a_2(1320)$ partial wave. It would be interesting to investigate how these features can be explained in a coupled channel model.

Mass (MeV/c^2)	Experiment	Reaction
$1929 \pm 24 \pm 18$	E852	$\pi^- p \to \eta\eta\pi^- p$
$1876 \pm 11 \pm 67$	E852	$\pi^- p \to \omega\pi^-\pi^0 p$
$2003 \pm 88 \pm 148$	E852	$\pi^- p \to \eta\pi^-\pi^+\pi^- p$
$1880 \pm 20 \pm 148$	CB	$\bar{p}p \to \eta\eta\pi^0\pi^0$
1895 ± 12	PDG average	
$1836 \pm 13 + 0 - 44$	COMPASS	$\pi^- Pb \to \pi^-\pi^+\pi^- Pb$
$1854 \pm 6^{+6}_{-9}$	COMPASS	$\pi^- Pb \to \pi^-\pi^+\pi^-\pi^+\pi^- Pb$

Table 6.5: Measured values for the mass of the $\pi_2(1880)$ resonances. As reported in [1] and compared to the COMPASS results.

A compilation of different results for the mass of the $\pi_2(1880)$ resonances is given in table 6.5 [1]. The data point in the 3π system measured by COMPASS has been obtained in a recent analysis [102]. The mass and width of the $\pi_2(1880)$ in both COMPASS analyzes is determined to be a bit lower than the E852 and Crystal Barrel results. Note, however, the large systematic uncertainties.

6.3 Search for $J^{PC} = 4^{-+}$ Resonances

In the introduction section 1.2 we have discussed the question whether there is a $J^{PC} = 4^{-+}$ at as mass of $2\,\mathrm{GeV}/c^2$, effectively a parity partner of the well known $a_4(2040)$. In the evolutionary waveset selection (see chapter 4) several spin 4 partial waves have been tested (see appendix B) but none has returned sufficient support from the data as to justify its inclusion in the model. There are several reasons why this might have happened. First, there is an extremely larger number of possible isobar decay amplitudes for a spin 4 state. Not all possibilities have been explored yet. Additionally the waveset evolution was dominated by the data in the $1.9\,\mathrm{GeV}/c^2$ region where spin 4 probably plays no big role yet. A bin-wise waveset optimization might produce a different result. Finally partial waves with high initial angular momentum produce complicated angular correlations, especially if high orbital angular momentum is involved in the decay. In order to resolve such correlations the acceptance, especially at the edges of the phase space has to be understood very well. In the mass region above $2\,\mathrm{GeV}/c^2$ the acceptance cuts discussed in section 3.6 might hamper the clear identification of such partial waves.

An inspection of the 4^{-+} partial waves fitted during the waveset evolution indeed confirms that these amplitudes do only receive a small part of the intensity. The most significant contribution is observed in the $4^{-+}0^{+}\rho(770)a_1(1260)\,P$-wave. It is possible to allow such a wave in the fixed 5-body mass partial wave decomposition. The resulting spin density matrix can then be studied to search for additional resonant signatures.

For this exercise all other partial waves in the mass-independent as well as the mass-dependent analysis have been used as in the model discussed above. Only the one $4^{-+}0^{+}\rho(770)a_1(1260)\,P$-wave has been added.

The result is interesting and puzzling at once.

Figure 6.20 shows the $4^{-+}\rho\, a_1\, D$-wave intensity in subfigure (d) together with the real (b) and imaginary (c) part of the interference term with the $1^{++}\pi f_1(1285)\,P$-wave as an example. The 4^{-+} intensity displays a clear peak at $m_{5\pi} = 2.3\,\mathrm{GeV}/c^2$, which would be in agreement with the existence of a $\pi_4(2250)$ as it is listed in [1] for the π_4 (the Breit Wigner parameters extracted in our fit are $m_{\pi_4} = 2239 \pm 10\,\mathrm{MeV}/c^2$ and $\Gamma_{\pi_4} = 309 \pm 15\,\mathrm{MeV}/c^2$). The mass-dependent parametrization shown here contains (in addition to the 7 resonances discussed above) one resonance with $J^{PC} = 4^{-+}$. At very high masses there is an excess of events, which might be due to multiperipheral background processes. There is, however, also one mass bin at $2\,\mathrm{GeV}/c^2$ showing significant excess. In the interference terms the situation is even more dramatic. In both real and imaginary part there are rapid movements which cannot be reproduced in this fit. A similar pattern can also be found in other elements of the spin-density matrix.

In face of the question whether there is another state at $2\,\mathrm{GeV}/c$ a second attempt including two 4^{-+} resonances has been made. The result for the spin-density matrix elements discussed above for this fit are shown in Figure 6.21.

Indeed the fit manages to describe the amplitudes better at $2\,\mathrm{GeV}/c^2$. Unfortunately, though, the width of the narrow resonance comes out unphysically small with a value of $9 \pm 3\,\mathrm{keV}$ and the suggested coupling coefficient is abnormally large. This solution thus cannot be taken seriously, especially since it also fails to describe the imaginary part of the interference term.

These results suggest the existence of at least one 4^{-+} resonance and indicate a complicated structure at $2\,\mathrm{GeV}/c^2$. No satisfying parametrization in terms of the model used here has been found, however. It should be kept in mind that the partial wave investigated here only carries a small fraction of the total intensity and further investigations would profit tremendously from

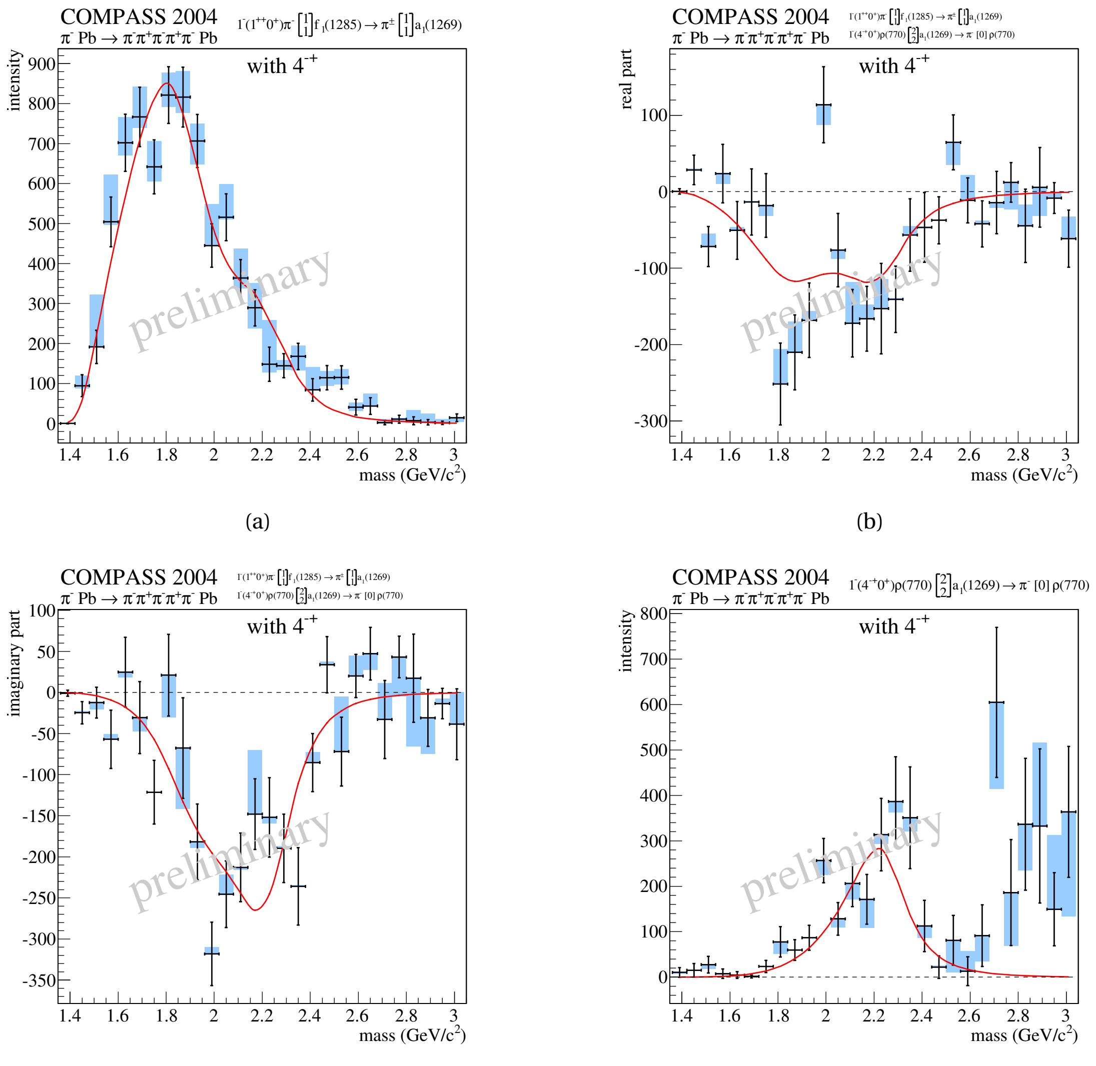

(a)

(b)

(c)

(d)

Figure 6.20: The $1^{++}\pi\, f_1(1285)$ (a) and $4^{-+}\rho\, a_1$ (d) amplitudes and their interference (c,b) as described by the fit with one π_4 resonance.

a larger data set. In particular it would be interesting to study 4^{-+} partial waves in other decay modes.

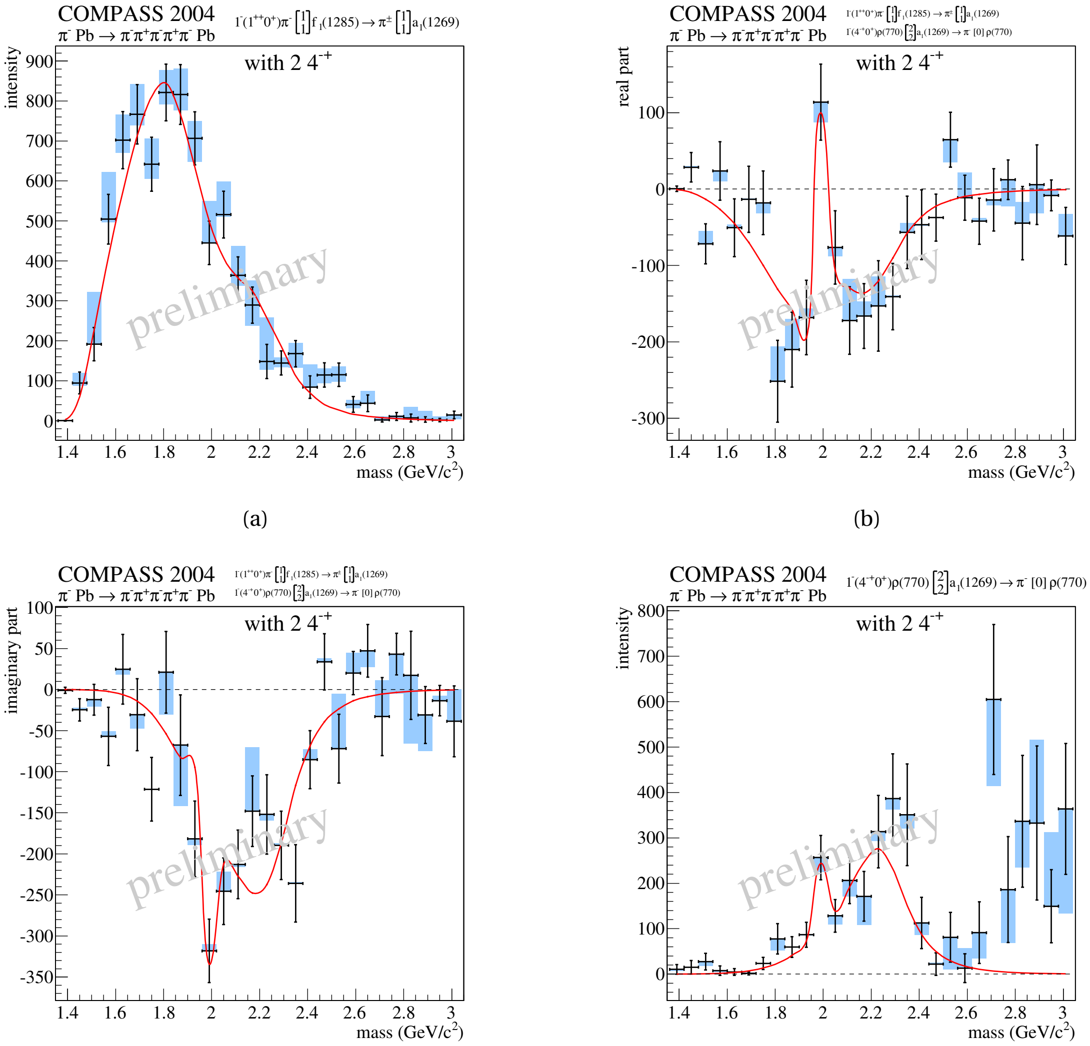

(a)

(b)

(c)

(d)

Figure 6.21: The $1^{++}\pi\, f_1(1285)$ (a) and $4^{-+}\rho\, a_1$ (d) amplitudes and their interference (c,b) as described by the fit with two π_4 resonances. The narrow structure can only be fitted with unphysical Breit-Wigner parameters in the model that is used here.

6.4 Conclusion

In the preceding section a mass-dependent parametrization of a subset of the spin-density matrix for diffractive production of 5 charged pions has been presented including a set of seven resonant contributions. It should be pointed out that the feasibility of finding resonances in the 5π system with the techniques developed in this thesis is an interesting result in itself. For the first time an amplitude analysis for a 5-body system has been conducted with the goal to search for 5-pion resonances. The analysis of the diffractively produced 5π system was done in two steps: First the angular correlations of the pions have been used to perform a partial-wave decomposition in fixed 5-body mass bins as explained in chapters 3 and 5. In a second step, presented in chapter 6.1, the mass-dependence of the resulting spin-density matrix elements has been investigated in order to search for resonant contributions.

The development of an evolutionary model selection algorithm based on a Bayesian analysis of the mass-independent fit is a crucial computational tool for the analysis of a complex final state like the five pions. 284 partial waves have been tested against the data in ~ 5000 different combinations. A final waveset containing 32 partial waves has been constructed. In addition the method allowed for the first time to give estimates of the systematic uncertainties, which are introduced with the choice of a particular waveset. The method as it has been developed in this thesis can be easily applied to similar analyses in other channels.

It has been found that the 5-pion system is dominated by partial waves with the quantum numbers $J^{PC}M^{\epsilon} = 0^{-+}0^{+}$, $1^{++}0^{+}$ and $2^{-+}0^{+}$ as would be expected from Regge-theory arguments for diffractive pion dissociation at $E_{\pi} = 190\,\text{GeV}$.

A subset of ten partial waves has been investigated in order to search for resonant contributions. The mass-dependence of the spin-density matrix has been parametrized with a model containing seven Breit-Wigner resonances and a coherent background in each wave. Two well known resonances, the $\pi_2(1670)$ and the $\pi(1800)$ have been found in good agreement with known parameters of theses states. These findings provide confidence in the consistency of the applied methods. Furthermore four additional heavy resonances, two 1^{++} and two 2^{-+} states have been identified. The extracted parameters are summarized in table 6.2. For the first time the quasi-two-body decays of the hybrid meson candidate $\pi_2(1880)$ into ρa_1 and ρa_2 have been observed.

Findings in the 4^{-+} partial wave are compatible with previous results on the existence of a $\pi_4(2250)$ resonance. However, the investigated amplitude shows unusual behavior at $2\,\text{GeV}/c^2$ which could not be explained in the Breit-Wigner resonance model.

There are hints in the partial wave decomposition of an isoscalar spin-exotic contribution to the 4π subsystem. A possible resonant nature of this amplitude has not been investigated yet.

A prototype analysis of the 4-pion subsystem has been performed, confirming the validity of the isobar-model amplitudes for the selected partial waves. There is evidence for the $f_1(1285)$ and the $f_2(1270)$ decaying into four charged pions to occur as isobar subsystems of the 5-pion final state. The methods tested here can be used to investigate the isobaric 4-pion amplitudes in isoscalar and isovector channels as explained in section 5.3. The techniques might be crucial to understand the 1^{--} partial waves and possible spin-exotic isoscalar 1^{-+} contributions.

In the course of this work an extensive partial-wave analysis software toolkit has been developed, which is now being used by the COMPASS collaboration for amplitude analyses in the $\pi^-\pi^0\pi^0$, $K^-\pi^+\pi^-$ and $K\bar{K}\pi^+\pi^-$ channels.

In summary the work presented here demonstrates novel methods for the amplitude analysis of multi-body systems and provides new insights into the physics of highly excited light-meson resonances. In particular it would be interesting to compare the results obtained here with the chiral-unitary hadronic models mentioned in section 1.1.5. The data analysis techniques developed here are ready to be applied to a wider variety of final states in order to understand the coupling effects between different multi-body channels.

Suggestions for future research:

- *Improve the amplitude parametrization to account for mixing between resonances.*
- *Investigate further parts of the spin-density matrix.*
- *Investigate possible background amplitudes such as multi-peripheral processes (section 2.2.2) and their effects on the phases.*
- *Include the information available from the* 5π *channel into coupled channel analyzes.*
- *Extend the analysis to diffractive dissociation at higher momentum transfer in order to facilitate the search for spin-exotic contributions to the* 5π *system.*

Chapter 7

Simulation of a High-Rate GEM-based Time Projection Chamber

> Lack of ambition is for baseline humans.
>
> Skade

The ability to record large data sets is a key feature of many modern particle physics experiments. This demand is driven not only by the search for rare processes beyond the standard model, but also the detailed understanding of effects on the amplitude level within the standard model requires huge data samples with full phase space coverage in many different final states as has been discussed in the first part of this thesis. Therefore the development of efficient detector systems capable of delivering measurements at large luminosities and high signal rates is needed.

Time Projection Chambers (TPCs) are well developed charged particle tracking detectors employed by many experiments [166, 167, 168, 169, 170, 171, 172] offering the coverage of very large detector volumes with precision space point measurements and a low material budget. The operation of these devices at high rates, however, is still a challenge. This chapter presents simulation studies that have been undertaken for the development of such a high-rate TPC.

The basic concept of operation of a time projection chamber as illustrated in Figure 7.1 requires a large, gas filled volume across which a preferably homogeneous electric field of typically a few hundred V/cm is applied by means of a suitable setup of high-voltage electrodes (the so called *field cage*). Charged particles traversing this *active volume* will ionize the gas molecules along their path of flight leaving a *track* of *primary* electron–ion pairs. In the electric *drift field* electrons and ions will be separated and will start to drift along the electric field-lines. Due to their large mass-difference the electrons reach a *drift velocity* that is typically three orders of magnitude larger than the drift velocity of the ions (depending on the composition, temperature and density of the gas as well as the electric and possible magnetic fields applied). After a time that depends on the drift velocity and the position at which the free electrons have been created they reach the anode side of the field cage. This plane is equipped with a position sensitive charge detector - usually multi-wire proportional chambers [173]. From the combined measurement of the impact position and the arrival time of the electrons at this *readout plane* the point in space where the ionization happened can be reconstructed, given that the electric field and in particular the drift velocity is known at every point inside the *drift volume*. A constant

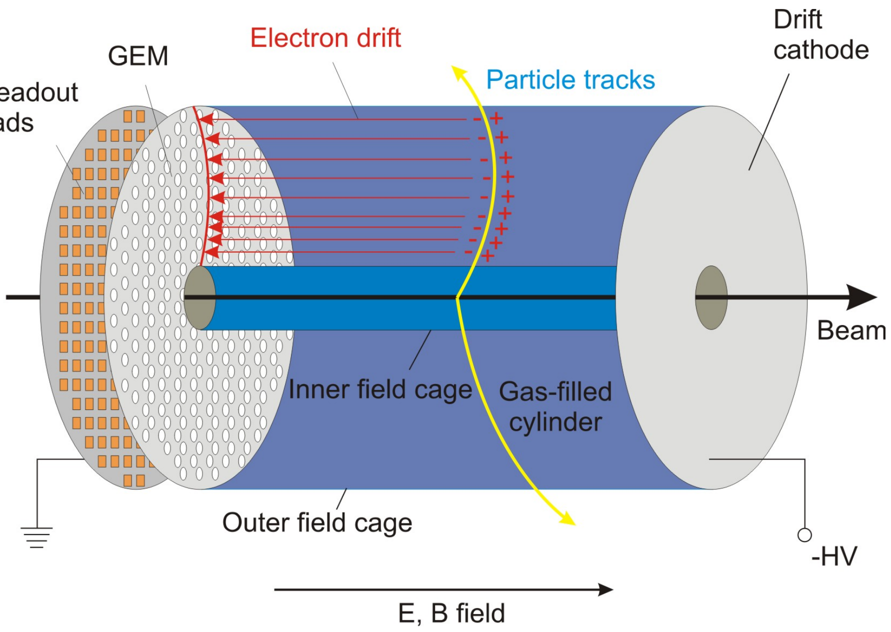

Figure 7.1: Working principle of a time projection chamber.

drift field, perpendicular to the readout plane results in a particularly simple, linear relation between the drift time and the position of the primary ionization in the chamber. Combining the measurements of all ionization electrons along a track thus yields a 3D image of the particle trajectory in space.

In most applications the TPC will be operated inside a magnetic field in order to measure particle momenta by observing the curvature of the tracks in the magnetic field. If the axis of the magnetic field is perfectly aligned with the drift direction there will on average act no Lorentz force on the drifting electrons. However, microscopically the electrons constantly collide with gas molecules and are thus diffused from the ideal path along the electric field lines. It was the realization that a parallel magnetic field actually would significantly reduce this *diffusion* effect which made the operation of large TPCs possible in the first place [166].

As such TPCs are ideal tracking devices to fulfill the above mentioned requirements for modern tracking detectors. However, the operation of such a detector at high luminosities until recently has been a considerable challenge. There are three main problems that need to be overcome in order to build a true high-rate capable TPC:

1. Gate-less ion backflow suppression: The major factor limiting the rates at which traditional TPCs could be operated was the need to install a so called *ion gate* in order to prevent positively charged ions to propagate back from the wire-chamber readout into the active volume of the TPC [174]. Otherwise the accumulation of ion space-charge would distort the drift field in the TPC and thus compromise the imaging capabilities of the detector. The switching of the high-voltage polarity on the ion gate, which is required during the measurement process, is limited to a rate of a few kHz. Mircopattern gaseous detectors and *Gas Electron Multipliers* (GEM)[175] in particular offer the possibility of an intrinsic ion backflow suppression in the gas-amplification stage of the TPC [176, 177, 178]. Therefore this technology is being applied to built TPCs with a continu-

ous, ungated operation [179]. The ion backdrift suppression, however, even under best conditions is not perfect and the question how to deal with the residual space-charge effects in the TPC will be discussed below in section 7.5.

2. Another challenge for high rate TPCs is *event mixing*. Typical time scales on which the electrons are in drift inside the active volume are of the order of $\sim 50\,\mu$s. For a high luminosity experiment the rate of primary interactions can easily be of the order of 20MHz[1]. Consequently during the time between the primary ionization and the registration of the corresponding signal in the TPC hundreds of other events may happen with thousands of particles depositing charge in the detector. The ionization tracks of different events will be recorded simultaneously. The task to assign a measured track to a physical event has been called *event deconvolution* and will be discussed in section 7.4.

3. A final challenge, which will not be discussed in detail in this thesis is the processing of the large amounts of data which are produced by a continuously running time projection chamber.

In order to simulate and explore these challenges during the design phase of a high rate TPC a detailed detector simulation has been created in an earlier work by the author [181]. This detector model has been since ported to two different software environments in the course of the PANDA software development project [182]. Section 7.1 summarizes the basic components of the simulation.

Section 7.2 discusses the methods that have been developed and implemented in order to find and reconstruct particle trajectories in a TPC. An important outcome of this work is the generic track fitting software package GENFIT, which has been developed by the author of this thesis in close collaboration with Christian Höppner [183]. The underlying concept has been published in [184] and the software is available from the sourceforge online repository [185]. It is now being used as basic solution for charged particle tracking by several particle physics experiments in particular PANDA and BELLE II. Section 7.3.2 gives an overview of the design ideas behind GENFIT.

7.1 TPC Detector Response Simulation

The goal of the detector response simulation is to setup a computer model which accurately reproduces the data that would be delivered by the actual device when one or several charged particles traverse the detector.

In order to study the various effects mentioned above a detailed simulation of the GEM-TPC was created as described in [181]. In the course of this thesis the model has been ported the BaBar software framework [186] and the FAIRROOT framework [182]. The latter version is the one which is being currently used for detailed studies and which will be described here.

The TPC detector simulation consists of the following steps:

1. The **propagation of particles** through the detector geometry, including external magnetic fields is simulated using the Virtual Monte Carlo [187] interface with the GEANT3 engine [188] as a backend. The detector geometry includes the specific materials from

---

[1] The numbers used here are examples taken from the PANDA experiment [180]

which the TPC hardware is built. This information is used by the simulation engine to determine the energy-loss on a given path length in the detector. For the following simulation of the electron drift it is important to get position information on all individual ionization events in the TPC. To achieve this the step-size control of the GEANT3 energy-loss routines has to be overwritten such that each step corresponds to a single ionization event. The mean ionization energy for the gas which is being used in the simulation has to be specified as an additional parameter (see [174, 189]). This scheme has first been proposed by the ALICE TPC group [190].

2. **Primary ionization:** The deposited energy at a ionization event as calculated in the previous step is converted into a cluster of individual electrons, taking into account the mean ionization energy.

3. For each electron the **drift** through the TPC is simulated taking into account diffusion effects, electron attachment and possible drift-field distortions.

4. The **charge amplification in the GEM** readout stage creates an *avalanche* of electrons taking into account gain and gain fluctuations in the gas amplification process. For performance reasons from this point on the simulation is not performed in terms of single electrons anymore but in terms of aggregate avalanche clouds of electrons.

5. **Signal induction** on the readout electrodes is represented with a simplified model which is valid for a GEM readout as described in [181] and takes into account the spread of a Gaussian charged profile over several electrodes. Different shapes of these readout *pads* are taken into account.

6. The last step is the **electronics simulation** which in itself consists of two substeps

   (a) At first the **analog signal-shape** on each readout channel is constructed modeling the response of the charge sensitive shaping amplifier. Subsequently this pulse-shape is converted to digitized information with a fixed digitization frequency and amplitude resolution.

   (b) On the time series of the resulting *samples* a **pulse shape analyses** is performed which reconstructs the time and amplitude information of single pulses on each channel individually.

   All parameters of the electronic simulation, as well as the pulse-shape of the employed shaping amplifier can be easily adjusted in the software to represent a variety of possible hardware solutions.

7. The result of the detector response simulation are data-structures called *digis* that contain the time, amplitude and channel-ID of each signal recorded in the device.

7.2 Charged Track Reconstruction

The ultimate goal a tracking detector is to infer the 3-momenta of charged particles and their points of origin. This process is commonly called the *track reconstruction* and can roughly be divided into three steps:

1. *Cluster finding* or hit reconstruction is the preparatory step where the electronic signals recorded by the detector are grouped into distinct spatial measurements.
2. The *pattern recognition* or track-finding step, which groups those hits together, which belong to one track. Also the ordering of the hits along the track is solved at this stage. For performance reasons often a simplified track model will be used in this step.
3. Therefore, in a subsequent *track fitting* the best estimate on the track-parameters, including the momentum will be inferred. In this step also information such as magnetic field inhomogeneities or the energy-loss of the particle along its flight-path through the detector material is taken into account.

The two following subsections describe the algorithms and tools that have been developed to solve cluster finding (section 7.3), pattern recognition (section 7.3.1) and track fitting (section 7.3.2) in a TPC in particular and in complex detector systems in general.

7.3 Cluster Finder

In between the detector-response simulation and the proper track reconstruction the measurements on single channels represented by the digis — containing channel ID, amplitude and a time stamp — are clustered into space-point hits in the TPC. This step helps to

- remove excessive correlations from the individual measurements,
- thereby improves the spatial resolution,
- allows to estimate uncertainties on the spatial measurements and
- reduces the amount of data that has to be processed in the subsequent steps.

Two cluster finder algorithms have been implemented. The standard version has been focused on achieving the best resolution results. It has been presented in [183]. Here we will explain the second version in a bit more detail, focusing on the possibilities to create an algorithm that could be implemented in a highly parallelized fashion. In order to cope with the huge amounts of raw data that are collected by high luminosity experiments modern detector concepts feature powerful readout electronics which are becoming capable of performing advanced data processing in a very early stage of the readout, enabling data compression but even more importantly providing information for advanced trigger algorithms [191]. Parallelization is one of the key methods to achieve the required processing speeds for such concepts. Fortunately due to its very localized nature the clustering problem in the TPC appears to be well suited for a parallel implementation.

The most basic level of parallelization that is offered by the detector are the individual readout channels. The clustering algorithm will combine information from neighboring and only neighboring channels. Realizing this feature of the problem makes *cellular automata* [192] the natural choice for an algorithm blueprint. In such an algorithm the computation is performed by a set of identical cells which may react on the states of their neighbors as well as to external signals.

Figure 7.2 illustrates the basic idea of clustering signals in the 2-dimensional readout plane with a cellular automaton-like algorithm. In brown is shown the projection of a track in the

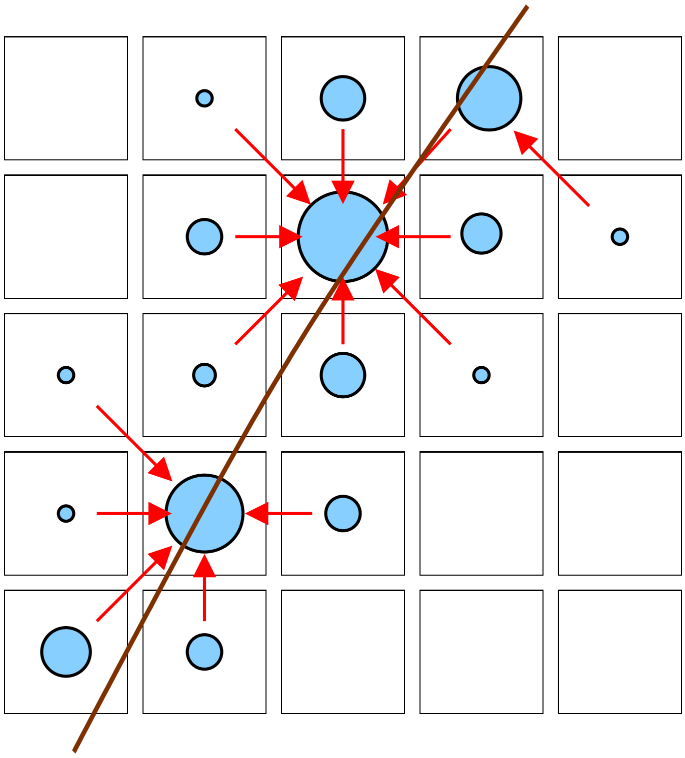

Figure 7.2: Principle of the cellular automaton clustering algorithm. The brown line is the projection of a track onto the readout plane. The blue circles indicate amplitudes measured on the different pads (black squares). In order to collect the data belonging to one cluster, single hits are transported to the neighbors with the largest amplitude.

TPC onto the readout plane, which is subdivided into quadratic pads. The blue circles indicate the amplitudes of signals recorded on each pad. Note that we expect the largest signals to be induced on those pads that are close to the track. In order to collect the information belonging to one cluster in one place the amplitudes on neighboring pads are compared to indicate local maxima and collect data from surrounding pads to the pad with the locally maximal amplitude as indicated by the red arrows. Indeed the signals also have a distribution in time. This is solved by processing the digis in slices of time. Adjacent digis are only combined into a cluster if the time-difference between them is below an adjustable value.

Each pad is assigned an identical state-machine. The operation of each of these so called *pad-processors* is shown diagrammatically in Figure 7.3. Each pad-processor begins in the *initial* state and is initialized with the measured amplitude on its corresponding pad (which can be 0). All pad-processors without any digi registered in their pad immediately transition into the passive *end* state. Those with data transition to the *compare* state. Here the amplitude and timestamp comparisons between neighbors are performed and thus data transfer between neighboring[2] pad-processors is necessary. Each pad-processor performs a comparison of its own amplitude with the amplitudes recorded on all neighbor pads. Also the time-stamps of

---

[2] Note that the neighbor relations can be freely defined in the setup of the cluster finder through the pad-plane configuration file.

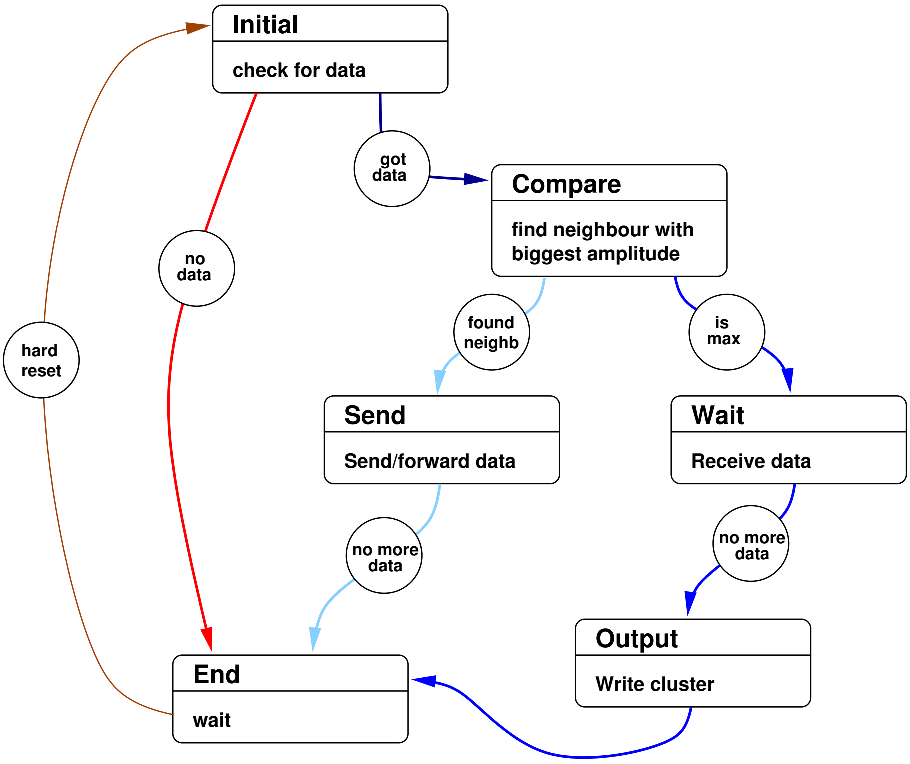

Figure 7.3: Pad-Processor state machine. See text for details.

the digis on the neighboring pads are compared. If there is a neighbor with larger [3] amplitude and lying within a predefined time-window centered around its own data the pad-processor transitions into the *send state*, setting the neighbor with the largest[4] amplitude as the *destination pad*. Otherwise the pad-processor transitions into the *wait* state. Pad-processors in the send state hand all digis which they have stored to their destination pad-processors. This data set might also include digis from other pads that have previously been handed to them. If a pad-processor does not receive any data after an adjustable number of cycles it transitions into the *end state*. If all pad-processors are in the end state the algorithm processes the digis which are now sorted into disjunct clusters to extract the 3D position information. It then resets itself, loads a new time slice of raw data and starts a new super-cycle.
The spatial coordinates of the cluster are calculated using the *center of gravity* method:

$$\vec{x}_{\text{cluster}} = \frac{1}{A_{\text{tot}}} \sum_i A_i \vec{x}_i$$

where the i runs over all digits in the cluster. A_i are the individual amplitudes for each digi and $A_{\text{tot}} = \sum_i A_i$ is the cluster amplitude. Note, that since the digis still contain time information it is here that the knowledge on the drift velocity (and potentially the drift direction) is used in

---

[3] There is also the possibility to split large clusters by requiring a minimum difference in amplitudes before a neighbor is considered a valid destination.

[4] In cases of equal amplitudes on neighboring pads an unambiguous but arbitrary choice is made by using the PadID.

order to calculate the position $\vec{x}_i$. The uncertainties $\sigma_{(x,y,z)}$ on each coordinate $\vec{x}_{\text{cluster}} = (x, y, z)$ can be estimated in the following way[5].

$$\begin{aligned}\sigma_x^2 &= \sum_i \left(\frac{\partial x}{\partial x_i}\right)^2 \sigma_i^2 \\ &= \frac{1}{A_{\text{tot}}^2} \sum_i A_i^2 \sigma_i^2\end{aligned}$$

where σ_i is the uncertainty of the position measurement on each individual pad. This uncertainty is dominated by the diffusion in the TPC. However, usually several primary electrons are collected onto one pad. This statistics has to be taken into account as

$$\sigma_i^2 = \frac{1}{N_i} \sigma_{\text{diff}}^2(z_i)$$

where N_i is the number o primary electrons contributing to the signal and the single-electron diffusion uncertainty σ_{diff} depends on the drift distance z and the transverse[6] diffusion coefficient c_t as

$$\sigma_{\text{diff}}^2(z_i) = c_t^2 \cdot z_i$$

Now the number of primary electrons is unknown but it is to good approximation proportional to the measured amplitude on the pad. One can therefore write

$$\sigma_i^2 = \frac{1}{C \cdot A_i} \sigma_{\text{diff}}^2$$

with C being a universal conversion constant, which primarily depends on the gain of the GEM but also on the charge-conversion and digitization characteristics of the readout electronics. The cluster error can finally be written as

$$\begin{aligned}\sigma_x^2 &= \frac{1}{A_{\text{tot}}^2} \sum_i A_i^2 \frac{1}{C \cdot A_i} \sigma_{\text{diff}}^2 \\ &= \frac{1}{A_{\text{tot}}^2} \sum_i \frac{A_i}{C} \sigma_{\text{diff}}^2 \\ &= \frac{1}{C A_{\text{tot}}} \sigma_{\text{diff}}^2\end{aligned}$$

where in the last step it has been assumed that C and $\sigma_{\text{diff}}^2(z)$ are the same for each pad. For the z-coordinate here the already reconstructed cluster-position is used.

This cluster-finder algorithm has been implemented in C++ as a part of the GEM-TPC software package [182]. The individual components of the algorithm, especially the cellular-automaton design is reproduced in the object-oriented structure of the code. Only the data-interfaces for input and output of digis and clusters respectively are done through a centralized facility. Also there is a central steering module which runs the algorithm in a serialized manner. No true parallel implementation has been done so far. Yet, the concept can be used as a basis for future developments on a parallel processing platform.

---

[5] Correlations between the coordinates are being neglected here.

[6] In order to estimate the uncertainty on the z-coordinate of course the longitudinal diffusion coefficient has to be used.

7.3.1 Pattern Recognition

Track-finding algorithms can be roughly classified [193] into two types: *local* track finders make use of the large correlations that are induced on the spatial measurements along a track to setup schemes where a track is "grown" based on localized hit-by-hit information. In contrast *global* track finders centralize the complete information from a detector (system) in order to construct a metric that allows the identification of patterns in the data. While the former type of algorithm promises a straight forward parallelizability and is suitable to problems with large redundancy in the provided measurements (which is usually the case for a TPC), the latter class of algorithms can also be employed if a minimal number of measurements is available and might be more robust to local disturbances (such as track-crossings for example).
For each type of algorithm a case study has been implemented as will be discussed below. All track finding methods rely on a model and a parametrization of the particle trajectories to identify those hits that lie along one track. We begin the discussion with the track-model used for both track-finding algorithms developed here.

Riemann Track Representation

We will treat here the case where the complete detector is embedded into a momentum-analyzing magnetic field. For the purpose track finding it is then often a good approximation to assume a constant $\vec{B}$-field and thus a constant radius of curvature of the trajectories of charged particles propagating in this field. In this approximation a track has the shape of a helix with its axis aligned to the direction of $\vec{B}$ and can be parametrized accordingly.
Indeed a helix can be trivially composed of a linear movement along the center axis, which we will choose to be along the z-coordinate and a circular motion in the x-y-plane. There is a linear relationship between z and the angular coordinate along the circle which connects the two motions. It is this latter circle pattern which makes track-fitting even then non-trivial if the magnetic field is constant, since there is no linear regression formula for the circle fit. A clever change of variables, however, can be applied to linearize the problem through a conformal transformation. The particular version of conformal transformation that will be used here has been first proposed in [194, 195] for fast circle fits.
A point on the x-y-plane with the polar coordinates (R, ϕ) is mapped to a sphere with unit radius through the transformation [194]

$$x' = R\cos\phi/(1+R^2) \tag{7.1a}$$

$$y' = R\sin\phi/(1+R^2) \tag{7.1b}$$

$$z' = R^2/(1+R^2) \tag{7.1c}$$

as is illustrated in Figure 7.4. Note that this is a transformation from the 2-dimensional plane onto a 2-dimensional sub-manifold of an auxiliary $\mathbb{R}^3$. This increase in dimensionality is the price to pay for the linearization of the problem. The key property of the transformation 7.1 is that points which lie on a circle in the plane will be mapped to a circle on the sphere and consequently lie in a *plane* in the 3-dimensional auxiliary space. Moreover circles will be mapped *uniquely* to a plane. A plane, however, can be linearly parametrized and there is also a simple regression formula for the fit of a plane to a set of points, which needs only one 3×3 matrix inversion as explained in [194].

Also note that while the south pole of the Riemann-sphere is identified with the origin of the x-y-plane no reference point on the circle is needed to perform the mapping (in contrast to other conformal transformations), which in practice means that no assumption on the origin of a track (like *coming from the primary vertex*) has to be made.

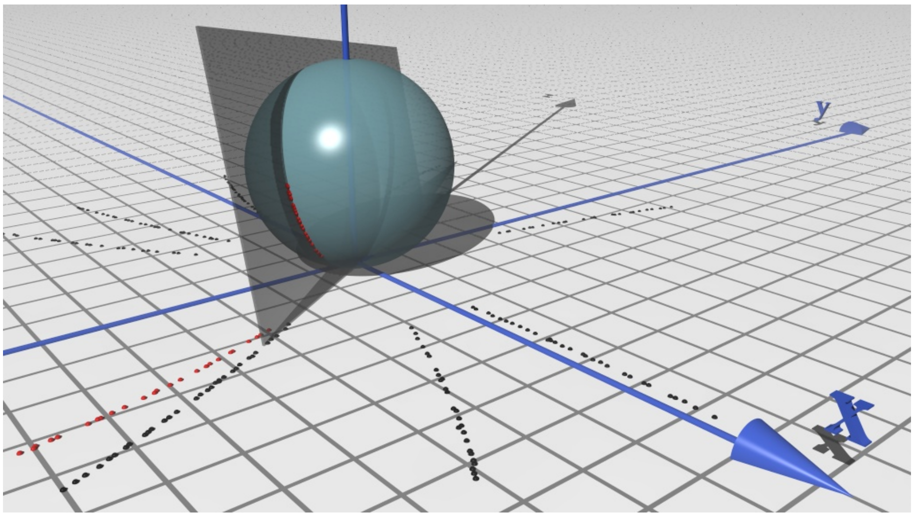

Figure 7.4: Illustration of the conformal mapping of a circular track onto the Riemann sphere. Graphics courtesy of Felix Böhmer [196].

It is in this form that the helix parametrization has been used for the two track-finding algorithms presented below.

Massively Parallel Hough-Transform on a GPU

The Hough-transform method [197] has been originally developed in order to speed up the analysis of bubble-chamber photographs [198]. As such it has a tradition in the application to track-finding although the method is now well established in many pattern recognition contexts.

The basic idea of the Hough-transform is best explained with the example of straight-line tracks in 2-dimensions. Each hit measured in a plane defines a family of lines which intersect at the hit but have different orientations in the plane. Each of these lines can be described by two parameters, slope m and intercept t for example. The constraint to pass through the hit induces a relation between slope and intercept for one family, mapping the point in the x-y-plane to a line in the m-t-plane. For two hits in x, y there are two lines in the so called *Hough space* spanned by m and t. The intersection of these two lines is a point (m_1, t_1) which describes the one line *in the x-y-plane* that connects both hits. Similarly for an arbitrary number of hits lying on a straight-line track there will be one point in the Hough-space where all lines in the m-t-plane intersect (although there will be many other intersections with a smaller number of lines). The problem of finding the parameters of the track is mapped to the problem of finding the point with the largest number of intersections in the Hough space. If measurement uncertainties are involved the intersection will not be perfectly realized. However, one can define a density in the Hough space which is build up of properly smeared track families. The search for intersections is the a search for the maximum density in the Hough space. If several tracks have been present then several local maxima will be found in the Hough space. In order to decide if a hit belongs to a certain track it can be check if that hit can contribute significantly to the region in Hough space which represents the track candidate. A minimum density in the Hough space has to be defined in order to define a lower cutoff for the number of hits that are required to form a track candidate.

The same principles can be applied to more complicated track topologies such as the helix track in the Riemann-sphere parametrization discussed in the previous section. Since 5 parameters are required to define such a helix the Hough space in this case will be 5-dimensional and the problem becomes considerably more involved.

The implementation of a helix Hough-transform has been done by Felix Böhmer and is documented in the diploma thesis [196]. In order to facilitate an efficient search for local density maxima in the 5-dimensional Hough space a so called *fast Hough transform* [199] algorithm has been employed here. The algorithm also offers the possibility for a massive parallelization of the problem and has been implemented on a *Graphics Processing Unit* (GPU) using the parallel-processing framework CUDA [200].

Track Following

The second track-finding algorithm, which has been initially designed and implemented by the author and undergone significant subsequent improvements developed by Johannes Rauch [201], is a local track finder which is based on the idea to *follow* the tracks composed of closely packed hits in the TPC. This track finder exploits the large data redundancy that is offered by the TPC detector concept allowing to record typically in the order of 20 to 100 hits on a single track depending on its orientation in the sensitive volume.

Starting from single hits, close neighbors are combined into small track pieces or *tracklets* which can further grow until a full track is assembled. Hits are added to a track candidate if they fulfill a series of *proximity* criteria in the helix variables. An essential issue in this approach is the sorting f the hits along the track which needs to be solved in order to avoid artificial gaps in the tracks and subsequent track-splitting. In [201] a multi-pass pre-sorting method has been developed, which solves this problem even in situations with high track densities. The track-follower described there has also been used at high track densities for the event deconvolution studies described in section 7.4 below.

7.3.2 GENFIT Track fitting Package

The inference of track parameters in particular the 3-momentum and the points where a charged particle has been produced or undergone a scattering event — the vertices — is a the main task of the track reconstruction software. In complex detector systems a track usually passes through several different detector subsystems. A typical sequence would be for example

- A vertex detector close to the interaction point (in a collider-type experiment) or the target (in a fixed target experiment) provides very high spatial resolution in order to provide a precise measurement of vertex positions.
- A large volume detector (such as for example a TPC) in combination with a strong magnetic field provides a large lever arm for precise momentum measurements. A high granularity and good spatial resolution allow the separation of close-by tracks and the reconstruction of secondary decay vertices.

- The tracking system might be followed by special detectors for particle identification, for example Cherenkov-radiation based devices such as *Ring Imaging Cherenkov Counters* (RICH) [202, 203] or a Detector for Internally Reflected Cherenkov light (DIRC) [204].

- Electromagnetic and hadronic calorimeters specialize on the detection of neutral particles, however, also charged particles hitting these systems will usually leave usable signals.

- The outer shell of an experiment might be equipped with mid to low-resolution tracking detectors dedicated to muon tracking behind the calorimeters and possible absorber material.

It is a considerable challenge during the design-phase but also during the operation of such complex systems to maintain a tracking software that is able to take into account all the technology-specific traits of such different devices and to extract the best possible track-parameter estimates from the data, while still being flexible enough to adapt to new knowledge becoming available as the operators learn more and more details about their detectors.
These considerations lead to the development of a *Generic Fitting* toolbox (GENFIT). The requirements derived for the software can be summarized as the following:

- Allow a detector-specific representation of the type of measurement that is provided by a device. In essence each detector can define its very specific *hit* in a coordinate system of its choice. Templates for commonly used types of hits, such as strip, pixel or space-point hits are pre-defined.

- Allow an easy exchange of the parametrization used to represent a track. Not only can special coordinate systems have specific advantages in different parts of the spectrometer, but also it might be desirable to work with various levels of detail for the treatment of material effects. The options offered by a flexible design in this area are especially useful during the design of an experiment.

- Allow an easy exchange of the fitting algorithm. A standard Kalman-filter [205] has been included already in the first version of the package but more advanced algorithms such as the Deterministic Annealing Filter (DAF) [206] have been added since and are constantly being updated.

Figure 7.5 illustrates the design that has been adopted in order to fulfill these requirements. The key idea is to separate the problem into four well defined components. According to the standard object oriented design philosophy of *encapsulation* each component carries a well defined set of responsibilities and only exposes that functionality to the rest of the system that is necessary for interaction.
All information that is related to the measurement in a particular detector is represented by a so called *reconstruction hit*. In principle this is (at least) a position measurement with a corresponding covariance matrix. GENFIT provides an abstract interface class *AbsRecoHit* which can be used to implement a detector specific version of a hit. This allows the programmer to tailor the hit object to the specific needs of her chosen detector technology. Several common types of RecoHits are already predefined inside GENFIT, such as hits representing detectors with strip, pixel, wire or space-point readout, making it easy to implement different types of

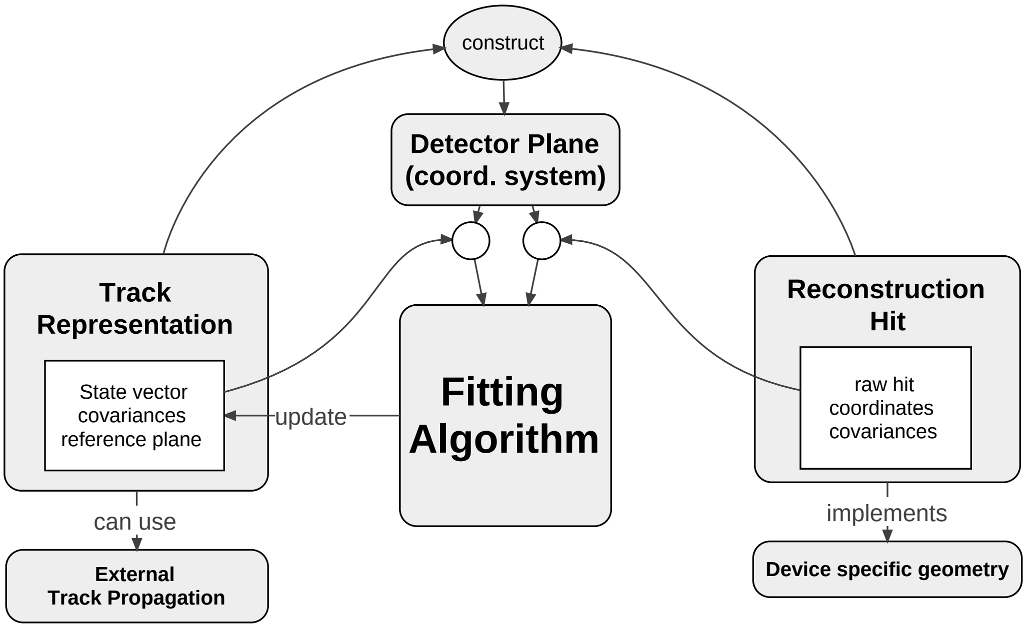

Figure 7.5: Modular concept of the GENFIT tracking software design.

detectors. However the big advantage of the concept is, that new types of detectors can very easily be realized and added to the system.

The second concept abstracts the representation of a particle trajectory and its parametrization. In GENFIT the corresponding objects are called *track representations*. Similarly to the free choice in which coordinates to represent the hit also the parameters describing the track can be chosen freely. For different detector setups specialized track parametrizations can be suitable, mainly depending on the magnetic field configurations used. Typical examples are helix parametrizations in a constant magnetic field or simple straight line representations in field-free spaces. Of course very general parametrizations taking into account arbitrary magnetic fields and also various material effects can be used. GENFIT offers the possibility to plug external, standalone track propagation software into the fitting package. The GEANE [207] code, which is part of the GEANT3 software [188], has been interfaced by the author in this way to be used with GENFIT. In the frame of the Diploma thesis by Johannes Rauch [201] another self-contained track extrapolator based on a forth order Runge-Kutta integrator has been implemented. A crucial problem that has to be solved by every such extrapolator is the calculation of correct estimates for the covariance matrix of the chosen track parametrizations at a given location in the presence of multiple scattering events as a charged particle traverses the detector material. GENFIT's modular design offers the possibility to continually improve the available models without the need to make changes to the rest of the fitting code.

With the free choices of coordinate systems that are allowed for the parametrizations of hits as well as tracks there is the need of a unifying concept in order to allow the calculation of meaningful residuals. This link is provided by the so called *detector plane*. Following the assumption that the flight-time coordinate along the track will not be resolved by the detector system it is clear the the track has to be treated as a 1-dimensional sub-manifold of the 3-dimensional space. Therefore, each measurement in a tracking detector can contribute *at most* two degrees of freedom to a likelihood function. In other words, the residual *along* the track at any given point can not be measured since it is unknown in this direction which point on the track belongs to a hit in a detector. It is therefore sufficient to define a 2-dimensional sub-manifold in which the coordinates of a hit relative to the track will be measured. The most simple such construction is a plane and arbitrary surfaces can be approximated by a tangential plane in a sufficiently small region around a given point. A plane will thus be used to setup a coordinate system in which hit and track coordinates as well as their covariances are measured. In order to keep the flexibility these detector planes are allowed to vary and indeed are constructed by using information of each individual hit and the track representation in the vicinity of the respective hit. The procedure how this is done resembles a negotiation between the hit and the track object. The result depends on the type of hit. For instance, if the detector which is represented already has a planar geometry (like a silicon strip detector for example) then the reconstruction hit will return the corresponding plane[7]. For more complicated hit geometries such as wires or space-point hits, where no obvious plane is defined by the detector geometry itself, information from the track is used to construct a so called *virtual* detector plane. For example, for a space-point measurement as in the TPC the track is extrapolated to the point of closest approach to the hit (in global coordinates) and the detector-plane is constructed perpendicular to the track at this position. For the orientation of the u, v coordinates in this plane an additional convention has to be used (for example such that $\vec{u}$ has a zero z-component in global coordinates).

The concept of the detector plane allows to combine the information from arbitrarily diverse detector geometries with different track parametrizations in a unified and modular way. It should be noted that in principle one could generalize the detector plane into a *detector-surface*, for example to represent deformed silicon wavers in precision tracker. However, the non-linear transformations of the covariances involved might lead to asymmetric errors which are not well handled by most fitting algorithms that are available at the moment. For future developments exploring such possibilities the modular structure of GENFIT provides a very flexible framework.

The final component of the track reconstruction toolkit is of course the fitting algorithm itself. There is no abstract fitting interface foreseen in GENFIT, such a thing would only complicate the design and not add much value since situations where several different fitters are dynamically instantiated in parallel are quite uncommon. The modular design of the components mentioned above, however, allows a simple implementation of any fitting algorithm desired. A standard Kalman filter [208, 205] has been implemented as the first example and is being used now for simulation studies and the reconstruction of data taken by the GEM-TPC collaboration at the FOPI experiment [179].

Also a deterministic annealing filter [206] has been implemented and due to its improved robustness against noisy measurements is being under discussion as the standard fitting code for BELLE II.

The core concepts of GENFIT have also been published in [184]. The code, which is open-source and constantly being developed is available from [185]. A detailed writeup on the software is also available in [183].

---

[7] A detector plane is defined by an origin given in a global coordinate system and two unit vectors u, v fixing the coordinate system in the plane and its orientation in global coordinates.

7.4 Event Deconvolution

Event mixing is an important issue for the exclusive reconstruction of separate physics events in high-luminosity experiments. With event mixing we mean any situation when the typical response time of a detector is equal or larger than the typical time-spacing between two consecutive events so that the signals in the detector system cannot be grouped into distinct events based on their time stamp alone. For a TPC due to the long drift time this challenge is of particular severity.

7.4.1 Event Mixing Simulation

We will present here a case study for which a TPC with a drift length of 150 cm and a gas mixture of 90% Ne and 10 % CO_2 at a drift field of 400 V/cm has been simulated [181, 201]. The chamber has an inner cylinder of $r = 15\,\text{cm}$ radius which provides space for a beam pipe and a silicon vertex detector. The outer radius of the TPC is 42 cm. The magnetic field assumed in the simulation has a nominal[8] flux density of 2 T . The electron drift velocity under these circumstances is predicted [210] to be $v_{\text{drift}} = 2.731\,\text{cm}/\mu\text{s}$ resulting in a maximum drift time (a *drift-frame*) over the 1.5 m drift length of $t_{\max} = 55\,\mu\text{s}$.

In order to simulate a high rate environment antiproton-proton interactions at $p_{\bar{p}} = 3.6772\,\text{GeV}/c$ with rates up to $2 \cdot 10^7\,\text{s}^{-1}$ have been generated using the DPM [211] Monte Carlo generator. At the highest rate the average gap between two events will be 50 ns and so about 1000 $p\bar{p}$-interactions typically happen while an ionization electron created in the first event is still drifting towards the TPC readout. The physics channel which has been chosen for this study is

$$\bar{p}p \to \eta_c \to \Phi\Phi \to K^+K^-K^+K^-$$

The FAIRROOT [182] software framework used to build the TPC simulation only supports event-wise data processing. In order to implement the massive event mixing necessary for the TPC simulation new infrastructure had to be constructed. To keep in line with the basic event-wise paradigm of the framework a strategy has been adopted where pre-generated background events are added on top of the data for each *physics event*. Ideally the event mixing would be done on the level of the electronic signals, which is the first point in the detector response simulation where significant non-linear pileup effects are anticipated (such as an ADC going into saturation). Unfortunately the massive amount of data that is required to realize this level of detail so far has inhibited an efficient implementation. Instead the mixing is done on the level of the digits described in section 7.1 so that the clustering is the first step where data from different events can pile up.

In order to prepare the background sample a standard simulation of the TPC (and surrounding detectors) with the desired parameters is run up to the output of the digitization. The background events are stored in a dedicated file. Depending on which rate of primary interactions should be simulated it is important to generate enough background events to cover the complete drift-frame belonging to one physics event. Thus roughly twice as many background events are needed as would happen during one drift-frame ($\sim$ 2000 events for the simulation parameters mentioned above).

During the simulation of the physics events a framework module is called which loads the background file and adds the data to the current event. The background events are reused but

---

[8] The magnetic field maps of the PANDA design studies have been used.[209]

randomized in time and sequence to generate a unique background pattern for each physics event. Of course this method only works properly if a large number of background events is available.

In the present simulation a constant luminosity is assumed. The gaps between the background events are exponentially distributed according to the event rate. The number of events observed in a given time interval follows the respective Poisson distribution. Fluctuations induced through a bunch-structure of the beam, as well as fluctuations in the target density, which are possible for internal targets used at storage rings [212], are not taken into account. More complicated time structuring can, however be easily implemented for future investigations.

The time t_0 when the physics event happens is defined as $t_0 = 0$. The interval for which background events will be admixed is two drift-frames long:

$$t_{\mathrm{bkg}} \in [t_0 - t_{\mathrm{max}}, t_0 + t_{\mathrm{max}}]$$

Here t_{bkg} is a time when a background event is generated. This ensures a complete coverage of the drift-frame of the physics event

$$[t_0, t_0 + t_{\mathrm{max}}]$$

with a constant track density. In a more realistic scenario the data stream would extend much longer before and after an physics event. The task of finding the right drift frame and extracting the physics event is part of the challenges for the trigger of such an experiment. Here we will assume that a kind of trigger signal is supplied by detectors outside the TPC so that t_0 is known and also the portion of data which has to be examined for the TPC is well defined.

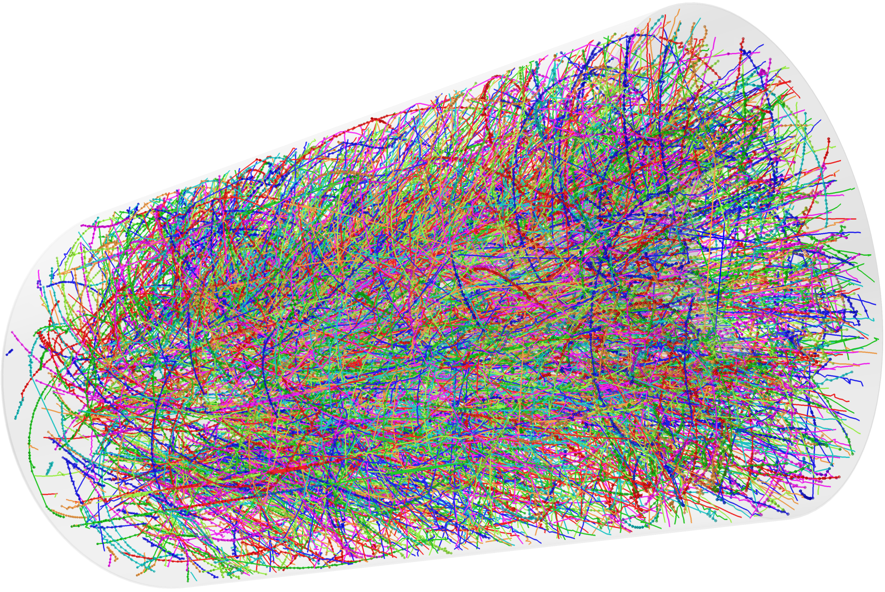

Figure 7.6: Simulation of 2000 overlapping events in the PANDA TPC. Graphics courtesy of Johannes Rauch [201]

Figure 7.6 shows the outcome of such a simulation. The gray cylinder indicates the boundaries of the TPC volume which is filled with the hits of 2000 overlapping events. The color code of the individual hits shows the result of the track-following pattern recognition (see section 7.3.1) that has already been performed here and has assigned the hits to helical tracks. The task of event deconvolution is now to decide which of these tracks originate from the one primary interaction that has happened at the time t_0. Before strategies to accomplish that are discussed we will comment on an important technical issue for event-mixing simulation studies.

Handling of MC-truth information in mixed events In order to benchmark the various pattern recognition, reconstruction and event deconvolution algorithms the so called *Monte Carlo truth* is a vital information. The Monte Carlo truth of any signal, hit or track in the simulation is a reference which allows to determine which particle in the original, generated event has lead to this particular detector response. It is also important if one wants to compare the result of a track-reconstruction program with the input track parameters that seeded the simulation in order to estimate resolutions and efficiencies of the detector systems under study.
In the presence of pileup or event mixing it is possible that this mapping from the reconstructed objects back to original particles is not unique anymore. For example if two tracks from different events cross in the TPC a cluster containing charge from both tracks might be formed. Similarly the pattern recognition might erroneously assign hits originating from different particles to the same track. It is thus necessary to have an system which keeps track of such complications.
For the TPC simulations a simple accounting system has been implemented. Its basic entity is a so called *MC identifier* which contains the event number (with the convention that the physics event has number 0 and background events are numbered according to their position in the background file (numbering starting at 1). For each data-object where mixing can occur a collection of such *MCids* is stored. The *MCIdCollection* also offers a weight for each contributing MCid. The unit for this weight is the proportional to electric charge for all hit-like objects (digis, clusters) and proportional to the number of hits in a track.
With this system it is possible to measure the degree of pileup at the different processing stages. It also allows the access to the full original MC truth data for mixed events.

7.4.2 Strategies for Event Deconvolution

There have been two different strategies developed to solve the problem of event deconvolution. The first works using the TPC standalone without any external information apart from a time signal defining t_0. The second strategy involves correlating measurements in the TPC with the rest of the detector system in particular with a vertex detector or other tracking chambers. Combined these methods are able to efficiently reconstruct single events from a highly mixed data stream as will be demonstrated below.

Target Pointing

In order to understand the reasoning that is behind the standalone event deconvolution it is useful to recapitulate the characteristics of the data which are delivered by a continuously running TPC at high rates.
All hits in the TPC will be time-stamped and thus tracks can be reconstructed in 3D as shown in Figure 7.6. For this reconstruction the event time t_0 is not known and not needed since all times are measured from an arbitrary starting point. The *relative* z-positions of the hits will be

correct. However, depending on the t_0 of a particular event, the tracks belonging to this event will appear at an *offset* in z corresponding to t_0. If this offset can be measured one has the means to determine the t_0 of a track. For this to work a reference point on the track is needed for which the z-position in the chamber is known.

There are two such cases which can be used: if a track penetrates one of the end caps of the chamber, then the z-position of the last hit is known to a few millimeters precision. It is important to achieve high efficiency for complete track reconstruction, meaning that all hits belonging to a track have to be found by the pattern recognition and attributed to exactly one track. Obviously this method only works for tracks which pass through one of the end caps of the TPC.

The second possibility is target pointing. Once a track has been reconstructed in the TPC it can be extrapolated to the position of the interaction point where the beam hits the target. If the track indeed originated from the primary vertex, then the z-coordinate of the resulting extrapolation directly yields the event offset. This method does not work for tracks coming from the decay of long-lived, neutral particles such as $K_s \rightarrow \pi^+\pi^-$ or $\Lambda \rightarrow p\pi^-$, but will work for the vast majority of tracks.

With a complete track reconstruction secondary vertices of neutral particles decaying inside the TPC can of course be identified and by reconstructing the 3-vector of the decay system a similar target pointing can be done.

If the t_0 for an interesting event is already known from an external trigger system then it is sufficient to select those tracks for which the z-offset falls close. All other tracks can be discarded at this stage of the processing. For the more complicated case that no external event time is available the target pointing information can still be used to define event times by clustering the information along the offset direction. However, since for the parameters mentioned above the average offset per event is only 1.4 mm a vertex resolution of the order of a few $100\,\mu$m or better is necessary for this.

In most situations therefore information from other detectors is needed to complete the event deconvolution.

Adding Information from other Detectors

For most other detector systems the time window in which event mixing can happen will be much shorter than in the TPC. This can be exploited to further clean up the data from the TPC by requiring that tracks found in the TPC connect to hits in fast detectors, such as a silicon vertex detector installed between the interaction point and the TPC.

In the case study presented here it was assumed that an event is well defined in the vertex detector. Performing the extrapolation and testing for matches between the two detectors is then mainly a computational issue.

7.4.3 Event Deconvolution Performance

Figure 7.7 show the performance of the combined pattern recognition, reconstruction and event deconvolution using only the TPC. The three data sets correspond to three different settings of drift distortions in the TPC. Drift distortions will be discussed in section 7.5. The green data points correspond to the case without drift distortions. Single track efficiency is the number of reconstructed physics tracks divided by the total number of all physics tracks. It will be one if *all* physics tracks are reconstructed. The event deconvolution purity is the number of physics tracks which are kept after the event deconvolution cuts divided by the sum of all tracks (including background) which survive the event deconvolution cuts. It will be one if *only* physics tracks are kept in the event. Finally the event deconvolution efficiency is defined as the fraction of events for which all physics tracks are reconstructed and survive the event deconvolution cuts.

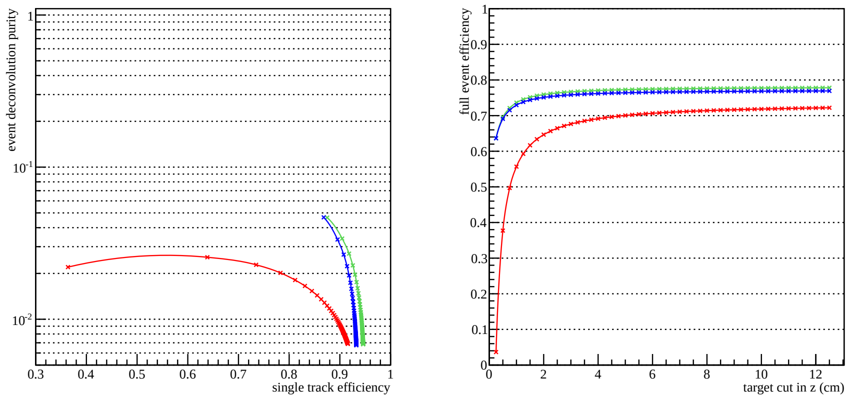

Figure 7.7: TPC standalone event deconvolution performance for the reaction $\eta_c \rightarrow \Phi\Phi \rightarrow K^+K^-K^+K^-$ with 2000 admixed background events. Single track efficiency, even deconvolution purity and efficiency as functions of the target pointing cut. The different colors correspond to different degrees of drift distortions from 0% (green), 20% (blue) to 100% (red). Drift distortion are discussed in chapter 7.5. Plot courtesy of Johannes Rauch [201]

These quantities are shown in Figure 7.7 as a function of the cut on the target pointing in the event deconvolution. With a target cut of around 2 cm a full event efficiency $\sim$ 75% can be reached. The event deconvolution purity which is achievable with the TPC in such a mode of operation is a few %. Distortions of the drift field (see section 7.5) slightly reduce the achievable full-event efficiency by a about 10% for the case studied here. Even in such a case the applied methods appear robust enough for a reliable operation of the detector.

As has been explained above the purity of the event deconvolution can be improved by requiring correlations of the found tracks with hits in the vertex detector. By requiring another at least two hits inside a road width of 3 mm around the extrapolated tracks improves the background suppression to such a level as to make physics analysis possible.

Figure 7.8 (left) shows the invariant mass of K^+K^- pairs which have been recovered from 2000 background events per physics event as described above. The clear peak at 1.02 GeV/c^2 corresponds to the ϕ. Combining two Φ per event yields a nice η_c peak which is practically background free. This demonstrates the possibility to recover physics events in a continuously running time projection chamber from a realistic background at high rates.

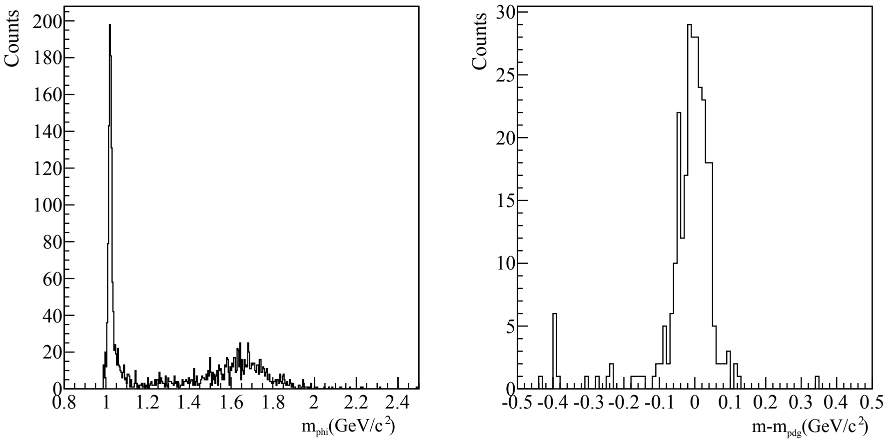

Figure 7.8: Event deconvolution performance for the reaction $\eta_c \rightarrow \Phi\Phi \rightarrow K^+K^-K^+K^-$ with 2000 admixed background events. The ϕ resonance is clearly visible in the invariant-mass spectrum of K^+K^- pairs (left). The invariant mass of the $\phi\phi$ system shows a clear peak at the mass of the η_c (which has been subtracted here). Plot courtesy of Johannes Rauch [201]

7.5 Space Charge Simulation

The buildup of space charge inside the TPC drift volume and the resulting distortions of the drift field are serious challenges for a high-rate TPC. Even with the use of ion-backflow suppressing technologies such as a GEM-based readout there will still be residual ion charge flowing back from the gas amplification stage into the drift volume.

In order to investigate the expected drift distortions and to test concepts for possible correction methods a space-charge simulation has been set up. The details of the methods employed are being published in a paper [213]. Here we will give a summary of the simulation and the results obtained.

Simulation of space-charge buildup

In order to simulate the high-rate environment and the charge deposited in the TPC antiproton-proton annihilations at a momentum of $p_{\bar{p}} = 2.0\,\mathrm{GeV}/c^2$ have been generated, using the DPM event generator [211]. The primary ionization caused by these events in the TPC drift volume has been evaluated with a GEANT3 simulation as described in section 7.1.

Although the initial distribution of electrons and ions is equivalent the electrons are quickly removed by the drift field while the ions with a drift velocity of $v_{\mathrm{ion}} = 1.767\,\mathrm{cm/ms}$ stay inside the drift volume three orders of magnitude longer. In the following discussion of the space charge density the electrons will therefore be treated as reaching the readout detector immediately after the ionization event in the TPC.

Upon arrival at the gas amplification stage the electrons create an avalanche of ionization processes, delivering enough charge to the pickup electrodes to induce a measurable signal but also liberating a large number of ions. In a GEM detector with asymmetric field configurations most of these ions are collected at the anode side of the GEM-foil [177, 178]. However, some ions travel along the drift field lines back into the TPC. The number of ions which escapes from the GEM detector per incoming electron is called the *ion back-flow* ϵ. For the simulations presented here a value of $\epsilon = 4$ has been used which is a realistic assumption for a GEM detector operated in a 2 T magnetic field (see for example [214]).

The time-resolved simulation of the space charge distribution in the TPC is realized in three steps. Note that the TPC is treated as rotationally symmetric for the purposes of this investigation. The space-charge density will only be studied in the z-r-plane of the TPC.

1. A *template* distribution of the primary ionization in the TPC is calculated by integrating the deposited charge over a short (on the scale of the ion drift) time interval without taking the intermediate ion drift into account.

2. The template distribution is then used to produce space charge in the TPC volume taking into account the ion drift and the backflow of ions from the amplification stage which is obtained by integrating the primary charge deposited in one time-frame over the drift direction and multiplying the resulting value with the ion back-flow ϵ. Note that in the model used here the ion drift is assumed to proceed on straight lines. No attempt at a self-consistent simulation of the ion drift has been made.

3. After one complete ion drift time an equilibrium is reached and the space charge distribution stabilizes. The fluctuating primary ionization is treated as a small perturbation on top of the equilibrium charge density and will be neglected here.

The result of this simulation is a static charge density as shown in Figure 7.9. For an event rate of $2 \cdot 10^7$ $\bar{p}p$ annihilations per second peak charge densities of 55 fC/cm^3 are found. This value is comparable to charge densities found in running TPCs at heavy ion colliders [215].

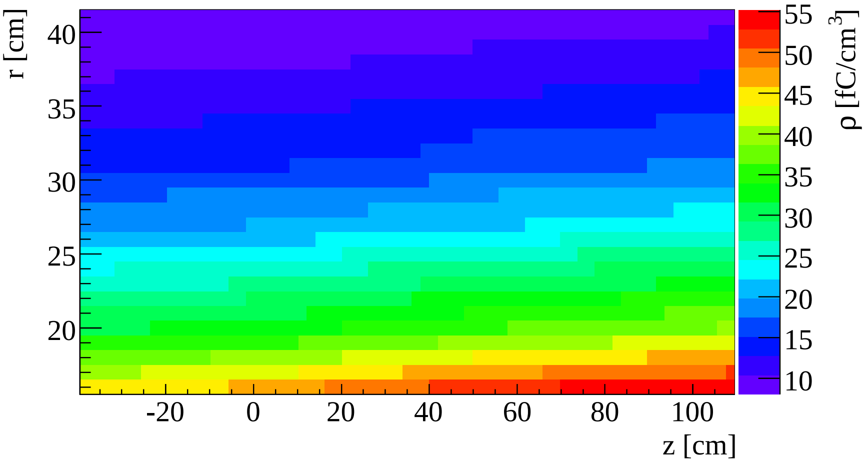

Figure 7.9: Monte Carlo simulation: Ion space charge density created in a GEM-TPC filled with Ne/CO$_2$ (90/10) operated with an ion-backflow $\epsilon = 4$ and exposed to $2 \cdot 10^7$ $\bar{p}p$ annihilations per second. The peak charge density found here is about 55 fC/cm^3.

.

Drift Distortions

The simulated space charge distribution can be used to calculate the distortions to the (homogeneous) drift field. For this purpose the field cage of the TPC has been assumed to be a perfect conductor. The finite-element software package DOLPHIN [216] has been used to solve the cylindrical symmetric Poisson's equation in the z-r dimensions to calculate the electrostatic potential generated by the (static) space charge distribution from which the resulting electric field can be easily computed.

Figure 7.10 shows the resulting electric field. Due to the angular symmetry of the TPC there is no component perpendicular to the z-r-plane. From these results it is clear that deviations in z-direction are below the %-level so that in good approximation the drift times will not be efected seriously. However, the field component in r-direction will cause significant distortions of the drift paths.

In order to convert the field map into a map of drift distortions the macroscopic equations of motion for a charge in magnetic and electric fields and with a constant *friction term* [174], which parametrizes the microscopic multiple collisions of the drifting electrons with the gas atoms, has been solved for test-charges place at different places throughout the TPC. The resulting map of drift distortions is shown in Figure 7.11. Due to the $E \times B$ effect there are sizable distortions also in the ϕ-direction perpendicular to the z-r-plane. The distortions are generally growing with larger drift paths and are biggest at the inner, forward corner of the chamber where also the space-charge density peaks.

The predicted distortions are in the order of a few mm and have to be corrected before the final

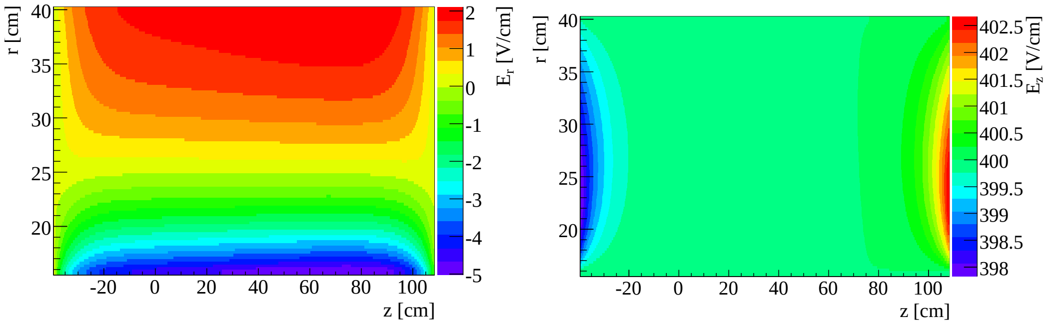

(a) E_r (b) E_z

Figure 7.10: Electric field created by the ion space charge shown in Figure 7.9 in a field cage with perfectly conducting walls. The nominal drift field of 400 V/cm in z-direction has already been superimposed (b).

.

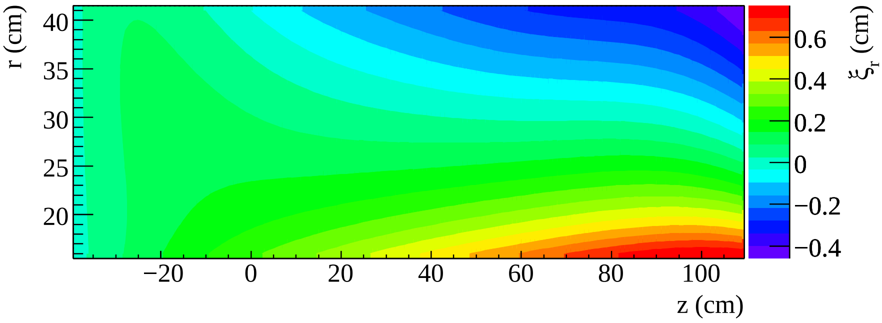

(a) r-direction

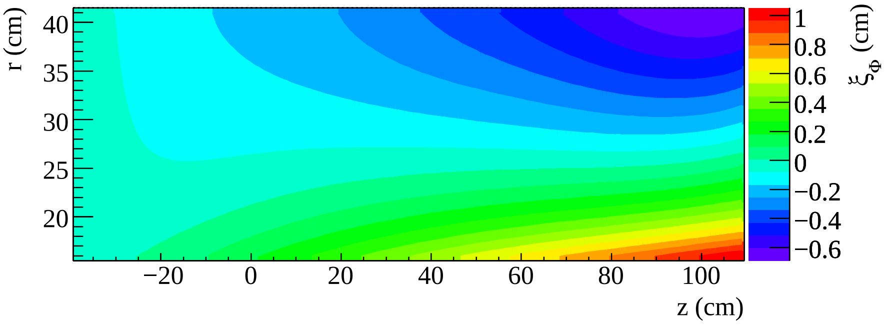

(b) ϕ-direction

Figure 7.11: Electron drift distortions — deviation from a straight line drift — caused by the ion space charge shown in Figure 7.9. The $E \times B$ effect induces drift distortions perpendicular to the z-r-plane even for azimuthal symmetric TPCs (b).

.

reconstruction of an event. However, it should be noted that for purposes of pattern recognition and event deconvolution these levels of distortion are acceptable as has been shown in section 7.4.2.

Distortion Corrections

For the precise determination of track parameters any drift distortions have to be corrected. This is possible if the distortions can be measured during operation of the TPC. To this end high power laser tracks have been used in running TPCs (see for example [217]) in order to monitor drift velocities and drift distortions. Such a system has been simulated to explore the possibilities for drift distortion correction in a high-rate GEM-TPC. First studies indicate that a correction of the drift distortions using laser tracks is indeed feasible [196, 213].

Appendix A

5π Phase-Space Acceptance

Accepted phase-space Monte Carlo distributions. For details see section 3.6.

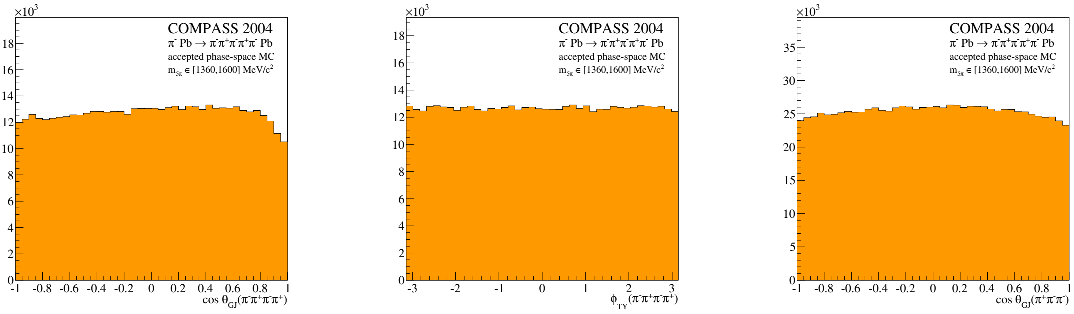

(a) $\cos\theta^{4\pi}_{\mathrm{GJ}}$ (b) $\phi^{4\pi}_{\mathrm{TY}}$ (c) $\cos\theta^{3\pi}_{\mathrm{GJ}}$

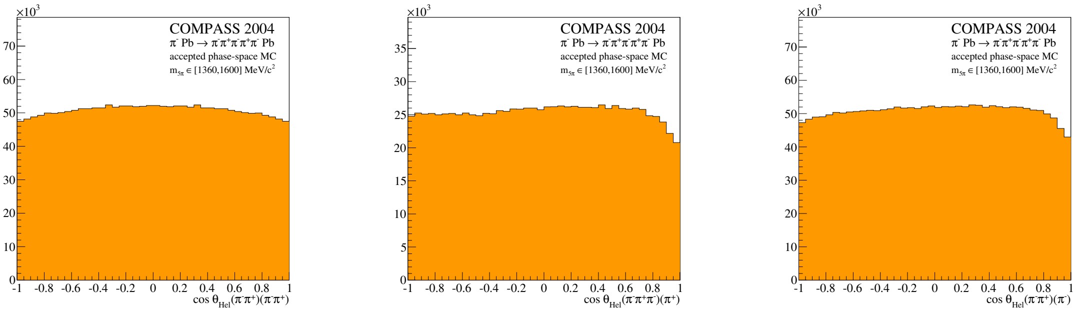

(d) $\cos\theta^{22}_{\mathrm{Hel}}$ (e) $\cos\theta^{31}_{\mathrm{Hel}}$ (f) $\cos\theta^{21}_{\mathrm{Hel}}$

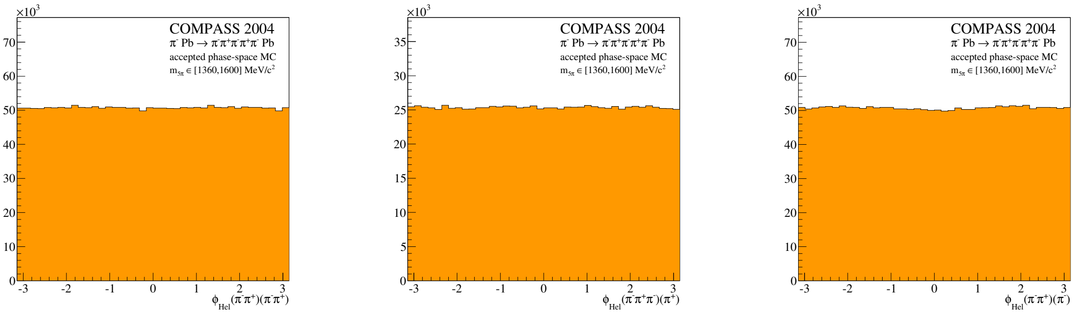

(g) ϕ^{22}_{Hel} (h) ϕ^{31}_{Hel} (i) ϕ^{21}_{Hel}

Figure A.1: Angular acceptance for the 5-pion final state as determined by Monte Carlo simulation. The distributions shown are projections of accepted phase-space events. Unmodified phase-space distributions would be flat in all variables. $m_{5\pi} \in [1.36, 1.60]\,\mathrm{GeV}/c^2$

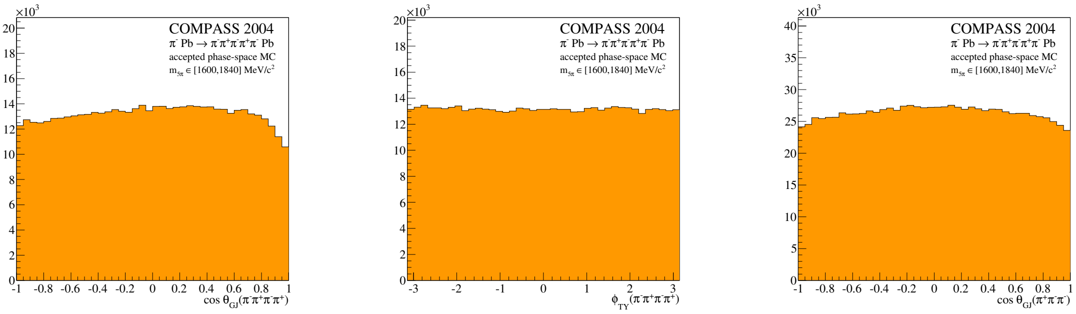

(a) $\cos\theta_{\mathrm{GJ}}^{4\pi}$ (b) $\phi_{\mathrm{TY}}^{4\pi}$ (c) $\cos\theta_{\mathrm{GJ}}^{3\pi}$

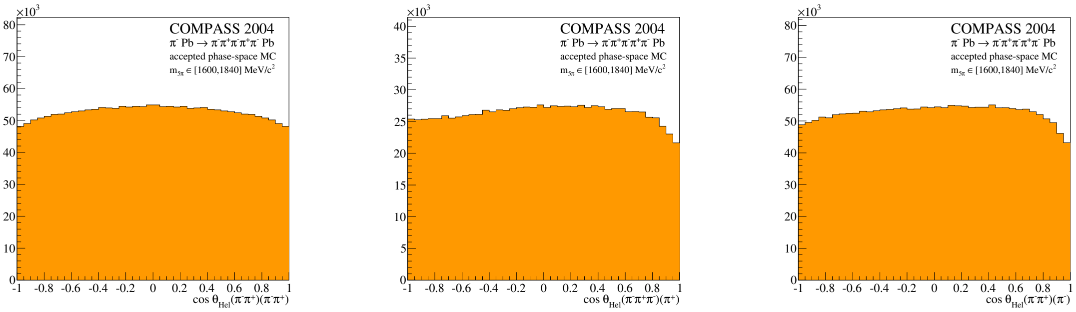

(d) $\cos\theta_{\mathrm{Hel}}^{22}$ (e) $\cos\theta_{\mathrm{Hel}}^{31}$ (f) $\cos\theta_{\mathrm{Hel}}^{21}$

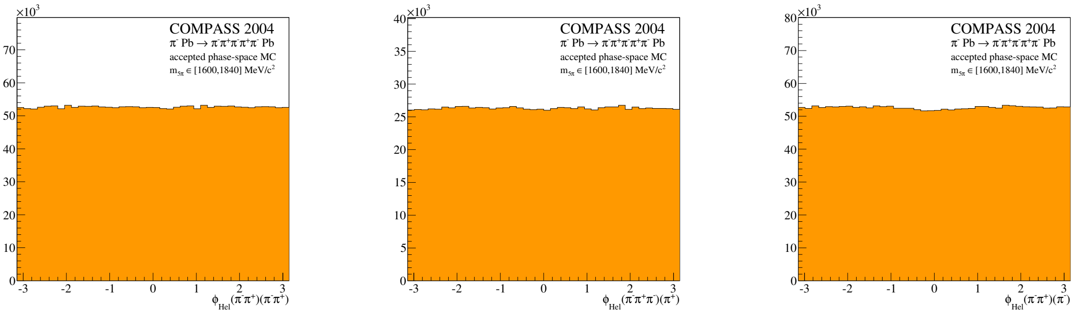

(g) ϕ_{Hel}^{22} (h) ϕ_{Hel}^{31} (i) ϕ_{Hel}^{21}

Figure A.2: Angular acceptance for the 5-pion final state as determined by Monte Carlo simulation. The distributions shown are projections of accepted phase-space events. Unmodified phase-space distributions would be flat in all variables. $m_{5\pi} \in [1.60, 1.84]\ \mathrm{GeV}/c^2$

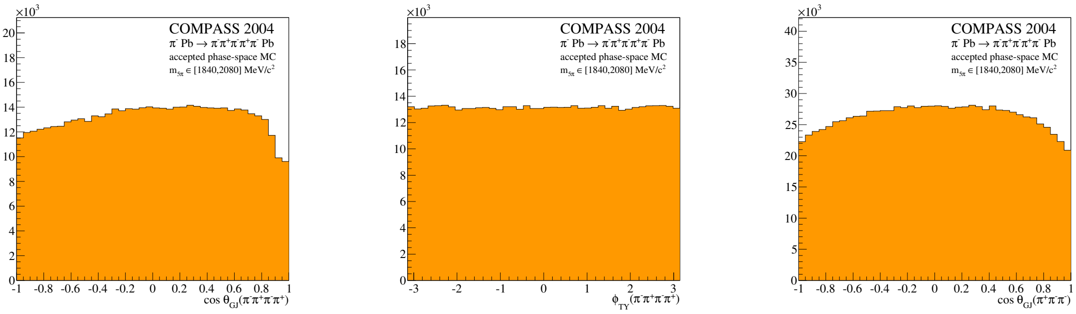

(a) $\cos\theta^{4\pi}_{\mathrm{GJ}}$ (b) $\phi^{4\pi}_{\mathrm{TY}}$ (c) $\cos\theta^{3\pi}_{\mathrm{GJ}}$

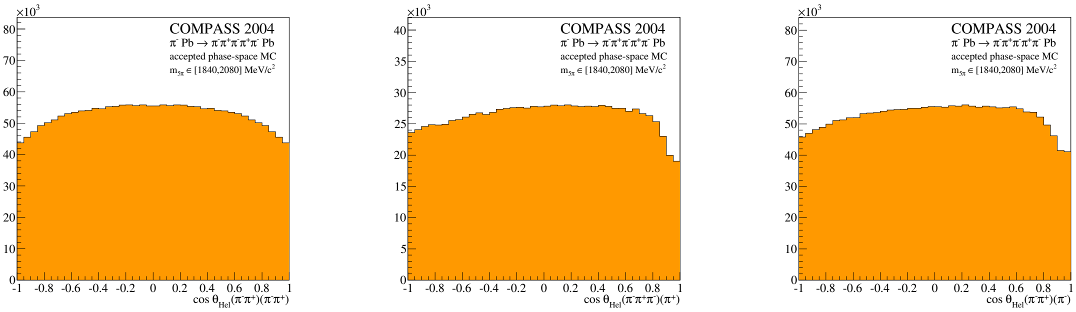

(d) $\cos\theta^{22}_{\mathrm{Hel}}$ (e) $\cos\theta^{31}_{\mathrm{Hel}}$ (f) $\cos\theta^{21}_{\mathrm{Hel}}$

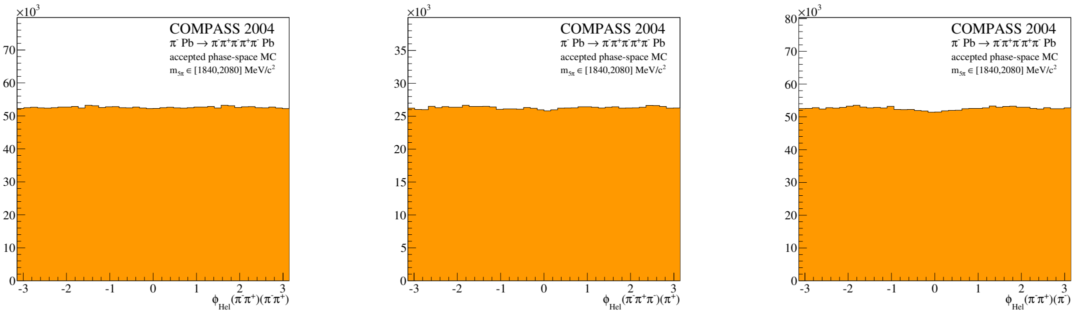

(g) ϕ^{22}_{Hel} (h) ϕ^{31}_{Hel} (i) ϕ^{21}_{Hel}

Figure A.3: Angular acceptance for the 5-pion final state as determined by Monte Carlo simulation. The distributions shown are projections of accepted phase-space events. Unmodified phase-space distributions would be flat in all variables. $m_{5\pi} \in [1.84, 2.08]\,\mathrm{GeV}/c^2$

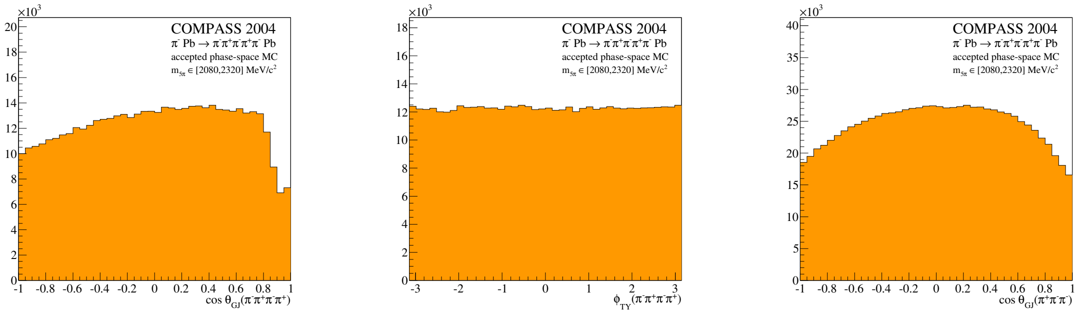

(a) $\cos\theta_{\mathrm{GJ}}^{4\pi}$ (b) $\phi_{\mathrm{TY}}^{4\pi}$ (c) $\cos\theta_{\mathrm{GJ}}^{3\pi}$

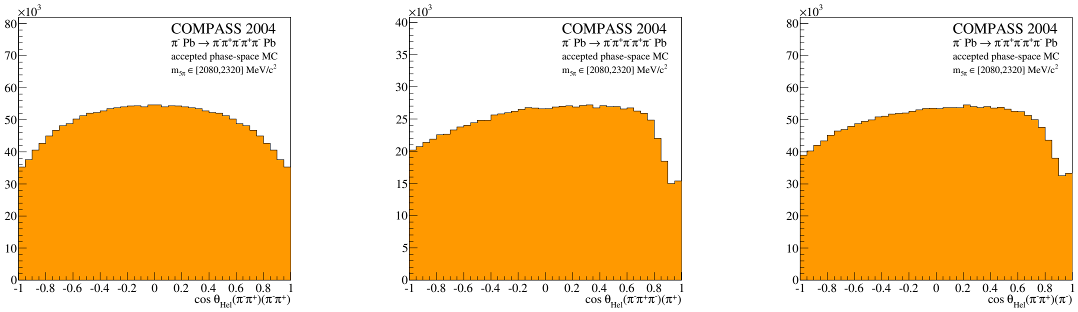

(d) $\cos\theta_{\mathrm{Hel}}^{22}$ (e) $\cos\theta_{\mathrm{Hel}}^{31}$ (f) $\cos\theta_{\mathrm{Hel}}^{21}$

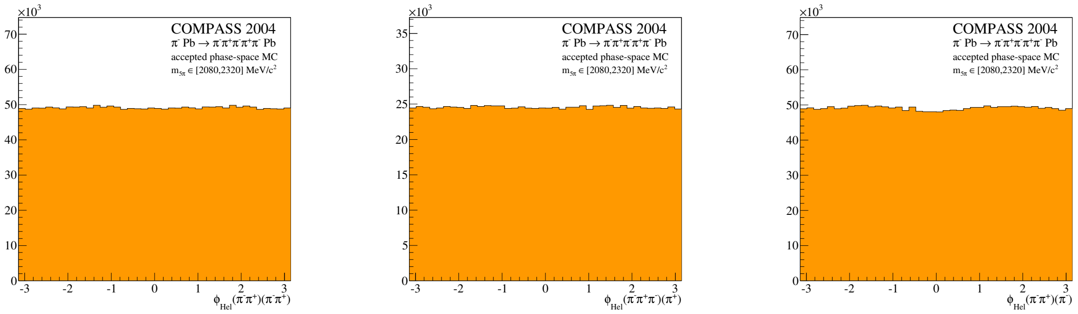

(g) ϕ_{Hel}^{22} (h) ϕ_{Hel}^{31} (i) ϕ_{Hel}^{21}

Figure A.4: Angular acceptance for the 5-pion final state as determined by Monte Carlo simulation. The distributions shown are projections of accepted phase-space events. Unmodified phase-space distributions would be flat in all variables. $m_{5\pi} \in [2.08, 2.32]\,\mathrm{GeV}/c^2$

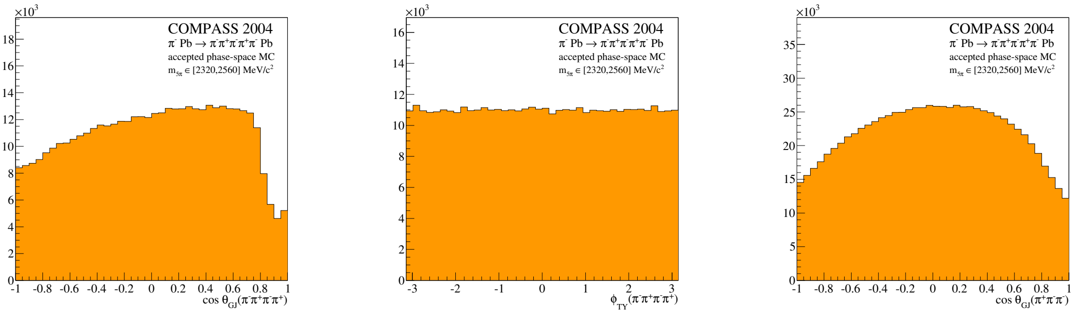

(a) $\cos\theta^{4\pi}_{\text{GJ}}$ (b) $\phi^{4\pi}_{\text{TY}}$ (c) $\cos\theta^{3\pi}_{\text{GJ}}$

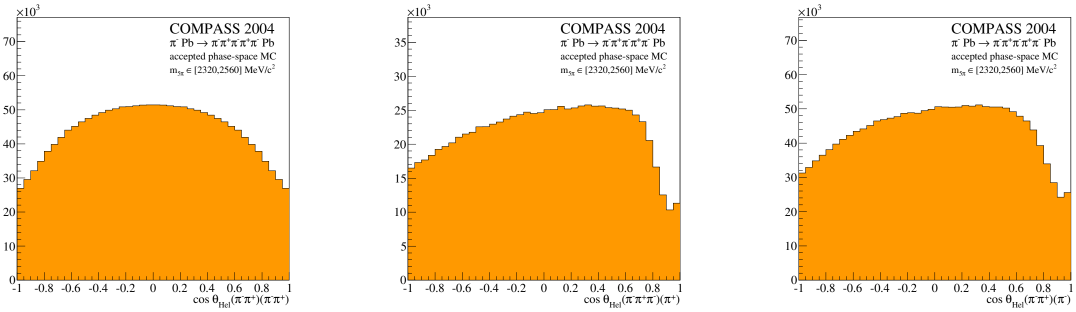

(d) $\cos\theta^{22}_{\text{Hel}}$ (e) $\cos\theta^{31}_{\text{Hel}}$ (f) $\cos\theta^{21}_{\text{Hel}}$

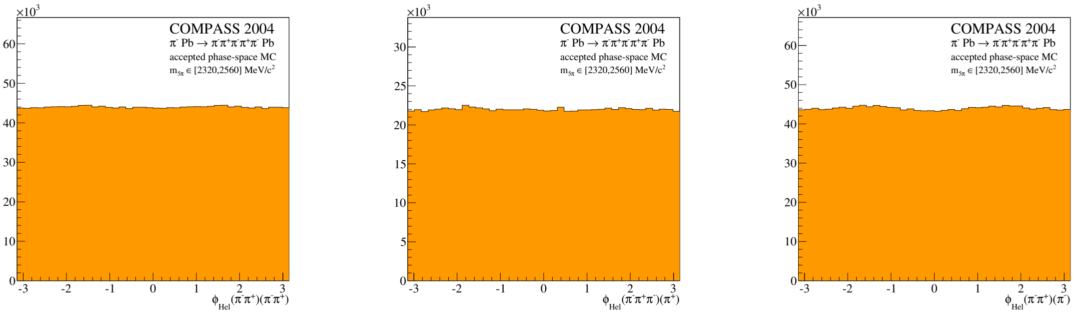

(g) ϕ^{22}_{Hel} (h) ϕ^{31}_{Hel} (i) ϕ^{21}_{Hel}

Figure A.5: Angular acceptance for the 5-pion final state as determined by Monte Carlo simulation. The distributions shown are projections of accepted phase-space events. Unmodified phase-space distributions would be flat in all variables. $m_{5\pi} \in [2.32, 2.56]\,\text{GeV}/c^2$

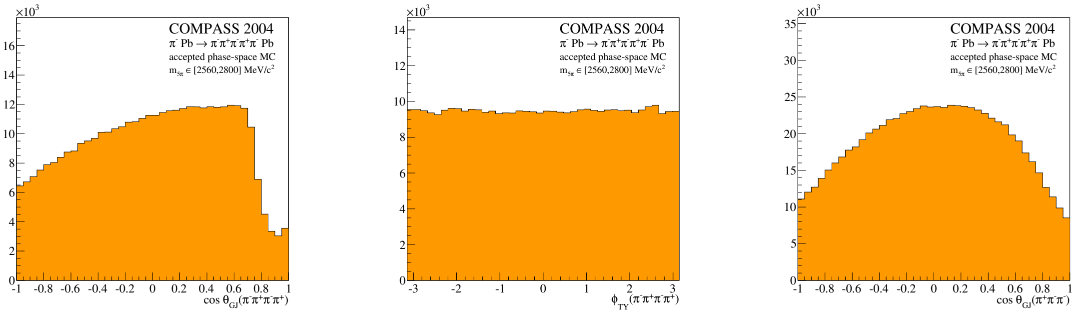

(a) $\cos\theta_{\mathrm{GJ}}^{4\pi}$ (b) $\phi_{\mathrm{TY}}^{4\pi}$ (c) $\cos\theta_{\mathrm{GJ}}^{3\pi}$

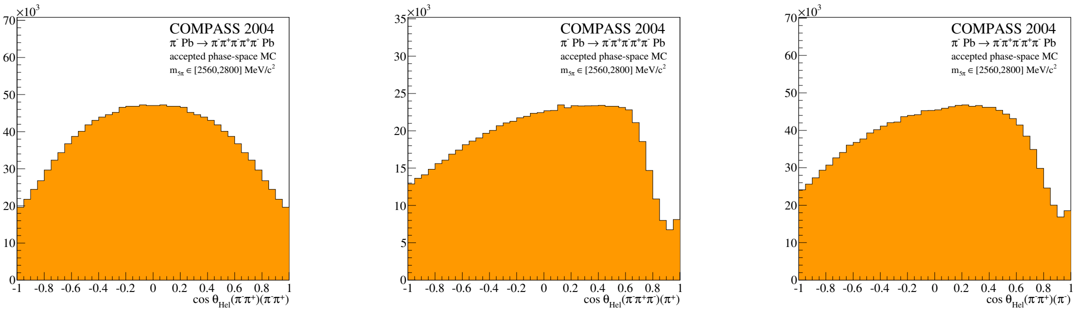

(d) $\cos\theta_{\mathrm{Hel}}^{22}$ (e) $\cos\theta_{\mathrm{Hel}}^{31}$ (f) $\cos\theta_{\mathrm{Hel}}^{21}$

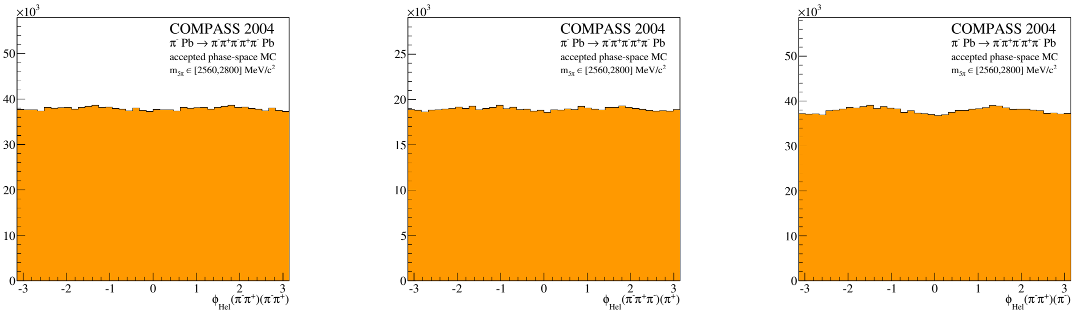

(g) ϕ_{Hel}^{22} (h) ϕ_{Hel}^{31} (i) ϕ_{Hel}^{21}

Figure A.6: Angular acceptance for the 5-pion final state as determined by Monte Carlo simulation. The distributions shown are projections of accepted phase-space events. Unmodified phase-space distributions would be flat in all variables. $m_{5\pi} \in [2.56, 2.800]\,\mathrm{GeV}/c^2$

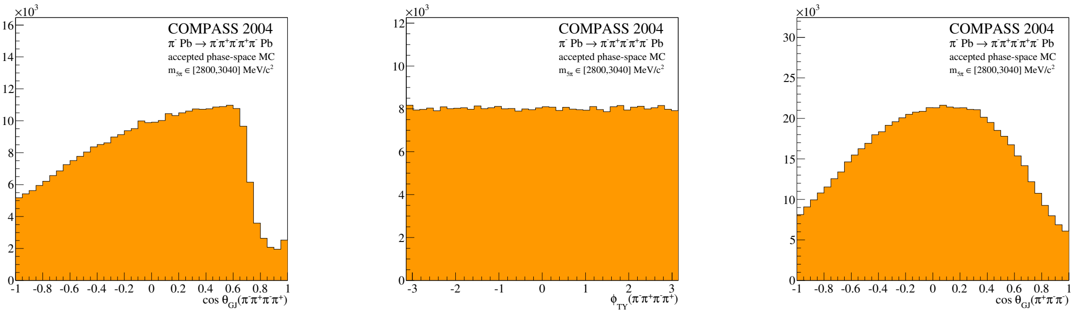

(a) $\cos\theta_{\mathrm{GJ}}^{4\pi}$ (b) $\phi_{\mathrm{TY}}^{4\pi}$ (c) $\cos\theta_{\mathrm{GJ}}^{3\pi}$

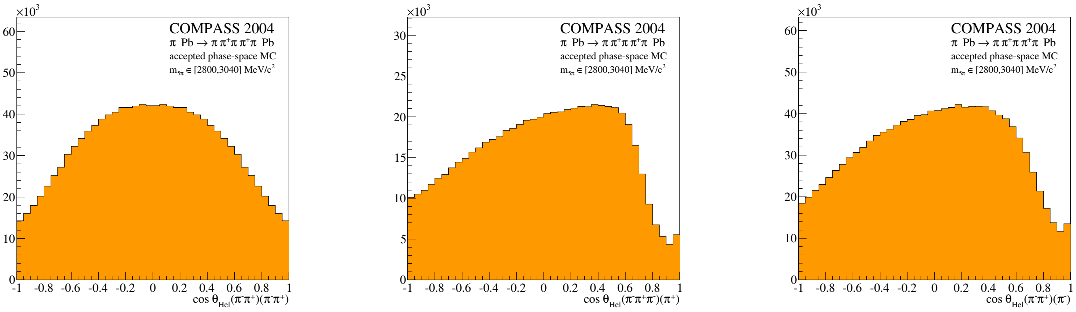

(d) $\cos\theta_{\mathrm{Hel}}^{22}$ (e) $\cos\theta_{\mathrm{Hel}}^{31}$ (f) $\cos\theta_{\mathrm{Hel}}^{21}$

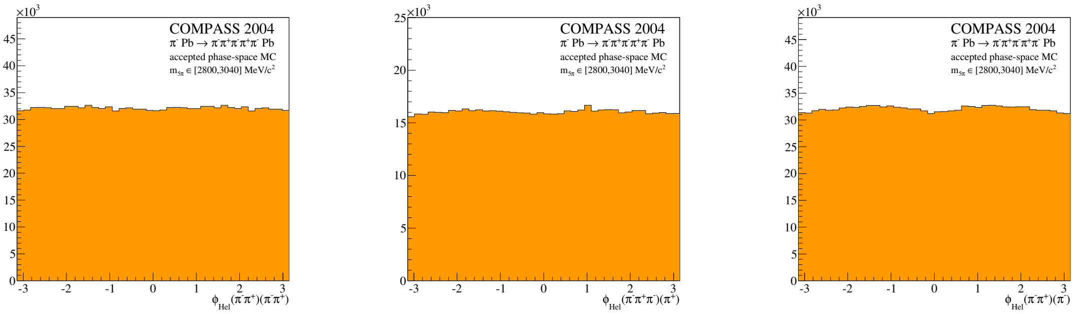

(g) ϕ_{Hel}^{22} (h) ϕ_{Hel}^{31} (i) ϕ_{Hel}^{21}

Figure A.7: Angular acceptance for the 5-pion final state as determined by Monte Carlo simulation. The distributions shown are projections of accepted phase-space events. Unmodified phase-space distributions would be flat in all variables. $m_{5\pi} \in [2.80, 3.04]\,\mathrm{GeV}/c^2$

Appendix B

Pool of Partial Amplitudes

The following partial amplitudes have been used in the genetic optimization (see section 4.2) to generate the final 5π isobar model and estimate the systematic errors associated with the choice of waveset.

$$1^-0^{-+}0^+ \quad f_2(1270)\begin{bmatrix}0\\0\end{bmatrix}\pi_2(1670)\to\pi^-\begin{bmatrix}0\\2\end{bmatrix}f_2(1270)$$

$$1^-0^{-+}0^+ \quad f_2(1270)\begin{bmatrix}1\\1\end{bmatrix}a_1(1269)\to\pi^-\begin{bmatrix}0\\1\end{bmatrix}\rho(770)$$

$$1^-0^{-+}0^+ \quad f_2(1270)\begin{bmatrix}1\\1\end{bmatrix}a_2(1320)\to\pi^-\begin{bmatrix}2\\1\end{bmatrix}\rho(770)$$

$$1^-0^{-+}0^+ \quad f_2(1270)\begin{bmatrix}3\\3\end{bmatrix}a_1(1269)\to\pi^-\begin{bmatrix}0\\1\end{bmatrix}\rho(770)$$

$$1^-0^{-+}0^+ \quad f_2(1270)\begin{bmatrix}3\\3\end{bmatrix}a_2(1320)\to\pi^-\begin{bmatrix}2\\1\end{bmatrix}\rho(770)$$

$$1^-0^{-+}0^+ \quad \pi^-\begin{bmatrix}0\\0\end{bmatrix}b_0(1800)\to\pi^\mp\begin{bmatrix}0\\0\end{bmatrix}\pi(1300)\to\pi^\mp\begin{bmatrix}0\\0\end{bmatrix}\sigma$$

$$1^-0^{-+}0^+ \quad \pi^-\begin{bmatrix}0\\0\end{bmatrix}b_0(1800)\to\pi^\mp\begin{bmatrix}1\\1\end{bmatrix}a_1(1269)\to\pi^\pm\begin{bmatrix}0\\1\end{bmatrix}\rho(770)$$

$$1^-0^{-+}0^+ \quad \pi^-\begin{bmatrix}0\\0\end{bmatrix}f_0(1370)\to\rho(770)\begin{bmatrix}0\\0\end{bmatrix}\rho(770)$$

$$1^-0^{-+}0^+ \quad \pi^-\begin{bmatrix}0\\0\end{bmatrix}f_0(1500)\to\rho(770)\begin{bmatrix}0\\0\end{bmatrix}\rho(770)$$

$$1^-0^{-+}0^+ \quad \pi^-\begin{bmatrix}0\\0\end{bmatrix}f_0(1500)\to\sigma[0]\sigma$$

$$1^-0^{-+}0^+ \quad \pi^-\begin{bmatrix}0\\0\end{bmatrix}\sigma\to\sigma[0]\sigma$$

$$1^-0^{-+}0^+ \quad \pi^-\begin{bmatrix}1\\1\end{bmatrix}\eta_1(1600)\to\pi^\mp\begin{bmatrix}0\\1\end{bmatrix}a_1(1269)\to\pi^\pm\begin{bmatrix}0\\1\end{bmatrix}\rho(770)$$

$$1^-0^{-+}0^+ \quad \pi^-\begin{bmatrix}1\\1\end{bmatrix}\eta_1(1600)\to\pi^\mp\begin{bmatrix}1\\0\end{bmatrix}\pi(1300)\to\pi^\pm\begin{bmatrix}0\\0\end{bmatrix}\sigma$$

$$1^-0^{-+}0^+ \quad \pi^-\begin{bmatrix}1\\1\end{bmatrix}\eta_1(1600)\to\pi^\mp\begin{bmatrix}1\\0\end{bmatrix}\pi(1300)\to\pi^\pm\begin{bmatrix}1\\1\end{bmatrix}\rho(770)$$

$$1^-0^{-+}0^+ \quad \pi^-\begin{bmatrix}1\\1\end{bmatrix}\rho(1600)\to\pi^\mp\begin{bmatrix}0\\1\end{bmatrix}a_1(1269)\to\pi^\pm\begin{bmatrix}0\\1\end{bmatrix}\rho(770)$$

$$1^-0^{-+}0^+ \quad \pi^-\begin{bmatrix}1\\1\end{bmatrix}\rho(1600)\to\pi^\mp\begin{bmatrix}1\\0\end{bmatrix}\pi(1300)\to\pi^\pm\begin{bmatrix}1\\1\end{bmatrix}\rho(770)$$

$$1^-0^{-+}0^+ \quad \pi^-\begin{bmatrix}1\\1\end{bmatrix}\rho(1600)\to\rho(770)\begin{bmatrix}0\\1\end{bmatrix}\sigma$$

$$1^-0^{-+}0^+ \quad \pi^-\begin{bmatrix}2\\2\end{bmatrix}b_2(1800)\to\pi^\mp\begin{bmatrix}1\\1\end{bmatrix}a_1(1269)\to\pi^\pm\begin{bmatrix}0\\1\end{bmatrix}\rho(770)$$

$$1^{-}0^{-+}0^{+} \quad \pi^{-}\begin{bmatrix}2\\2\end{bmatrix} b_2(1800)\to\pi^{\mp}\begin{bmatrix}1\\2\end{bmatrix} a_2(1320)\to\pi^{\pm}\begin{bmatrix}2\\1\end{bmatrix}\rho(770)$$

$$1^{-}0^{-+}0^{+} \quad \pi^{-}\begin{bmatrix}2\\2\end{bmatrix} f_2(1270)\to\pi^{\mp}[1]a_1(1269)\to\pi^{\pm}[0]\rho(770)$$

$$1^{-}0^{-+}0^{+} \quad \pi^{-}\begin{bmatrix}2\\2\end{bmatrix} f_2(1270)\to\sigma[2]\sigma$$

$$1^{-}0^{-+}0^{+} \quad \pi^{-}\begin{bmatrix}2\\2\end{bmatrix} f_2(1565)\to\pi^{\mp}[1]a_1(1269)\to\pi^{\pm}[0]\rho(770)$$

$$1^{-}0^{-+}0^{+} \quad \pi^{-}\begin{bmatrix}2\\2\end{bmatrix} f_2(1565)\to\sigma[2]\sigma$$

$$1^{-}0^{-+}0^{+} \quad \rho(770)\begin{bmatrix}0\\0\end{bmatrix} a_1(1269)\to\pi^{-}[0]\rho(770)$$

$$1^{-}0^{-+}0^{+} \quad \rho(770)\begin{bmatrix}0\\0\end{bmatrix} a_1(1269)\to\pi^{-}[1]\sigma$$

$$1^{-}0^{++}0^{-} \quad \rho(770)\begin{bmatrix}1\\1\end{bmatrix} a_1(1269)\to\pi^{-}[0]\rho(770)$$

$$1^{-}0^{++}0^{-} \quad \rho(770)\begin{bmatrix}1\\1\end{bmatrix} a_2(1320)\to\pi^{-}[2]\rho(770)$$

$$1^{-}0^{-+}0^{+} \quad \rho(770)\begin{bmatrix}1\\1\end{bmatrix} \pi(1300)\to\pi^{-}\begin{bmatrix}0\\0\end{bmatrix}\sigma$$

$$1^{-}0^{-+}0^{+} \quad \rho(770)\begin{bmatrix}1\\1\end{bmatrix} \pi(1300)\to\pi^{-}[1]\rho(770)$$

$$1^{-}0^{-+}0^{+} \quad \rho(770)\begin{bmatrix}2\\2\end{bmatrix} a_1(1269)\to\pi^{-}\begin{bmatrix}0\\1\end{bmatrix}\rho(770)$$

$$1^{-}0^{-+}0^{+} \quad \rho(770)\begin{bmatrix}2\\2\end{bmatrix} a_1(1269)\to\pi^{-}[1]\sigma$$

$$1^{-}0^{-+}0^{+} \quad \rho(770)\begin{bmatrix}2\\2\end{bmatrix} a_2(1320)\to\pi^{-}\begin{bmatrix}2\\1\end{bmatrix}\rho(770)$$

$$1^{-}0^{++}0^{-} \quad \rho(770)\begin{bmatrix}2\\2\end{bmatrix} \pi_2(1670)\to\pi^{-}[0]f_2(1270)$$

$$1^{-}0^{-+}0^{+} \quad \sigma\begin{bmatrix}0\\0\end{bmatrix} \pi(1300)\to\pi^{-}\begin{bmatrix}0\\0\end{bmatrix}\sigma$$

$$1^{-}0^{-+}0^{+} \quad \sigma\begin{bmatrix}0\\0\end{bmatrix} \pi(1300)\to\pi^{-}\begin{bmatrix}1\\1\end{bmatrix}\rho(770)$$

$$1^{-}0^{-+}0^{+} \quad \sigma\begin{bmatrix}1\\1\end{bmatrix} a_1(1269)\to\pi^{-}[0]\rho(770)$$

$1^-0^{++}0^-$	$\sigma \begin{bmatrix} 2 \\ 2 \end{bmatrix} a_2(1320) \rightarrow \pi^-[2]\rho(770)$
$1^-0^{-+}0^+$	$\sigma \begin{bmatrix} 2 \\ 2 \end{bmatrix} \pi_2(1670) \rightarrow \pi^- \begin{bmatrix} 0 \\ 2 \end{bmatrix} f_2(1270)$
$1^-1^{++}0^+$	$f_2(1270) \begin{bmatrix} 0 \\ 1 \end{bmatrix} a_1(1269) \rightarrow \pi^- \begin{bmatrix} 0 \\ 1 \end{bmatrix} \rho(770)$
$1^-1^{++}0^+$	$f_2(1270) \begin{bmatrix} 0 \\ 1 \end{bmatrix} a_2(1320) \rightarrow \pi^- \begin{bmatrix} 2 \\ 1 \end{bmatrix} \rho(770)$
$1^-1^{++}0^+$	$f_2(1270) \begin{bmatrix} 1 \\ 0 \end{bmatrix} \pi_2(1670) \rightarrow \pi^- \begin{bmatrix} 0 \\ 2 \end{bmatrix} f_2(1270)$
$1^-1^{++}0^+$	$f_2(1270) \begin{bmatrix} 1 \\ 2 \end{bmatrix} \pi_2(1670) \rightarrow \pi^- \begin{bmatrix} 0 \\ 2 \end{bmatrix} f_2(1270)$
$1^-1^{++}0^+$	$f_2(1270) \begin{bmatrix} 2 \\ 1 \end{bmatrix} a_1(1269) \rightarrow \pi^- \begin{bmatrix} 0 \\ 1 \end{bmatrix} \rho(770)$
$1^-1^{++}0^+$	$f_2(1270) \begin{bmatrix} 2 \\ 1 \end{bmatrix} a_2(1320) \rightarrow \pi^- \begin{bmatrix} 2 \\ 1 \end{bmatrix} \rho(770)$
$1^-1^{++}0^+$	$f_2(1270) \begin{bmatrix} 2 \\ 2 \end{bmatrix} a_1(1269) \rightarrow \pi^- \begin{bmatrix} 0 \\ 1 \end{bmatrix} \rho(770)$
$1^-1^{++}0^+$	$f_2(1270) \begin{bmatrix} 2 \\ 2 \end{bmatrix} a_2(1320) \rightarrow \pi^- \begin{bmatrix} 2 \\ 1 \end{bmatrix} \rho(770)$
$1^-1^{++}0^+$	$f_2(1270) \begin{bmatrix} 2 \\ 3 \end{bmatrix} a_1(1269) \rightarrow \pi^- \begin{bmatrix} 0 \\ 1 \end{bmatrix} \rho(770)$
$1^-1^{++}0^+$	$f_2(1270) \begin{bmatrix} 2 \\ 3 \end{bmatrix} a_2(1320) \rightarrow \pi^- \begin{bmatrix} 2 \\ 1 \end{bmatrix} \rho(770)$
$1^-1^{++}0^+$	$f_2(1270) \begin{bmatrix} 4 \\ 3 \end{bmatrix} a_1(1269) \rightarrow \pi^- \begin{bmatrix} 0 \\ 1 \end{bmatrix} \rho(770)$
$1^-1^{++}0^+$	$f_2(1270) \begin{bmatrix} 4 \\ 3 \end{bmatrix} a_2(1320) \rightarrow \pi^- \begin{bmatrix} 2 \\ 1 \end{bmatrix} \rho(770)$
$1^-1^{++}0^+$	$f_2(1270) \begin{bmatrix} 4 \\ 4 \end{bmatrix} a_2(1320) \rightarrow \pi^- \begin{bmatrix} 2 \\ 1 \end{bmatrix} \rho(770)$
$1^-1^{-+}0^-$	$\pi^- \begin{bmatrix} 0 \\ 1 \end{bmatrix} b_1(1800) \rightarrow \pi^\mp \begin{bmatrix} 1 \\ 1 \end{bmatrix} a_1(1269) \rightarrow \pi^\pm[0]\rho(770)$
$1^-1^{++}0^+$	$\pi^- \begin{bmatrix} 0 \\ 1 \end{bmatrix} \eta_1(1600) \rightarrow \pi^\mp \begin{bmatrix} 0 \\ 1 \end{bmatrix} a_1(1269) \rightarrow \pi^\pm \begin{bmatrix} 0 \\ 1 \end{bmatrix} \rho(770)$
$1^-1^{++}0^+$	$\pi^- \begin{bmatrix} 0 \\ 1 \end{bmatrix} \eta_1(1600) \rightarrow \pi^\mp \begin{bmatrix} 1 \\ 0 \end{bmatrix} \pi(1300) \rightarrow \pi^\pm \begin{bmatrix} 0 \\ 0 \end{bmatrix} \sigma$

$$1^-1^{++}0^+ \quad \pi^- \begin{bmatrix}0\\1\end{bmatrix} \eta_1(1600) \to \pi^\mp \begin{bmatrix}1\\0\end{bmatrix} \pi(1300) \to \pi^\pm \begin{bmatrix}1\\1\end{bmatrix} \rho(770)$$

$$1^-1^{++}0^+ \quad \pi^- \begin{bmatrix}0\\1\end{bmatrix} \rho(1600) \to \pi^\mp \begin{bmatrix}0\\1\end{bmatrix} a_1(1269) \to \pi^\pm \begin{bmatrix}0\\1\end{bmatrix} \rho(770)$$

$$1^-1^{++}0^+ \quad \pi^- \begin{bmatrix}0\\1\end{bmatrix} \rho(1600) \to \pi^\mp \begin{bmatrix}1\\0\end{bmatrix} \pi(1300) \to \pi^\pm \begin{bmatrix}1\\1\end{bmatrix} \rho(770)$$

$$1^-1^{++}0^+ \quad \pi^- \begin{bmatrix}0\\1\end{bmatrix} \rho(1600) \to \rho(770) \begin{bmatrix}0\\1\end{bmatrix} \sigma$$

$$1^-1^{++}0^+ \quad \pi^- \begin{bmatrix}1\\0\end{bmatrix} b_0(1800) \to \pi^\mp \begin{bmatrix}0\\0\end{bmatrix} \pi(1300) \to \pi^\pm \begin{bmatrix}0\\0\end{bmatrix} \sigma$$

$$1^-1^{++}0^+ \quad \pi^- \begin{bmatrix}1\\0\end{bmatrix} b_0(1800) \to \pi^\mp \begin{bmatrix}1\\1\end{bmatrix} a_1(1269) \to \pi^\pm \begin{bmatrix}0\\1\end{bmatrix} \rho(770)$$

$$1^-1^{++}0^+ \quad \pi^- \begin{bmatrix}1\\0\end{bmatrix} f_0(1370) \to \rho(770) \begin{bmatrix}0\\0\end{bmatrix} \rho(770)$$

$$1^-1^{++}0^+ \quad \pi^- \begin{bmatrix}1\\0\end{bmatrix} f_0(1500) \to \rho(770) \begin{bmatrix}0\\0\end{bmatrix} \rho(770)$$

$$1^-1^{++}0^+ \quad \pi^- \begin{bmatrix}1\\0\end{bmatrix} f_0(1500) \to \sigma[0]\sigma$$

$$1^-1^{++}0^+ \quad \pi^- \begin{bmatrix}1\\0\end{bmatrix} \sigma \to \sigma[0]\sigma$$

$$1^-1^{++}0^+ \quad \pi^- \begin{bmatrix}1\\1\end{bmatrix} b_1(1235) \to \pi^\mp \begin{bmatrix}1\\1\end{bmatrix} a_1(1269) \to \pi^\pm[0]\rho(770)$$

$$1^-1^{++}0^+ \quad \pi^- \begin{bmatrix}1\\1\end{bmatrix} b_1(1235) \to \sigma \begin{bmatrix}1\\1\end{bmatrix} \rho(770)$$

$$1^-1^{++}0^+ \quad \pi^- \begin{bmatrix}1\\1\end{bmatrix} b_1(1800) \to \pi^\mp \begin{bmatrix}1\\1\end{bmatrix} a_1(1269) \to \pi^\pm[0]\rho(770)$$

$$1^-1^{++}0^+ \quad \pi^- \begin{bmatrix}1\\1\end{bmatrix} f_1(1285) \to \pi^\mp \begin{bmatrix}1\\1\end{bmatrix} a_1(1269) \to \pi^\pm[0]\rho(770)$$

$$1^-1^{++}0^+ \quad \pi^- \begin{bmatrix}1\\1\end{bmatrix} f_1(1285) \to \pi^\mp \begin{bmatrix}1\\1\end{bmatrix} a_1(1269) \to \pi^\pm[1]\sigma$$

$$1^-1^{++}0^+ \quad \pi^- \begin{bmatrix}1\\2\end{bmatrix} b_2(1800) \to \pi^\mp \begin{bmatrix}1\\1\end{bmatrix} a_1(1269) \to \pi^\pm \begin{bmatrix}0\\1\end{bmatrix} \rho(770)$$

$$1^-1^{++}0^+ \quad \pi^- \begin{bmatrix}1\\2\end{bmatrix} b_2(1800) \to \pi^\mp \begin{bmatrix}1\\2\end{bmatrix} a_2(1320) \to \pi^\pm \begin{bmatrix}2\\1\end{bmatrix} \rho(770)$$

$$1^-1^{++}0^+ \quad \pi^- \begin{bmatrix}1\\2\end{bmatrix} f_2(1270) \to \pi^\mp[1]a_1(1269) \to \pi^\pm[0]\rho(770)$$

$$1^-1^{++}0^+ \quad \pi^- \begin{bmatrix}1\\2\end{bmatrix} f_2(1270) \to \sigma[2]\sigma$$

$$1^-1^{++}0^+ \quad \pi^- \begin{bmatrix}1\\2\end{bmatrix} f_2(1565) \to \pi^\mp[1]a_1(1269) \to \pi^\pm[0]\rho(770)$$

$$1^-1^{++}0^+ \quad \pi^- \begin{bmatrix}1\\2\end{bmatrix} f_2(1565) \to \sigma[2]\sigma$$

$$1^-1^{++}0^+ \quad \pi^- \begin{bmatrix}2\\1\end{bmatrix} \rho(1600) \to \pi^\mp \begin{bmatrix}0\\1\end{bmatrix} a_1(1269) \to \pi^\pm \begin{bmatrix}0\\1\end{bmatrix} \rho(770)$$

$$1^-1^{++}0^+ \quad \pi^- \begin{bmatrix}2\\1\end{bmatrix} \rho(1600) \to \pi^\mp \begin{bmatrix}1\\0\end{bmatrix} \pi(1300) \to \pi^\pm \begin{bmatrix}1\\1\end{bmatrix} \rho(770)$$

$$1^-1^{++}0^+ \quad \pi^- \begin{bmatrix}2\\1\end{bmatrix} \rho(1600) \to \rho(770) \begin{bmatrix}0\\1\end{bmatrix} \sigma$$

$$1^-1^{++}0^+ \quad \pi^- \begin{bmatrix}2\\2\end{bmatrix} \eta_2(1645) \to \pi^\mp \begin{bmatrix}0\\2\end{bmatrix} a_2(1320) \to \pi^\pm \begin{bmatrix}2\\1\end{bmatrix} \rho(770)$$

$$1^-1^{++}0^+ \quad \pi^- \begin{bmatrix}2\\3\end{bmatrix} \rho_3(1690) \to \rho(770) \begin{bmatrix}2\\1\end{bmatrix} \sigma$$

$$1^-1^{++}0^+ \quad \rho_3(1690) \to \rho(770) \begin{bmatrix}1\\2\end{bmatrix} \rho(770) \begin{bmatrix}2\\3\end{bmatrix} \pi^-$$

$$1^-1^{-+}0^- \quad \rho(770) \begin{bmatrix}0\\1\end{bmatrix} a_1(1269) \to \pi^-[0]\rho(770)$$

$$1^-1^{-+}0^- \quad \rho(770) \begin{bmatrix}0\\1\end{bmatrix} a_2(1320) \to \pi^-[2]\rho(770)$$

$$1^-1^{++}0^+ \quad \rho(770) \begin{bmatrix}0\\1\end{bmatrix} \pi_1(1600) \to \pi^-[1]\rho(770)$$

$$1^-1^{++}0^+ \quad \rho(770) \begin{bmatrix}0\\1\end{bmatrix} \pi(1300) \to \pi^- \begin{bmatrix}0\\0\end{bmatrix} \sigma$$

$$1^-1^{++}0^+ \quad \rho(770) \begin{bmatrix}0\\1\end{bmatrix} \pi(1300) \to \pi^-[1]\rho(770)$$

$$1^-1^{++}0^+ \quad \rho(770) \begin{bmatrix}1\\0\end{bmatrix} a_1(1269) \to \pi^-[0]\rho(770)$$

$$1^-1^{++}0^+ \quad \rho(770) \begin{bmatrix}1\\1\end{bmatrix} a_1(1269) \to \pi^-[0]\rho(770)$$

$$1^-1^{++}0^+ \quad \rho(770) \begin{bmatrix}1\\1\end{bmatrix} a_2(1320) \to \pi^- \begin{bmatrix}2\\1\end{bmatrix} \rho(770)$$

$$1^-1^{++}0^+ \quad \rho(770) \begin{bmatrix}1\\2\end{bmatrix} a_1(1269) \to \pi^-[0]\rho(770)$$

$$1^-1^{++}0^+ \quad \rho(770)\begin{bmatrix}1\\2\end{bmatrix} a_2(1320)\to\pi^-[2]\rho(770)$$

$$1^-1^{-+}0^- \quad \rho(770)\begin{bmatrix}2\\1\end{bmatrix} a_1(1269)\to\pi^-[0]\rho(770)$$

$$1^-1^{++}0^+ \quad \rho(770)\begin{bmatrix}2\\1\end{bmatrix} \pi(1300)\to\pi^-\begin{bmatrix}0\\0\end{bmatrix}\sigma$$

$$1^-1^{++}0^+ \quad \rho(770)\begin{bmatrix}2\\1\end{bmatrix} \pi(1300)\to\pi^-[1]\rho(770)$$

$$1^-1^{++}0^+ \quad \rho(770)\begin{bmatrix}2\\2\end{bmatrix} \pi_2(1670)\to\pi^-[0]f_2(1270)$$

$$1^-1^{++}0^+ \quad \sigma\begin{bmatrix}0\\1\end{bmatrix} a_1(1269)\to\pi^-[0]\rho(770)$$

$$1^-1^{++}0^+ \quad \sigma\begin{bmatrix}0\\1\end{bmatrix} a_1(1269)\to\pi^-[1]\sigma$$

$$1^-1^{++}0^+ \quad \sigma\begin{bmatrix}1\\0\end{bmatrix} \pi(1300)\to\pi^-\begin{bmatrix}0\\0\end{bmatrix}\sigma$$

$$1^-1^{++}0^+ \quad \sigma\begin{bmatrix}1\\0\end{bmatrix} \pi(1300)\to\pi^-\begin{bmatrix}1\\1\end{bmatrix}\rho(770)$$

$$1^-1^{-+}0^- \quad \sigma\begin{bmatrix}1\\1\end{bmatrix} a_1(1269)\to\pi^-[0]\rho(770)$$

$$1^-1^{++}0^+ \quad \sigma\begin{bmatrix}1\\1\end{bmatrix} \pi_1(1600)\to\pi^-[1]\rho(770)$$

$$1^-1^{-+}0^- \quad \sigma\begin{bmatrix}1\\2\end{bmatrix} a_2(1320)\to\pi^-[2]\rho(770)$$

$$1^-1^{++}0^+ \quad \sigma\begin{bmatrix}1\\2\end{bmatrix} \pi_2(1670)\to\pi^-\begin{bmatrix}0\\2\end{bmatrix}f_2(1270)$$

$$1^-1^{++}0^+ \quad \sigma\begin{bmatrix}2\\1\end{bmatrix} a_1(1269)\to\pi^-[0]\rho(770)$$

$$1^-1^{++}0^+ \quad \sigma\begin{bmatrix}2\\1\end{bmatrix} a_1(1269)\to\pi^-[1]\sigma$$

$$1^-1^{++}0^+ \quad \sigma\begin{bmatrix}2\\2\end{bmatrix} a_2(1320)\to\pi^-[2]\rho(770)$$

$$1^-2^{-+}0^+ \quad f_2(1270)\begin{bmatrix}0\\2\end{bmatrix} \pi_2(1670)\to\pi^-\begin{bmatrix}0\\2\end{bmatrix}f_2(1270)$$

$$1^-2^{-+}0^+ \quad f_2(1270)\begin{bmatrix}1\\1\end{bmatrix} a_1(1269)\to\pi^-\begin{bmatrix}0\\1\end{bmatrix}\rho(770)$$

$$1^-2^{-+}0^+ \quad f_2(1270)\begin{bmatrix}1\\1\end{bmatrix}a_2(1320)\rightarrow\pi^-\begin{bmatrix}2\\1\end{bmatrix}\rho(770)$$

$$1^-2^{-+}0^+ \quad f_2(1270)\begin{bmatrix}1\\2\end{bmatrix}a_1(1269)\rightarrow\pi^-\begin{bmatrix}0\\1\end{bmatrix}\rho(770)$$

$$1^-2^{-+}0^+ \quad f_2(1270)\begin{bmatrix}1\\2\end{bmatrix}a_2(1320)\rightarrow\pi^-\begin{bmatrix}2\\1\end{bmatrix}\rho(770)$$

$$1^-2^{-+}0^+ \quad f_2(1270)\begin{bmatrix}1\\3\end{bmatrix}a_1(1269)\rightarrow\pi^-\begin{bmatrix}0\\1\end{bmatrix}\rho(770)$$

$$1^-2^{-+}0^+ \quad f_2(1270)\begin{bmatrix}1\\3\end{bmatrix}a_2(1320)\rightarrow\pi^-\begin{bmatrix}2\\1\end{bmatrix}\rho(770)$$

$$1^-2^{-+}0^+ \quad f_2(1270)\begin{bmatrix}2\\0\end{bmatrix}\pi_2(1670)\rightarrow\pi^-\begin{bmatrix}0\\2\end{bmatrix}f_2(1270)$$

$$1^-2^{-+}0^+ \quad f_2(1270)\begin{bmatrix}2\\2\end{bmatrix}\pi_2(1670)\rightarrow\pi^-\begin{bmatrix}0\\2\end{bmatrix}f_2(1270)$$

$$1^-2^{-+}0^+ \quad f_2(1270)\begin{bmatrix}3\\1\end{bmatrix}a_1(1269)\rightarrow\pi^-\begin{bmatrix}0\\1\end{bmatrix}\rho(770)$$

$$1^-2^{-+}0^+ \quad f_2(1270)\begin{bmatrix}3\\1\end{bmatrix}a_2(1320)\rightarrow\pi^-\begin{bmatrix}2\\1\end{bmatrix}\rho(770)$$

$$1^-2^{-+}0^+ \quad f_2(1270)\begin{bmatrix}3\\2\end{bmatrix}a_1(1269)\rightarrow\pi^-\begin{bmatrix}0\\1\end{bmatrix}\rho(770)$$

$$1^-2^{-+}0^+ \quad f_2(1270)\begin{bmatrix}3\\2\end{bmatrix}a_2(1320)\rightarrow\pi^-\begin{bmatrix}2\\1\end{bmatrix}\rho(770)$$

$$1^-2^{-+}0^+ \quad f_2(1270)\begin{bmatrix}3\\3\end{bmatrix}a_1(1269)\rightarrow\pi^-\begin{bmatrix}0\\1\end{bmatrix}\rho(770)$$

$$1^-2^{-+}0^+ \quad f_2(1270)\begin{bmatrix}3\\3\end{bmatrix}a_2(1320)\rightarrow\pi^-\begin{bmatrix}2\\1\end{bmatrix}\rho(770)$$

$$1^-2^{-+}0^+ \quad f_2(1270)\begin{bmatrix}3\\4\end{bmatrix}a_2(1320)\rightarrow\pi^-\begin{bmatrix}2\\1\end{bmatrix}\rho(770)$$

$$1^-2^{-+}0^+ \quad \pi^-\begin{bmatrix}0\\2\end{bmatrix}b_2(1800)\rightarrow\pi^\mp\begin{bmatrix}1\\1\end{bmatrix}a_1(1269)\rightarrow\pi^\pm\begin{bmatrix}0\\1\end{bmatrix}\rho(770)$$

$$1^-2^{-+}0^+ \quad \pi^-\begin{bmatrix}0\\2\end{bmatrix}b_2(1800)\rightarrow\pi^\mp\begin{bmatrix}1\\2\end{bmatrix}a_2(1320)\rightarrow\pi^\pm\begin{bmatrix}2\\1\end{bmatrix}\rho(770)$$

$$1^-2^{-+}0^+ \quad \pi^-\begin{bmatrix}0\\2\end{bmatrix}f_2(1230)\rightarrow\pi^\mp[1]a_1(1269)\rightarrow\pi^\pm[0]\rho(770)$$

$$1^-2^{-+}0^+ \quad \pi^-\begin{bmatrix}0\\2\end{bmatrix}f_2(1250)\rightarrow\pi^\mp[1]a_1(1269)\rightarrow\pi^\pm[0]\rho(770)$$

$1^-2^{-+}0^+$	π^-	$\begin{bmatrix}0\\2\end{bmatrix} f_2(1270) \to \pi^\mp[1]a_1(1269) \to \pi^\pm[0]\rho(770)$
$1^-2^{-+}0^+$	π^-	$\begin{bmatrix}0\\2\end{bmatrix} f_2(1270) \to \sigma[2]\sigma$
$1^-2^{-+}0^+$	π^-	$\begin{bmatrix}0\\2\end{bmatrix} f_2(1290) \to \pi^\mp[1]a_1(1269) \to \pi^\pm[0]\rho(770)$
$1^-2^{-+}0^+$	π^-	$\begin{bmatrix}0\\2\end{bmatrix} f_2(1310) \to \pi^\mp[1]a_1(1269) \to \pi^\pm[0]\rho(770)$
$1^-2^{-+}0^+$	π^-	$\begin{bmatrix}0\\2\end{bmatrix} f_2(1565) \to \pi^\mp[1]a_1(1269) \to \pi^\pm[0]\rho(770)$
$1^-2^{-+}0^+$	π^-	$\begin{bmatrix}0\\2\end{bmatrix} f_2(1565) \to \sigma[2]\sigma$
$1^-2^{++}0^-$	π^-	$\begin{bmatrix}1\\1\end{bmatrix} b_1(1800) \to \pi^\mp \begin{bmatrix}1\\1\end{bmatrix} a_1(1269) \to \pi^\pm[0]\rho(770)$
$1^-2^{-+}0^+$	π^-	$\begin{bmatrix}1\\1\end{bmatrix} \eta_1(1600) \to \pi^\mp \begin{bmatrix}0\\1\end{bmatrix} a_1(1269) \to \pi^\pm \begin{bmatrix}0\\1\end{bmatrix} \rho(770)$
$1^-2^{-+}0^+$	π^-	$\begin{bmatrix}1\\1\end{bmatrix} \eta_1(1600) \to \pi^\mp \begin{bmatrix}1\\0\end{bmatrix} \pi(1300) \to \pi^\pm \begin{bmatrix}0\\0\end{bmatrix} \sigma$
$1^-2^{-+}0^+$	π^-	$\begin{bmatrix}1\\1\end{bmatrix} \eta_1(1600) \to \pi^\mp \begin{bmatrix}1\\0\end{bmatrix} \pi(1300) \to \pi^\pm \begin{bmatrix}1\\1\end{bmatrix} \rho(770)$
$1^-2^{-+}0^+$	π^-	$\begin{bmatrix}1\\1\end{bmatrix} \rho(1600) \to \pi^\mp \begin{bmatrix}0\\1\end{bmatrix} a_1(1269) \to \pi^\pm \begin{bmatrix}0\\1\end{bmatrix} \rho(770)$
$1^-2^{-+}0^+$	π^-	$\begin{bmatrix}1\\1\end{bmatrix} \rho(1600) \to \pi^\mp \begin{bmatrix}1\\0\end{bmatrix} \pi(1300) \to \pi^\pm \begin{bmatrix}1\\1\end{bmatrix} \rho(770)$
$1^-2^{-+}0^+$	π^-	$\begin{bmatrix}1\\1\end{bmatrix} \rho(1600) \to \rho(770) \begin{bmatrix}0\\1\end{bmatrix} \sigma$
$1^-2^{-+}0^+$	π^-	$\begin{bmatrix}1\\2\end{bmatrix} \eta_2(1645) \to \pi^- \begin{bmatrix}0\\2\end{bmatrix} a_2(1320) \to \pi^+ \begin{bmatrix}2\\1\end{bmatrix} \rho(770)$
$1^-2^{-+}0^+$	π^-	$\begin{bmatrix}1\\2\end{bmatrix} \eta_2(1645) \to \pi^+ \begin{bmatrix}0\\2\end{bmatrix} a_2(1320) \to \pi^- \begin{bmatrix}2\\1\end{bmatrix} \rho(770)$
$1^-2^{-+}0^+$	π^-	$\begin{bmatrix}1\\3\end{bmatrix} \rho_3(1690) \to \rho(770) \begin{bmatrix}2\\1\end{bmatrix} \sigma$
$1^-2^{-+}0^+$	π^-	$\begin{bmatrix}2\\0\end{bmatrix} b_0(1800) \to \pi^\mp \begin{bmatrix}0\\0\end{bmatrix} \pi(1300) \to \pi^\pm \begin{bmatrix}0\\0\end{bmatrix} \sigma$
$1^-2^{-+}0^+$	π^-	$\begin{bmatrix}2\\0\end{bmatrix} b_0(1800) \to \pi^\mp \begin{bmatrix}1\\1\end{bmatrix} a_1(1269) \to \pi^\pm \begin{bmatrix}0\\1\end{bmatrix} \rho(770)$

$1^{-}2^{-+}0^{+} \quad \pi^{-}\begin{bmatrix}2\\0\end{bmatrix} f_0(1500)\to\rho(770)\begin{bmatrix}0\\0\end{bmatrix}\rho(770)$

$1^{-}2^{-+}0^{+} \quad \pi^{-}\begin{bmatrix}2\\0\end{bmatrix} f_0(1500)\to\sigma[0]\sigma$

$1^{-}2^{-+}0^{+} \quad \pi^{-}\begin{bmatrix}2\\0\end{bmatrix} \sigma\to\sigma[0]\sigma$

$1^{-}2^{-+}0^{+} \quad \pi^{-}\begin{bmatrix}2\\1\end{bmatrix} f_1(1285)\to\pi^{\mp}\begin{bmatrix}1\\1\end{bmatrix} a_1(1269)\to\pi^{\pm}\begin{bmatrix}0\\1\end{bmatrix}\rho(770)$

$1^{-}2^{-+}0^{+} \quad \pi^{-}\begin{bmatrix}2\\1\end{bmatrix} f_1(1285)\to\pi^{\mp}\begin{bmatrix}1\\1\end{bmatrix} a_1(1269)\to\pi^{\pm}[1]\sigma$

$1^{-}2^{++}0^{-} \quad \pi^{-}\begin{bmatrix}2\\1\end{bmatrix} \rho(1600)\to\pi^{\mp}\begin{bmatrix}0\\1\end{bmatrix} a_1(1269)\to\pi^{\pm}\begin{bmatrix}0\\1\end{bmatrix}\rho(770)$

$1^{-}2^{++}0^{-} \quad \pi^{-}\begin{bmatrix}2\\1\end{bmatrix} \rho(1600)\to\rho(770)\begin{bmatrix}0\\1\end{bmatrix}\sigma$

$1^{-}2^{-+}0^{+} \quad \pi^{-}\begin{bmatrix}2\\2\end{bmatrix} f_2(1270)\to\pi^{\mp}\begin{bmatrix}1\\1\end{bmatrix} a_1(1269)\to\pi^{\pm}\begin{bmatrix}0\\1\end{bmatrix}\rho(770)$

$1^{-}2^{-+}0^{+} \quad \pi^{-}\begin{bmatrix}2\\2\end{bmatrix} f_2(1270)\to\pi^{\mp}[1]a_1(1269)\to\pi^{\pm}[0]\rho(770)$

$1^{-}2^{-+}0^{+} \quad \pi^{-}\begin{bmatrix}2\\2\end{bmatrix} f_2(1270)\to\sigma[2]\sigma$

$1^{-}2^{-+}0^{+} \quad \pi^{-}\begin{bmatrix}2\\2\end{bmatrix} f_2(1565)\to\pi^{\mp}[1]a_1(1269)\to\pi^{\pm}[0]\rho(770)$

$1^{-}2^{-+}0^{+} \quad \pi^{-}\begin{bmatrix}2\\2\end{bmatrix} f_2(1565)\to\sigma[2]\sigma$

$1^{-}2^{-+}0^{+} \quad \pi^{-}\begin{bmatrix}3\\1\end{bmatrix} \rho(1600)\to\pi^{\mp}\begin{bmatrix}0\\1\end{bmatrix} a_1(1269)\to\pi^{\pm}\begin{bmatrix}0\\1\end{bmatrix}\rho(770)$

$1^{-}2^{-+}0^{+} \quad \pi^{-}\begin{bmatrix}3\\1\end{bmatrix} \rho(1600)\to\pi^{\mp}\begin{bmatrix}1\\0\end{bmatrix} \pi(1300)\to\pi^{\pm}\begin{bmatrix}1\\1\end{bmatrix}\rho(770)$

$1^{-}2^{-+}0^{+} \quad \pi^{-}\begin{bmatrix}3\\1\end{bmatrix} \rho(1600)\to\rho(770)\begin{bmatrix}0\\1\end{bmatrix}\sigma$

$1^{-}2^{-+}0^{+} \quad \rho_3(1690)\to\pi^{\mp}\begin{bmatrix}2\\1\end{bmatrix} a_1(1269)\to\pi^{\pm}[0]\rho(770)\begin{bmatrix}1\\3\end{bmatrix}\pi^{-}$

$1^{-}2^{++}0^{-} \quad \rho_3(1690)\to\pi^{\mp}\begin{bmatrix}2\\1\end{bmatrix} a_1(1269)\to\pi^{\pm}[0]\rho(770)\begin{bmatrix}2\\3\end{bmatrix}\pi^{-}$

$1^{-}2^{-+}0^{+} \quad \rho_3(1690)\to\rho(770)\begin{bmatrix}0\\3\end{bmatrix} f_2(1270)\begin{bmatrix}1\\3\end{bmatrix}\pi^{-}$

$1^-2^{++}0^- \quad \rho_3(1690) \to \rho(770) \begin{bmatrix} 0 \\ 3 \end{bmatrix} f_2(1270) \begin{bmatrix} 2 \\ 3 \end{bmatrix} \pi^-$

$1^-2^{-+}0^+ \quad \rho_3(1690) \to \rho(770) \begin{bmatrix} 1 \\ 2 \end{bmatrix} \rho(770) \begin{bmatrix} 1 \\ 3 \end{bmatrix} \pi^-$

$1^-2^{++}0^- \quad \rho_3(1690) \to \rho(770) \begin{bmatrix} 1 \\ 2 \end{bmatrix} \rho(770) \begin{bmatrix} 2 \\ 3 \end{bmatrix} \pi^-$

$1^-2^{-+}0^+ \quad \rho(770) \begin{bmatrix} 0 \\ 2 \end{bmatrix} a_1(1269) \to \pi^-[0]\rho(770)$

$1^-2^{-+}0^+ \quad \rho(770) \begin{bmatrix} 0 \\ 2 \end{bmatrix} a_1(1269) \to \pi^-[1]\sigma$

$1^-2^{-+}0^+ \quad \rho(770) \begin{bmatrix} 0 \\ 2 \end{bmatrix} a_2(1320) \to \pi^-[2]\rho(770)$

$1^-2^{++}0^- \quad \rho(770) \begin{bmatrix} 1 \\ 1 \end{bmatrix} a_1(1269) \to \pi^-[0]\rho(770)$

$1^-2^{++}0^- \quad \rho(770) \begin{bmatrix} 1 \\ 1 \end{bmatrix} a_1(1269) \to \pi^-[1]\sigma$

$1^-2^{++}0^- \quad \rho(770) \begin{bmatrix} 1 \\ 1 \end{bmatrix} a_2(1320) \to \pi^-[2]\rho(770)$

$1^-2^{-+}0^+ \quad \rho(770) \begin{bmatrix} 1 \\ 1 \end{bmatrix} \pi_1(1600) \to \pi^-[1]\rho(770)$

$1^-2^{-+}0^+ \quad \rho(770) \begin{bmatrix} 1 \\ 1 \end{bmatrix} \pi(1300) \to \pi^- \begin{bmatrix} 0 \\ 0 \end{bmatrix} \sigma$

$1^-2^{-+}0^+ \quad \rho(770) \begin{bmatrix} 1 \\ 1 \end{bmatrix} \pi(1300) \to \pi^-[1]\rho(770)$

$1^-2^{++}0^- \quad \rho(770) \begin{bmatrix} 1 \\ 2 \end{bmatrix} a_1(1269) \to \pi^-[1]\sigma$

$1^-2^{++}0^- \quad \rho(770) \begin{bmatrix} 1 \\ 2 \end{bmatrix} a_2(1320) \to \pi^-[2]\rho(770)$

$1^-2^{-+}0^+ \quad \rho(770) \begin{bmatrix} 1 \\ 2 \end{bmatrix} \pi_1(1600) \to \pi^-[1]\rho(770)$

$1^-2^{-+}0^+ \quad \rho(770) \begin{bmatrix} 1 \\ 2 \end{bmatrix} \pi_2(1670) \to \pi^-[0]f_2(1270)$

$1^-2^{-+}0^+ \quad \rho(770) \begin{bmatrix} 2 \\ 0 \end{bmatrix} a_1(1269) \to \pi^-[0]\rho(770)$

$1^-2^{-+}0^+ \quad \rho(770) \begin{bmatrix} 2 \\ 0 \end{bmatrix} a_1(1269) \to \pi^-[1]\sigma$

$1^-2^{-+}0^+$	$\rho(770)\begin{bmatrix}2\\1\end{bmatrix}a_1(1269)\rightarrow\pi^-\begin{bmatrix}0\\1\end{bmatrix}\rho(770)$
$1^-2^{-+}0^+$	$\rho(770)\begin{bmatrix}2\\1\end{bmatrix}a_1(1269)\rightarrow\pi^-[1]\sigma$
$1^-2^{-+}0^+$	$\rho(770)\begin{bmatrix}2\\1\end{bmatrix}a_2(1320)\rightarrow\pi^-[2]\rho(770)$
$1^-2^{-+}0^+$	$\rho(770)\begin{bmatrix}2\\2\end{bmatrix}a_1(1269)\rightarrow\pi^-\begin{bmatrix}0\\1\end{bmatrix}\rho(770)$
$1^-2^{-+}0^+$	$\rho(770)\begin{bmatrix}2\\2\end{bmatrix}a_1(1269)\rightarrow\pi^-[1]\sigma$
$1^-2^{-+}0^+$	$\rho(770)\begin{bmatrix}2\\2\end{bmatrix}a_2(1320)\rightarrow\pi^-[2]\rho(770)$
$1^-2^{-+}0^+$	$\rho(770)\begin{bmatrix}2\\3\end{bmatrix}a_2(1320)\rightarrow\pi^-[2]\rho(770)$
$1^-2^{++}0^-$	$\sigma\begin{bmatrix}0\\2\end{bmatrix}a_2(1320)\rightarrow\pi^-[2]\rho(770)$
$1^-2^{-+}0^+$	$\sigma\begin{bmatrix}0\\2\end{bmatrix}\pi_2(1670)\rightarrow\pi^-\begin{bmatrix}0\\2\end{bmatrix}f_2(1270)$
$1^-2^{-+}0^+$	$\sigma\begin{bmatrix}1\\1\end{bmatrix}a_1(1269)\rightarrow\pi^-[0]\rho(770)$
$1^-2^{-+}0^+$	$\sigma\begin{bmatrix}1\\2\end{bmatrix}a_2(1320)\rightarrow\pi^-[2]\rho(770)$
$1^-2^{-+}0^+$	$\sigma\begin{bmatrix}2\\0\end{bmatrix}\pi(1300)\rightarrow\pi^-\begin{bmatrix}0\\0\end{bmatrix}\sigma$
$1^-2^{-+}0^+$	$\sigma\begin{bmatrix}2\\0\end{bmatrix}\pi(1300)\rightarrow\pi^-\begin{bmatrix}1\\1\end{bmatrix}\rho(770)$
$1^-2^{++}0^-$	$\sigma\begin{bmatrix}2\\1\end{bmatrix}a_1(1269)\rightarrow\pi^-[0]\rho(770)$
$1^-2^{-+}0^+$	$\sigma\begin{bmatrix}2\\1\end{bmatrix}\pi_1(1600)\rightarrow\pi^-[1]\rho(770)$
$1^-2^{-+}0^+$	$\sigma\begin{bmatrix}2\\2\end{bmatrix}\pi_2(1670)\rightarrow\pi^-\begin{bmatrix}0\\2\end{bmatrix}f_2(1270)$
$1^-3^{++}0^+$	$f_2(1270)\begin{bmatrix}0\\3\end{bmatrix}a_1(1269)\rightarrow\pi^-\begin{bmatrix}0\\1\end{bmatrix}\rho(770)$
$1^-3^{++}0^+$	$f_2(1270)\begin{bmatrix}0\\3\end{bmatrix}a_2(1320)\rightarrow\pi^-\begin{bmatrix}2\\1\end{bmatrix}\rho(770)$

$$1^-3^{++}0^+ \quad f_2(1270)\begin{bmatrix}2\\1\end{bmatrix}a_1(1269)\to\pi^-\begin{bmatrix}0\\1\end{bmatrix}\rho(770)$$

$$1^-3^{++}0^+ \quad f_2(1270)\begin{bmatrix}2\\1\end{bmatrix}a_2(1320)\to\pi^-\begin{bmatrix}2\\1\end{bmatrix}\rho(770)$$

$$1^-3^{++}0^+ \quad f_2(1270)\begin{bmatrix}2\\2\end{bmatrix}a_1(1269)\to\pi^-\begin{bmatrix}0\\1\end{bmatrix}\rho(770)$$

$$1^-3^{++}0^+ \quad f_2(1270)\begin{bmatrix}2\\2\end{bmatrix}a_2(1320)\to\pi^-\begin{bmatrix}2\\1\end{bmatrix}\rho(770)$$

$$1^-3^{++}0^+ \quad f_2(1270)\begin{bmatrix}2\\3\end{bmatrix}a_1(1269)\to\pi^-\begin{bmatrix}0\\1\end{bmatrix}\rho(770)$$

$$1^-3^{++}0^+ \quad f_2(1270)\begin{bmatrix}2\\3\end{bmatrix}a_2(1320)\to\pi^-\begin{bmatrix}2\\1\end{bmatrix}\rho(770)$$

$$1^-3^{++}0^+ \quad f_2(1270)\begin{bmatrix}2\\4\end{bmatrix}a_2(1320)\to\pi^-\begin{bmatrix}2\\1\end{bmatrix}\rho(770)$$

$$1^-3^{++}0^+ \quad f_2(1270)\begin{bmatrix}4\\1\end{bmatrix}a_1(1269)\to\pi^-\begin{bmatrix}0\\1\end{bmatrix}\rho(770)$$

$$1^-3^{++}0^+ \quad f_2(1270)\begin{bmatrix}4\\1\end{bmatrix}a_2(1320)\to\pi^-\begin{bmatrix}2\\1\end{bmatrix}\rho(770)$$

$$1^-3^{++}0^+ \quad f_2(1270)\begin{bmatrix}4\\2\end{bmatrix}a_1(1269)\to\pi^-\begin{bmatrix}0\\1\end{bmatrix}\rho(770)$$

$$1^-3^{++}0^+ \quad f_2(1270)\begin{bmatrix}4\\2\end{bmatrix}a_2(1320)\to\pi^-\begin{bmatrix}2\\1\end{bmatrix}\rho(770)$$

$$1^-3^{++}0^+ \quad f_2(1270)\begin{bmatrix}4\\3\end{bmatrix}a_1(1269)\to\pi^-\begin{bmatrix}0\\1\end{bmatrix}\rho(770)$$

$$1^-3^{++}0^+ \quad f_2(1270)\begin{bmatrix}4\\3\end{bmatrix}a_2(1320)\to\pi^-\begin{bmatrix}2\\1\end{bmatrix}\rho(770)$$

$$1^-3^{++}0^+ \quad f_2(1270)\begin{bmatrix}4\\4\end{bmatrix}a_2(1320)\to\pi^-\begin{bmatrix}2\\1\end{bmatrix}\rho(770)$$

$$1^-3^{++}0^+ \quad \pi^-\begin{bmatrix}0\\3\end{bmatrix}\rho_3(1690)\to\rho(770)\begin{bmatrix}2\\1\end{bmatrix}\sigma$$

$$1^-3^{++}0^+ \quad \pi^-\begin{bmatrix}1\\2\end{bmatrix}f_2(1565)\to\pi^\mp[1]a_1(1269)\to\pi^\pm[0]\rho(770)$$

$$1^-3^{++}0^+ \quad \pi^-\begin{bmatrix}2\\1\end{bmatrix}\rho(1600)\to\pi^\mp\begin{bmatrix}0\\1\end{bmatrix}a_1(1269)\to\pi^\pm\begin{bmatrix}0\\1\end{bmatrix}\rho(770)$$

$$1^-3^{++}0^+ \quad \pi^-\begin{bmatrix}2\\1\end{bmatrix}\rho(1600)\to\pi^\mp\begin{bmatrix}1\\0\end{bmatrix}\pi(1300)\to\pi^\pm\begin{bmatrix}1\\1\end{bmatrix}\rho(770)$$

$$1^-3^{++}0^+ \quad \pi^- \begin{bmatrix}2\\1\end{bmatrix} \rho(1600) \to \rho(770) \begin{bmatrix}0\\1\end{bmatrix} \sigma$$

$$1^-3^{++}0^+ \quad \pi^- \begin{bmatrix}2\\2\end{bmatrix} \eta_2(1645) \to \pi^- \begin{bmatrix}0\\2\end{bmatrix} a_2(1320) \to \pi^+ \begin{bmatrix}2\\1\end{bmatrix} \rho(770)$$

$$1^-3^{++}0^+ \quad \pi^- \begin{bmatrix}2\\2\end{bmatrix} \eta_2(1645) \to \pi^+ \begin{bmatrix}0\\2\end{bmatrix} a_2(1320) \to \pi^- \begin{bmatrix}2\\1\end{bmatrix} \rho(770)$$

$$1^-3^{++}0^+ \quad \pi^- \begin{bmatrix}3\\0\end{bmatrix} \sigma \to \sigma[0]\sigma$$

$$1^-3^{++}0^+ \quad \rho_3(1690) \to \pi^\mp \begin{bmatrix}2\\1\end{bmatrix} a_1(1269) \to \pi^\pm[0]\rho(770) \begin{bmatrix}0\\3\end{bmatrix} \pi^-$$

$$1^-3^{++}0^+ \quad \rho_3(1690) \to \rho(770) \begin{bmatrix}0\\3\end{bmatrix} f_2(1270) \begin{bmatrix}0\\3\end{bmatrix} \pi^-$$

$$1^-3^{++}0^+ \quad \rho_3(1690) \to \rho(770) \begin{bmatrix}1\\2\end{bmatrix} \rho(770) \begin{bmatrix}0\\3\end{bmatrix} \pi^-$$

$$1^-3^{++}0^+ \quad \rho_3(1690) \to \rho(770) \begin{bmatrix}1\\2\end{bmatrix} \rho(770) \begin{bmatrix}2\\3\end{bmatrix} \pi^-$$

$$1^-3^{-+}0^- \quad \rho(770) \begin{bmatrix}0\\3\end{bmatrix} a_2(1320) \to \pi^-[2]\rho(770)$$

$$1^-3^{++}0^+ \quad \rho(770) \begin{bmatrix}1\\2\end{bmatrix} a_1(1269) \to \pi^-[0]\rho(770)$$

$$1^-3^{++}0^+ \quad \rho(770) \begin{bmatrix}1\\3\end{bmatrix} a_2(1320) \to \pi^-[2]\rho(770)$$

$$1^-3^{-+}0^- \quad \rho(770) \begin{bmatrix}2\\1\end{bmatrix} a_1(1269) \to \pi^-[0]\rho(770)$$

$$1^-3^{-+}0^- \quad \rho(770) \begin{bmatrix}2\\1\end{bmatrix} a_1(1269) \to \pi^-[1]\sigma$$

$$1^-3^{++}0^+ \quad \rho(770) \begin{bmatrix}2\\1\end{bmatrix} \pi(1300) \to \pi^- \begin{bmatrix}0\\0\end{bmatrix} \sigma$$

$$1^-3^{++}0^+ \quad \rho(770) \begin{bmatrix}2\\1\end{bmatrix} \pi(1300) \to \pi^-[1]\rho(770)$$

$$1^-3^{-+}0^- \quad \rho(770) \begin{bmatrix}2\\2\end{bmatrix} a_1(1269) \to \pi^-[1]\sigma$$

$$1^-3^{++}0^+ \quad \rho(770) \begin{bmatrix}2\\2\end{bmatrix} \pi_2(1670) \to \pi^-[0]f_2(1270)$$

$$1^-3^{-+}0^- \quad \sigma \begin{bmatrix}1\\2\end{bmatrix} a_2(1320) \to \pi^-[2]\rho(770)$$

$$1^-3^{++}0^+ \quad \sigma \begin{bmatrix} 2 \\ 1 \end{bmatrix} a_1(1269) \rightarrow \pi^-[0]\rho(770)$$

$$1^-3^{++}0^+ \quad \sigma \begin{bmatrix} 2 \\ 2 \end{bmatrix} a_2(1320) \rightarrow \pi^-[2]\rho(770)$$

$$1^-3^{++}0^+ \quad \sigma \begin{bmatrix} 3 \\ 0 \end{bmatrix} \pi(1300) \rightarrow \pi^- \begin{bmatrix} 0 \\ 0 \end{bmatrix} \sigma$$

$$1^-3^{++}0^+ \quad \sigma \begin{bmatrix} 3 \\ 0 \end{bmatrix} \pi(1300) \rightarrow \pi^- \begin{bmatrix} 1 \\ 1 \end{bmatrix} \rho(770)$$

$$1^-3^{++}1^+ \quad \pi^- \begin{bmatrix} 1 \\ 2 \end{bmatrix} f_2(1270) \rightarrow \sigma[2]\sigma$$

$$1^-3^{-+}1^- \quad \rho(770) \begin{bmatrix} 0 \\ 3 \end{bmatrix} a_2(1320) \rightarrow \pi^-[2]\rho(770)$$

$$1^-3^{-+}1^+ \quad \rho(770) \begin{bmatrix} 0 \\ 3 \end{bmatrix} a_2(1320) \rightarrow \pi^-[2]\rho(770)$$

$$1^-3^{-+}1^+ \quad \rho(770) \begin{bmatrix} 1 \\ 2 \end{bmatrix} \pi_2(1670) \rightarrow \pi^-[0]f_2(1270)$$

$$1^-3^{-+}1^- \quad \sigma \begin{bmatrix} 1 \\ 2 \end{bmatrix} a_2(1320) \rightarrow \pi^-[2]\rho(770)$$

$$1^-3^{-+}1^+ \quad \sigma \begin{bmatrix} 1 \\ 2 \end{bmatrix} a_2(1320) \rightarrow \pi^-[2]\rho(770)$$

$$1^-3^{++}1^- \quad \sigma \begin{bmatrix} 2 \\ 2 \end{bmatrix} a_2(1320) \rightarrow \pi^-[2]\rho(770)$$

$$1^-3^{++}1^+ \quad \sigma \begin{bmatrix} 2 \\ 2 \end{bmatrix} a_2(1320) \rightarrow \pi^-[2]\rho(770)$$

$$1^-4^{-+}0^+ \quad f_2(1270) \begin{bmatrix} 0 \\ 4 \end{bmatrix} \pi_2(1670) \rightarrow \pi^- \begin{bmatrix} 0 \\ 2 \end{bmatrix} f_2(1270)$$

$$1^-4^{-+}0^+ \quad f_2(1270) \begin{bmatrix} 1 \\ 3 \end{bmatrix} a_1(1269) \rightarrow \pi^- \begin{bmatrix} 0 \\ 1 \end{bmatrix} \rho(770)$$

$$1^-4^{-+}0^+ \quad f_2(1270) \begin{bmatrix} 1 \\ 3 \end{bmatrix} a_1(1269) \rightarrow \pi^-[0]\rho(770)$$

$$1^-4^{-+}0^+ \quad f_2(1270) \begin{bmatrix} 1 \\ 3 \end{bmatrix} a_2(1320) \rightarrow \pi^- \begin{bmatrix} 2 \\ 1 \end{bmatrix} \rho(770)$$

$$1^-4^{-+}0^+ \quad f_2(1270) \begin{bmatrix} 1 \\ 4 \end{bmatrix} a_2(1320) \rightarrow \pi^- \begin{bmatrix} 2 \\ 1 \end{bmatrix} \rho(770)$$

$$1^-4^{-+}0^+ \quad f_2(1270) \begin{bmatrix} 1 \\ 4 \end{bmatrix} a_2(1320) \rightarrow \pi^-[2]\rho(770)$$

$1^{-}4^{-+}0^{+}$	$f_2(1270)\begin{bmatrix}3\\1\end{bmatrix}a_1(1269)\rightarrow\pi^{-}\begin{bmatrix}0\\1\end{bmatrix}\rho(770)$
$1^{-}4^{-+}0^{+}$	$f_2(1270)\begin{bmatrix}3\\1\end{bmatrix}a_2(1320)\rightarrow\pi^{-}\begin{bmatrix}2\\1\end{bmatrix}\rho(770)$
$1^{-}4^{-+}0^{+}$	$f_2(1270)\begin{bmatrix}3\\2\end{bmatrix}a_1(1269)\rightarrow\pi^{-}\begin{bmatrix}0\\1\end{bmatrix}\rho(770)$
$1^{-}4^{-+}0^{+}$	$f_2(1270)\begin{bmatrix}3\\2\end{bmatrix}a_2(1320)\rightarrow\pi^{-}\begin{bmatrix}2\\1\end{bmatrix}\rho(770)$
$1^{-}4^{-+}0^{+}$	$f_2(1270)\begin{bmatrix}3\\3\end{bmatrix}a_1(1269)\rightarrow\pi^{-}\begin{bmatrix}0\\1\end{bmatrix}\rho(770)$
$1^{-}4^{-+}0^{+}$	$f_2(1270)\begin{bmatrix}3\\3\end{bmatrix}a_2(1320)\rightarrow\pi^{-}\begin{bmatrix}2\\1\end{bmatrix}\rho(770)$
$1^{-}4^{-+}0^{+}$	$f_2(1270)\begin{bmatrix}3\\4\end{bmatrix}a_2(1320)\rightarrow\pi^{-}\begin{bmatrix}2\\1\end{bmatrix}\rho(770)$
$1^{-}4^{-+}0^{+}$	$\pi^{-}\begin{bmatrix}1\\3\end{bmatrix}\rho_3(1690)\rightarrow\rho(770)\begin{bmatrix}2\\1\end{bmatrix}\sigma$
$1^{-}4^{-+}0^{+}$	$\pi^{-}\begin{bmatrix}3\\1\end{bmatrix}\rho(1600)\rightarrow\pi^{\mp}\begin{bmatrix}0\\1\end{bmatrix}a_1(1269)\rightarrow\pi^{\pm}\begin{bmatrix}0\\1\end{bmatrix}\rho(770)$
$1^{-}4^{-+}0^{+}$	$\pi^{-}\begin{bmatrix}3\\1\end{bmatrix}\rho(1600)\rightarrow\rho(770)\begin{bmatrix}0\\1\end{bmatrix}\sigma$
$1^{-}4^{-+}0^{+}$	$\pi^{-}\begin{bmatrix}4\\0\end{bmatrix}\sigma\rightarrow\sigma[0]\sigma$
$1^{-}4^{-+}0^{+}$	$\pi^{-}\begin{bmatrix}4\\1\end{bmatrix}f_1(1285)\rightarrow\pi^{\mp}\begin{bmatrix}1\\1\end{bmatrix}a_1(1269)\rightarrow\pi^{\pm}\begin{bmatrix}0\\1\end{bmatrix}\rho(770)$
$1^{-}4^{-+}0^{+}$	$\rho_3(1690)\rightarrow\pi^{\mp}\begin{bmatrix}2\\1\end{bmatrix}a_1(1269)\rightarrow\pi^{\pm}[0]\rho(770)\begin{bmatrix}1\\3\end{bmatrix}\pi^{-}$
$1^{-}4^{++}0^{-}$	$\rho_3(1690)\rightarrow\pi^{\mp}\begin{bmatrix}2\\1\end{bmatrix}a_1(1269)\rightarrow\pi^{\pm}[0]\rho(770)\begin{bmatrix}2\\3\end{bmatrix}\pi^{-}$
$1^{-}4^{-+}0^{+}$	$\rho_3(1690)\rightarrow\rho(770)\begin{bmatrix}0\\3\end{bmatrix}f_2(1270)\begin{bmatrix}1\\3\end{bmatrix}\pi^{-}$
$1^{-}4^{++}0^{-}$	$\rho_3(1690)\rightarrow\rho(770)\begin{bmatrix}0\\3\end{bmatrix}f_2(1270)\begin{bmatrix}2\\3\end{bmatrix}\pi^{-}$
$1^{-}4^{-+}0^{+}$	$\rho_3(1690)\rightarrow\rho(770)\begin{bmatrix}1\\2\end{bmatrix}\rho(770)\begin{bmatrix}1\\3\end{bmatrix}\pi^{-}$
$1^{-}4^{++}0^{-}$	$\rho_3(1690)\rightarrow\rho(770)\begin{bmatrix}1\\2\end{bmatrix}\rho(770)\begin{bmatrix}2\\3\end{bmatrix}\pi^{-}$

$1^-4^{++}0^-$	$\rho(770)\left[\begin{array}{c}1\\3\end{array}\right]a_2(1320)\rightarrow\pi^-[2]\rho(770)$
$1^-4^{-+}0^+$	$\rho(770)\left[\begin{array}{c}2\\2\end{array}\right]a_1(1269)\rightarrow\pi^-[0]\rho(770)$
$1^-4^{-+}0^+$	$\rho(770)\left[\begin{array}{c}2\\2\end{array}\right]a_2(1320)\rightarrow\pi^-\left[\begin{array}{c}2\\1\end{array}\right]\rho(770)$
$1^-4^{-+}0^+$	$\rho(770)\left[\begin{array}{c}2\\3\end{array}\right]a_2(1320)\rightarrow\pi^-[2]\rho(770)$
$1^-4^{++}0^-$	$\rho(770)\left[\begin{array}{c}3\\1\end{array}\right]a_1(1269)\rightarrow\pi^-[1]\sigma$
$1^-4^{++}0^-$	$\rho(770)\left[\begin{array}{c}3\\2\end{array}\right]a_1(1269)\rightarrow\pi^-[1]\sigma$
$1^-4^{-+}0^+$	$\rho(770)\left[\begin{array}{c}4\\0\end{array}\right]a_1(1269)\rightarrow\pi^-\left[\begin{array}{c}0\\1\end{array}\right]\rho(770)$
$1^-4^{-+}0^+$	$\rho(770)\left[\begin{array}{c}4\\1\end{array}\right]a_1(1269)\rightarrow\pi^-\left[\begin{array}{c}0\\1\end{array}\right]\rho(770)$
$1^-4^{-+}0^+$	$\rho(770)\left[\begin{array}{c}4\\1\end{array}\right]a_2(1320)\rightarrow\pi^-\left[\begin{array}{c}2\\1\end{array}\right]\rho(770)$
$1^-4^{-+}0^+$	$\rho(770)\left[\begin{array}{c}4\\2\end{array}\right]a_1(1269)\rightarrow\pi^-\left[\begin{array}{c}0\\1\end{array}\right]\rho(770)$
$1^-4^{-+}0^+$	$\rho(770)\left[\begin{array}{c}4\\2\end{array}\right]a_2(1320)\rightarrow\pi^-\left[\begin{array}{c}2\\1\end{array}\right]\rho(770)$
$1^-4^{-+}0^+$	$\rho(770)\left[\begin{array}{c}4\\3\end{array}\right]a_2(1320)\rightarrow\pi^-\left[\begin{array}{c}2\\1\end{array}\right]\rho(770)$
$1^-4^{-+}0^+$	$\sigma\left[\begin{array}{c}2\\2\end{array}\right]\pi_2(1670)\rightarrow\pi^-\left[\begin{array}{c}0\\2\end{array}\right]f_2(1270)$
$1^-4^{-+}0^+$	$\sigma\left[\begin{array}{c}4\\0\end{array}\right]\pi(1300)\rightarrow\pi^-\left[\begin{array}{c}1\\1\end{array}\right]\rho(770)$
$1^-4^{++}1^+$	$\rho(770)\left[\begin{array}{c}3\\2\end{array}\right]a_1(1269)\rightarrow\pi^-[1]\sigma$

Appendix C

Error Propagation of Amplitude Analysis Observables

In this appendix some rules for the propagation of uncertainties on the observables of the partial-wave decomposition discussed in section 3.5 are given.
An examination of the Hesse-matrix of the log-likelihood-function 3.21 at the maximum likelihood solution yields an estimate for the covariance matrix of the fit parameters. The fit parameters are of course real-valued quantities which correspond to real and imaginary parts of the production amplitudes. In principle a polar representation of the amplitudes in terms of magnitude and phase would be more natural. However, there exists no minimization algorithm that the author is aware of that can efficiently deal with the cyclical variables that would be introduced by such a formulation of the problem.
For complex quantities such as the spin-density matrix elements the propagation of uncertainties is a task that might be unfamiliar to most experimentalists. In order to give the reader some insight into what is involved, this sections gives the basic formulas needed. The approach described below has been used by the author to implement the error propagation inside the `rootpwa` framework.
The following rules are developed according to the method proposed in the paper by B. D. Hall [218].

Matrix representation of complex numbers First note that a complex number (as a measured quantity) can be represented as a 2-tuple:

$$z = a + ib \quad \rightarrow \quad \begin{pmatrix} a \\ b \end{pmatrix}$$

$$a = \mathrm{Re}(z) \quad b = \mathrm{Im}(z)$$

The uncertainty on z is not a number but instead is conveniently expressed as a 2×2 covariance matrix

$$C = \begin{pmatrix} \sigma^2_{\mathrm{Re}} & \mathrm{cov}(\mathrm{Re},\mathrm{Im}) \\ \mathrm{cov}(\mathrm{Im},\mathrm{Re}) & \sigma^2_{\mathrm{Im}} \end{pmatrix}$$

The goal is to calculate this matrix for a given complex-valued function $z = f(T)$ which depends on n complex parameters T_α for which the (complex) co-variances are known. When the complex numbers are viewed as 2-dimensional vectors we can use standard techniques for the propagation of multivariate uncertainties with the Jacobian J.

$$J(f) = \left(J_1(f) J_2(f) ... J_n(f)\right) \tag{C.1}$$

Where the sub-matrices corresponding to the parameters T_α have been labeled J_α.

$$J_\alpha(f) = \begin{pmatrix} \frac{\partial \mathrm{Re}(f)}{\partial \mathrm{Re}(T_\alpha)} & \frac{\partial \mathrm{Re}(f)}{\partial \mathrm{Im}(T_\alpha)} \\ \frac{\partial \mathrm{Im}(f)}{\partial \mathrm{Re}(T_\alpha)} & \frac{\partial \mathrm{Im}(f)}{\partial \mathrm{Im}(T_\alpha)} \end{pmatrix} \tag{C.2}$$

Note that J is a $2 \times 2n$ matrix as expected for a complex valued function of n complex parameters.

For analytic functions one can use complex derivatives to write the sub-matrices more compactly. To show this the matrix representation of complex numbers will be used:

$$M(z) = \begin{pmatrix} a & -b \\ b & a \end{pmatrix}$$

These matrices behave like complex numbers under the usual arithmetic operations, where division is represented by multiplication with the inverse and the complex conjugate is represented by the transposition of the matrix.
For an analytic function $f(z)$ the Cauchy-Riemann relations hold and so we can write the complex derivative in matrix-notation as

$$M\left(\frac{\partial f}{\partial z}\right) = \begin{pmatrix} \frac{\partial \mathrm{Re}(f)}{\partial \mathrm{Re}(z)} & \frac{\partial \mathrm{Re}(f)}{\partial \mathrm{Im}(z)} \\ \frac{\partial \mathrm{Im}(f)}{\partial \mathrm{Re}(z)} & \frac{\partial \mathrm{Im}(f)}{\partial \mathrm{Im}(z)} \end{pmatrix} \tag{C.3}$$

Where $\frac{\partial f}{\partial z}$ denotes the complex valued partial derivative of f.
So if f is analytic in T_α the corresponding sub-Jacobian can be written as:

$$J_i(f) = M\left(\frac{\partial f}{\partial T_\alpha}\right)$$

One important special case occurs for the non-analytic $f(z) = z^*$. Working out the Jacobian explicitly for $z = a + ib$ using equation (C.2) gives

$$\begin{pmatrix} \frac{\partial a}{\partial a} & \frac{\partial a}{\partial b} \\ \frac{\partial b}{\partial a} & \frac{\partial(-b)}{\partial b} \end{pmatrix} = \begin{pmatrix} 1 & 0 \\ 0 & -1 \end{pmatrix} \tag{C.4}$$

This obviously does not fulfill the Cauchy-Riemann relations so the complex derivatives cannot be used to write down the Jacobian. The form of equation C.4 can, however, be used for the purpose of error propagation without further problems.
With these tools the error propagation law for complex numbers can be written down. Suppose we have a complex valued function f which depends on a vector of n complex numbers T_α.

$$z = f(T)$$

For the $2n$ components of the parameters the covariance matrix shall be given by:

$$C_{\alpha\beta} = \mathrm{cov}(T_\alpha, T_\beta) \in \mathbb{R}^{2n\times 2n}$$

The covariance of z can now be written as

$$\mathrm{cov}(z) = J(f)CJ^T(f) \tag{C.5}$$

with J given in equation C.1.

Error propagation for $|z|^2$:
Let

$$C = \begin{pmatrix} c_{11} & c_{12} \\ c_{21} & c_{22} \end{pmatrix}$$

be the covariance of $z = a + ib$.
$f(z) = zz^*$ is not analytic. Obviously it is not even a complex valued function so the Jacobian has to be determined explicitly. In order to explore how the different terms of cov(z) contribute to the error matrix the general result is given here.
Obviously

$$\mathrm{Re}(zz^*) = a^2 + b^2 \qquad \mathrm{Im}(zz^*) = 0$$

$$J = \begin{pmatrix} 2a & 2b \\ 0 & 0 \end{pmatrix}$$

So for the error propagation we get:

$$\mathrm{cov}(zz^*) = JCJ^T = \begin{pmatrix} 2a & 2b \\ 0 & 0 \end{pmatrix} \begin{pmatrix} c_{11} & c_{12} \\ c_{21} & c_{22} \end{pmatrix} \begin{pmatrix} 2a & 0 \\ 2b & 0 \end{pmatrix}$$

using $c_{12} = c_{21}$ we get

$$\mathrm{cov}(zz^*) = 4\begin{pmatrix} a^2c_{11} + 2abc_{12} + b^2c_{22} & 0 \\ 0 & 0 \end{pmatrix} \tag{C.6}$$

$$\sigma^2 = 4(a^2c_{11} + 2abc_{12} + b^2c_{22})$$

which is the expected error (squared) for the length of a $2d$ vector.

Error propagation for z^*A :
For $A = k + im$ explicit calculation gives

$$J = \begin{pmatrix} k & m \\ m & -k \end{pmatrix} = M(A)\begin{pmatrix} 1 & 0 \\ 0 & -1 \end{pmatrix} \tag{C.7}$$

Note from which side the factor for the complex conjugate has to be multiplied.

Error propagation for the Intensity Function :
The $2n \times 2n$ covariance matrix C for the production amplitudes T_α contains the information on the errors of the observables defined in section 3.5. In order to propagate these uncertainties one has to construct the Jacobian of I in the form of equation (C.1).
As an example the error propagation for the intensity 3.26 is shown here. Because of the sum over the different waves the sub-matrices separate into three terms

$$J_i = 2 \begin{pmatrix} \mathrm{Re}(T_\alpha) & \mathrm{Im}(T_\alpha \\ 0 & 0 \end{pmatrix} M(I_{\alpha\alpha}) + \sum_{\beta \neq \alpha} M(T^*_\beta I_{\alpha\beta}) + \sum_{\beta \neq \alpha} M(T_\beta I_{\beta\alpha}) \begin{pmatrix} 1 & 0 \\ 0 & -1 \end{pmatrix}$$

Here the results (C.6) and (C.7) have been used. Realizing that for the normalization integrals the following relation holds

$$I_{\beta\alpha} = I^*_{\alpha\beta}$$

and so

$$J_i = 2 \begin{pmatrix} \mathrm{Re}(T_\alpha) & \mathrm{Im}(T_\alpha) \\ 0 & 0 \end{pmatrix} M(I_{\alpha\alpha}) + \sum_{\alpha \neq \beta} M^T(T_\beta I_{\beta\alpha}) + M(I_\beta I_{\beta\alpha}) \begin{pmatrix} 1 & 0 \\ 0 & -1 \end{pmatrix}$$

the Jacobian can be further simplified using the rule

$$\begin{aligned} M(z)^T + M(z) \begin{pmatrix} 1 & 0 \\ 0 & -1 \end{pmatrix} &= \begin{pmatrix} a & b \\ -b & a \end{pmatrix} + \begin{pmatrix} a & -b \\ b & a \end{pmatrix} \begin{pmatrix} 1 & 0 \\ 0 & -1 \end{pmatrix} \\ &= \begin{pmatrix} a & b \\ -b & a \end{pmatrix} + \begin{pmatrix} a & b \\ b & -a \end{pmatrix} \\ &= 2 \begin{pmatrix} a & b \\ 0 & 0 \end{pmatrix} \end{aligned}$$

The result for the Jacobian with respect to T_α is:

$$J_\alpha = 2 \begin{pmatrix} \mathrm{Re}(T_\alpha) & \mathrm{Im}(T_\alpha) \\ 0 & 0 \end{pmatrix} M(I_{\alpha\alpha}) + \sum_{\beta \neq \alpha} 2 \begin{pmatrix} \mathrm{Re}(T_\beta I_{\beta\alpha}) & \mathrm{Im}(T_\beta I_{\beta\alpha}) \\ 0 & 0 \end{pmatrix} \tag{C.8}$$

Noting that $\mathrm{Im}(I_{\alpha\alpha}) = 0$ one obtains

$$J_\alpha = 2 \sum_\beta \begin{pmatrix} \mathrm{Re}(T_\beta I_{\beta\alpha}) & \mathrm{Im}(T_\beta I_{\beta\alpha}) \\ 0 & 0 \end{pmatrix} \tag{C.9}$$

From these blocks full Jacobian can be build

$$J(I) = (J_1 J_2 \ldots J_n) \tag{C.10}$$

Equation (C.5) then gives the final error on the intensity.
Similar arguments can be used to construct covariance matrices for all the observables one is interested in.

Bibliography

[1] K. Nakamura and others(Particle Data Group), "Review of particle physics," *J. Phys.* , vol. G37, p. 075021, 2010. *cited on pages 3, 10, 12, 14, 15, 16, 43, 57, 60, 62, 63, 64, 65, 82, 117, 130, 131, 134, 148, 149, 151, and 152.*

[2] H. Yukawa, "On the interaction of elementary particles," *Proc. Phys. Math. Soc. Jap.* , vol. 17, p. 48, 1935. *cited on page 4.*

[3] G. P. S. Occhialini and C. F. Powell, "Nuclear disintegration produced by small charged particles with small mass," *Nature*, vol. 159, p. 186, 1947. *cited on page 4.*

[4] M. Gell-Mann and Y. Ne'Eman, *The Eightfold Way.* W. A. Benjamin, Inc. , 1964. *cited on page 4.*

[5] M. Gell-Mann, "A schematic model of baryons and mesons," *Phys. Lett.* , vol. 8, p. 214, 1964. *cited on page 5.*

[6] K. Nakamura and others (Particle Data Group), "Quark model – in review of particle physics," *J. Phys.* , vol. G 37, p. 075021, 2020. *cited on page 5.*

[7] M. G. e. A. Alekseev, "Observation of a $J^{PC} = 1^{-+}$ exotic resonance in diffractive dissociation of 190 GeV/c π^- into $\pi^-\pi^-\pi^+$," *Phys. Rev. Lett.*, vol. 104, no. 24, p. 241803, Jun 2010. *cited on pages 6, 14, 52, 58, and 64.*

[8] C. A. Meyer and Y. V. Haarlem, "The status of exotic-quantum-number mesons," *Phys. Rev.* , vol. C82, p. 025208, 2010. *cited on pages 6 and 14.*

[9] S. Godfrey and N. Isgur, "Mesons in a relativized quark model with chromodynamics," *Phys. Rev.* , vol. D32, no. 1, pp. 189–231, Jul 1985. *cited on pages 6 and 63.*

[10] E. Klempt and A. Zaitsev, "Glueballs, hybrids, multiquarks. experimental facts versus QCD inspired concepts," *Phys. Rep.* , vol. 454, p. 1, 2007. *cited on pages 7 and 14.*

[11] M. Pennington, "Light 0^{++} mesons: Scalargators in florida," *AIP Conf. Proc.* , vol. 1257, p. 27, 2010. *cited on page 7.*

[12] M. Schumacher, "Structure of scalar mesons and the higgs sector of strong interaction," *J. Phys.* , vol. G38, p. 083001, 2011. *cited on page 7.*

[13] J. D. Bjorken and E. A. Paschos, "Inelastic electron-proton and γ-proton scattering and the structure of the nucleon," *Phys. Rev.* , vol. 185, p. 1975, 1969. *cited on page 7.*

[14] S. Weinberg, "Non-abelian gauge theories of the strong interactions," *Phys. Rev. Lett.* , vol. 31, p. 494, 1973. *cited on page 7.*

[15] H. Fritzsch, M. Gell-Mann, and H. Leutwyler, "Advantages of the Color Octet Gluon Picture," *Phys. Lett.* , vol. B47, pp. 365–368, 1973. *cited on page 7.*

[16] G. 't Hooft and M. J. G. Veltman, "Regularization and renormalization of gauge fields," *Nucl. Phys.* , vol. B44, p. 189, 1972. *cited on page 7.*

[17] D. J. Gross and F. Wilczek, "Ultraviolet behavior of non-abelian gauge theories," *Phys. Rev. Lett.* , vol. 30, p. 1343, 1973. *cited on page 7.*

[18] H. D. Politzer, "Reliable perturbative results for strong interactions?" *Phys. Rev. Lett.* , vol. 30, p. 1346, 1973. *cited on page 7.*

[19] J. Gasser and H. Leutwyler, "Quark masses," *Phys. Rep.* , vol. 3, p. 77, 1982. *cited on page 7.*

[20] P. Colangelo, "QCD sum rules, a modern perspective," *CERN-TH/2000-296*, 2000. *cited on page 8.*

[21] C. D. Roberts *et al.*, "Aspects of hadron physics," *Eu. Phys. J.* , vol. 140, p. 53, 2007. *cited on page 8.*

[22] J. Gasser and H. Leutwyler, "Chiral perturbation theory to one loop," *Ann. Phys.* , vol. 158, p. 142, 1984. *cited on page 8.*

[23] V. Bernard and U.-G. Meißner, "Chiral perturbation theory," *Annu. Rev. Nucl. Part. Sci.* , vol. 57, p. 33, 2007. *cited on page 8.*

[24] S. Scherer and M. R. Schindler, "A chiral perturbation theory primer," *arXiv:hep-ph/0505265v1*, 2005. *cited on page 8.*

[25] G. Colangelo *et al.*, "$\pi\pi$ scattering," *Nucl. Phys.* , vol. B603, p. 125, 2001. *cited on page 8.*

[26] N. Kaiser, "Chiral corrections to $\pi^-\gamma \rightarrow 3\pi$ processes at low energies," *Nucl. Phys.* , vol. A848, p. 198, 2010. *cited on page 8.*

[27] M. G. Alekseev *et al.*, "First measurement of chiral dynamics in $\pi^-\gamma \rightarrow \pi^-\pi^-\pi^+$," *CERN-PH-EP-2011-176.* *cited on page 8.*

[28] J. Carlson, J. B. Kogut, and V. R. Pandharipande, "Hadron spectroscopy in a flux-tube quark model," *Phys. Rev.* , vol. D28, p. 2807, 1983. *cited on page 9.*

[29] N. Isgur and J. Paton, "Flux-tube model for hadrons in QCD," *Phys. Rev.* , vol. D31, no. 11, p. 31, 1985. *cited on page 9.*

[30] A. D. Giacomo *et al.*, "Evidence for flux tubes from cooled QCD configurations," *Phys. Lett.* , vol. B236, p. 199, 1990. *cited on page 9.*

[31] G. S. Bali, "QCD forces and heavy quark bound states," *Phys. Rep.* , vol. 343, p. 1, 2001. *cited on page 9.*

[32] R. Kokoski and N. Isgur, “Meson decays by flux-tube breaking,” *Phys. Rev.* , vol. D35, no. 3, p. 35, 1987. *cited on page 9.*

[33] F. E. Close and P. R. Page, “The production and decay of hybrid mesons by flux-tube breaking,” *Nucl. Phys.* , vol. B443, p. 233, 1995. *cited on page 9.*

[34] P. R. Page, E. S. Swanson, and A. P. Szczepaniak, “Hybrid meson decay phenomenology,” *Phys. Rev.* , vol. D59, p. 034016, 1999. *cited on pages 9, 14, 15, 43, and 135.*

[35] P. D. B. Collins, “Regge theory and particle physics,” *Phys. Rep.* , vol. 1, no. 4, pp. 103–234, 1971. *cited on pages 9, 36, and 38.*

[36] T. Banks and A. Casher, “Chiral symmetry breaking in confining theories,” *Nucl. Phys.* , vol. B169, p. 103, 1980. *cited on page 9.*

[37] L. Y. Glozman, “Chiral multiplets of excited mesons,” *Phys. Lett.* , vol. B587, p. 69, 2004. *cited on page 9.*

[38] R. F. Wagenbrunn and L. Y. Glozman, “Effective restoration of chiral symmetry in excited mesons,” *Phys. Lett.* , vol. B643, p. 98, 2006. *cited on page 9.*

[39] L. Y. Glozman and A. V. Nefediev, “Chiral symmetrie and the string description of excited hadrons,” *Phys. Rev.* , vol. D76, p. 096004, 2007. *cited on page 9.*

[40] P. Bicudo, “Large degeneracy of excited hadronsand quark models,” *Phys. Rev.* , vol. D76, p. 096005, 2007. *cited on page 9.*

[41] M. Shifman and A. Vainshtein, “Highly excited mesons, linear regge trajectories, and the pattern of chiral symmetry realization,” *Phys. Rev.* , vol. D77, p. 034002, 2008. *cited on pages 9 and 11.*

[42] E. Aker *et al.*, “The crystal barrel spectrometer at lear,” *Nucl. Instrum. Methods*, vol. A321, p. 69, 1992. *cited on page 10.*

[43] A. V. Anisovich, V. V. Anisovich, and A. V. Sarantsev, “Systematics of $q\bar{q}$ states in the (n, M^2) and (J, M^2) planes,” *Phys. Rev.* , vol. D62, p. 051502, 2000. *cited on page 10.*

[44] D. Bugg, “Four sorts of mesons,” *Phys. Rep.* , vol. 397, p. 257, 2004. *cited on page 10.*

[45] J. Maldazena, “The large n limit of superconformal field theories and supergravity,” *Int. J. Theo. Phys.* , vol. 38, p. 1113, 1999. *cited on page 11.*

[46] J. Erdmenger *et al.*, “Mesons in gauge/gravity duals,” *Eur. Phys. J.* , vol. A35, p. 81, 2007. *cited on page 11.*

[47] R. J. Eden *et al.*, *The Analytic S-Matrix.* Cambridge University Press, 1966. *cited on page 12.*

[48] A. D. Martin and T. D. Spearman, *Elementary Particle Theory.* North-Holland Pub. Co. , 1970. *cited on pages 12, 17, 36, and 49.*

[49] J. A. Oller *et al.*, “Meson-meson interaction in a non-perturbative chiral approach,” *Phys. Rev.* , vol. D59, p. 074001, 1999. *cited on page 12.*

[50] J. R. Pelaez and F. J. Yndurain, "Pion-pion scattering amplitude," *Phys. Rev.* , vol. D71, p. 074016, 2005. *cited on page 12.*

[51] R. Kaminsky, J. R. Pelaez, and F. J. Yndurain, "Pion-pion scattering amplitude II. improved analysis above $K\bar{K}$ threshold," *Phys. Rev.* , vol. D74, p. 014001, 2006. *cited on page 12.*

[52] ——, "Pion-pion scattering amplitude III. improving the analysis with forward dispersion relations and Roy equations," *Phys. Rev.* , vol. D77, p. 054015, 2008. *cited on page 12.*

[53] U.-G. Meißner, "Low-energy hadron physics from effective chiral lagrangians with vector mesons," *Phys. Rep.* , vol. 5, p. 213, 1988. *cited on page 12.*

[54] L. S. Geng and E. Oset, "Vector meson – vector meson interaction in a hidden gauge unitary approach," *Phys. Rev.* , vol. D79, p. 074009, 2009. *cited on page 12.*

[55] L. Roca and E. Oset, "Description of the $f_2(1270)$, $\rho_3(1690)$, $f_4(2050)$, $\rho_5(2350)$, and $f_6(2510)$ resonances as multi-$\rho(770)$ states," *Phys. Rev.* , vol. D82, p. 054013, 2011. *cited on page 12.*

[56] K. G. Wilson, "Confinement of quarks," *Phys. Rev.* , vol. D10, p. 2445, 1974. *cited on page 13.*

[57] J. Kogut and L. Susskind, "Hamiltonian formulation of wilson's lattice gauge theories," *Phys. Rev.* , vol. D11, p. 395, 1975. *cited on page 13.*

[58] J. Dudek *et al.*, "Towards the excited meson spectrum of dynamical QCD," *Phys. Rev.* , vol. D82, p. 034508, 2010. *cited on page 13.*

[59] ——, "Isoscalar meson spectroscopy from lattice QCD," *Phys. Rev.* , vol. D83, p. 111502, 2011. *cited on page 13.*

[60] J. Dudek, "The lightest hybrid meson supermuliplet in QCD," *arXiv:1106.5515v1[hep-ph]*, 2011. *cited on pages 13, 14, 15, and 64.*

[61] T. Luu and M. J. Savage, "Extracting scattering phase shifts in higher partial waves from lattice QCD calculations," *Phys. Rev.* , vol. D83, p. 114508, 2011. *cited on page 13.*

[62] T. J. Burns and F. E. Close, "Hybrid-meson properties in lattice QCD and flux-tube models," *Phys. Rev.* , vol. D74, p. 034003, 2006. *cited on page 14.*

[63] J. Kuhn *et al.*, "Exotic meson production in the $f_1(1285)\pi^-$ system observed in the reaction $\pi^- p \rightarrow \eta\pi^+\pi^-\pi^- p$ at 18 GeV/c," *Phys. Lett.* , vol. B595, p. 109, 2004. *cited on pages 14, 66, 111, 116, 135, 139, 150, and 151.*

[64] D.-M. Li and S. Zhou, "Nature of the $\pi_2(1880)$," *Phys. Rev.* , vol. D79, p. 014014, 2009. *cited on page 15.*

[65] D. Bugg, "A study in depth of the $f_0(1370)$," *The European Physical Journal C - Particles and Fields*, vol. 52, pp. 55–74, 2007. *cited on pages 15, 18, 19, 22, 23, 60, and 64.*

[66] W. Ochs, "No indication of $f_0(1370)$ in $\pi\pi$ phase shift analyses," *AIP Conf. Proc.* , vol. 1257, p. 252, 2010. *cited on pages 15 and 64.*

[67] "Study of f_0 decays into 4 neutral pions," *Eur. Phys. J.* , vol. C19, p. 667, 2001. *cited on pages 15, 52, and 65.*

[68] L. Y. Glozman, "Chiral symmetry restoration in excited hadrons and dense matter," *Chin. Phys.* , vol. C34, p. 1212, 2010. *cited on page 16.*

[69] ——, *Pers. Com. (article in preparation)*, 2010. *cited on page 16.*

[70] N. A. Törnqvist, "Understanding the scalar meon $q\bar{q}$ nonet," *Z. Phys.* , vol. C 68, p. 647, 1995. *cited on pages 18, 20, and 21.*

[71] A. V. Anisovich *et al.*, "Scalar glueball: Analysis of the $(IJ^{PC} = 00^{++})$-wave," *Z. Phys.* , vol. A 359, p. 173, 1997. *cited on pages 18 and 20.*

[72] V. Baru *et al.*, "Flatté-like distributions and the $a_0(980)/f_0(980)$ mesons," *Eur. Phys. J.* , vol. A23, p. 523, 2004. *cited on page 22.*

[73] D. Bugg, "Synchronisation of resonances with thresholds," *IJMP*, vol. A24, p. 394, 2009. *cited on page 22.*

[74] "The COMPASS experiment at CERN," *NIM*, vol. A577, no. 455-518, 2007. *cited on pages 25, 27, 28, and 29.*

[75] H. Primakoff, "Photo-production of neutral mesons in nuclear electric fields and the mean life of the neutral meson," *Phys. Rev.* , vol. 81, p. 899, 1951. *cited on page 25.*

[76] S. Grabmüller, "$\pi^- Pb \to \pi^-\pi^-\pi^+ Pb$ at low momentum transfer. release note," 2011. *cited on page 26.*

[77] Y. Giomataris *et al.*, "Micromegas: a high-granularity position-sensitive gaseous detector for high particle flux environments," *Nucl. Inst. Methods*, vol. A376, pp. 29–35, 1996. *cited on page 28.*

[78] D. Thers *et al.*, "Micromegas as large microstrip detector for the COMPASS experiment," *Nucl. Inst. Methods*, vol. A469, p. 133, 2001. *cited on page 28.*

[79] F. Sauli, "GEM: A new concept for electron amplification in gas detectors," *Nucl. Inst. Methods*, vol. A386, pp. 531–534, 1997. *cited on page 28.*

[80] B. Ketzer *et al.*, "Triple GEM tracking detectors for COMPASS," *IEEE Trans. Nucl. Sci.*, vol. 49, pp. 2403–2410, 2002, cERN-OPEN-2002-004. *cited on page 28.*

[81] C. Altunbas *et al.*, "Construction, test and comissioning of the triple-GEM tracking detector for COMPASS," *CERN-EP*, no. 02-008, 2002. *cited on page 28.*

[82] B. Ketzer *et al.*, "A fast tracker for COMPASS based on the GEM," *Nucl. Phys.*, vol. B125, pp. 368–373, 2003. *cited on page 28.*

[83] ——, "Performance of triple GEM tracking detectors in the COMPASS experiment," *Nucl. Inst. Methods*, vol. A535, pp. 314–318, 2004. *cited on page 28.*

[84] (2004, November) COMPASS run-logbook: Comments 11729, 11732 and 11694. [Online]. Available: http://wwwcompass.cern.ch/runLogbook/dirphp/ *cited on page 28.*

[85] T. Nagel, “Cinderella: an online filter for the COMPASS experiment,” Diploma thesis, TU München, 2005. *cited on page 30.*

[86] S. Gerassimov. PHAST, physics analysis tools for COMPASS. [Online]. Available: http://ges.home.cern.ch/ges/phast/index.html *cited on page 32.*

[87] S. U. Chung *et al.*, “Diffractive dissociation for COMPASS,” *COMPASS internal note*, 2008. *cited on page 35.*

[88] T. Regge, “Introduction to complex angular momenta,” *Nuovo Cimento*, vol. 14, p. 951, 1959. *cited on page 36.*

[89] G. F. Chew and S. C. Frautschi, “Principle of equivalence for all strongly interacting particles within the S-matrix framework,” *Phys. Rev. Lett.* , vol. 7, p. 394, 1961. *cited on pages 36 and 38.*

[90] V. N. Gribov, “Asymptotic behaviour of the scattering amplitude at high energies,” *Nucl. Phys.* , vol. 22, p. 249, 1961. *cited on page 36.*

[91] A. C. Irving and R. P. Worden, “Regge phenomenology,” *Phys. Rep.*, vol. 34, no. 3, pp. 117–231, 1977. *cited on pages 36, 38, and 39.*

[92] P. D. B. Collins, *An Introduction to Regge Theory and High Energy Physics.* Cambridge University Press, 1977. *cited on pages 36, 37, and 39.*

[93] R. C. Brower, J. Polchinsky *et al.*, “The pomeron and gauge/string duality,” *Journal of High Energy Physics*, vol. 2007, no. 12, p. 005, 2007. *cited on page 36.*

[94] I. Y. Pomeranchuk, “Equality between the interaction cross sections of high energy nucleons and antinucleons,” *Zh. Eksp. Teor. Fiz.* , vol. 34, p. 725, 1958. *cited on page 38.*

[95] V. N. Gribov, “Reggeon diagram technique,” *Zh. Eksp. Teor. Fiz.* , vol. 53, p. 654, 1967. *cited on page 38.*

[96] L. L. Foldy and R. F. Peierls, “Isotopic spin of exchanged systems,” *Phys. Rev.* , vol. 130, no. 4, pp. 1585–1589, May 1963. *cited on page 38.*

[97] J. R. Cudell *et al.*, “Hadronic scattering amplitudes: Medium-energy constraints on asymptotic behavior,” *Phys. Rev.*, vol. D65, p. 074024, 2002. *cited on pages 38 and 39.*

[98] A. Donnachie and P. V. Landshoff, “pp and $\bar{p}p$ elastic scattering,” *Nucl. Phys.* , vol. B231, p. 189, 1984. *cited on page 39.*

[99] R. Harris *et al.*, “Study of diffractively produced five-pion final states,” *Phys. Lett.*, vol. 59B, p. 187, Aug 1975. *cited on page 40.*

[100] ——, “Diffractive dissociation of pions in $\pi^- d$ interactions at 15 GeV/c,” *Z. Phys.*, vol. C9, p. 275, 1981. *cited on page 40.*

[101] U. Amaldi, M. Jacob, and G. Matthiae, "Diffraction of hadronic waves," *Ann. Rev. Nucl. Sci.* , vol. 26, p. 385, 1976. *cited on page 42.*

[102] Q. Weitzel, "Precision meson spectroscopy: Diffractive production at COMPASS and development of a gem-based tpc for panda," PhD thesis, TU München, 2008. *cited on pages 43, 60, 64, 77, 78, and 151.*

[103] T. Nakano and N. Nishijima, "Charge independence for V-particles," *Prog. Th. Phys.* , vol. 10, p. 581, 1955. *cited on page 48.*

[104] M. Gell-Mann, "The interpretation of the new particles as displaced charged multiplets," *Il Nuovo Cim.*, vol. 4S2, p. 285, 1956. *cited on page 48.*

[105] S. U. Chung and T. L. Trueman, "Positivity conditions on the spin density matrix: A simple parametrization," *Phys. Rev. D*, vol. 11, no. 3, pp. 633–646, Feb 1975. *cited on pages 48, 51, and 73.*

[106] K. M. Watson, "The effect of final state interactions on reaction cross sections," *Phys. Rev.*, vol. 88, no. 5, pp. 1163–1171, Dec 1952. *cited on page 51.*

[107] D. C. Peaslee, "Pion production ratios," *Phys. Rev.*, vol. 94, no. 4, p. 1085, May 1954. *cited on page 51.*

[108] S. J. Lindenbaum and R. M. Sternheimer, "Isobaric nucleon model for pion production in nucleon-nucleon collisions," *Phys. Rev.*, vol. 105, no. 6, pp. 1874–1899, Mar 1957. *cited on page 51.*

[109] E. L. Hart, R. I. Louttit, D. Luers, T. W. Morris, W. J. Willis, and S. S. Yamamoto, "Multiple meson production in proton-proton collisions at 2.85 bev," *Phys. Rev.*, vol. 126, no. 2, pp. 747–756, Apr 1962. *cited on page 52.*

[110] G. N. Fleming, "Recoupling effects in the isobar model. i. general formalism for three-pion scattering," *Phys. Rev.*, vol. 135, no. 2B, pp. B551–B560, Jul 1964. *cited on page 52.*

[111] I. J. R. Aitchison and J. J. Brehm, "Are there important unitarity corrections to the isobar model?" *Physics Letters B*, vol. 84, pp. 349–353, Jul. 1979. *cited on page 52.*

[112] P. Guo, R. Mitchell, and A. P. Szczepaniak, "The role of P-wave inelasticity in J/ψ to $\pi^+\pi^-\pi^0$," 2010. *cited on pages 52 and 57.*

[113] G. Ascoli *et al.*, "Partial-wave analysis of the 3π decay of the a_2," *Phys. Rev. Lett.* , vol. 25, p. 962, 1970. *cited on pages 52 and 58.*

[114] G. Thompson *et al.*, "Partial-wave analysis of the low-mass $\pi^+\pi^+\pi^-$ system produced by incident π^+ mesons at 13 GeV/c," *Phys. Rev.* , vol. D9, p. 560, 1974. *cited on pages 52 and 58.*

[115] S. U. Chung *et al.*, "Exotic and $q\bar{q}$ resonances in the $\pi^+\pi^-\pi^-$ system produced in π^-p collisions at 18 GeV/c," *Phys. Rev.* , vol. D65, p. 072001, 2002. *cited on pages 52, 58, and 81.*

[116] J. H. Lee. (2012, February) The bnl four-body partial wave analysis system. [Online]. Available: hadron.physics.fsu.edu/~e852/reviews/pwa.ps *cited on page 52.*

[117] "4π-decays of scalar and vector mesons," *Eur. Phys. J.*, vol. C21, p. 261, 2001. *cited on pages 52, 62, 64, and 65.*

[118] S. U. Chung, "Spin formalisms," *BNL-QGS-02-0900*, 2008. *cited on pages 53, 54, and 56.*

[119] F. von Hippel and C. Quigg, "Centrifugal-barrier effects in resonance partial decay widths, shapes, and production amplitudes," *Phys. Rev.*, vol. D5, p. 624, 1972. *cited on page 55.*

[120] Brehm, "Simplified parameterization of 3π final state interactions," *Phys. Rev.*, vol. D25, p. 3069, 1982. *cited on page 55.*

[121] S. U. Chung and J. Friedrich, "Covariant helicity-coupling amplitudes: A new formulation," *Phys. Rev.*, vol. D78, p. 074027, 2008. *cited on page 56.*

[122] D. Bugg, "Experimental disagreements with extended unitarity," *Eu. Phys. J.*, vol. C54, p. 73, 2008. *cited on page 57.*

[123] R. Kaminski, J. R. Peláez, and F. J. Ynduráin, "Pion-pion scattering amplitude. III. improving the analysis with forward dispersion relations and Roy equations," *Phys. Rev. D*, vol. 77, no. 5, p. 054015, Mar 2008. *cited on pages 57 and 58.*

[124] A. Dobado and J. R. Peláez, "Inverse amplitude method in chiral perturbation theory," *Phys. Rev. D*, vol. 56, no. 5, pp. 3057–3073, Sep 1997. *cited on page 58.*

[125] J. R. Peláez and F. J. Ynduráin, "Pion-pion scattering amplitude," *Phys. Rev. D*, vol. 71, no. 7, p. 074016, Apr 2005. *cited on page 58.*

[126] R. Kaminski, J. R. Peláez, and F. J. Ynduráin, "Pion-pion scattering amplitude. II. improved analysis above $K\bar{K}$ threshold," *Phys. Rev. D*, vol. 74, no. 1, p. 014001, Jul 2006. *cited on page 58.*

[127] K. L. Au, D. Morgan, and M. R. Pennington, "Meson dynamics beyond the quark model: Study of final-state interactions," *Phys. Rev. D*, vol. 35, no. 5, pp. 1633–1664, Mar 1987. *cited on pages 58 and 59.*

[128] R. T. Deck, "Kinematical interpretation of the first $\pi - p$ resonances," *Phys. Rev. Lett.*, vol. 13, p. 169, 1964. *cited on page 59.*

[129] M. G. Bowler *et al.*, "Diffraction dissociation, the deck mechanism and diffractive resonance production," *Nucl. Phys.*, vol. B97, p. 227, 1975. *cited on page 59.*

[130] S. Schael *et al.*, "Branching ratios and spectral functions of τ decays: Final aleph measurements and physics implications," *Phys. Rep.*, vol. 421, p. 191, 2005. *cited on page 59.*

[131] A. Donnachie and H. Mirzaie, "Evidence for two $\rho'(1600)$ resonances," *Z. Phys.*, vol. C33, p. 407, 1987. *cited on pages 62 and 63.*

[132] K. W. Edwards *et al.*, "Resonant structure of $\tau \to 3\pi\pi^0\nu_\tau$ and $\tau \to \omega\tau\nu_\tau$ decays," *Phys. Rev.*, vol. D61, p. 072003, 2000. *cited on page 62.*

[133] T. B. Collaboration, "High-statistics study of the $\tau^- \to \pi^-\pi^0\nu_\tau$ decay," *Phys. Rev.* , vol. D78, p. 072006, 2008. *cited on page 62.*

[134] J. P. Cummings and D. P. Weygand, "An object-oriented approach to partial wave analysis," *arXiv:physics/0309052v1*, 2003. *cited on page 69.*

[135] S. Neubert and B. Grube. (2011, November) ROOTPWA, a suite of tools for partial wave analysis in hadron spectroscopy. [Online]. Available: http://sourceforge.net/projects/rootpwa/ *cited on pages 69 and 92.*

[136] J. D. Hansen *et al.*, "Formalism and assumptions invovled in partial wave-wave analysis of three-meson systems," *Nucl. Phys.* , vol. B81, p. 403, 1974. *cited on page 69.*

[137] P. Jasinski, "Analysis of diffractive dissociation of K into $K\pi^+\pi$ on a liquid hydrogen target at the COMPASS spectrometer," PhD thesis, Universität Mainz, 2012. *cited on page 69.*

[138] N. Berger, "Partial wave analysis at BES III harnessing the power of GPUs," *arXiv:1108.5673v1*, 2011. *cited on page 70.*

[139] F. James, "Monte Carlo phase space," *CERN Yellow Report 68-15*, 1968. *cited on pages 73, 77, and 126.*

[140] R. Barlow, "Extended maximum likelihood," *NIM*, vol. A297, p. 496, 1990. *cited on page 74.*

[141] F. James. Minuit2 minimization package. [Online]. Available: http://seal.web.cern.ch/seal/MathLibs/Minuit2/html/ *cited on pages 75 and 127.*

[142] R. Brun and F. Rademakers. ROOT. [Online]. Available: http://root.cern.ch *cited on pages 76 and 77.*

[143] COMGEANT. [Online]. Available: http://wwwcompass.cern.ch/compass/software/offline_old/comgeant/comgeant/ *cited on page 77.*

[144] B. Gobbo. CORAL, the COMPASS reconstruction program. [Online]. Available: http://coral.web.cern.ch/coral/ *cited on page 77.*

[145] A. R. Dzierba *et al.*, "A partial wave analysis of the $\pi^-\pi^-\pi^+$ and $\pi^-\pi^0\pi^0$ systems and the search for a $J^{PC} = 1^{-+}$ meson," *Phys. Rev.* , vol. D73, p. 072001, 2006. *cited on page 81.*

[146] D. MacKay, *Information Theory, Inference and Learning Algorithms.* Camebrigde University Press, 2003. *cited on pages 82 and 83.*

[147] C. M. Bishop, *Pattern Recognition and Machine Learning.* Springer New York, 2006. *cited on page 82.*

[148] R. E. Kass and A. E. Raftery, "Bayes factors," *J. Am. Stat. Assoc.* , vol. 90, p. 773, 1995. *cited on pages 83 and 87.*

[149] R. E. Kass and L. Wassermann, "The selection of prior distributions by formal rules," *J. Am. Stat. Assoc.* , vol. 91, p. 1343, 1996. *cited on page 84.*

[150] H. Jeffreys, *Theory of Probability*. Oxford University Press, 1961. *cited on page 84.*

[151] D. V. Lindley, “The present postion in bayesian statistics,” *Stat. Sci.* , vol. 5, p. 44, 1990. *cited on page 84.*

[152] J. Holland, *Adaption in Natural and Artificial Systems*. University Michigan Press, 1975. *cited on page 88.*

[153] D. E. Goldberg, *Genetic Algorithms in Search, Optimization, and Machine Learning*. Addison-Wesley, 1989. *cited on page 88.*

[154] E. Schöneburg *et al.*, *Genetische Algorithmen und Evolutionsstrategien*. Addison-Wesley, 1999. *cited on page 88.*

[155] T. Weise. (2009) Global optimization algorithms. [Online]. Available: http://www.it-weise.de *cited on page 88.*

[156] D. E. Goldberg and K. Deb, “A comparative analysis of selection schemes used in genetic algorithms,” in *Foundations of Genetic Algorithms*. Morgan Kaufmann, 1991, p. 69. *cited on page 90.*

[157] Oracle. (2011, November) Sun grid engine documentation center. [Online]. Available: http://wikis.sun.com/display/sungridengine/Home *cited on page 92.*

[158] A. C. Rencher, *Methods of Multivariate Analysis*. Wiley-Interscience, 2002. *cited on page 108.*

[159] E. M. Aitila *et al.*, “Model-independent measurement of s-wave $k^-\pi^+$ systems using $d^+ \to k\pi\pi$ decays from fermilab e791,” *Phys. Rev.* , vol. D73, p. 032004, 2006. *cited on page 120.*

[160] D. Ryabchikov, “On mass-dependent isobar fits,” *Pers. com.* , 2011. *cited on page 122.*

[161] S. U. Chung *et al.*, “Mass dependence of invariant phase-space elements,” *COMPASS internal note*, 2011. *cited on page 126.*

[162] P. E. et al, “Observation of the $\pi(1800)$ and $pi_2(1880)$ mesons in $\eta\eta\pi^-$ decay,” *Physics Letters B*, vol. 660, no. 5, pp. 466 – 470, 2008. *cited on page 134.*

[163] D. V. Amelin *et al.*, “Study of diffractive reaction $\pi^- A \to \eta\eta\pi^- A$ at the momentum $p_{\pi^-} = 37\,\mathrm{GeV}/c$,” *Yad. Fiz.* , vol. 59, p. 1021, 1996. *cited on page 134.*

[164] A. V. Anisovich *et al.*, “A fresh look at $\eta_2(1645)$, $\eta_2(1870)$, $\eta_2(2030)$ and $f_2(1910)$ in $\bar{p}p \to \pi^0\pi^0\pi^0$,” *Eur. Phys. J.* , vol. C71, p. 1511, 2011. *cited on page 148.*

[165] M. Lu *et al.*, “Exotic meson decay to $\omega\pi^0\pi^-$,” *Phys. Rev. Lett.*, vol. 94, no. 3, p. 032002, Jan 2005. *cited on page 150.*

[166] D. Nygren, “Proposal to investigate the feasibility of a novel concept in particle detection,” *LBL internal report*, 1974. *cited on pages 157 and 158.*

[167] J. Marx, “The PEP-4 facility (TPC) as the initial detector at SLC: Letter of intent,” sLAC-PROPOSAL-SLC-05. *cited on page 157.*

[168] T. Kamae *et al.*, "The Topaz time projection chamber," *Nucl. Inst. Methods Phys. Res.*, vol. A252, pp. 423–430, 1986. *cited on page 157.*

[169] C. Brand *et al.*, "The Delphi time projection chamber," *Nucl. Inst. Methods Phys. Res.*, vol. A283, pp. 567–572, 1989. *cited on page 157.*

[170] M. Fuchs *et al.*, "Very high multiplicity tracking in heavy ion collisions with the NA49 time projection chambers (TPCs)," *Nucl. Inst. Methods Phys. Res.*, vol. A367, pp. 394–397, 1995. *cited on page 157.*

[171] M. Anderson *et al.*, "The STAR time projection chamber: a unique tool for studying high multiplicity events at RHIC," *Nucl. Inst. Methods Phys. Res.*, vol. A499, pp. 659–678, 2003. *cited on page 157.*

[172] A. collaboration, "ALICE technical design report: Time projection chamber," CERN, Tech. Rep., 2000. *cited on page 157.*

[173] G. Charpak, R. Bouclier, T. Bressani, J. Favier, and C. Zupancic, "The use of multiwire proportional counters to select and localize charged particles," *Nucl. Inst. Methods*, vol. 62, pp. 262–268, 1968. *cited on page 157.*

[174] W. Blum and L. Rolandi, *Particle Detection with Drift Chambers*, 1st ed. Springer, 1993. *cited on pages 158, 160, and 178.*

[175] F. Sauli and A. Sharma, "Micropattern gaseous detectors," *Nucl. Part. Sci.*, vol. Annual Review, 1999. *cited on page 158.*

[176] F. Sauli, S. Kappler, and L. Ropelewski, "Electron collection and ion feedback in GEM-based detectors," *IEEE Nucl. Sci. Symposium*, November 2002. *cited on page 158.*

[177] F. Sauli *et al.*, "Electron collection and ion feedback in GEM-based detectors," *IEEE Trans. Nucl. Sci.*, vol. 50, p. 803, 2003. *cited on pages 158 and 177.*

[178] A. Bondar *et al.*, "Study of ion feedback in multi-GEM structures," *Nucl. Inst. Methods*, vol. A496, pp. 325–332, 2003. *cited on pages 158 and 177.*

[179] L. Fabietti *et al.*, "The PANDA GEM-based TPC prototype," *Nucl. Instrum. Methods*, vol. A628, p. 204, 2011. *cited on pages 159 and 170.*

[180] "PANDA: Technical progress report," GSI FAIR, Tech. Rep., 2005. *cited on page 159.*

[181] S. N., "A GEM based TPC for PANDA - simulations and prototype design," Diploma Thesis, TU München, 2005. *cited on pages 159, 160, and 171.*

[182] M. Al-Turany. !FAIR ROOT. [Online]. Available: http://fairroot.gsi.de/ *cited on pages 159, 164, and 171.*

[183] C. Höppner, "First measurement of the cross section for the production of hadrons with high transverse momenta at COMPASS, and developments for particle tracking in high-rate experiments," PhD Thesis, TU München, 2012. *cited on pages 159, 161, and 170.*

[184] C. Höppner *et al.*, "A novel generic framework for track fitting in complex detector systems," *NIM*, vol. A620, p. 518, 2010. *cited on pages 159 and 170.*

[185] C. Hoeppner and S. N. [Online]. Available: http://genfit.sourceforge.net/Main.html *cited on pages 159 and 170.*

[186] J. Perl *et al.* Workbook for BaBar offline users. [Online]. Available: http://www.slac.stanford.edu/BFROOT/www/doc/workbook/workbook.html *cited on page 159.*

[187] I. Hrivnacova *et al.* VMC. [Online]. Available: http://root.cern.ch/drupal/content/vmc *cited on page 159.*

[188] CERN, "GEANT - detector description and simulation tool," *CERN Program Library Long Write-up*, vol. W5013, 1993. *cited on pages 159 and 169.*

[189] R. Veenhof, "Choosing a gas mixture for the ALICE TPC," *ALICE internal note*, vol. ALICE-INT-2003-29, 2003. *cited on page 160.*

[190] M. Kowalski, "ALICE TPC slow simulator," *ALICE Internal Note*, vol. 96-36, 1996. *cited on page 160.*

[191] M. Liu *et al.*, "Trigger algorithm development on FPGA-based compute nodes," *J. Phys*, vol. Conf. Ser. 119, p. 022027. *cited on page 161.*

[192] J. V. Neumann and A. W. Burks, *Theory of self-reproducing automata.* University of Illinois Press, 1966. *cited on page 161.*

[193] R. Mankel, "Pattern recognition and event reconstruction in particle physics experiments," *Rep. Prog. Phys.* , vol. 67, p. 553, 2004. *cited on page 165.*

[194] A. Strandlie, J. Wroldsen, R. Frühwirth, and B. Lillekjendlie, "Particle Tracks Fitted on the Riemann Sphere," *Computer Physics Communications*, vol. 131, no. 1-2, 2000. *cited on page 165.*

[195] A. S. R. Frühwirth and W. Waltenberger, "Helix Fitting by an Extended Riemann Fit," *NIM*, vol. A490, no. 1-2, 2002. *cited on page 165.*

[196] F. V. Böhmer, "A high-rate time projection chamber for PANDA: Simulation studies and gpu-based track-finding," Diploma Thesis, TU München, 2009. *cited on pages 166, 167, and 180.*

[197] P. V. C. Hough, "Method and means for recognizing complex patterns," U.S. Patent 3069654, 1962. *cited on page 166.*

[198] P. V. C. Hough and B. W. Powell, "A method for faster analysis of bubble chamber photographs," *Il Nuovo Cimento*, vol. 18, no. 6, p. 1184, 1960. *cited on page 166.*

[199] H. Li, M. A. Lavin, and R. J. Le Master, "Fast Hough Transform: A hierarchical approach," *Computer Vision, Graphics and Image Processing*, vol. 36, 1986. *cited on page 167.*

[200] NVIDIA Corp., *NVIDIA*^{TM} *CUDA*^{TM} *Programming Guide*, 2009, vol. 2.2.1. *cited on page 167.*

[201] J. Rauch, "Tracking with a high-rate GEM-TPC," Diploma Thesis, TU München, 2011. *cited on pages 167, 169, 171, 172, 175, and 176.*

[202] T. Ypsilantis, "Cerenkov ring imaging," *Phys. Scr.*, vol. 23, p. 371, 1981. *cited on page 168.*

[203] E. Anassontzis *et al.*, "The barrel ring imaging Cherenkov counter of DELPHI," *NIM*, vol. A323, no. 1âĂŞ2, pp. 351 – 362, 1992. *cited on page 168.*

[204] T. B.-D. Collaboration, "Dirc, the internally reflecting ring imaging cherenkov detector for babar," *IEEE Trans. Nucl. Sci.* , vol. 45, p. 657, 1998. *cited on page 168.*

[205] R. Frühwirth, "Application of Kalman filtering to track and vertex fitting," *NIM*, vol. A262, p. 444, 1987. *cited on pages 168 and 170.*

[206] R. Frühwirth and A. Strandlie, "Track fitting with ambiguities and noise: a study of elastic tracking an nonlinear filters," *Comp. Phys. Comm.* , vol. 120, p. 197, 1999. *cited on pages 168 and 170.*

[207] A. Fontana *et al.*, "Use of GEANE for tracking in virtual Monte Carlo," *J. Phys: Conf. Ser.*, vol. 190, p. 032018, 2008. *cited on page 169.*

[208] R. E. Kalman, "A new approach to linear filtering and prediction problems," *Trans. ASME*, vol. D82, pp. 35–45, 1960. *cited on page 170.*

[209] W. Erni *et al.*, "Technical design report for the panda solenoid and dipole spectrometer magnets," *arXiv:0907.0169v1 [physics.ins-det].* *cited on page 171.*

[210] R. Veenhof. Simulation of gaseous detectors. [Online]. Available: http://consult.cern.ch/writeup/garfield/ *cited on page 171.*

[211] A. Capella, U. Sukhatme, C. I. Tan, and J. T. T. Van, "Dual parton model," *Physics Reports*, vol. 236, no. 4-5, pp. 225 – 329, 1994. *cited on pages 171 and 177.*

[212] D. Reistad *et al.*, "Experiences of operating celsius with a hydrogen pellet target," *Nucl. Inst. Methods*, vol. A532, pp. 118–122, 2004. *cited on page 172.*

[213] F. V. Böhmer *et al.*, "Simulation and correction of space charge effects in a GEM-based high-rate TPC," *to be published*, 2012. *cited on pages 177 and 180.*

[214] S. B. S. Lotze *et al.*, "Charge transfer of GEM structures in high magnetic fields," in *9th Topical Seminar on Innovative Particle and Radiation Detectors*, Siena, italy, May 2004. [Online]. Available: http://www.physik.rwth-aachen.de/group/IIIphys/TESLA/en/index.html *cited on page 177.*

[215] H. Wieman. STAR TPC luminosity limitations (talk). [Online]. Available: http://www.star.bnl.gov/STAR/meetings_l/collab_l/future/hwieman/ *cited on page 178.*

[216] A. Logg, G. N. Wells *et al.* DOLFIN project. [Online]. Available: http://fenicsproject.org/ *cited on page 178.*

[217] J. Abele *et al.*, "The laser system for the STAR time projection chamber," *Nucl. Inst. Meth. Section A*, vol. 499, no. 2-3, pp. 692 – 702, 2003. *cited on page 180.*

[218] P. D. Hall, “On the propagation of uncertainty in complex valued quantities,” *Metrologica*, vol. 41, p. 173, 2004. *cited on page 207.*

Own Contributions

The complete analysis from the selection of the data from the COMPASS data summary tapes, the detector simulation and the two-step amplitude analysis have been done by myself. The data selection has been cross-checked by Johannes Bernhard. For the initial data handling and the detector simulation I have used COMPASS software infrastructure. For the main steps of the data refinement as well as the complete partial wave analysis new software has been developed by myself. In particular the genetic waveset selection was my own idea and responsibility.
In the later stages of the `rootpwa` project I collaborated with Boris Grube, who cross-checked and improved the code of the mass-independent analysis in many places. In the meantime this software package has been used by several researchers, who also contributed to the code.
The 5-pion analysis has been cross-checked by Dima Ryabchikov who also contributed valuable advice to all analysis steps. I also was responsible for the cross-check of the partial wave analysis of the 3π system using the `rootpwa` program.
I have defended the results obtained in this analysis in front of the COMPASS collaboration.
In addition during my time as graduate student I have represented the COMPASS hadron-analysis group several times at international workshops and conferences including group reports, overview talks and workshop lectures.
As part of the GEM group at E18 I was responsible for the operation of the GEM trackers at COMPASS taking "on call" duties for this subsystem. In addition I did regular shifts for the complete COMPASS spectrometer. Also I have designed and built a thin foil target for the 2009 COMPASS hadron run, which has been used to record πPb and πW interactions.
As member of the PANDA computing group I was the primary author of the TPC simulation code. I was also engaged in the working-group on the PANDA software framework(s) and the tracking subgroup, which I briefly had the honor of chairing. The TPC pattern recognition algorithms have been designed by me in close exchange with the GEM-TPC group. The implementation was completed by two Diploma students under my supervision. The GENFIT tracking software has been developed in very close collaboration with Christian Höppner with an equal-parts sharing of responsibilities. Both the event-deconvolution studies as well as the space-charge simulations have been designed and supervised by me but have been completed by Diploma students.